Semiconductor Lasers:
New Geometries and Spectral Properties

Thesis by

Robert J. Lang

In Partial Fulfillment of the Requirements

for the Degree of

Doctor of Philosophy

California Institute of Technology

Pasadena, California

1986

(Submitted May 14, 1986)

Acknowledgments

This thesis is the result of three years of work at Caltech. It would not exist but for the unfailing support of my advisor, Dr. Amnon Yariv. His advice and encouragement have been a source of inspiration while I have been at Caltech, and will remain so throughout my professional career.

Much of the work contained in the following pages was performed in close collaboration with Dr. Kerry Vahala and Dr. Joseph "Yosi" Salzman. It has been my great pleasure to interact with them on matters scientific; yet I value even more their friendship.

I would also like to thank the following for collaborations and discussions that contributed to this work: Michael Mittelstein, Venky Venkatesan, Yasuhiko Arakawa, Shlomo Margalit, and Joel Paslaski.

My deepest thanks go to Desmond Armstrong for expert technical assistance, and Jana Mercado for assistance in day-to-day matters.

Special thanks go to Diane Davis for comments on grammar and style, for proofreading, and for general moral support.

In addition, I am grateful for fellowship support from the National Science Foundation and IBM Corporation.

To

Jim
Carolyn
Greg
Marla

Abstract

This thesis is an investigation into the spectral properties of two broad classes of semiconductor lasers. They are (1) broad-area lasers with non-planar mirrors, specifically, those with an unstable resonator configuration, and (2) coupled-cavity semiconductor lasers.

The use of non-planar mirrors on broad-area lasers can substantially improve their properties. Chapter 2 focuses on the experimental realization of several unstable resonator semiconductor lasers, while chapter 3 presents a method of analyzing the modes of such a device.

Coupling two cavities together can drastically alter the dynamic and spectral properties of a semiconductor laser. In chapter 4 we present experimental measurements and explain the properties of a laser consisting of two side-by-side coupled cavities. We then turn to the theoretical problem of analyzing the dynamic properties of multicavity lasers. In chapter 5, we derive a general expression for the dynamic response of a multielement laser. In the process, we develop a formalism for treating the dynamics of any semiconductor laser system with particular ease of application to single-mode multielement lasers. In chapter 6, we show that 2 or more cavities can lead to bistability and bimodality. The quantum fluctuation-induced noise properties of multicavity lasers are analyzed in chapter 7. In chapter 8, we return to the single-element laser and calculate non-quantum noise contributions--specifically, thermal and diffusion noise-- which give rise to a 1/f spectrum. In chapter 9 we present a new method of deriving multicavity rate equations and point out a shortcoming of the existing coupled-mode treatments.

Table of Contents

Chapter 4 Laterally Coupled-Cavity Semiconductor Lasers

Chapter 5 Dynamic Analysis of Multielement Semiconductor Lasers

Chapter 6 Intermodal Stability of a Coupled-Cavity Laser

Chapter 7 Semiclassical Theory of Noise in Multielement Semiconductor Lasers

Chapter 8 The Effect of Spatially Dependent Temperature and Carrier Fluctuations on Noise in Semiconductor Lasers

Chapter 9 Local Field Rate Equations for Coupled Optical Resonators

Chapter 1

Introduction

1.1 Historical Perspective

The history of the laser is a short one; the time from the first demonstration of an optical maser in ruby [1] to the present has been a mere 26 years. Within a few short years of that first demonstration, however, a flood of new laser systems appeared, including the helium-neon laser in 1961 [2], the ion laser in 1964 [3], and a host of solid-state lasers through the mid-1960's [4-5]. Among the latter was the semiconductor injection laser.

The idea predated the implementation, of course. While Schawlow and Townes in 1958 had formulated the general conditions for a visible laser in a medium consisting of localized atomic states [6], semiconducting material, with its delocalized states and important phonon processes, presented special difficulties to the analysts. Bernard and Duraffourg showed in 1961 [7] that the necessary condition for stimulated emission in a semiconductor was that the imrefs (quasi-Fermi levels) for the electrons and holes in a semiconductor be separated by more than the energy of the emitted radiation. In the same year, Basov *et al.* proposed that the necessary conditions could be met by injecting electrons and holes across a *p*-*n* junction [8]. Initially, the workers concentrated their efforts on III-V compounds, and in 1962 four different groups demonstrated working devices [9-12], three of them based on GaAs, one on GaAsP. The lasers all had one feature in common; they were all fabricated by diffusing a *p*-type dopant into an *n*-type wafer, and because the junction and the surrounding region were made of the same material, they were dubbed *homojunctions* (figure 1.1).

Semiconducting material suffers from high optical loss at the wavelengths at which lasing was being considered--typically, the absorption length is a few μm. Consequently, high optical gain is required for laser action. The achievement of sufficient gain to overcome the losses requires a high concentration of both electrons and holes in the active region. Homojunctions suffer from poor carrier confinement, however; the active region (the region of high optical gain) is determined by the overlap of high electron and high hole concentrations (figure 1.2), which is already a narrow region. Furthermore, at room temperature the distributions become further smeared out and the gain is correspondingly reduced. This feature limited the early devices to low-temperature operation. In fact, while the years following 1962 saw an increase in the number of lasing systems to include GaInAs, InP, and InAsP [13-15], there was no such increase in the efficiency of the devices. Threshold currents stayed high (35–50 kA/cm^2) and efficiencies low. The semiconductor laser remained a pulsed, low-temperature device suited for the laboratory only.

The first glimmers of continuous-wave (CW) operation and commercial practicality came in the late 1960's with the development of the stripe contact to limit the current to a narrow region of the laser. The second great innovation was the *heterojunction*, composed of dissimilar materials. Although Kroemer [16] had suggested as far back as 1963 that a sandwich of a narrow-bandgap material between two wide-bandgap materials would confine the carriers more effectively, serious work on the concept did not begin until 1966-67. At that time, one of the rare generosities of Nature occured when it was realized that GaAs and AlAs are almost perfectly lattice-matched (figure 1.3). Thus, layers of GaAs and AlAs (or any mixture thereof) could be grown with few defects at the

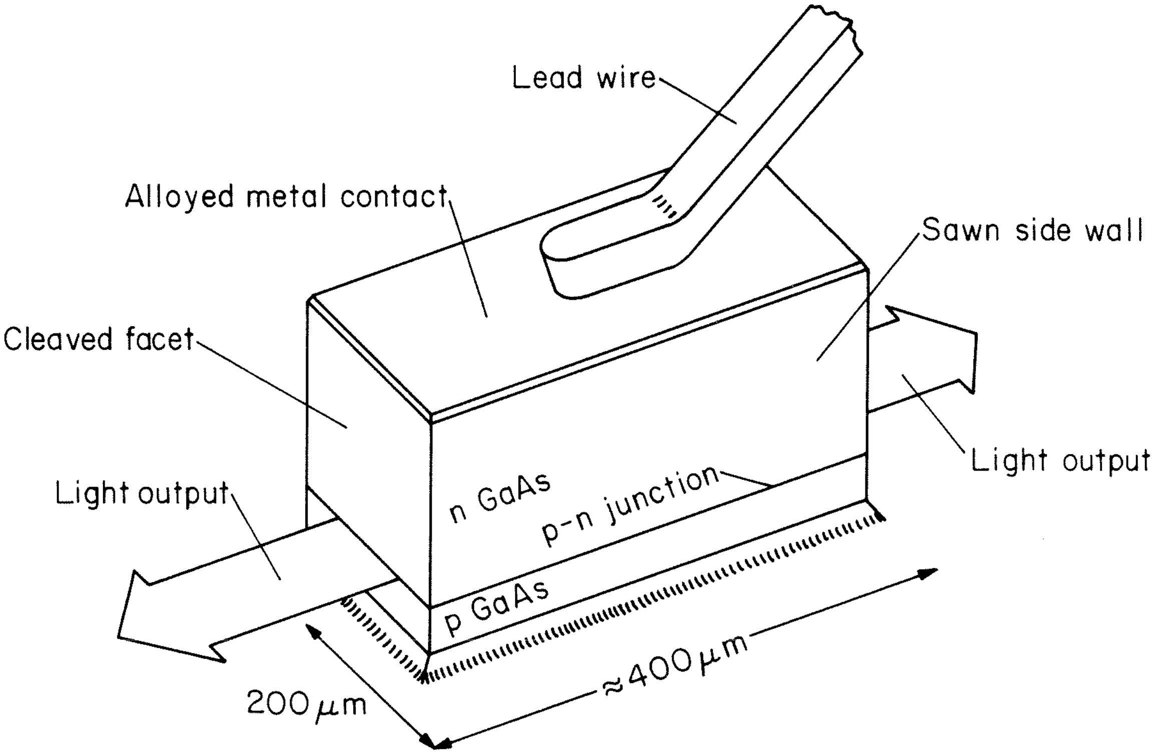

Figure 1.1: Schematic of a broad-area homojunction semiconductor laser. The facets are cleaved while the sidewalls are sawn to prevent spurious lasing action.

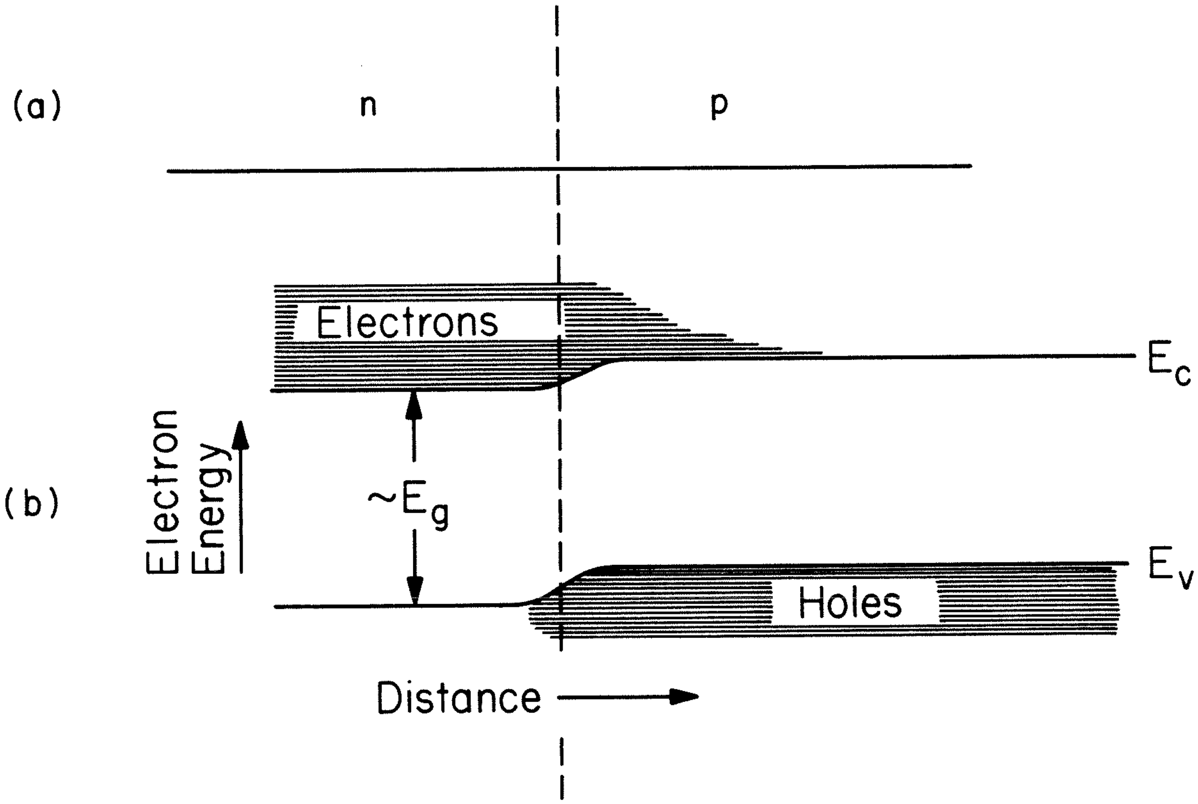

Figure 1.2: Schematic of the electron and hole populations in a homojunction. High gain exists only in the overlapping region of electrons and holes.

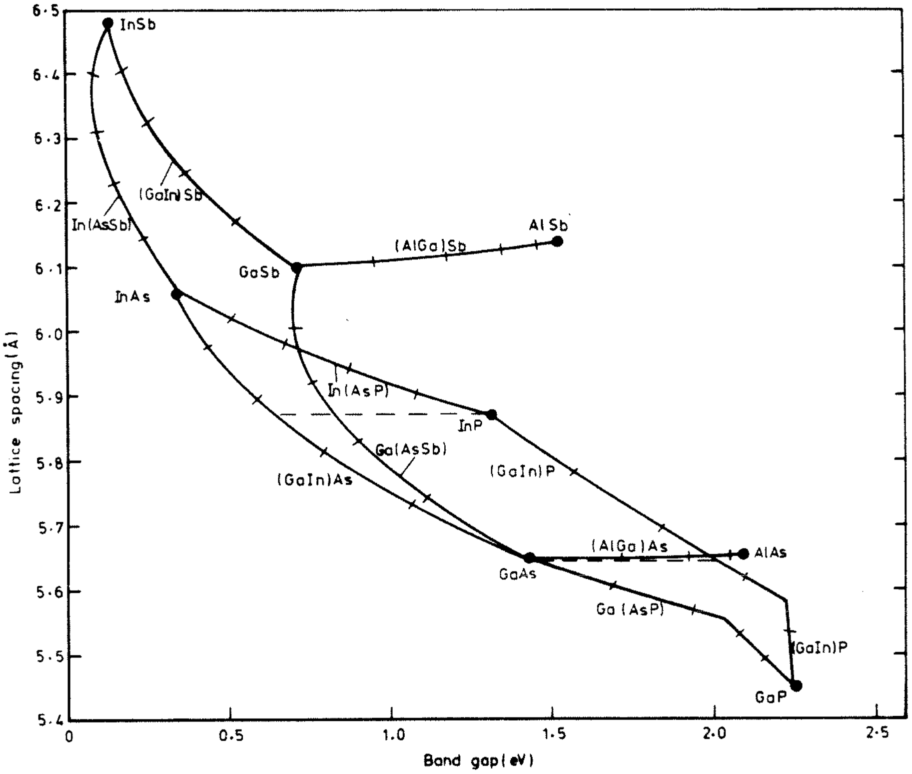

Figure 1.3: Lattice parameter versus bandgap of various III-V compounds. Note that the lattice parameter is almost constant for $Ga_xAl_{1-x}As$ compounds.

junction, giving high efficiency and the benefits of a heterostructure. Throughout 1968-69 several researchers worked towards lowering the room-temperature threshold current of single and double heterostructures [17-18], and in 1970, Hayashi and Panish demonstrated room-temperature CW operation of a GaAlAs-GaAs double heterostructure laser [19-20]. Since that time, a steady stream of improvements has lowered the threshold, increased the speed and power, improved the spectral properties, and otherwise set the semiconductor laser on the course that has brought us the ubiquitous device of the present.

And what a device it is. In recent years, semiconductor lasers have been demonstrated to reach 80% differential quantum efficiency [21]--that is, of every ten electrons injected into the active region, eight produce photons. A 50% "wall-plug" efficiency (total optical power out divided by total electrical power in) is not unreasonable, and while the standard "workhorse" CW lasers produce 5-10 mW of optical output power, single devices are commercially available with powers up to 100 mW CW [22], while phased arrays have been reported to produce up to 5.4 W CW [23]. At the other end of the power spectrum, threshold currents as low as 2.5 mA have been reported. Extrapolated room-temperature lifetimes are in excess of 10^7 hours, with degradation rates of $\approx 10^{-5}$ hr^{-1} at 100 C° [24]. One of the great advantages to semiconductor lasers is the fact that their output can be directly modulated by voltages on the order of 2 volts or so, which makes them eminently suitable for use with electronics in communications systems. With the advent of low-loss, low dispersion optical fibers, transmission distance-bandwidth products can be achieved that would be impossible with coaxial systems. For example, a recent experiment demonstrated 1 Gbit/sec repeaterless transmission over 120 km of fiber [25]. In recent years, the modulation bandwidth of a semiconductor laser has been pushed up well above 10 GHz. Currently, the record bandwidth is DC to 15 GHz [26], but with new developments being reported at every scientific conference, it is a record that is not likely to stand.

Semiconductor lasers have the additional property that their output wavelength can be varied by altering the stochiometry of the growth materials. For example, $Ga_xAl_{1-x}As$ lasers operate in the range .8–.9 μm, $In_xGa_{1-x}As_yP_{1-y}$ lasers in the range 1.1–1.7 μm, $Pb_xSn_{1-x}Te$ lasers in the range 2–20 μm. The wavelength can be further altered by use of quantum well structures to shift the energy bands of the semiconductor, and GaAlAs lasers have been produced by this technique with wavelengths well into the visible region of the spectrum. Currently, the shortest wavelength semiconductor laser known is a GaAsP-GaAlAsP laser lasing at .6617 μm [27]. The immediate goal of short-wavelength research is to reach the "magic" HeNe wavelength of .633 μm; as it approaches, many potential applications involving the replacement of HeNe lasers are becoming apparent. While GaAlAs lasers have historically undergone the most development, the InGaAsP system is now seeing a great deal of work aimed at exploiting low-loss "windows" in optical fiber systems near 1.3 and 1.55 μm wavelength. In recent years, the main thrust of research in ultrafast electronics has turned from silicon to gallium arsenide due to the latter's higher speed (higher electron mobility) leading to visions of lasers and fast electronics integrated upon the same chip; now, however, it appears that the future of high-speed laser communications lies with the quaternary (InGaAsP) system for low-dispersion, low-loss transmission through optical fibers.

1.2 Lasing Action in Semiconductors

While a general familiarity of operation of semiconductor lasers is assumed throughout this thesis, a bit of an overview of their properties and operation is in order, if only to establish some consistent terminology. At its most basic level, a laser is an electronic oscillator, albeit one that works at optical frequencies. Like any oscillator, it consists of an amplifier and a feedback mechanism. The amplification in a diode laser comes from a semiconducting medium in which free electrons and holes are (a) present, (b) free to recombine via an optical transition. The second requirement restricts the field to direct-bandgap materials, e.g., GaAs, for in indirect-bandgap semiconductors, e.g., silicon or germanium, absorption of a photon requires absorption of a phonon as well (figure 1.4a-b). In addition, the material must not possess alternate paths for electron-hole recombination favored over that of absorption of an optical photon (figure 1.4c), or it will be difficult or impossible to maintain a population inversion. Impurities and crystal defects provide intermediate energy levels within the bandgap and create such alternate pathways. Thus, pure crystalline materials with a minimum of defects are a necessity for efficient lasing action.

In figure 1.5, we show a schematic of a typical double-heterostructure laser. It consists of a *p-n* junction with several additional layers providing optical and/or carrier confinement. When a bias voltage is applied, electrons (holes) are injected into the active region from the bottom (top). The purpose of the heterostructure is to create a shallow well in the conduction and valence bands, which tends to prevent the electrons and holes from escaping before undergoing stimulated emission. In yet another of the generosities of Nature, the index of refraction of the active layer is larger than that of the surrounding layers so that any light generated within the active region remains confined by a dielectric waveguide. Light traveling perpendicularly to the two cleaved facets is reflected back upon itself by the discontinuity in the index of refraction. As it traverses the active region it stimulates the electron-hole pairs to recombine and give off coherent photons (one per pair) in the process. In this fashion, light is continuously reflected back and forth between the two cleaved facets with the

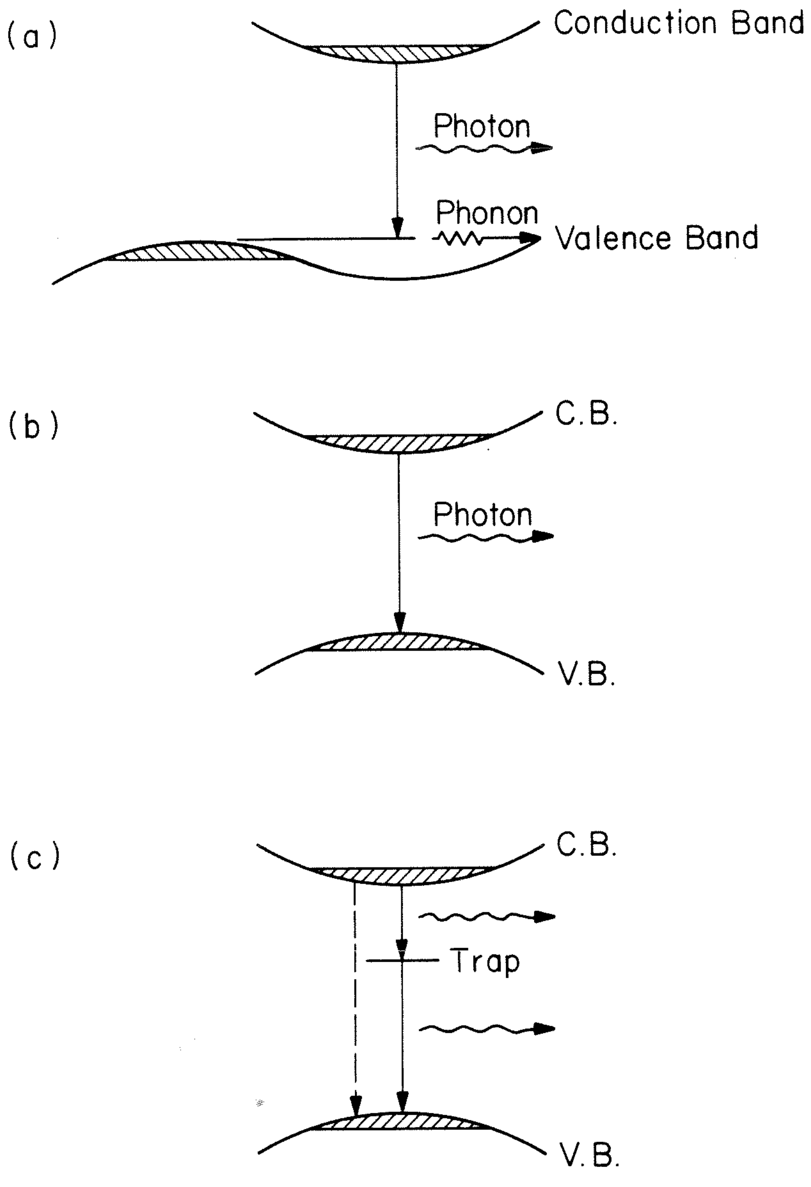

Figure 1.4: (a) Electron-hole recombination in an indirect-bandgap material. A phonon is required for recombination. (b) Recombination in a direct-bandgap semiconductor, requiring no phonon. (c) Recombination via an impurity level.

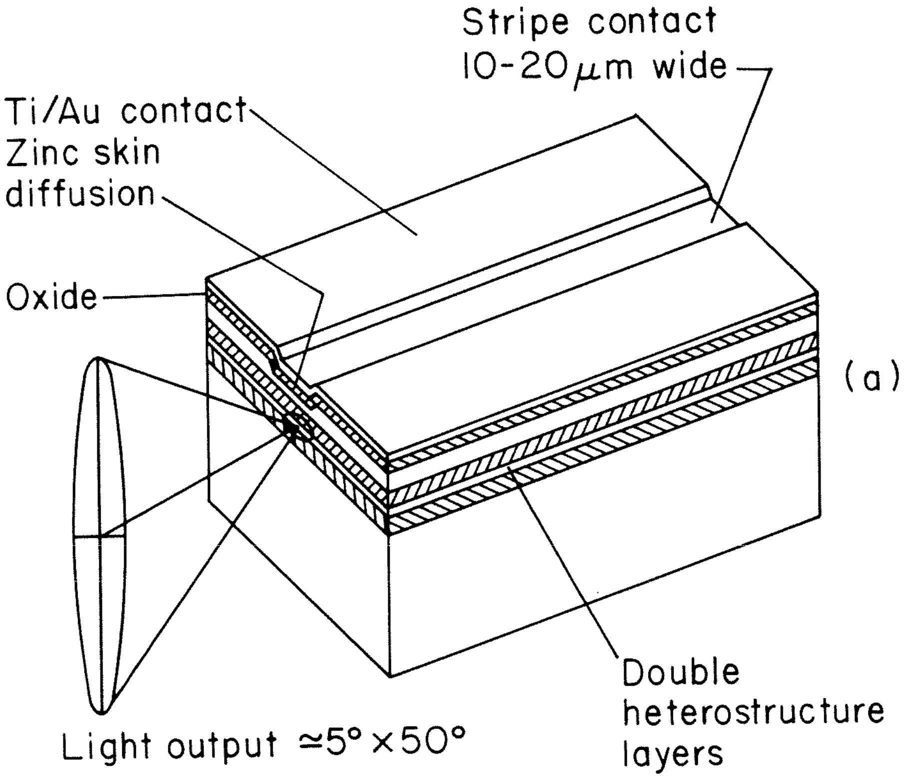

Figure 1.5: Schematic of a typical double-heterostructure semiconductor laser. The active region, possessing a smaller bandgap and large index of refraction, is surrounded by cladding layers with a larger bandgap and smaller index of refraction.

light lost through the facet replenished by stimulated emission. The spectrum of the light is shaped by both the response of the medium and, primarily, the characteristics of the resonator. The light that is not reflected at the facets is, of course, the output.

Beyond threshold, the point at which the gain equals the loss in the resonator, the intensity of the light emitted from the device is proportional to the injected current. This gives rise to a light-current characteristic illustrated in figure 1.6. The linear light-current response and low voltages and currents used (typically 2 V and 10–100 mA) suggests direct linear electrical modulation of the light out by modulating the pump current. Several characteristic time scales--carrier lifetime, photon lifetime, and stimulated emission rate--give rise to a frequency response that is typically flat from DC to about 1 GHz, then rises in a resonance peak before dropping off at 40 dB/decade. This response is illustrated in figure 1.7.

As semiconductor lasers have increased in commercial importance, more emphasis has been placed on reliability. As a consequence, the quality of all facets of laser production--materials, fabrication, and the final device--has improved. The operating characteristics of early lasers were governed more by parasitics and defects than by design. Now, however, modern commercial lasers actually begin to closely resemble the theory of their physics, and as fabrication techniques become more reproducible, more and more subtle effects are becoming apparent (for example, well-defined filamentary modes [28]). Consequently, semiconductor lasers are returning to the laboratory, not as subjects of investigation in their own right, but as tools for modeling other physical systems and for studying material physics.

Depending upon the exact configuration, the dynamics of semiconductor laser operation can be quite complex. Analytically, they can be approached in

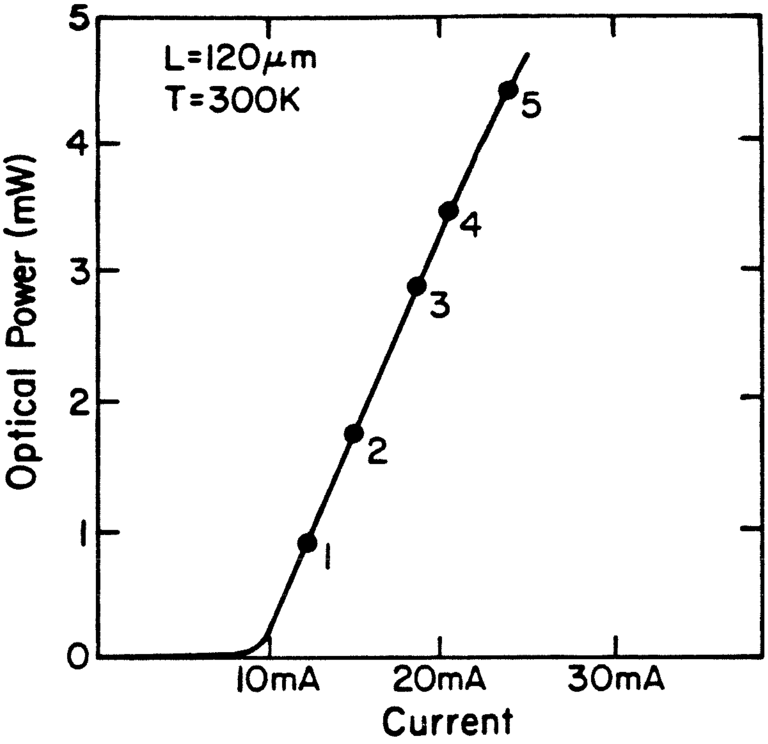

Figure 1.6: Typical light-current characteristic of a semiconductor laser.

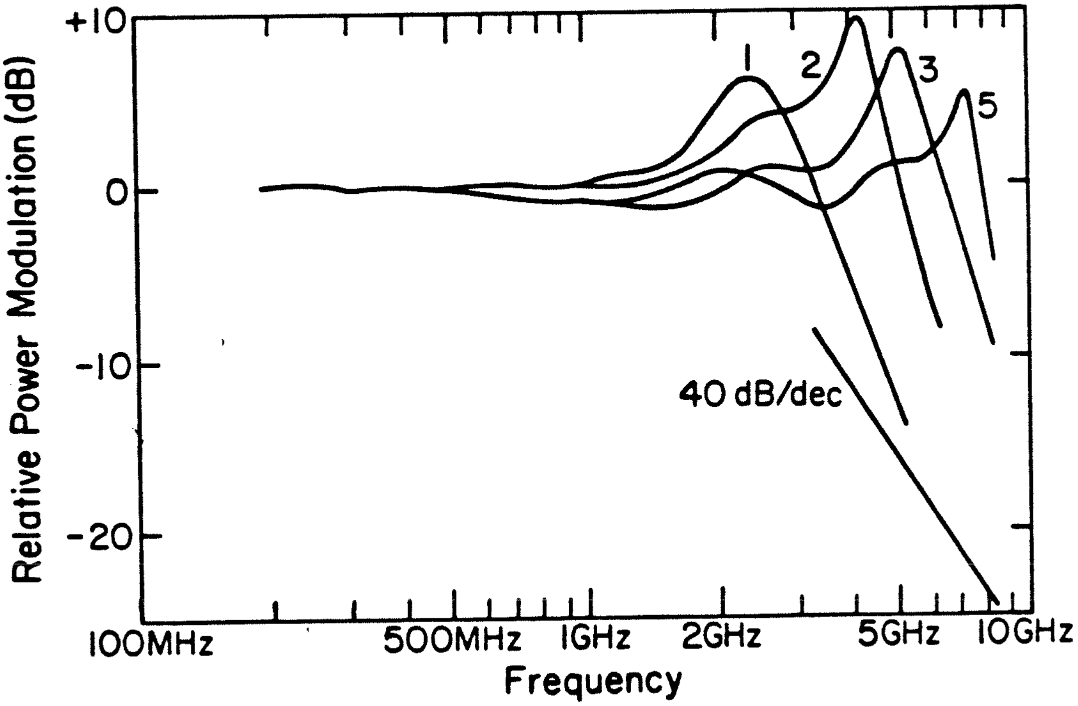

Figure 1.7: Modulation response of a semiconductor laser at the bias powers marked in figure 1.6, illustrating the relaxation resonance and its dependence upon operating power.

many ways. The most strictly rigorous derives from quantum mechanics and includes both quantized atomic states and a quantized electric field [29-30]. In semiconductor lasers, the discrete atomic states are replaced by Bloch states appropriate to the crystalline lattice [31]; inhomogeneities, as well, can be included in a purely quantum theory by several means, e.g., [32]. The quantum mechanical approach has the advantage of rigor, but it carries the disadvantage of being non-intuitive. A more intuitive, and still successful, approach is the semiclassical approximation. In this approximation, purely quantum phenomena are modeled classically--for example, spontaneous emission becomes a driving source for Maxwell's equations, while stimulated emission can be modeled as a negative conductivity. Carriers in the semiconductor are presumed to follow the classical semiconductor master equations for transport. Such an approximation assumes that the band structure of the semiconductor is parabolic and that the conduction and valence bands remain in quasi-equilibrium--assumptions that are easily justified in the common material systems.

The basic semiclassical equations of motion of a semiconductor laser then, are second order in time; with the assumption of harmonic fields, they can be reduced to a system of first order nonlinear ordinary differential equations via the "rate equation approximation." Spatial derivatives can also be eliminated by volume-averaging the rate equations, although this approximation overlooks effects due to inhomogeneities (as we will see). The rate equations are the starting points for a host of interesting behavior. Being nonlinear, they have an immensely rich structure and are a theoretician's delight, leading to behavior (observed, as well as calculated) hysteretic, oscillatory, and chaotic, as well as yielding the more familiar steady-state behavior.

All is not ideal in the semiconductor laser, however. Its small size, a boon to systems, limits the available output power. Though it may emit only a few mW of output power, the power density at the μm-sized exit facet can approach MW/cm^2. The result: when operated at high powers, the laser destroys its own mirrors. The obvious solution is to increase the emitting area of the laser, but that brings with it a host of new problems, including the excitation of high-order lateral modes and filamentation. The latter is the formation of localized "hot spots" on the mirrors, which are incoherent with each other and unpredictably hop around under modulation; they result from the nonlinearities in the gain and refractive index in the active region.

Yet another difficulty arises from the high spontaneous emission and the relatively poor cavities typical of semiconductor lasers; the photon lifetime in a semiconductor laser is generally a few picoseconds, leading to a Q of a few hundred, while in a helium-neon laser, for example, the photon lifetime will be closer to microseconds, with a Q of a few million. The spontaneous emission manifests itself as a relatively large linewidth--typically, 100 MHz or so. This large linewidth is a boon to those studying quantum noise properties--the quantum noise swamps out other noise sources save one (see chapter 8)--but it is a limiting factor in commercial use of semiconductor lasers for communications. Furthermore, the rate at which a semiconductor laser can be modulated varies with the cavity loss rate (as the one-half power), so a lossier cavity will make a faster laser. Unfortunately, the fraction of spontaneous emission coupled into the lasing mode also increases (linearly) with the cavity loss rate, leading designers to make a choice between fast and noisy lasers, or slow and quiet ones.

Another problem arises due to the semiconductor laser's operation as a detuned oscillator. That is, the peak of the gain spectrum (which establishes the operating point) is not the zero of the corresponding dispersion curve, as would be the case in a homogeneously broadened atomic medium. Consequently, a fluctuation in the gain leads to a fluctuation in the index of refraction, and thereby causes a perturbation to the resonance of the cavity and lasing frequency. This property not only broadens the linewidth by a factor of 30 or so over what it would be otherwise [33]; it also leads to an appreciable phase response under modulation which increases linearly with increasing frequency (the so-called "chirp"). Chirping increases the dynamic linewidth of a laser under modulation, and ultimately limits the transmission of data through a dispersive fiber.

Several schemes have been proposed to mitigate these difficulties. One solution to the problems of getting high output powers is phase-locked arrays of lasers [34] (figure 1.8a), in which several individual lasers are coupled together. Indeed, it was a phased-array laser that produced the 5.4 W of power as mentioned earlier. Another approach has been tailored-gain lasers, in which the gain of the active region varies in the lateral direction [35] (figure 1.8b). This method provides higher gain selectivity among the lateral modes than an otherwise unadorned active region does. Both of the schemes seek to modify the gain in the active region in the lateral direction while retaining the flat, cleaved mirrors of the laser; the reverse is also possible. By appending curved mirrors to a normal active region, one can fabricate such geometries as the unstable resonator configuration [36] (figure 1.9). While the technique of "inhomogeneous mirrors" is technologically younger than that of "inhomogeneous gain," both seek to increase the optical power by spreading the output beam over a large region of the laser in a predictable and repeatable fashion.

Ostensibly, a semiconductor laser is an inhomogeneously broadened laser--the different energies in the absorption band come from electrons in different *k*-states. However, the relaxation rate between different *k*-states is so great (with

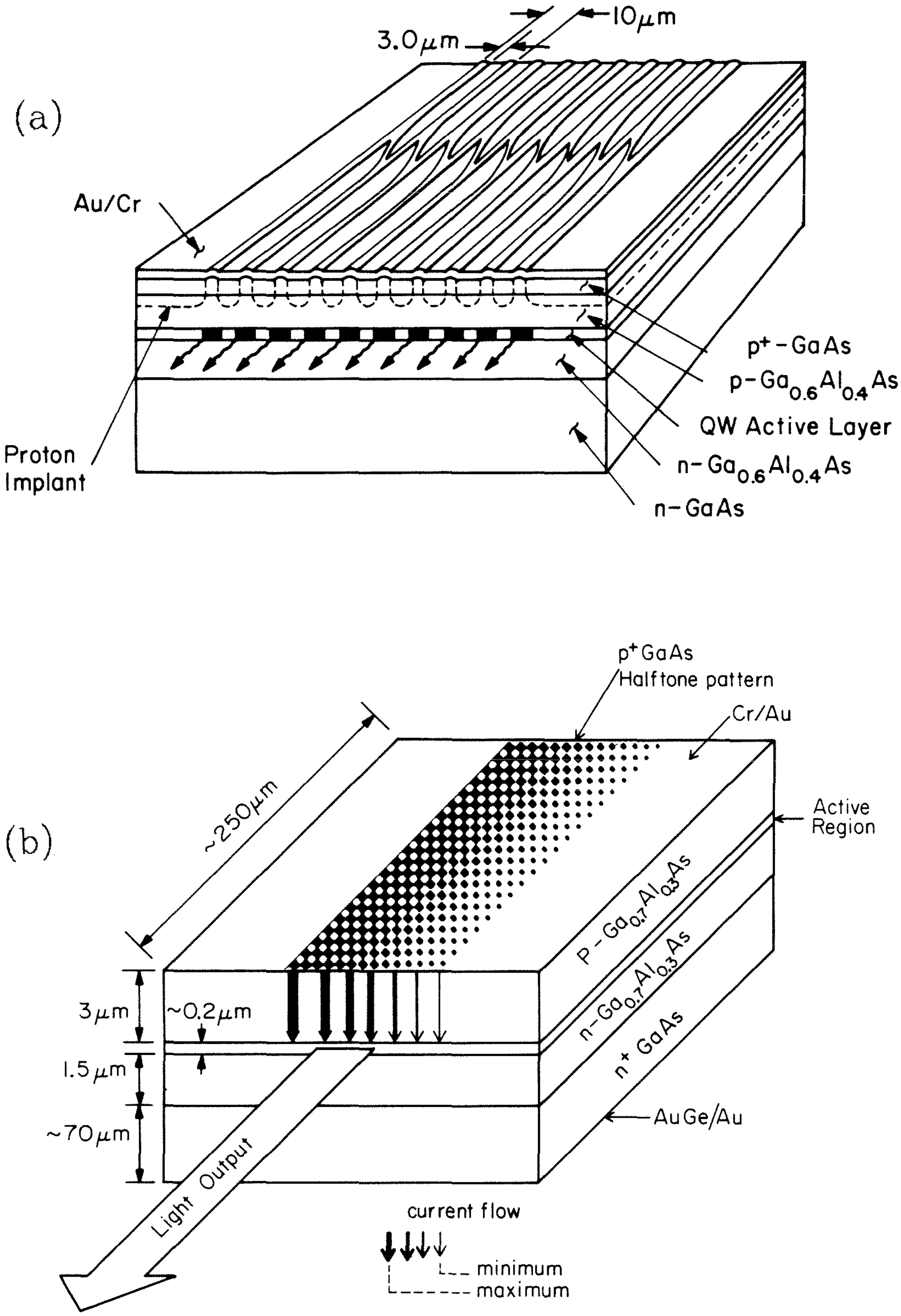

Figure 1.8: (a) Schematic of a phased array of semiconductor lasers. (b) Schematic of a tailored-gain semiconductor laser.

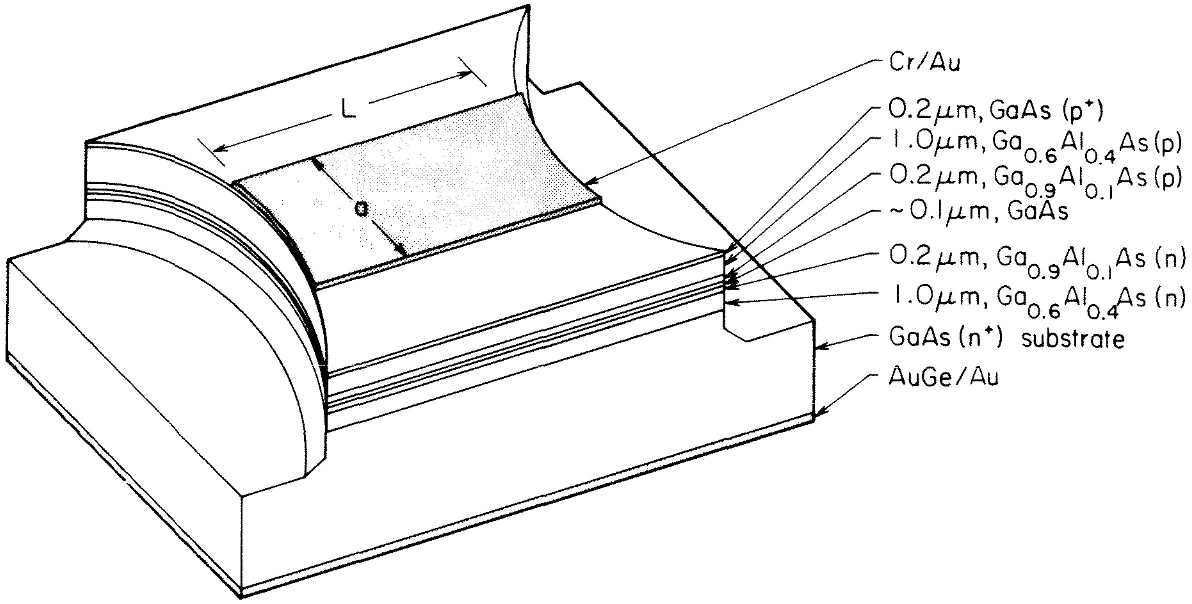

Figure 1.9: Schematic of an unstable resonator semiconductor laser.

a lifetime on the order of femtoseconds) that the laser behaves as if it were homogeneously broadened; an incident optical field saturates the entire inversion uniformly. One of the benefits of homogeneously broadened lasers is that they run in only a single longitudinal mode of the resonator. Again, however, the semiconductor laser is a contrary breed--the spontaneous emission into the lasing mode in a semiconductor laser is so great (due to the low Q of the resonator), and the gain spectrum so broad, that left to its own devices, a semiconductor laser will generally run in multiple longitudinal modes. This property is a disadvantage to transmission systems, where one would like the spectrum of a transmitted signal to be no wider than the Fourier limit. Also in a multimode laser there is an increase in the total noise due to fluctuations between modes ("partition noise" [37]). Consequently, there is considerable effort to induce single-longitudinal mode operation. The techniques range from distributed-feedback lasers [38] (figure 1.10a) and distributed-Bragg-reflector lasers [39] (figure 1.10b), in which a grating is incorporated into the active region or end mirrors, to axial [40] (figure 1.11a), transverse [41] (figure 1.11b) and lateral [42] (figure 1.11c) coupled cavities. In the "distributed" lasers, a frequency-dependent grating provides mode selectivity, while in the coupled-cavity designs, mode selectivity arises from the interference between the modes of the individual cavities.

Broad-area lasers with non-planar mirrors are technologically less developed than the phased arrays, yet they show great promise for high-power operation. Chapter 2 presents some of the pioneering work in the area of non-planar mirror semiconductor lasers. Our efforts have been concentrated on unstable resonator geometries. Unstable resonators are the historical choice for high-gain lasers; in addition, they have the very useful property that they tend to continuously demagnify the optical field. This property disrupts the evo-

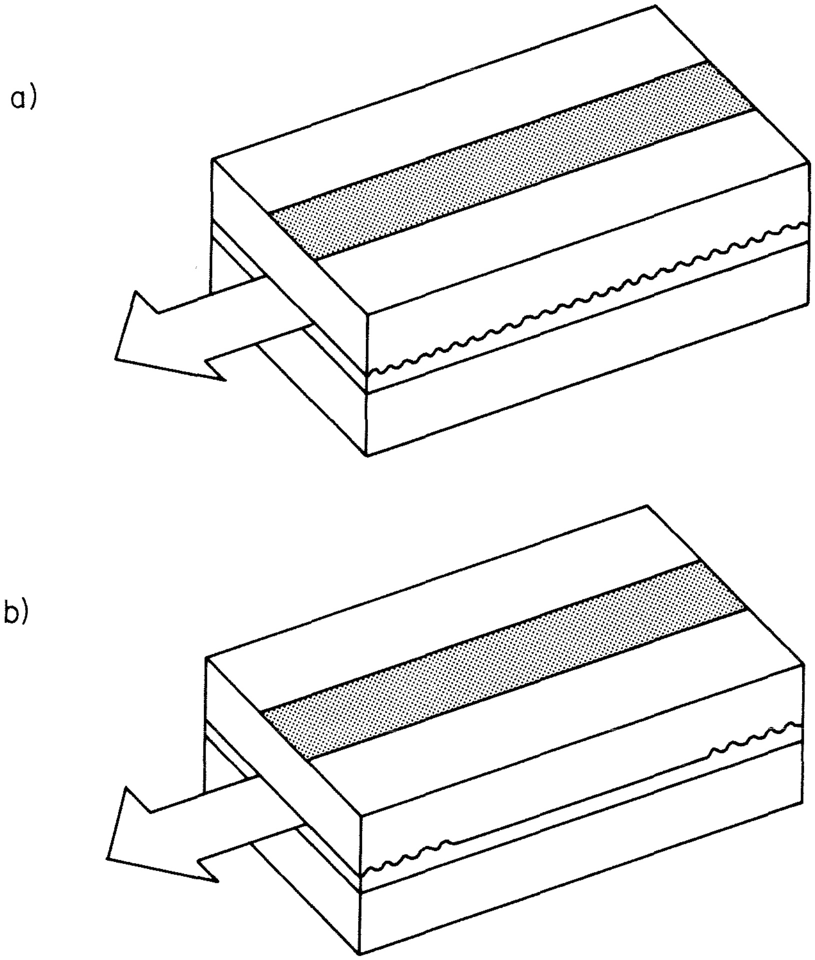

Figure 1.10: Techniques for producing single-longitudinal mode operation. (a) Distributed feedback laser, incorporating a grating within the active region. (b) Distributed Bragg reflector, incorporating a grating into the end mirrors.

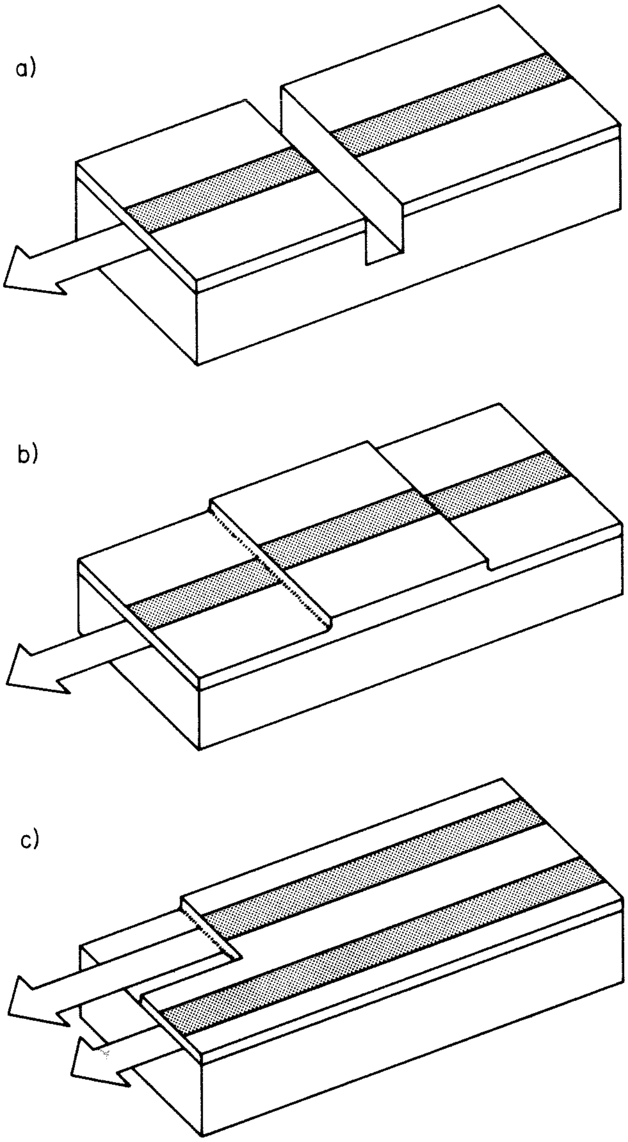

Figure 1.11: Coupled cavity lasers. (a) Axial (longitudinal) coupled cavity. (b) Transverse coupled cavity. (c) Laterally coupled cavity.

lution of damaging filaments. Semiconductor lasers, because they are planar devices, also allow one to exploit the properties of quasi-two-dimensional optical systems, and one such device--a tilted-mirror resonator--is presented. The modes of laser geometries with non-planar mirrors are considerably more difficult to analyze than the modes of phased arrays and tailored-gain structures, and chapter 3 is devoted to a technique that gives good agreement with the experimental results of chapter 2.

We then turn to coupled-cavity structures. In chapter 4 we present the laterally-coupled-cavity laser invented at Caltech, experimental measurements, and an analysis of the dispersion relations that give the steady-state lasing frequency. The dynamic properties of coupled-cavity lasers are far more difficult to characterize, and in chapter 5 we work out analytic expressions for the amplitude and phase response to a direct current modulation of a general coupled-cavity laser. This analysis uses a novel analytic technique in which the AC modulation properties are determined from the analytic continuation of the DC resonance equation. The technique, used in chapters 5-7, is developed formally in chapter 5 from a complete multimode theory and a proof of the relation between the dynamic photon lifetime, stimulated emission rate, and the cavity loss rate is given in the appendix. The results of chapter 5 show that it is possible to null out the phase response with more than one cavity, and consequently improve the spectral properties of a modulated signal. An additional feature of multielement lasers is the possibility of bimodality (two operating longitudinal modes independent of spontaneous emission) and bistability; we prove this analytically and give conditions for its existence in chapter 6.

The ultimate limit to linewidth of the coupled-cavity laser is given by the quantum noise, and in chapter 7 we calculate analytic expressions for the various noise spectra. The analytic expressions, though general, are formidable. We also calculate a simpler approximate expression for the linewidth of a coupled-cavity laser that shows its upon both the material parameters and relative tuning of the laser; in other words, one can change the linewidth (among other things) by varying the relative tunings of the cavities. This theory accounts for the noise properties above 1 MHz of lasers consisting of an arbitrary number of cavities. Below that frequency, however, all semiconductor lasers exhibit a marked rise in noise that has not been explained by theory. In chapter 8 we analyze a single-cavity laser and explicitly account for non-quantum noise (thermal and diffusion noise) and provide an explanation for such observed noise.

In chapters 5-7, the optical field is characterized by a single parameter giving the average amplitude of the optical field within the composite cavity. While this method is certainly sufficient to describe all of the physics of the device, some intuition can be gained by using a coupled-mode approach to the description of the field. However, all coupled-mode theories of longitudinally coupled cavities exhibit a fatal flaw that prevents them from ever attaining anything but vague qualitative predictions. In chapter 9, we identify this flaw and present a new method of analyzing multielement resonators which does not suffer from the flaws of coupled-mode theory.

The material presented in this thesis is based on work published in references 42-56.

References

[1] T. H. Maiman, Nature, vol. 187, p. 493 (1960).

[2] A. Javan, W. B. Bennett, Jr., and D. R. Herriott, Phys. Rev. Lett., vol. 6, p. 106 (1961).

[3] W. B. Bridges, Appl. Phys. Lett., vol. 4, p. 128 (1964).

[4] J. E. Geusic, H. M. Marcos and L. G. Van Uitert, Appl. Phys. Lett., vol. 4, p. 182 (1964).

[5] T. Kushida, H. M. Marcos and J. E. Geusic, Phys. Rev., vol. 167, p. 1289 (1968).

[6] A. L. Schawlow and C. H. Townes, Phys. Rev., vol. 112, p. 1940 (1958).

[7] M. G. Bernard and G. Duraffourg, Phys. Stat. Solidi, vol. 1, p. 699 (1961).

[8] N. G. Basov, O. N. Kroklin and Yu. M. Popov, Sov. Phys. JETP, vol. 13, p. 1320 (1961)

[9] R. N. Hall, G. E. Fenner, J. D. Kingsley, T. J. Soltys and R. O. Carlson, Phys. Rev. Lett., vol. 9, p. 366 (1962).

[10] M. I. Nathan, W. P. Dumke, G. Burns, F. H. Dill Jr. and G. Lasher, Appl. Phys. Lett., vol. 1, p. 62 (1962).

[11] N. Holonyak and S. F. Bevaqua, Appl. Phys. Lett., vol. 1, pp. 82 (1962).

[12] T. M. Quist, R. H. Rediker, R. J. Keyes, W. E. Krag, B. Lax, A. L. McWhorter and H. J. Zeigler, Appl. Phys. Lett., vol. 1, p. 91 (1962).

[13] I. Melngailis and R. H. Rediker, IEEE Trans. Elect. Dev., vol. ED-10, p. 333 (1963).

[14] R. F. Broom, C. H. Gooch, K. G. Hambleton, C. Hilsum and D. J. Oliver, IEEE Trans. Elect. Dev., vol. ED-10, p. 334 (1963).

[15] F. B. Alexander, V. R. Bird, D. R. Carpenter, G. W. Manley, P. S. McDermott, J. R. Peloke, H. F. Quinn, R. J. Riley and L. R. Yetter, Appl. Phys. Lett., vol. 4, p. 13 (1964).

[16] H. Kroemer, Proc. IEEE, vol. 51, 1972 (1963).

[17] I. Hayashi, M. B. Panish and P. W. Foy, IEEE J. Quant. Elect., vol. QE-5, p. 211 (1969).

[18] H. Kressel and H. Nelson, RCA Rev., vol. 30, p. 106 (1969).

[19] I. Hayashi and M. B. Panish, Device Research Conference, Seattle, Washington, June 1970.

[20] I. Hayashi, M. B. Panish, P. W. Foy and S. Sumski, Appl. Phys. Lett., vol. 17, p. 109 (1970).

[21] W. T. Tsang and R. A. Logan, Elect. Lett., vol. 18, p. 845 (1982).

[22] *Lasers and Applications 1986 Buyer's Guide*, p. 156 (1986).

[23] G. L. Harnagel, D. R. Scifres, H. H. Kung, D. F. Welch, D. P. Worland, P. S. Cross and R. D. Burnham, paper #ThDD3, presented at Integrated and Guided Wave Optics Conference, Atlanta, Georgia, February 26-28, 1986.

[24] D. Botez, Appl. Phys. Lett., vol. 36, p. 190 (1980).

[25] R. A. Linke, Optical Fiber Conference, New Orleans, Louisiana, January 1984.

[26] C. B. Su, V. Lanzisera, W. Powzinik, E. Meland, R. Olshansky and R. B. Lauer, Paper #WH3, Conference on Lasers and Electro-Optics, Baltimore, Maryland, May 1985.

[27] K. Kobayashi, Elect. Lett., vol. 21, p. 1162 (1985).

[28] M. Mittelstein, J. Salzman, A. Larsson and A. Yariv, 'Emission characteristics of single quantum well graded-index separate confinement broad area lasers," unpub.

[29] W. E. Lamb Jr., Phys. Rev., vol. 134, p. 1429 (1964).

[30] H. Haken, *Laser Theory* (Springer-Verlag, New York, 1983).

[31] H. Haug, Phys. Rev., vol. 184, p. 338 (1969).

[32] K. Vahala and A. Yariv, Phys. Rev. A, vol. 32, p. 345 (1985).

[33] M. Fleming and A. Mooradian, Appl. Phys. Lett., vol. 38, p. 511 (1981).

[34] D. Scifres, R. D. Burnham and W. Streifer, Appl. Phys. Lett., vol. 33, p. 1015

(1978).

[35] C. Lindsey, D. Mehuys and A. Yariv, 'Tailored-gain broad area lasers," unpub.

[36] A. P. Bogatov, P. G. Eliseev, M. A. Man'ko, G. T. Mikaelyan and Yu. M. Popov, Sov. J. Quant. Elect., vol. 10, p. 620 (1980).

[37] K. Vahala, doctoral thesis, California Institute of Technology, 1985.

[38] M. Nakamura, K. Aiki, J-I Umeda, A. Yariv, H. W. Yen and T. Morkawa, Appl. Phys. Lett., vol. 25, p. 487 (1974).

[39] H. W. Yen, W. Ng, I. Samid and A. Yariv, Opt. Comm., vol. 17, p. 213 (1976).

[40] W. T. Tsang and N. A. Olsson, Appl. Phys. Lett., vol. 42, p. 650 (1983).

[41] Y. Suematsu, M. Yamada and K. Hayashi, J. Quant. Elect., vol. QE-11, p. 457 (1975).

[42] J. Salzman, T. Venkatesan, R. Lang, M. Mittelstein and A. Yariv, Appl. Phys. Lett., vol. 46, p. 218 (1985).

[43] J. Salzman, R. Lang, T. Venkatesan, M. Mittelstein and A. Yariv, Appl. Phys. Lett., vol. 47, p. 445 (1985).

[44] J. Salzman, R. Lang and A. Yariv, Elect. Lett., vol. 21, p. 820 (1985).

[45] J. Salzman, R. Lang and A. Yariv, 'Confocal unstable resonator semiconductor laser," Optics Lett., (1986), to be published.

[46] M. Mittelstein, J. Salzman, T. Venkatesan, R. Lang and A. Yariv, Appl. Phys. Lett., vol. 46, p. 923 (1985).

[47] J. Salzman, R. Lang, S. Margalit and A. Yariv, Appl. Phys. Lett., vol. 47, p. 9 (1985).

[48] R. J. Lang, J. Salzman and A. Yariv, IEEE J. Quant. Elect., vol. QE-22, p. 463 (1986).

[49] J. Salzman, R. Lang and A. Yariv, Opt. Lett., vol. 10, p. 387 (1985).

[50] J. Salzman, R. Lang and A. Yariv, Appl. Phys. Lett., vol. 47, p. 195 (1985).

[51] R. J. Lang and A. Yariv, IEEE J. Quant. Elect., vol. QE-21, p. 1683 (1985).

[52] R. J. Lang and A. Yariv, IEEE J. Quant. Elect., vol. QE-22, no. 5 (1986), to be published.

[53] R. J. Lang and A. Yariv, IEEE J. Quant. Elect., vol. QE-22, p. 436 (1986).

[54] R. J. Lang, K. Vahala and A. Yariv, IEEE J. Quant. Elect., vol. QE-21, p. 443 (1985).

[55] R. J. Lang and A. Yariv, 'Local field rate equations for coupled optical resonators," unpub.

[56] R. J. Lang and A. Yariv, 'Coupling coefficients for coupled cavity lasers," unpub.

*

*

*

Chapter 2

Unstable Resonator Semiconductor Lasers: Experimental Work

2.1 Introduction

One of the driving forces in semiconductor laser design has been the desire for higher output power than the usual 1-10 mW. As we pointed out in chapter 1, the small size of semiconductor lasers makes it difficult to meet even these modest demands. While bulk GaAs can withstand quite high optical intensities, the semiconductor-air interface that constitutes the output mirrors cannot. It forms the limiting element in the semiconductor laser because a small fraction of the output light is absorbed by the mirrors (e.g., by surface states). Sufficiently intense light will destroy them. Consequently, it is desirable to increase the size of the emitting area of the laser to decrease the intensity for a given total output power.

With two dimensions to play with, research has gone in two directions. The first has been to increase the transverse dimension of the laser (along the direction perpendicular to the junction). The simplest approach along these lines is to make the active layer thicker. However, such a scheme decreases the carrier density and increases the threshold current of the laser. The next alternative is to add layers to separately confine the optical radiation to a larger volume than that of the active region, the Separate-Confinement Heterostructure (SCH) or Large Optical Cavity (LOC) [1-2]. Even so, however, the thickness of the confining layers can be increased to only about 1 μm before higher-order modes of the slab waveguide are excited. The higher-order modes emit in multi-lobed patterns in the far field, and are undesirable.

While the transverse dimension is limited to no more than 1 μm, the lateral dimension (parallel to the junction) offers many more possibilities. Because changes in the lateral index of refraction (or rather, the effective lateral index [3]) are smaller and more easily controlled, fundamental lateral modes as wide as 6 μm can be sustained with higher-order modes remaining beyond cutoff. The combination of an LOC with a lateral waveguiding structure has produced single lateral mode lasers with outputs into the tens of mW. Beyond a lateral dimension of 6-10 μm, however, the differences between the losses of the various modes are smaller than imperfections and inhomogeneities in the lasers, and wider lasers run in an unpredictable combination of higher-order lateral modes. Frequently, the modes are coupled by nonlinearities into localized regions of self-focusing, or filaments, which form and re-form irregularly with variations in pump current.

More advanced structures than a simple waveguide are required to impose order on the lateral mode structure of broad-area lasers. The most successful of these structures to date has been the phased array of lasers [4,5], in which many lasers individually too narrow to support higher-order modes are placed side-by-side and allowed to couple via their evanescent fields. The modes of the individual lasers couple to form the so-called supermodes [6], only one of which has the desirable single-lobed far field. Early research in the field concentrated upon persuading the array to operate in the fundamental supermode; it is now recognized that chirping, or varying the elements of the array, is one means of accomplishing this task, at the expense of getting an off-axis far field [7]. More recently, tailored-gain lasers with a linearly varying gain profile in the lateral direction have also shown promise [8]. However, both lasers rely upon incompletely pumping portions of the gain region, and neither has yet produced consistent CW operation in the desirable single lateral mode.

The problems with getting high power from a broad-area laser stem from the high gain and high power of the device. It behooves us to examine the historical solution to this problem in macroscopic lasers. Since the early 1960's, it has been recognized that the unstable resonator geometry offers inherently large mode volumes. In addition, the defocusing nature of the mirrors tends to suppress nonlinearities that lead to self-focusing. The unstable resonator, then, seems a natural choice for a semiconductor laser. That it has been on the whole overlooked stems from the universal use of plane parallel mirrors to form the resonator of a semiconductor laser.

Plane parallel mirrors are used for virtually all semiconductor lasers for the simple reason that they are absurdly simple to fabricate; the crystalline substrate naturally cleaves along parallel planes, producing flat surfaces of optical quality (at least, over the dimensions of the laser). So, despite the fact that the plane parallel resonator is the configuration most sensitive to imperfections and inhomogeneities, it is the one in common use. Any other resonator requires non-planar mirrors that must be fabricated by some means other than cleaving, and methods of fabricating such mirrors have not been forthcoming.

That is, they have not been forthcoming until recently. Etched mirrors, both wet and dry, have been demonstrated by several groups [9-10]. The transverse quality of the mirrors is excellent; the lateral quality has been more variable. Using techniques developed at Caltech for etching mirrors, we fabricated several geometries of unstable resonator semiconductor lasers; they are the subject of this chapter. One of the advantages semiconductor lasers have over their macroscopic counterparts is that the lateral design is inherently two-dimensional, and it allows for several geometries that are impossible or undesirable in a three-dimensional structure (e.g. a tilted-mirror resonator). In section 2.2, we review the basic theory of unstable resonators as put forward by Siegman [11] and others. In sections 2.3-2.6, we present experimental measurements on a symmetric unstable resonator semiconductor laser (URSL), a symmetric URSL with a lateral waveguide, a confocal URSL, and a tilted-mirror URSL. In section 2.7, we summarize the experimental results.

2.2 Theory of Operation

A typical unstable resonator geometry is shown in figure 2.1. We will normalize all dimensions to the distance between the centers of the two mirrors. In the geometrical approximation, the two convex mirrors M_1 and M_2 are circular with radii R_1 and R_2, respectively; the counterpropagating beams of radiation have curved phase fronts with virtual sources located at distances r_1 and r_2, respectively, from the two mirrors. A good first approximation to the losses is given by Siegman [11]; we will follow his derivations in this section. We will frequently refer to the g-parameters of the resonator defined by

$$g_i \equiv 1 + \frac{1}{R_i} \tag{1}$$

and the sign of $R_{1,2}$ is defined as positive for the curvatures shown in figure 1. Also useful are the h-parameters

$$h_i \equiv g_i^{-1} = \frac{R_i}{1+R_i} \tag{2}$$

The distance from the center of the left mirror back to the virtual source of the rightward-going wave is

$$r_1 = \frac{+\sqrt{1 - g_1^{-1}g_2^{-1}} - 1 + g_1^{-1}}{2 - g_1^{-1} - g_2^{-1}} = \frac{+\sqrt{1 - h_1h_2} - (1 - h_1)}{(1 - h_1) + (1 - h_2)} \tag{3}$$

where the $+\sqrt{}$ indicates the positive square root. The expression for the other virtual source is the same with subscripts reversed.

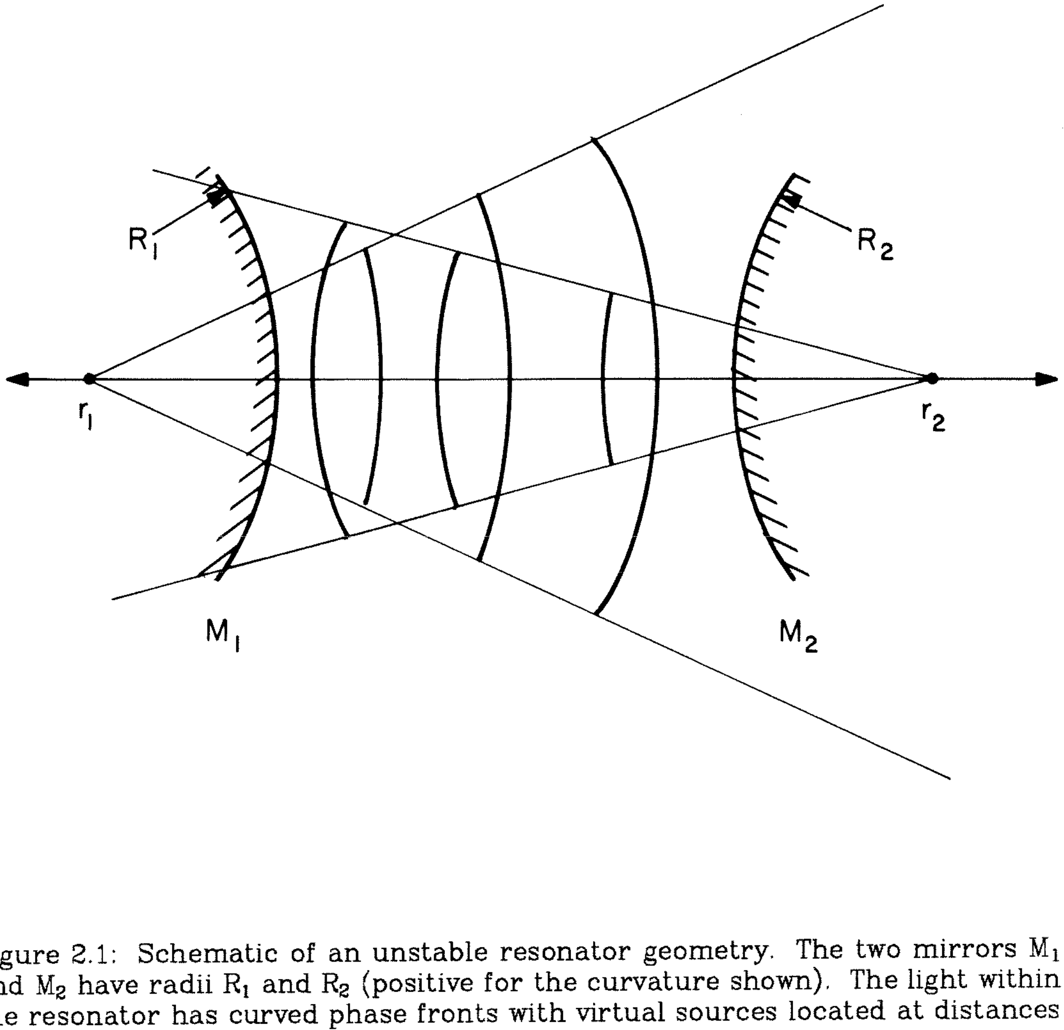

Figure 2.1: Schematic of an unstable resonator geometry. The two mirrors M_1 and M_2 have radii R_1 and R_2 (positive for the curvature shown). The light within the resonator has curved phase fronts with virtual sources located at distances r_1 and r_2 behind the mirrors. All dimensions are normalized to the distance between the centers of the mirrors.

The original unstable resonator theory was for "strip" (i.e., one-dimensional) mirrors, although the major applications were to "disk" (two-dimensional) mirrors. Semiconductor lasers, however, are true two-dimensional optical systems when the transverse waveguide structure has been eliminated from the analysis. The one-dimensional mirror theory is precisely what is necessary.

For a laser with mirrors of diameters a_1 and a_2, the fraction of energy emitted from one mirror that subtends the opposite mirror can easily be shown from geometrical considerations to be

$$|\gamma_1|^2 = \frac{a_1 r_1}{a_2(r_1 + 1)} \tag{4}$$

for the beam emitted from mirror 1, while

$$|\gamma_2|^2 = \frac{a_2 r_2}{a_1(r_2 + 1)} \tag{5}$$

for the beam emitted from mirror 2. Consequently, the fraction of energy that remains in the cavity after one round trip is

$$\gamma^2 = \left| \frac{r_1 r_2}{(r_1 + 1)(r_2 + 1)} \right| = \left| \frac{1 - \sqrt{1 - h_1 h_2}}{1 + \sqrt{1 - h_1 h_2}} \right| \tag{6}$$

where we have taken $\gamma_1\gamma_2 \equiv \gamma$. We will frequently speak of the "magnification" M of an unstable resonator. Magnification is a geometric concept; the magnification is the relative change in the size of a portion of a phase front after one round trip. Obviously, it requires that such a portion reproduce itself in some recognizable form, so that a ray picture of the resonator is appropriate. Such is not always the case, particularly for SL's, as we will see. However, when the magnification is a well-defined quantity, it can be related to the cavity losses simply:

$$M_{\mathbf{roundtrip}} = \gamma^{-2} \tag{7}$$

There are several references in the literature [12-13] that utilize a "per-pass" magnification M (usually in reference to a symmetric resonator). In these cases, $M_{\mathbf{per\ pass}} = |\gamma_1|^{-2} = |\gamma|^{-1}$. In this chapter, M is always meant to be the round-trip magnification. We will use $|\gamma_1|^2$ or $|\gamma_2|^2$ when we need an expression for "per pass" power losses.

In a semiconductor laser, one is also interested in the quantum efficiency of the device, including unsaturable material losses and the finite reflectivity at the mirrors. A general formulation has been given in terms of scattering coefficients [14]. If the power scattering coefficients of the mirrors are $S_{1,2}$ for scattered radiation, $T_{1,2}$ for transmitted radiation, and $R_{1,2}$ for reflected radiation, then the external quantum efficiency is given by

$$\eta_d = \eta_i \left[1 - \frac{2\alpha L}{\ln(R_1 R_2)} \right]^{-1} \times \left\{ 1 - \frac{S_1 R_2^{(1/2)} + S_2 R_2^{(1/2)}}{[1-(R_1 R_2)][R_1^{(1/2)} R_2^{(1/2)}]} \right\} \tag{8}$$

where η_i is the internal quantum efficiency and α is the material (non-saturable) loss.

The scattering coefficents for an unstable resonator with mirrors of real amplitude reflectivity ρ_i are

$$R_i = \gamma_i^2 \rho_i^2, \quad S_i = (1-\gamma^2)\rho_i^2, \quad T_i = 1-\rho_i^2 \tag{9}$$

Clearly, $R_i + T_i + S_i = 1$. The external quantum efficiency becomes

$$\eta_d = \eta_i \left[1 - \frac{\alpha L}{\ln\rho_1 + \ln\rho_2 + \ln\gamma_1 + \ln\gamma_2} \right]^{-1} \times \frac{\gamma_1\rho_1(1-\rho_2^2) + \gamma_2\rho_2(1-\rho_1^2)}{[\gamma_1\rho_1 + \gamma_2\rho_2][1-\gamma_1\gamma_2\rho_1\rho_2]} \tag{10}$$

For the symmetric case where $\gamma_1 = \gamma_2 \equiv \gamma^{1/2}$ and $\rho_1 = \rho_2 \equiv R^{1/2}$, this formula becomes

$$\eta_d = \eta_i \left[1 - \frac{\alpha L}{\ln R + \ln|\gamma|} \right]^{-1} \frac{1-R}{1-|\gamma|R} \tag{11}$$

or, in terms of the magnification M,

$$\eta_d = \eta_i \left[1 - \frac{\alpha L}{\ln R - \ln(M^{1/2})} \right]^{-1} \frac{M^{1/2}(1-R)}{M^{1/2} - R} \tag{12}$$

The brackets show the increase in η_d due to a decrease in the effective feedback into the resonator which is equivalent to the increase in η_d in Fabry-Perot (FP) lasers when the mirror reflectivity R is reduced to $|\gamma|^{1/2}R$. (However, it also causes an increase in the threshold current.) The last factor in equation (12) represents the decrease in η_d due to unrecoverable losses (coupling to radiation modes upon reflection, with subsequent absorption of the light by the semiconductor medium beyond the contact region). Note that this factor is in the range [1,1−R] for $0 \leq \gamma \leq 1$. Therefore, for a given resonator design (a given $|\gamma|$), the degradation in η_d due to scattering can be reduced by reducing the mirror reflectivity as shown in figure 2.2. The figure shows that for very low values of R, one can achieve a value of η_d not significantly different from that of the FP resonator, but it may not be practical owing to the increase in the laser threshold current. (Note: some confusion may arise over the use of R for both mirror radius and reflectivity; for the rest of this chapter, we will use it only for mirror radius.) One other formula of interest; in a diffraction analysis of open-walled unstable resonators, Smith showed [15] that while the few lowest-order lateral modes trade the title of 'lowest-loss mode" among themselves for large equivalent Fresnel numbers, below a certain point one mode separates permanently from the others. The critical point is given by

$$N_{eq.crit} \approx 11.5/(\ln M)^3 \tag{13}$$

2.3 Symmetric Unstable Resonator Semiconductor Laser (URSL)

A. Design Considerations

One of the reasons for fabricating curved mirror lasers is so that the mirrors will dominate local defects and inhomogeneities in determining the modes of the structure. In particular, we would like to suppress filaments by continuously defocusing the radiation within the laser. A first estimate of mirror size can be achieved by modeling the filament as a quadratic fluctuation in the index

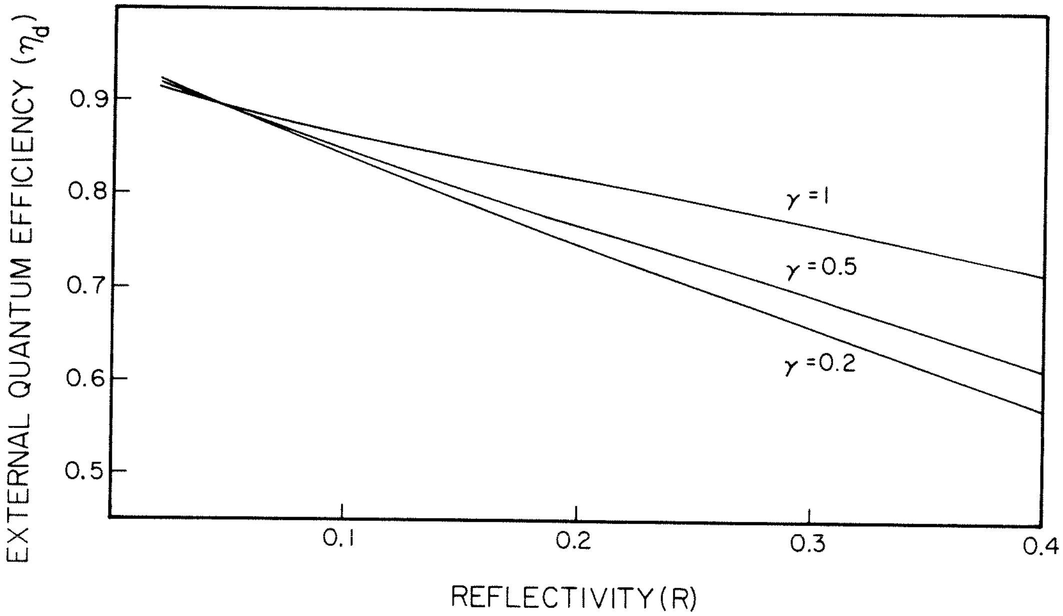

Figure 2.2: External quantum efficiency of a symmetric unstable resonator semiconductor laser as a function of mirror reflectivity for different values of γ and with $\eta_i \equiv 1$.

of refraction that has one confined mode, and requiring that the curved mirror smear out the filament over the laser width after one round trip. This assumption is obviously overkill, since if the filament never forms, there is no quadratic variation in the index of refraction; nevertheless, it serves as a good first iteration to choose resonator size, and leads [12] to the requirement $R \approx L$. Maximizing the efficiency of a semiconductor laser dictates a maximum length of 200–300 μm, so our first devices were 200 μm long with 250 μm mirrors at either end. Using the geometrical theory of the last section, we find that the magnification of such a symmetrical resonator is

$$M = \left\{ \left[1 + \frac{1}{R} \right] + \left[\frac{1}{R^2} + \frac{2}{R} \right]^{1/2} \right\}^2 \tag{14}$$

where, as we said, R is normalized to the length of the laser. For these dimensions, $M \approx 11$. There is another consideration; the light generated within the laser must somehow get out of it. This is a real problem in URSL's; at the lasing wavelength, the index of refraction of the core and cladding is about $\mu = 3.5$; at the interface with the air, the angle for total internal reflection (TIR) is only 16–17°. Consequently, any rays striking the mirror at angles greater than the TIR angle are never coupled out of the resonator. Furthermore, any rays that miss the gain region are absorbed by the surrounding region within the space of a few microns; consequently, the diffraction losses that constitute the useful output in macroscopic unstable resonators are true losses in URSL's. Thus, there is no reason to pump the laser in a region wider than the region of nonzero transmission on the mirror. We define μ as the index of refraction of the semiconductor (and assume that the laser is bounded by air). For mirror 1, if we define the quantity

$$\kappa_1 \equiv \frac{R_1}{1 + r_2 + R_1}$$

then the distance from the axis to the point of TIR on mirror number 1 is

$$d_1 = \frac{R_1}{\mu^2}\left[\sqrt{\mu^2 - \kappa_1^2} - \kappa_1\sqrt{\mu^2 - 1}\right] \tag{15}$$

Similar relations (with switched subscripts) govern mirror 2. Note that r_2 appears in the equation for κ_1, so that the location of the point of TIR depends upon the curvatures of both mirrors. For the dimensions chosen above, the maximum width is 80 μm, and so the gain stripe was made 80 μm wide to take full advantage of the potential width.

B. Fabrication

We grew GaAs/GaAlAs double heterostructures by liquid phase epitaxy, both simple heterostructures and LOC structures. The top layer of the structure was a "masking" layer of high aluminum content GaAlAs. Standard photolithographic techniques were then used to form resist patterns on top of the wafers with the shape of the desired mirrors. They were etched in a H_2SO_4:H_2O_2:H_2O (1:8:1) solution at low temperature (typically, 3-7 minutes at -5 to +5 °C). In some devices, the high aluminum layer was used as a secondary mask for reactive ion etching to make the walls of the device vertical. Otherwise, purely wet etching was used, and the high aluminum layer served to advance the upper portion of the etch front so that the walls of the channels that formed the mirrors were straight, rather than dovetailed (figure 2.3).

After mirror fabrication, the devices were lapped to 75–100 μm thickness, and contacts (AuCr, Au/AuGe) were evaporated onto the devices. They were then cleaved into bars of 5-10 lasers and tested unmounted. The finished device is illustrated schematically in figure 2.4.

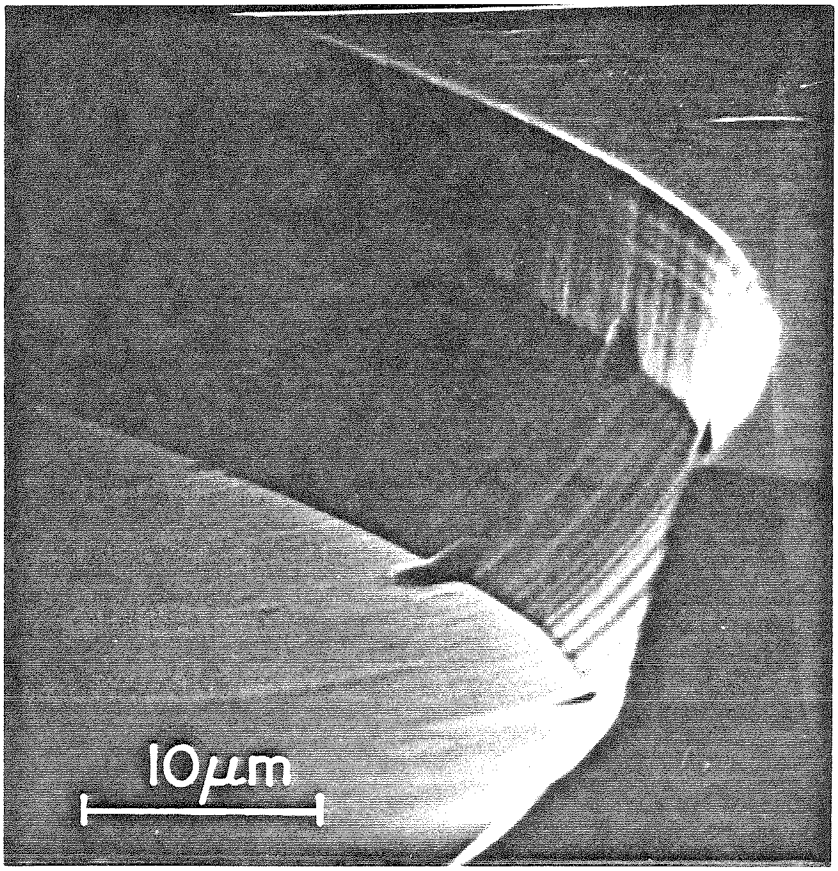

Figure 2.3: Scanning electron micrograph of the curved, etched mirrors illustrating the verticality of the walls.

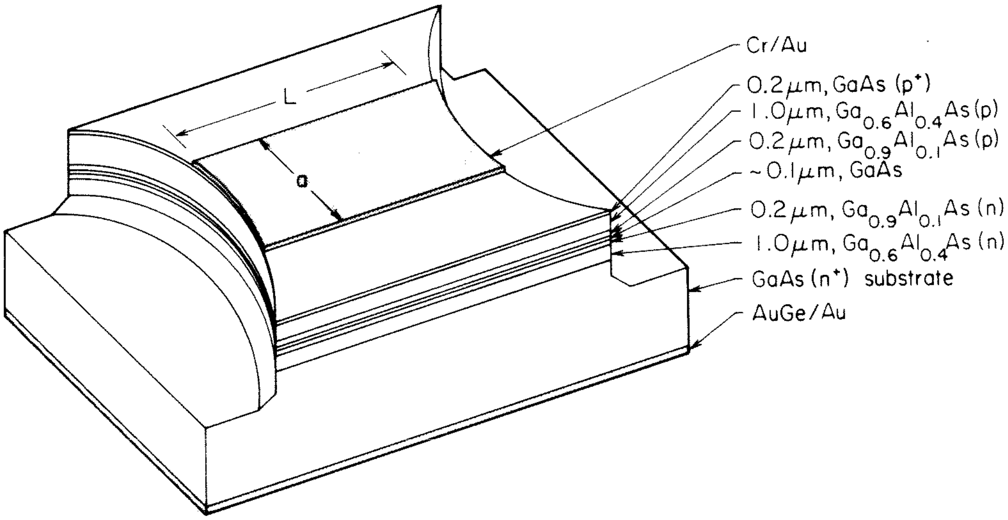

Figure 2.4: Schematic picture of the symmetric unstable resonator cavity on a double heterostructure GaAlAs/GaAs laser.

C. Measurement

Figure 2.5 shows the near field pattern of the unstable resonator for $I=1.8I_{th}$ with the laser driven with 100 ns pulses at a 500 kHz repetition rate. The field distribution is very stable, as can be seen in figure 2.6, where the near field is recorded for different values of the injection current. The laser operates in a single longitudinal mode up to $I \approx 2I_{th}$ and in only two modes up to $I \approx 2.6I_{th}$. The far field pattern for two different currents is depicted in figure 2.7. We note that the far field distribution is very wide, as expected from a theoretical analysis of the symmetric unstable cavity [16] (unlike the far field distribution reported in ref. [17]). In fact, the recorded distributions shown in figures 2.5-7 were limited by the acceptance angle of the optical system. By scanning a photodetector manually, we were able to detect some radiation at angles as high as 70° from the laser axis.

The achievement of a collimated output would require a confocal UR geometry (see section 2.5). Although the fabrication of a laser with a confocal unstable resonator involves stringent requirements on R_1, R_2 and L, the primary limitation is the etching of both mirrors with high quality curved surfaces. The operation of the lasers reported here suggests that the confocal unstable resonator semiconductor laser is a feasible device. The ripples observed in figure 2.6 are most likely due to variations in the field distribution of the lowest order mode (see chapter 3), or scattering off of the mirrors, rather than interference between multiple lateral modes.

The threshold current and external quantum efficiency for the unstable resonator cavity were $I_{th} = 700$ mA and $\eta_d = 0.22$, respectively. These figures compare favorably with the measure values $I_{th} = 300$ mA and $\eta_d = 0.32$ for cleaved broad area (reference) lasers fabricated from the same wafer. Using

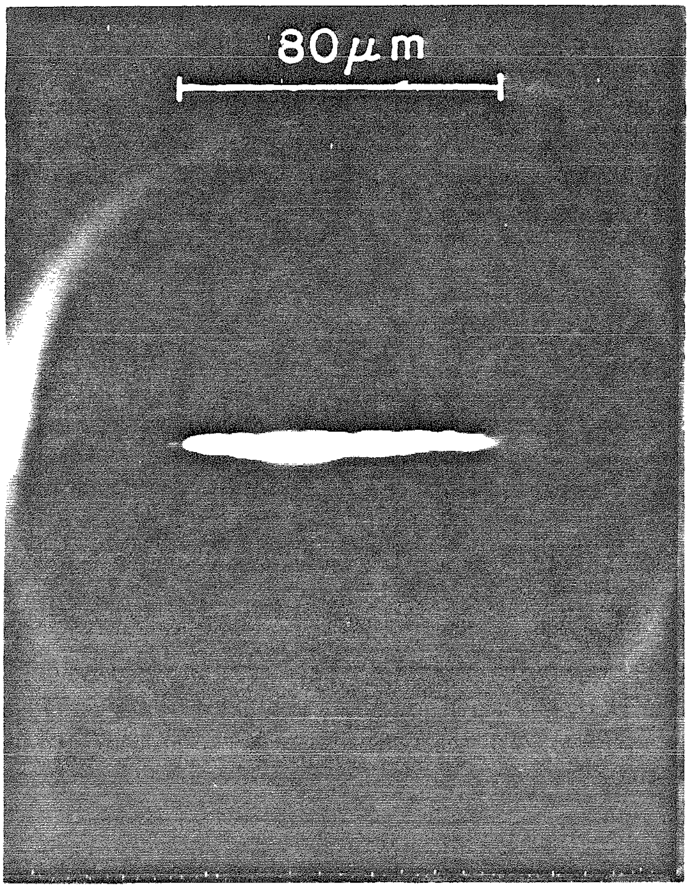

Figure 2.5: Near field pattern of the unstable resonator for I = 1.8 I_{th}.

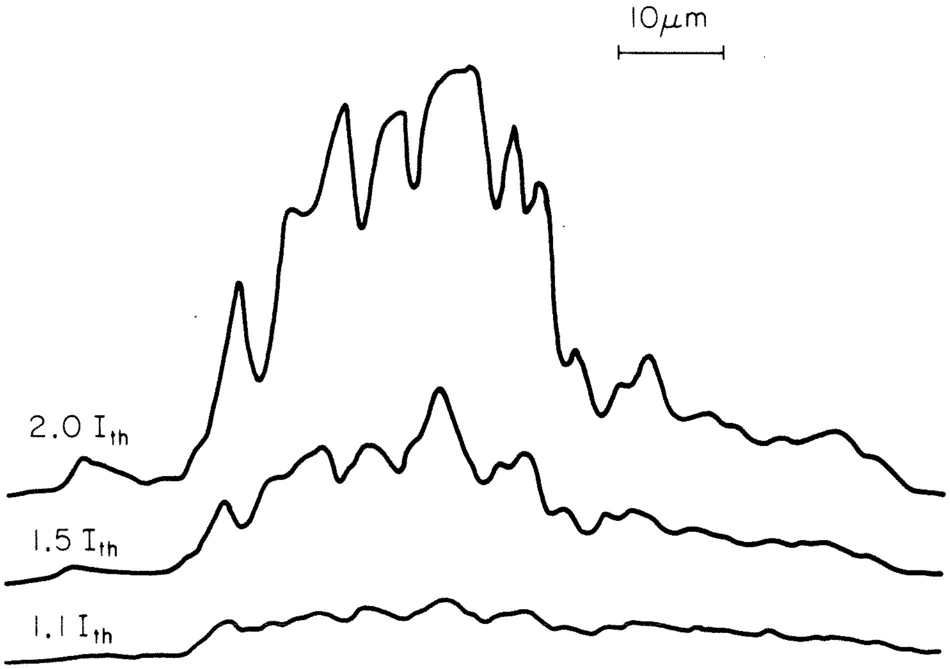

Figure 2.6: Recorded near field intensity distribution for three different values of the injection current.

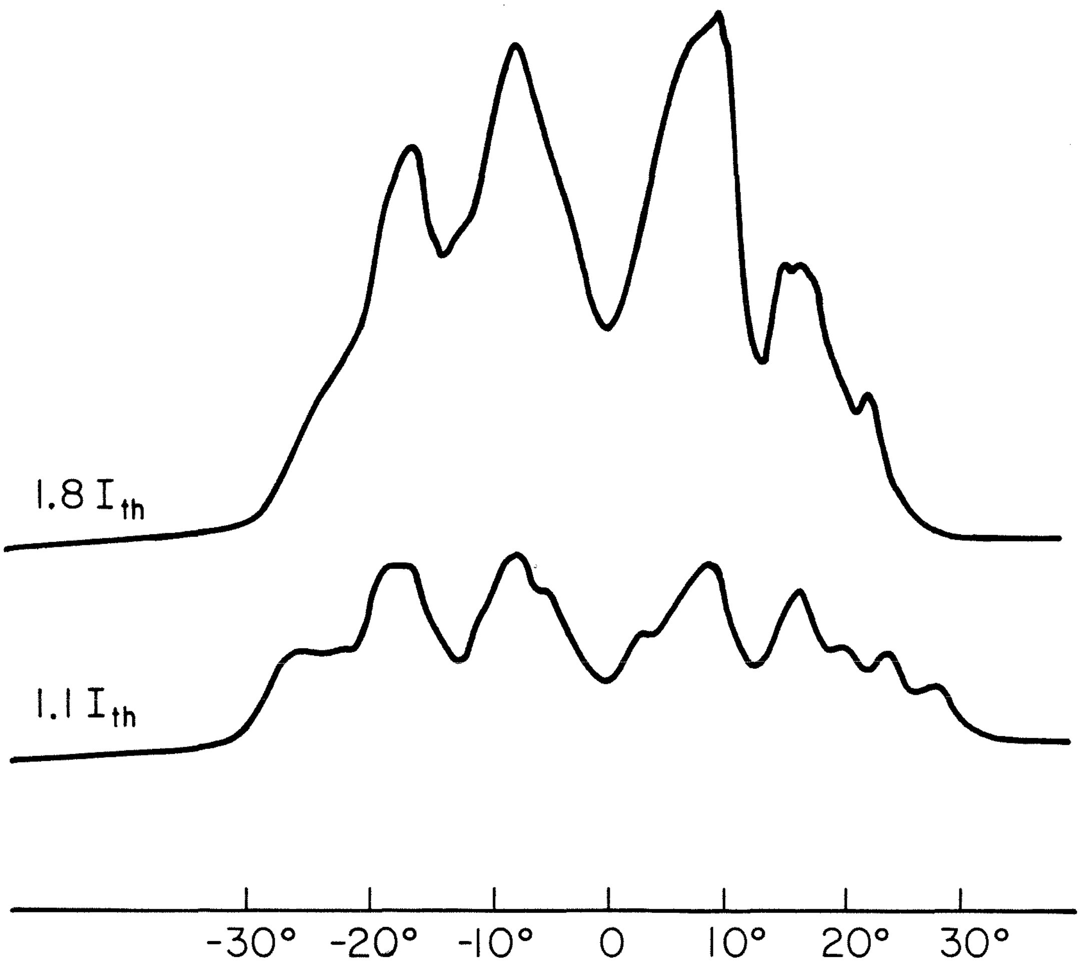

Figure 2.7: Far field intensity distribution in relative units as a function of far field angle. The acceptance angle of the camera is ± 30°.

formula (12) for the ratio between quantum efficiencies, we find that $\eta_{d(\text{unstable})} \approx .73\eta_{d(\text{cleaved})}$, while according to the measured values, $\eta_{d(\text{unstable})} \approx .7\eta_{d(\text{cleaved})}$, yielding good agreement. Typical maximum power in a single lateral mode was .35 W.

Lateral mode properties were measured by two techniques: first, by imaging the virtual source of the mode, and second, by performing an interferometric measurement of the lateral field distribution [18]. Since the output beam of an UR laser is expected to be highly astigmatic, we investigate the minimum spatial extension of the beam in the principal planes. In the plane perpendicular to the *p-n* junction, the beam waist is at the facet, whereas in the plane of the junction, the light appears to originate at a virtual source located deep behind the laser facet, due to the curved phase of the wavefront and the refraction that occurs at the curved output facet.

The depth of this virtual source (S′ in figure 2.8) was measured with the aid of a microscope objective, and a value of S′ 50± 5 μm was obtained. The intensity distribution of this virtual source in the plane of the *p-n* junction was studied as a function of injection current, and a dramatic narrowing was observed when the injection current was increased from threshold (I_{th}) to $3I_{th}$ (figure 2.9). At $3I_{th}$, the measured width of this virtual source (FWHM) was 5 μm with negligible intensity in the wings.

These results can be explained with the aid of the following simple model: the light inside the UR that propagates toward the output coupling mirror (figure 2.8) can be described in the geometrical optics approximation as a spherical wave originating at a point O, whose distance from the exit facet is given from equations (2) and (3) to be

$$S = \left[\frac{RL}{2} + \left(\frac{L}{2}\right)^2\right]^{\frac{1}{2}} + \frac{L}{2} = 339\ \mu\text{m} \qquad (16)$$

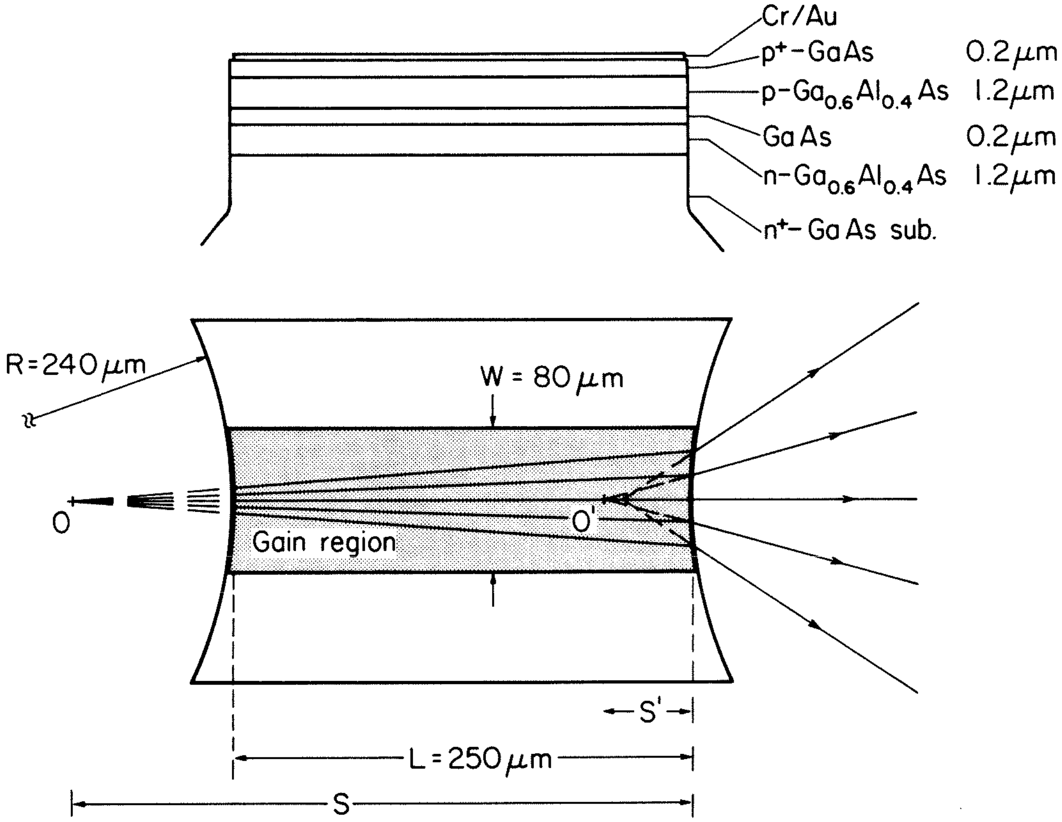

Figure 2.8: Top view of the laser with geometrical-ray description of the URSL. Radiation emanating from a virtual source at point O is refracted through the output mirror, resulting in a virtual source of the output beam at point O'. Shown also is the spherical aberration at O'.

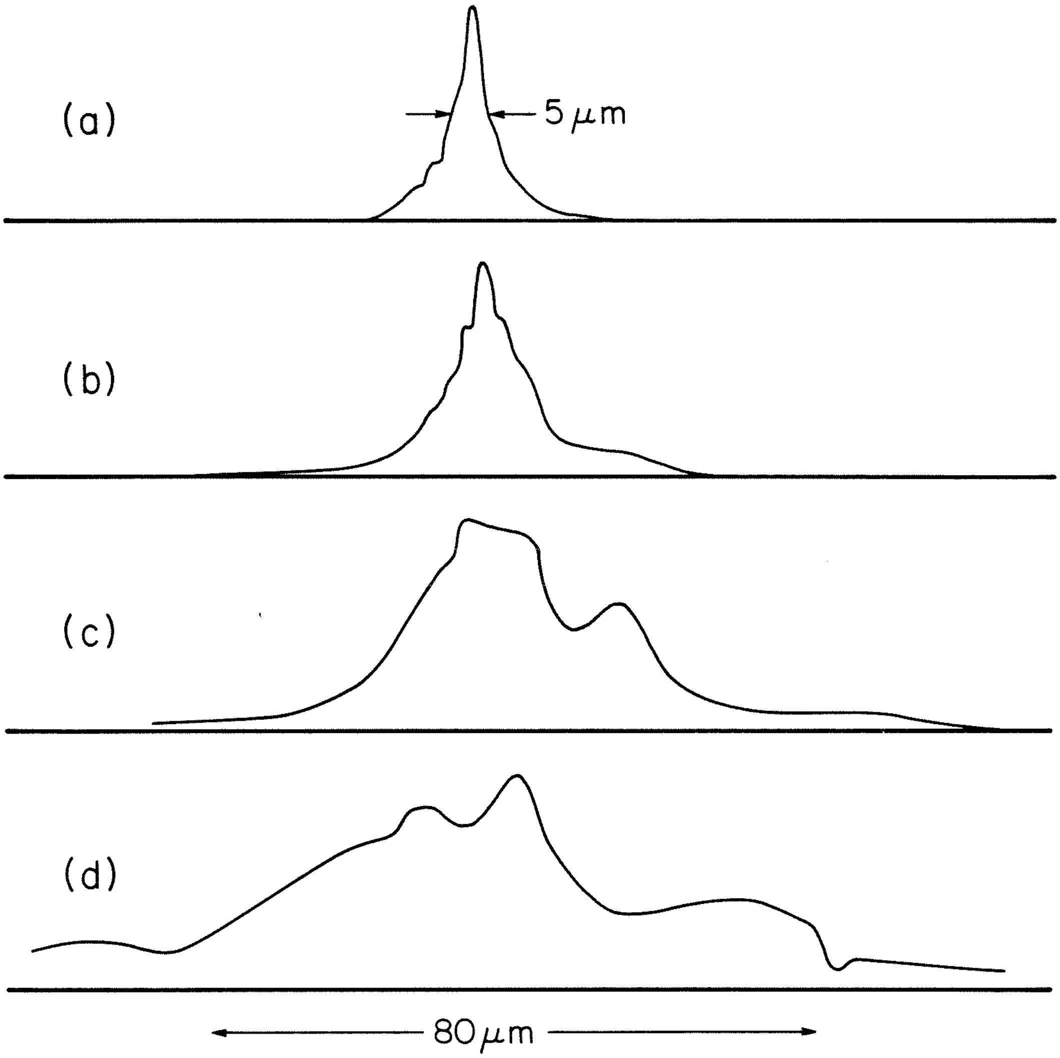

Figure 2.9: Normalized intensity profiles at the virtual source plane as as function of injection current I. (a) $I = 3I_{th}$; (b) $I = 1.9I_{th}$; (c) $I = 1.4I_{th}$; (d) $I = I_{th}$.

After refraction at the cylindrical surface, we obtain for the depth of the virtual source point in the small angle approximation,

$$S' = \left[\frac{(n-1)}{R} + \frac{n}{S}\right]^{-1} = 48\,\mu m \qquad (17)$$

where the index of refraction of the medium is taken to be $n = 3.5$. This result is in good agreement with the measured value of 50± 5 μm. The apparent sharpening of the intensity distribution with increasing injection current at the virtual source plane is expected from the fact that below threshold, the light output is due mainly to spontaneous emission and amplified spontaneous emission, which is not influenced by the resonator feedback. At higher currents, the feedback effect dominates and the laser output exhibits the mode properties of the unstable resonator. It should be noted that the FWHM of the virtual source in the lasers reported here is affected by a strong spherical abberration. A sharper image may be obtained from an aspherical output coupler.

The lateral mode characteristics of the UR laser can be studied by measuring the spatial degree of coherence of the output beam as a function of lateral position. In the multimode case, high spatial coherence is expected only between two points corresponding to comparable intensities of the same lateral mode, whereas two points whose intensities correspond to different modes will exhibit a low degree of spatial coherence. Spatial coherence between two points can be measured by observing the fringe visibility function (FVF) in an interference pattern produced by the radiation transmitted through two narrow slits at these points (Young's double slit experiment). By scanning the slits across the near field of the laser, the coherence function between any two points on the laser output facet can be obtained.

The experimental apparatus is shown in figure 2.10. The laser near field is imaged and magnified to the plane D, which contains the double slit screen. The slit variations and their positions relative to the laser near field could be varied.

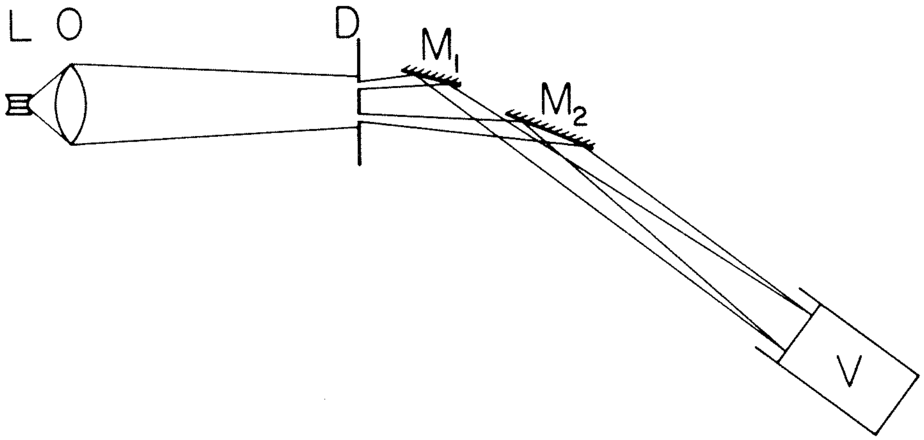

Figure 2.10: Schematic of the double slit interference experiment. L = UR laser; O = microscope objective; D = double slit; $M_{1,2}$ = plane mirrors; V = vidicon camera.

The beam exiting from each slit was nearly diffraction limited. Due to the angular separation between these two beams, additional mirrors were required to produce two overlapping (and interfering) beams, as shown in figure 2.10. A high degree of spatial coherence was observed over the entire spatial extent of the laser output, without dependence on lateral position. Figure 2.11a and 2.11b are examples of the interference patterns recorded with a FVF of approximately 0.6. When the injection current was increased over $3I_{th}$, the fringe visibility function decreased, presumably indicating the onset of higher-order modes. Similar measurements with broad area lasers with cleaved facets (Fabry-Perot cavities), fabricated from the same wafer, showed substantially lower visibility of the interference pattern and a spatial degree of coherence varying with position and injection current. This provides strong evidence that the UR structure results in a single lateral mode at high injection currents in spite of the wide (80 μm) gain stripe and laser mode.

2.4 Lateral Waveguide URSL

The external quantum efficiency of the previous devices was considerably lower than that of cleaved (Fabry-Perot) devices; similarly, the threshold was higher. This is because unstable resonators have naturally higher losses. Semiconductor lasers are peculiar UR's because the diffraction losses, which in most UR's are the desired output, are truly lost in URSL's due to the highly absorptive material surrounding the gain stripe. If this energy could somehow be channeled back into the structure, then, one would expect, the losses would improve. This channeling can be accomplished by incorporating a dielectric waveguide into the resonator. The dielectric step reflects energy back into the resonator and thus decreases the losses.

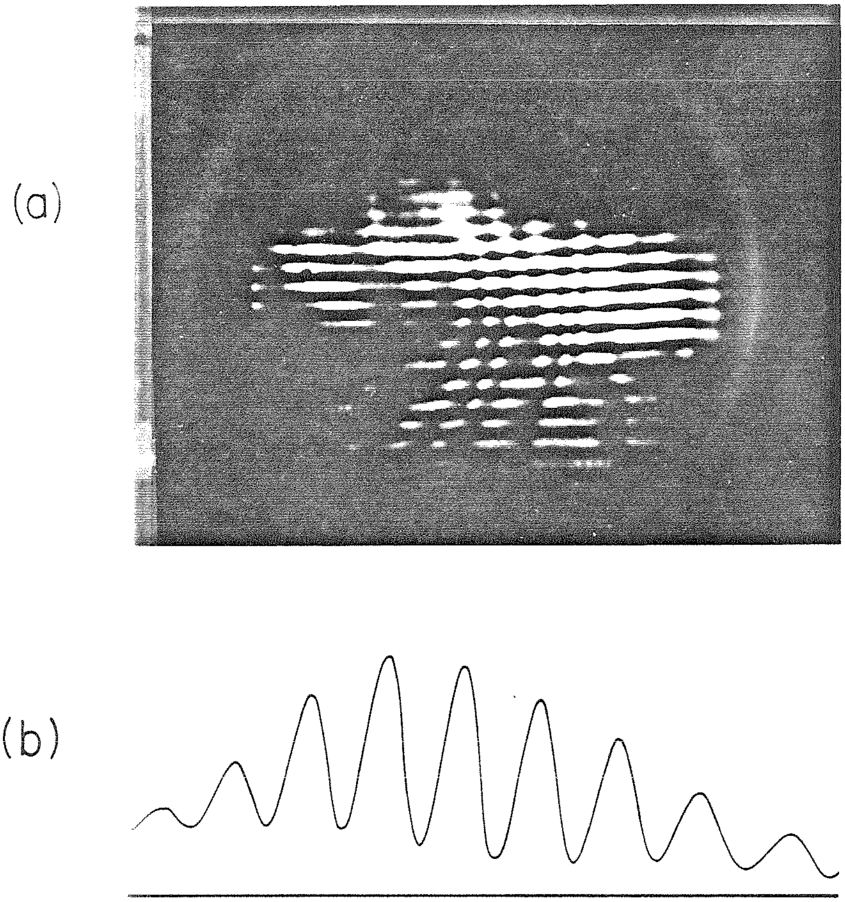

Figure 2.11: (a) Photograph of the interference pattern. (b) Intensity trace of the interference pattern.

However, upon inclusion of such a means of confinement, the geometric theory of unstable resonators no longer becomes valid, and the magnification M is no longer a well-defined quantity. Instead, we must talk of the cavity round-trip factor γ as the indicator of losses. We have calculated loss as a function of index step (see reference [13] or chapter 3), and the results indicate that lower losses and maintained gain selectivity are possible. With that goal in mind, we fabricated URSL's with a built-in lateral dielectric waveguide.

The lasers were fabricated on GaAs/GaAlAs separate confinement double heterostructures grown by liquid phase epitaxy. The epilayers were grown upon a < 111> oriented GaAs n^+-doped substrate. This results in a very uniform crystal growth that manifests itself in low threshold current density for laser operation (in 300 μm-length Fabry-Perot lasers, as low as 600 A/cm^2). A ridge waveguide 80 μm wide was etched in a H_2SO_4:H_2O_2:H_2O (1:8:1) solution down to approximately 0.3 μm from the active layer (figure 2.12). The additional steps in the device fabrication were identical to those in the previous section. The lasers were tested with 200 ns pulses at a 1 kHz repetition rate, and the near field intensity distribution was observed with an infrared vidicon camera. Figures 2.13 and 2.14 show the near field pattern for three different values of the injection currents. Here, a complicated structure is observed, unlike the case of a gain-guided unstable resonator. Note, however, that the field structure remains constant as the current is changed; such would not be the case if random filamentation were occurring.

The high spatial frequencies evident in the near field plot are the result of the coherent superposition of the waveguide modes in the (single) resonator mode. To check this point, the spatial coherence of the output field was tested using the double slit experiment of the previous section. High visibility (FVF$\approx$ 0.5-0.6) fringes were observed. This is to be compared with filamentary

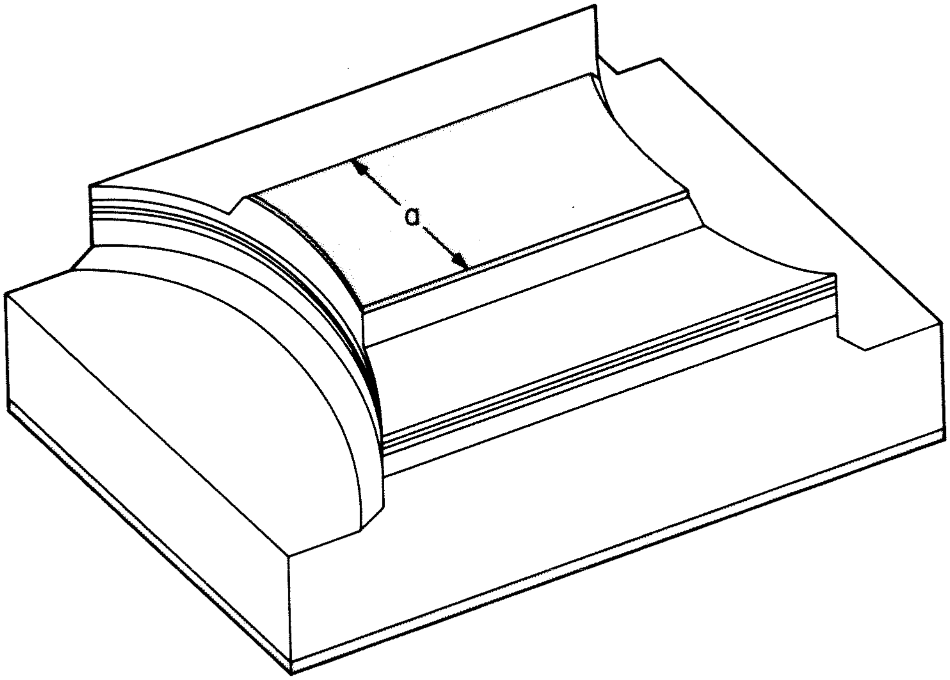

Figure 2.12: Schematic drawing of the unstable resonator ridge waveguide laser.

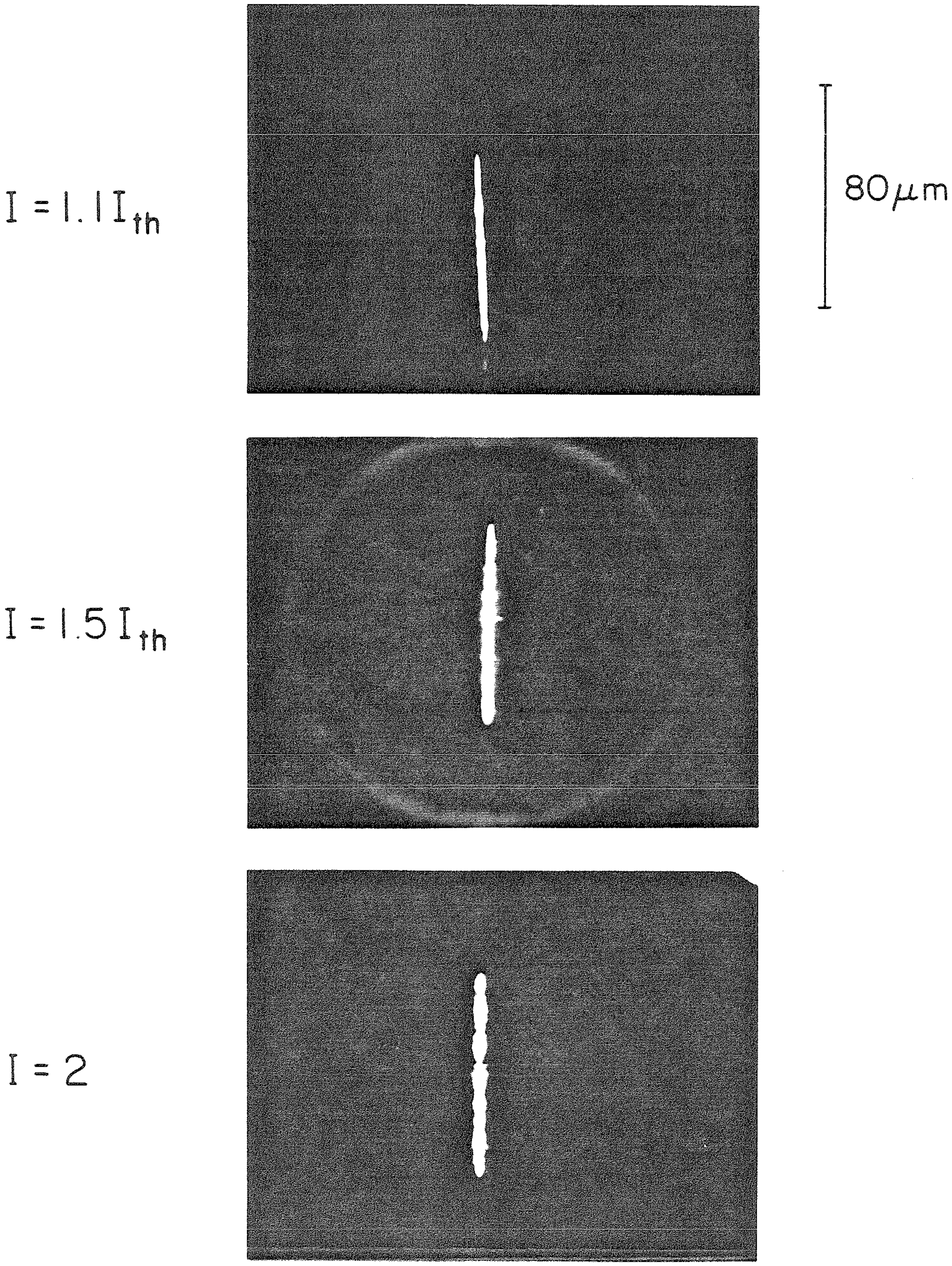

Figure 2.13: Near field pattern for different values of the injection current.

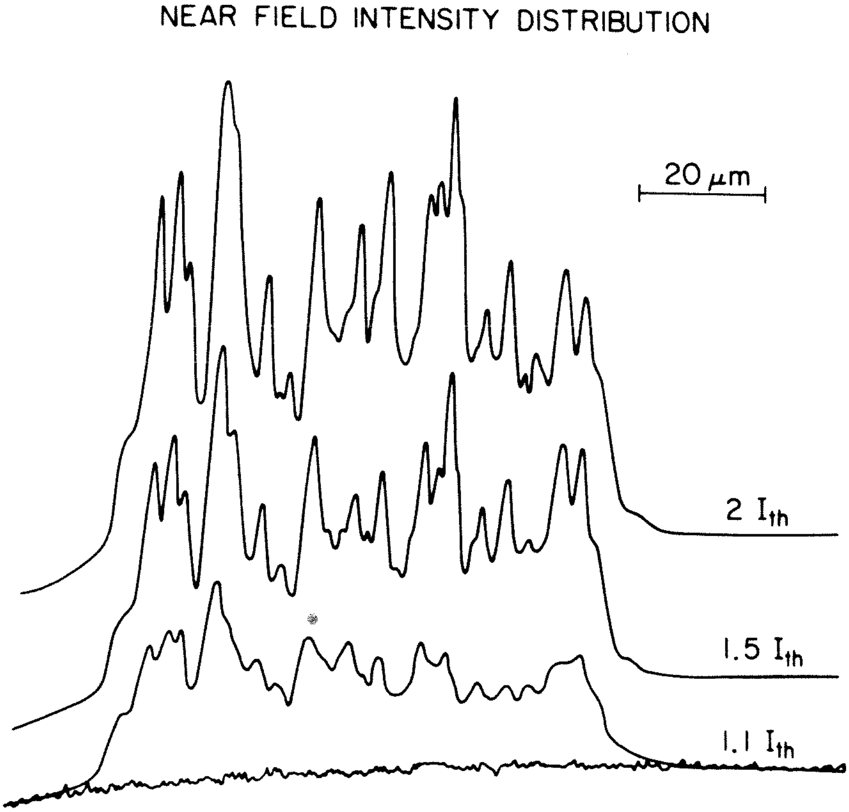

Figure 2.14: Intensity trace of near field patterns at different pump currents.

broad area lasers, which typically have a fluctuating FVF of 0.3 or less. The spatial coherence was maintained up to an injection current of $4I_{th}$ with an output power of over 400 mW. We assume that at this point, a second resonator mode was excited.

As we have said, the lateral waveguide reduces the cavity losses by a significant amount. The threshold current and quantum efficiency for the unstable resonator with a lateral waveguide was I_{th}=300 mA and $\eta_d = 0.28$. A comparison between different broad area laser geometries in terms of threshold current and quantum efficiency is given in table 2.1. From the table and the above discussion, we can conclude that the incorporation of a lateral waveguide to the unstable resonator semiconductor laser results in a significant decrease of the cavity losses. The near field intensity distribution is degraded by ripples that arise from the interference effects between the coupled waveguide modes. Yet, the suppression of filamentation associated with UR's is retained.

2.5 Confocal URSL

In this, and all previous work on URSL's [17,19], all devices emitted a diverging beam from the output facet. This is due to both the curved phase of the light inside the resonator, and the refraction the light undergoes upon exiting the laser. In the macroscopic world of unstable resonators, collimated output beams are achievable, however, using the confocal geometry [20], and such a geometry should be scalable to URSL's. In this section, we present the fabrication of and measurements upon such a confocal URSL.

A positive-branch confocal resonator is illustrated schematically in figure 2.15. The cavity is composed of a large concave mirror M_1 and a small convex mirror M_2 with radii of curvature R_1 and R_2, respectively, satisfying the confocal condition $R_1 + R_2 = 2L$, with L the cavity length. The geometrical magnification M

Table 1

Threshold current and external quantum efficiency of different lasers.

Laser Geometry	I_{th}	η_d
Broad Area Fabry Perot (cleaved) laser	250 mA	0.34
Unstable Resonator (Ref. 1)	700 mA	0.22
Ridge Waveguide Unstable Resonator	300 mA	0.28

Table 2.1: Comparison between different broad area laser geometries.

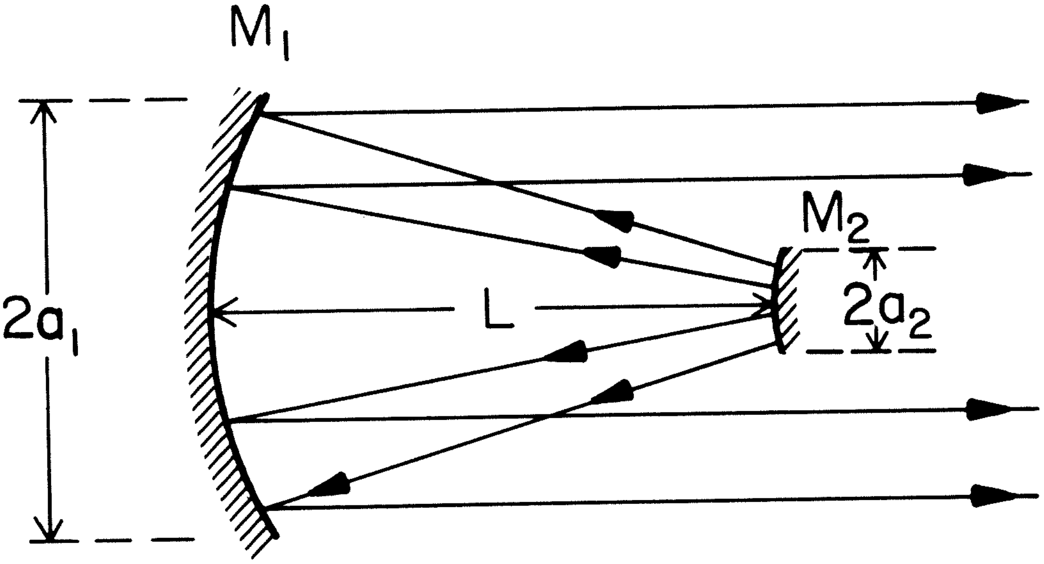

Figure 2.15: Geometry of a positive-branch confocal unstable resonator.

is given by the ratio of the mirror lateral sizes a_1/a_2. The output beam is that portion of radiation reflected by M_1 that misses striking M_2. A remarkable feature of this cavity is that its fundamental mode is a collimated two-section beam (or a collimated annular beam for a three-dimensional resonator).

Figure 2.16 shows the geometry of the confocal URSL. GaAs/GaAls double heterostructures were grown by molecular beam epitaxy, and conventional photolithographic methods were used to define the desired pattern for mirror etching and metallization. Apart from the slight complication needed to provide three separate electrical contacts, the fabrication is similar to that of the two previous URSL's. The cavity dimensions are $2a_1 = 150\ \mu m$, $2a_2 = 30\ \mu m$, $R_1 = 400\ \mu m$, $R_2 = -80\ \mu m$, $L = 160\ \mu m$, leading to a geometrical magnification of $M = 5$ and an equivalent Fresnel number $N_{eq} = 350$. We note that, unlike in other UR lasers in which the cavity is defined by external optics, the output beam in a URSL is refracted by a semiconductor-air interface. Reflections from this interface may complicate the mode pattern and reduce the lateral mode discrimination. An additional problem is that the radiation reflected by M_1 is nearly collimated. Thus, the outer parts of the cavity (sections II and III in figure 2.16) are susceptible to regenerative self-focusing and the formation of isolated filaments. These problems can be avoided to some extent by providing separate electrical contacts to the output couplers (section II and III) so that the central part of the laser--the resonator--can be operated above threshold, and the output couplers given a low injection current (i.e., pumped to transparency). Furthermore, additional properties of the resonator can be studied by independently changing the current in the different sections.

A scanning electron micrograph of the etched mirror M_2 is shown in figure 2.16b (the rough sections on top of the device are the Cr/Au contact pads). Here, ripples in the etched mirror on the order of $0.1\ \mu m$ can be observed.

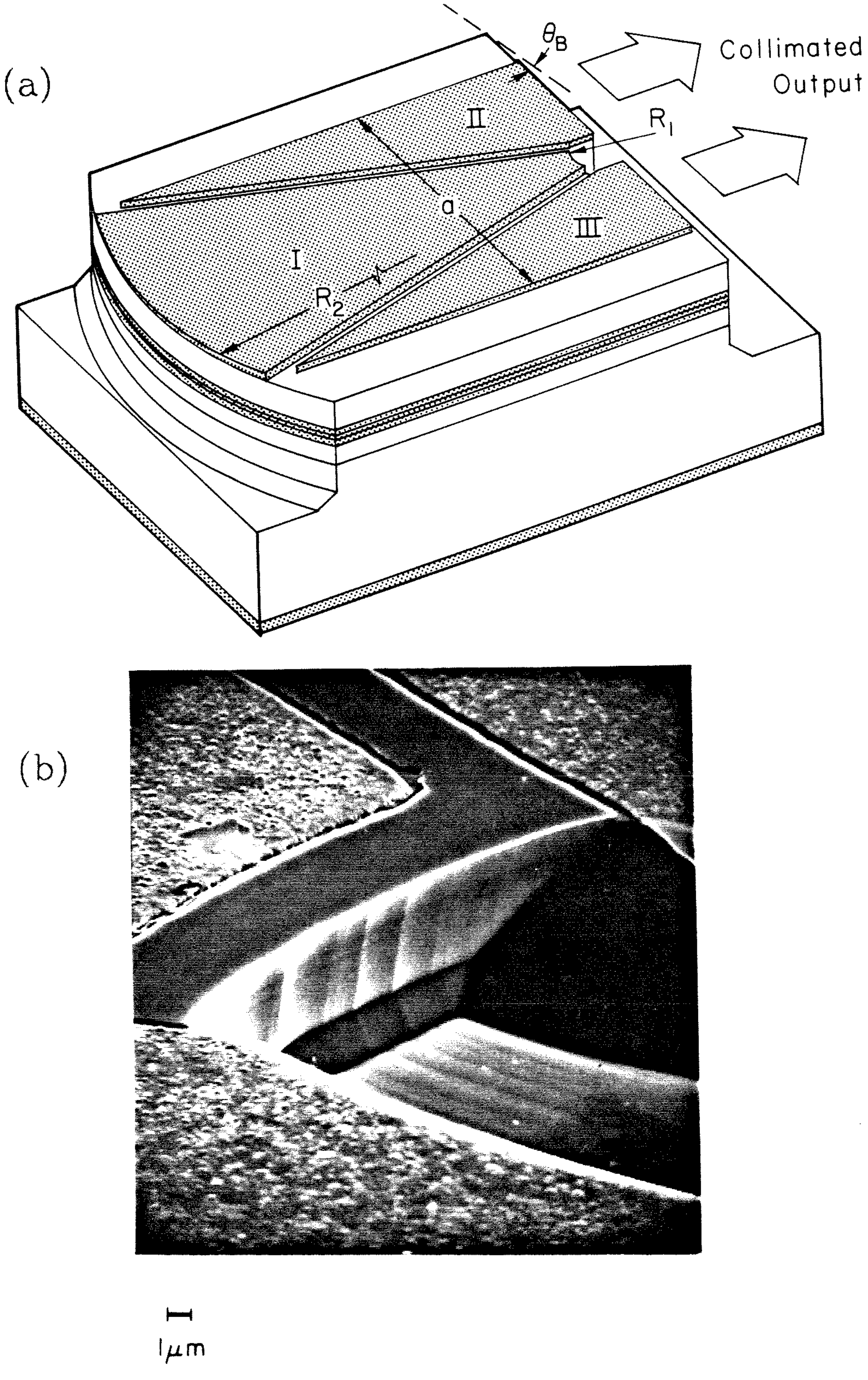

Figure 2.16: (a) Schematic of the confocal unstable resonator. (b) Scanning electron micrograph of the etched mirror.

Slight misalignment of the mirrors caused by undercut in the etched facets was also noticed in the measured devices.

An estimate of the output beam characteristics can be obtained by considering the fundamental lateral mode of a 2D confocal UR in the geometrical approximation. The near field of this mode consists of a uniformly illuminated, constant phase aperture of width $2a_1$ with a central obscuration $2a_2$ wide. The far field intensity distribution $I(\vartheta)$ corresponding to this aperture is given by

$$I(\vartheta) = I_0 \frac{\sin^2[\vartheta(u_1 - u_2)]}{[\vartheta(u_1 - u_2)]^2} \cos^2[\vartheta(u_1 + u_2)] \tag{18}$$

where $u_{1,2} = a_{1,2}/\lambda$ and λ is the optical wavelength. ϑ is the far-field angle. By inserting the values of a_1 and a_2 from our device, we find that the main lobe of an ideal cavity far field pattern is 0.27°.

Of course, a more rigorous analysis of the device would result in a much more complicated radiation pattern than that predicted by equation (18). Diffraction at the edges of the mirrors will introduce ripples into the near field pattern, while reflections at the output coupler may result in oscillation of high-order transverse Hermite-Gaussian modes. Finally, imperfections in the mirrors, a misalignment of the cavity, and index inhomogeneities may cause distortions and a degradation of the beam quality.

The lasers were tested with the usual 200 ns pulses at a 1 kHz repetition rate. The output pattern was monitored with a vidicon camera. In figure 2.17 the near field intensity distribution is recorded for different values of the injection current. Figure 2.17a shows the spontaneous emission in sections II and III. When section I is operated below threshold, the near field pattern becomes nearly constant over the aperture, and high spatial frequency ripples, characteristic of the confocal fundamental mode [21] appear (2.17b). When section I (the resonator) is above threshold, the output is peaked in the regions adjacent

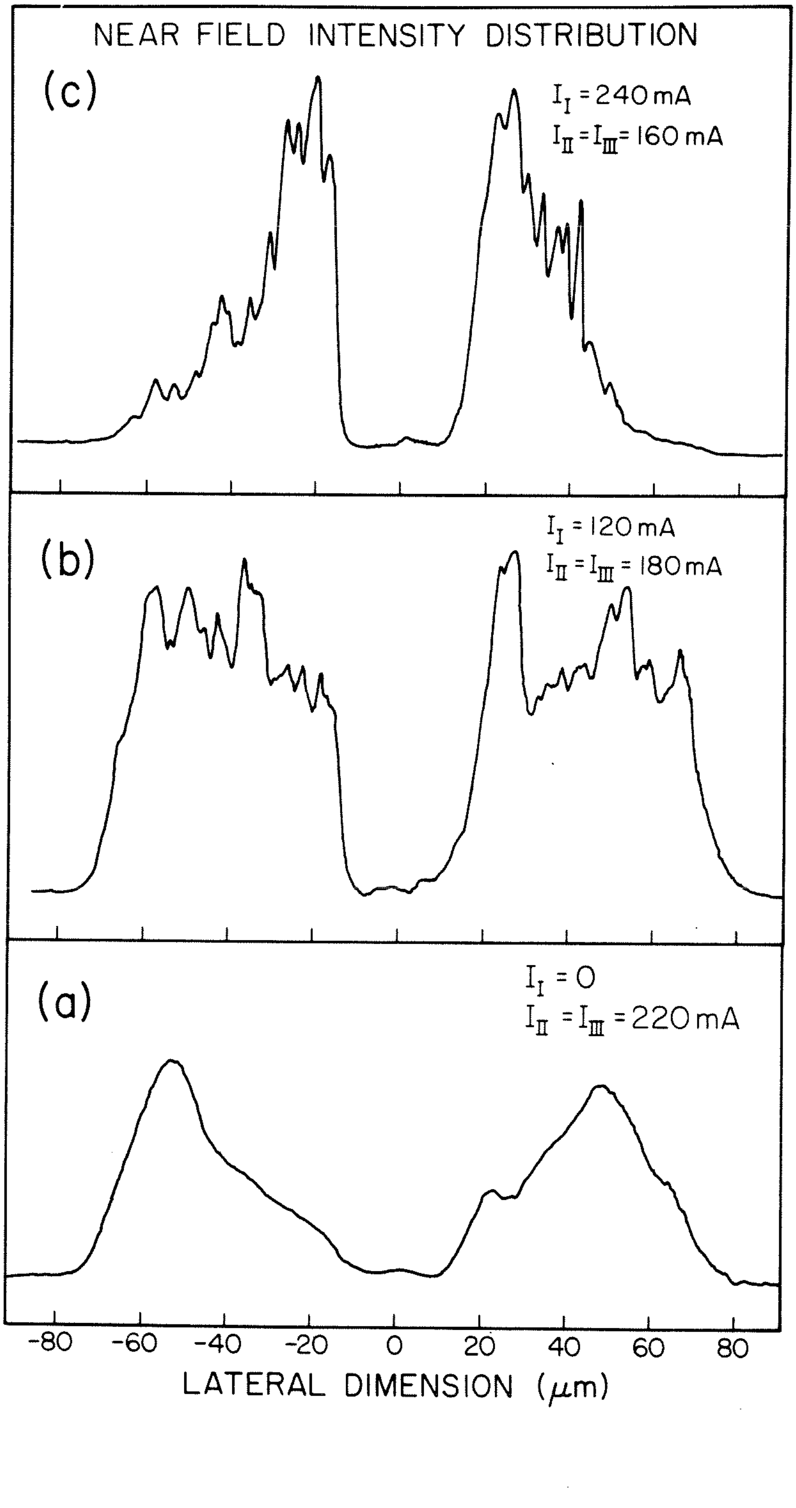

Figure 2.17: Near field intensity distribution of the confocal URSL for different pump currents.

to the central obscuration, indicating that the cavity is not exactly in the confocal condition (2.17c). However, by measuring the spectrally resolved near field we confirmed that the two beams of figure 2.17c were phase-locked to each other. A misalignment of the cavity was revealed also by observing the far field pattern, and changing the injection current in sections II and III. When only one of the sections was operated, a very narrow beam was observed. The position of this beam varied from device to device, typically being off-axis at 10± 6°. When both sections were operated simultaneously, a very complicated interference pattern was observed. In figure 2.18 a far field intensity distribution with a central peak of FWHM 1.9° located 16° off axis is shown.

The misalignment problems mentioned above can be understood by considering the sensitivity of the output beam to variations in the confocal cavity parameters. A perturbation analysis of the output beam characteristics results in the following tolerances on L, R_1, and R_2:

$$\left|\frac{\Delta L}{L}\right| \approx \left|\frac{\Delta R_1}{2L}\right| \approx \left|\frac{\Delta R_2}{2L}\right| \approx \frac{L\lambda}{16a_1^2} \qquad (19)$$

This represents an accuracy of better than $\pm 0.1\ \mu m$ in L, and mirror shapes smooth to within ± 200 Å. These figures are beyond the resolution of the conventional photolithography used to define the cavity in this work.

By antireflection coating of the output coupler, high-reflectivity coating of the mirrors, and fabricating only a single side of the confocal resonator, an efficient, high-power semiconductor laser could be fabricated. The results reported in this section suggest that with the improvement of sub-micron pattern transfer techniques (e.g., e-beam photolithography) and the further development of reliable etching procedures, new cavity configurations can be incorporated monolithically into semiconductor lasers. The resonator geometry can then be designed to fit specific optical output requirements.

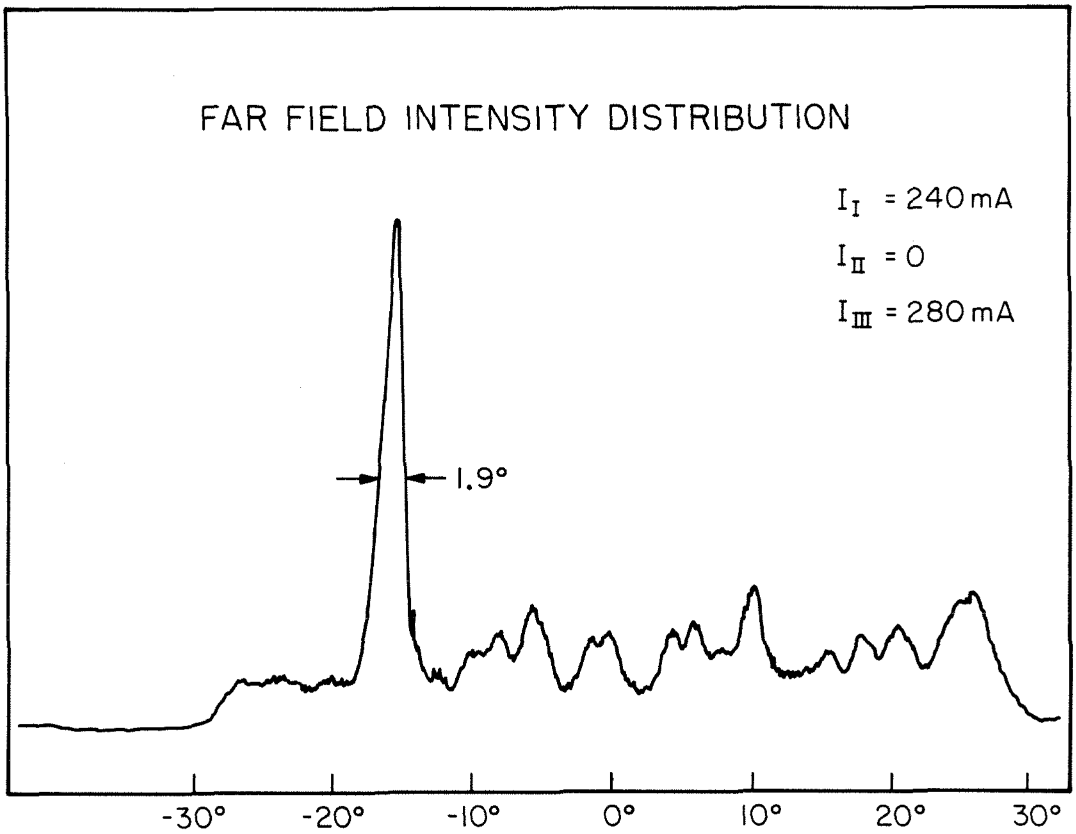

Figure 2.18: Far field distribution of the confocal URSL.

2.6 Tilted-Mirror URSL

One of the reasons for using UR's is to suppress filaments; the magnifying effect of the mirrors tends to suppress them by defocusing any incipient filament. One could also eliminate a filament simply by shifting it laterally with each round trip by misaligning the mirrors of a Fabry-Perot resonator. In fact, FP resonators with tilted mirrors have been analyzed before [22-23], but in these works, the tilt was considered to be a very small perturbation to the ideal cavity, and its effect was studied from the point of view of tolerances of FP cavities to mechanical imperfections. However, in order to completely suppress filaments in a semiconductor laser, we must consider very large tilt angles--on the order of several degrees--and the approximations made in prior work break down.

In this section, we report on the fabrication and operation of broad area GaAs/GaAlAs lasers with tilted mirrors [24]. One is illustrated schematically in figure 2.19. This geometry is interesting and unusual because the geometrical approximation says it won't work. Consider--even in unstable resonators, there is always one ray that reproduces itself and "seeds" the resonator; but no such ray appears to exist in the tilted-mirror resonator. Because the device is gain-guided, however, the lossy region on the short end of the resonator "drags" the phase of the light that extends into it, resulting in a sharply curved phase front at the edge of the gain stripe (see figure 2.20). A portion of this phase front is thus in a position to reproduce itself and act as a "seed" for the rest of the resonator. However, since this phase drag is a diffractive effect, geometrical considerations will not account for it.

The GaAs/GaAsAs double heterostructures were grown by liquid phase epitaxy, and subsequently standard photolithographic techniques were used to

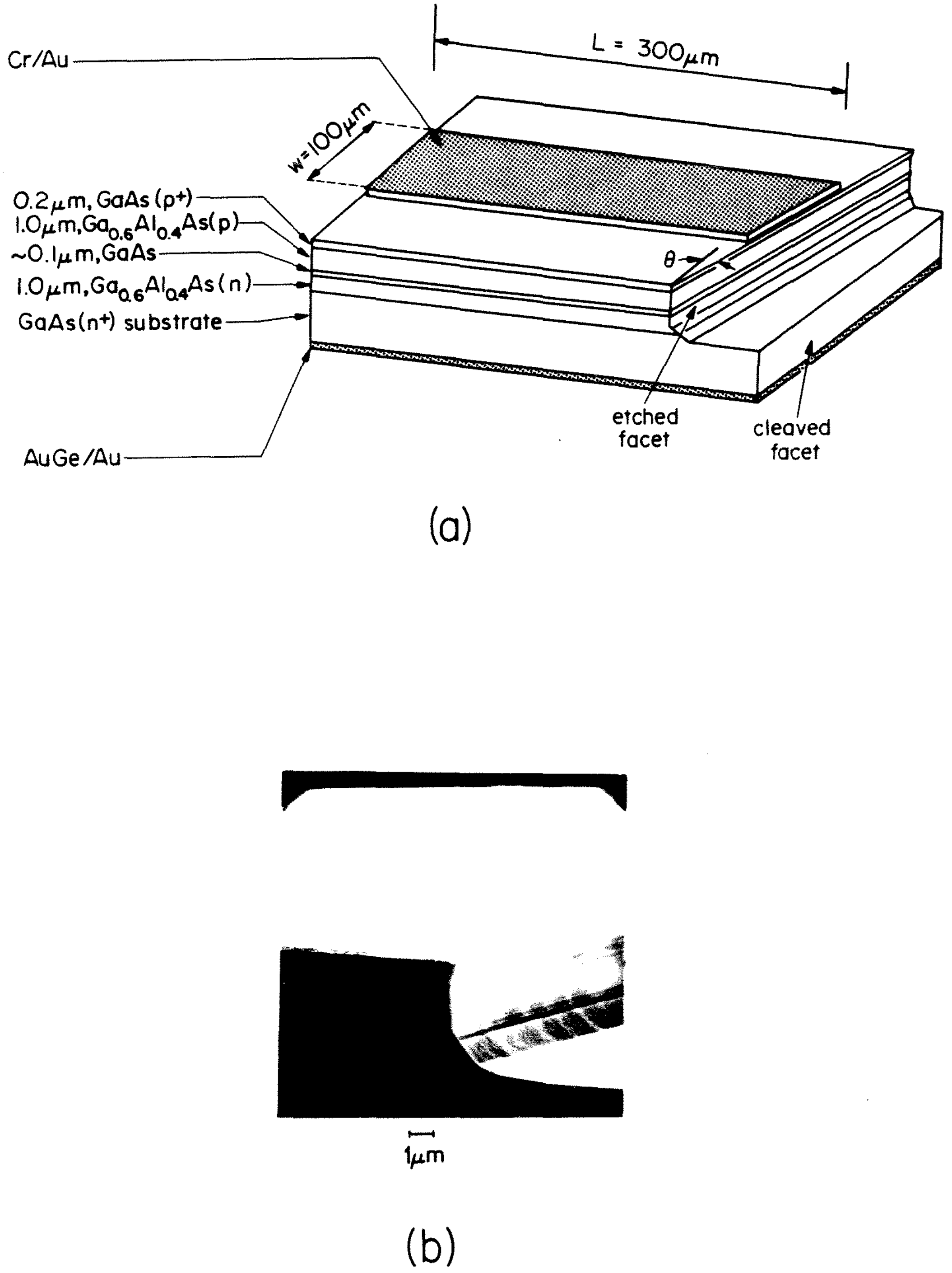

Figure 2.19: (a) Schematic of a tilted-mirror URSL. (b) Scanning electron micrograph of the etched facet.

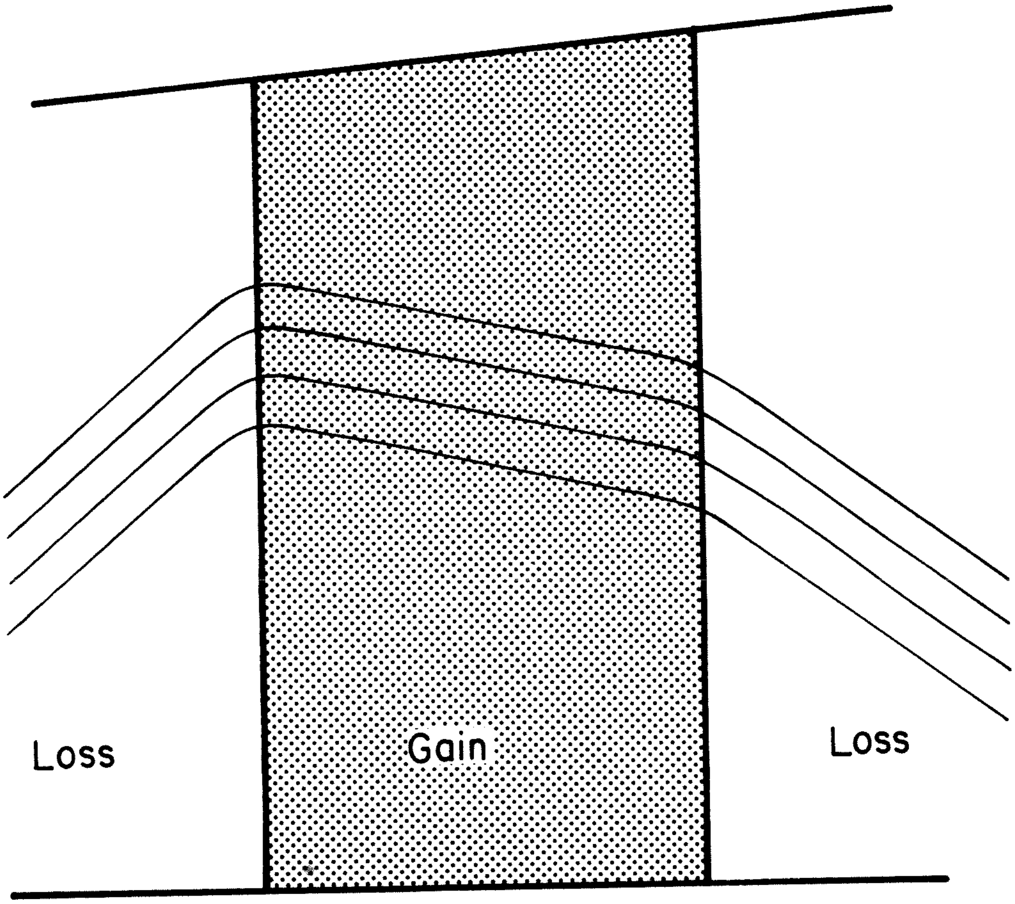

Figure 2.20: Schematic of top view of laser, illustrating phase drag. The lossy region on the outsides drags the ramped phase, creating a curved phase front on the short side that self-replicates.

form resist patterns on top of the DH wafers. These were then etched, using procedures similar to those used in the previous sections. The fabrication was completed by contact metallization. We obtained an estimate of the necessary tilt angle by requiring that the optical field be shifted by $10\mu m$ (the filament width) after one round trip. In order to compare the losses and modes of lasers with different tilt angles, we fabricated on the same wafer, side by side, lasers having an etched mirror facet at angles 0, 5, 10, and 15°.

Figure 2.21 shows the near field pattern of a tilted-mirror laser ($r = 10°$) for $I = 1.2 I_{th}$ with the laser driven with 100 ns pulses at 1 kHz. The field distribution is very smooth and stable, as can be observed in figure 2.21b, where the near field was recorded for different values of the injection current. The slight maxima at both sides of the emission stripe were present in all the lasers tested both above and below threshold. In many lasers without tilt ($r=0$), these were the places where filaments originated. The increase of the output intensity at the edges of the gain region may be caused by the fact that heating effects are less severe there. The extremely smooth and stable near field pattern can be explained in terms of the mirror-coupled mode analysis of the next chapter.

In order to measure the degree of spatial coherence of the output beam, the Young's double-slit experiment was performed, revealing high visibility fringes, indicating high spatial coherence. This experiment shows that the device operates in a single lateral mode (although not necessarily a single longitudinal mode) even though the gain-guided stripe can support many lateral modes.

The light-current characteristics of tilted-mirror lasers for different tilt angles is given in figure 2.22. As we saw earlier, the cavity losses are approximately proportional to η_d^{-1}, where η_d is the external differential quantum efficiency. This is plotted in the inset to figure 2.22, showing a highly nonlinear increase in the losses with increasing tilt angle.

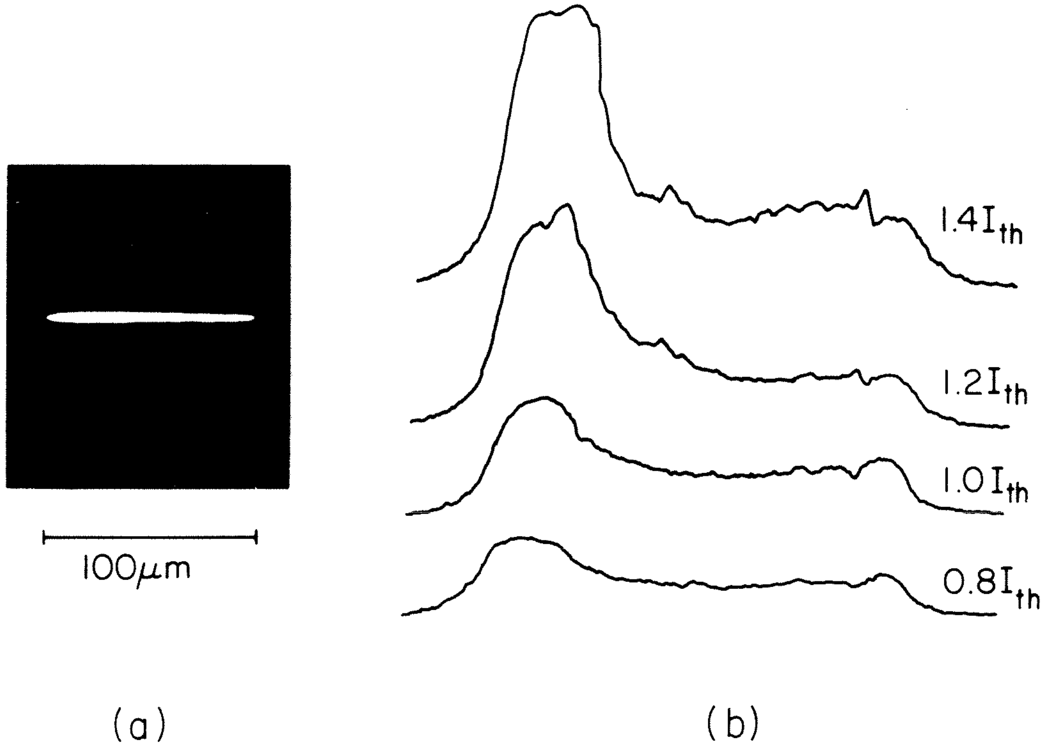

Figure 2.21: (a) Near field of the tilted-mirror laser. (b) Intensity trace of the near field for different pump currents.

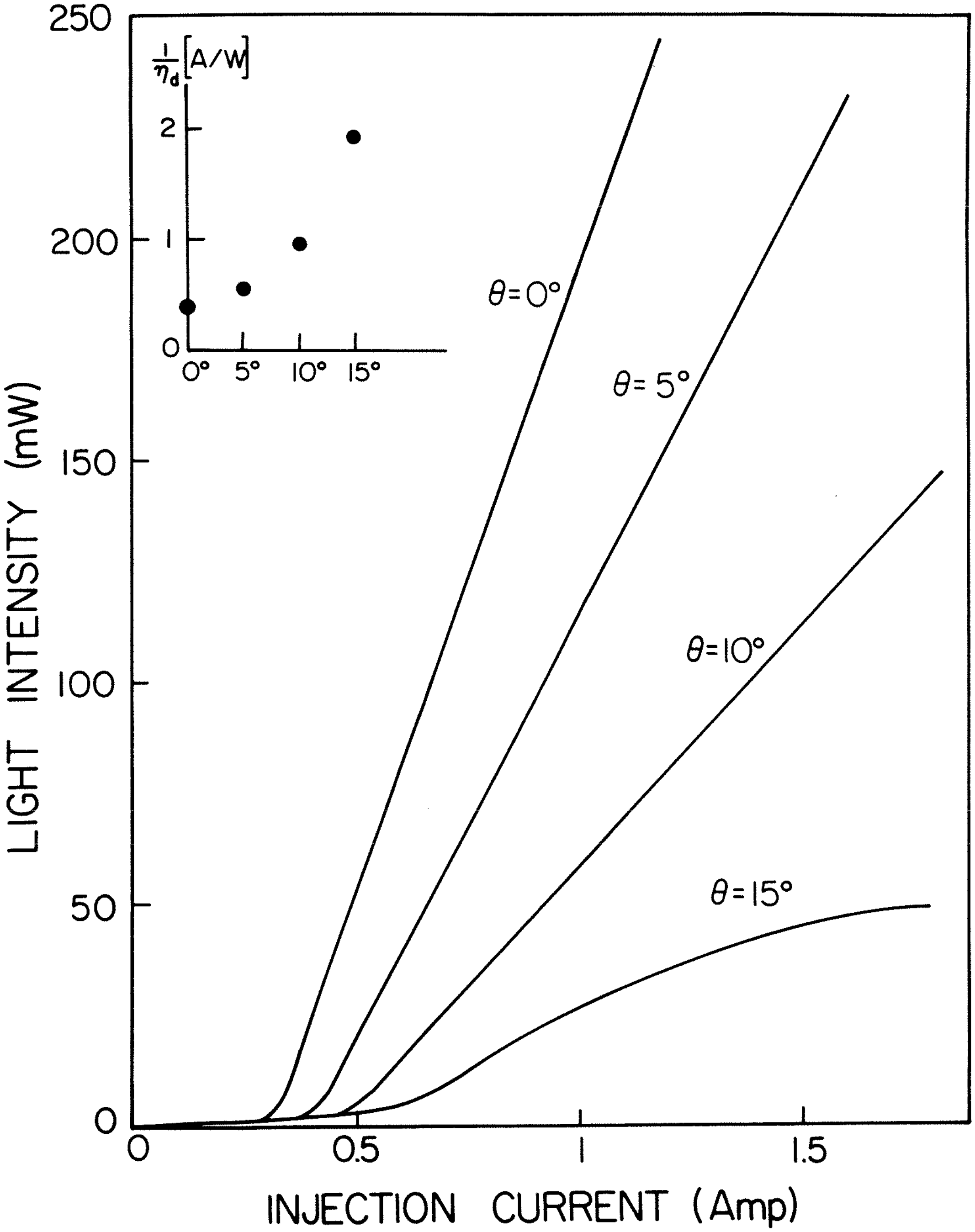

Figure 2.22: Light-current characteristic for lasers with different tilt angles. The inset plots the loss (proportional to the inverse of the quantum efficiency) as a function of tilt angle.

By observing the output of a large number of devices, we found that unlike the case of FP broad area lasers, the near field patterns in almost all the devices are quite similar, showing a high degree of reproducibility. This suggests that the tilted-mirror URSL may be an appropriate candidate for high power applications.

2.7 Conclusions

In this chapter, we have investigated several different unstable resonator semiconductor laser geometries. Beginning with the symmetric URSL, we found that stable lateral mode operation is possible. The magnifying structure of the laser tends to suppress filaments and stabilize the device, at the expense of higher losses and lower external quantum efficiency. The losses can be improved by incorporating into the laser a lateral waveguide to aid in confining the channel losses. However, here, too, a tradeoff exists: the waveguide increases the ripples in the near field of the laser. Also, all symmetric configurations exhibit extremely wide far fields, due to the curved phase inside the laser and the refraction at the output facet.

On the other hand, a collimated beam can be achieved by using the confocal geometry, and we demonstrated narrow-far-field operation of just such a device. We also demonstrated a different version of an unstable resonator, a tilted-mirror resonator, which can have very smooth near fields. The tilted-mirror resonator is interesting since geometric optics suggests that it will not lase, but, as we demonstrated, it quite obviously does.

The results presented in this chapter suggest two more questions: what remains to be done to make semiconductor lasers commercially feasible, and how accurate are the analytic models of the devices? Concerning the first question, the best results we obtained were for unusually good mirror processings.

Noise or ripples on the mirrors on the order of 0.1 μm were sufficient in many cases to disrupt the modal patterns of the devices. Furthermore, as the magnification of the device decreased (as in the confocal devices), the sensitivity to mirror imperfections increased. For a commercial device, one would like a rather low magnification, so as to have low loss and an efficient device; however, low magnification URSL's are more sensitive to the mirror imperfections. We can safely say that the state of the art of URSL's is currently mirror-quality-limited. The requirements, however, are not beyond the capabilities of industry; commercial semiconductor processing facilities are currently at the sub-micron resolution stage, with smoothnesses considerably below that. For experimental purposes, e-beam lithography appears to give the desired resolution, and we should expect that such a technique will eventually push back the mirror limitation.

As far as the accuracy of the current models goes, while the geometric approximation gives a rough handle on the expected losses of unstable resonators, it has its shortcomings (e.g., its failure to handle the tilted-mirror resonator). The gain in SL's is so high that the variations in gain and index refraction distort the field considerably from its geometric idealization. A better model would explicitly take into account diffraction and the gain- and index-guiding effects of the gain stripe. Such a model is presented in the next chapter--a coupled-mode analysis of URSL's.

References

[1] J. K. Butler and D. Botez, IEEE J. Quant. Elect., vol. QE-18, p. 952 (1982).

[2] R. D. Burnham, D. R. Scifres, W. Streifer and S. Peled, Appl. Phys. Lett., vol. 35, p. 734 (1979).

[3] W. Streifer and E. Kapon, Appl. Opt., vol. 18, p. 3724 (1979).

[4] H. Temkin, R. A. Logan, J. P. Van der Ziel, C. L. Reynolds and S. M. Tharaldsen, Appl. Phys. Lett., vol. 46, p. 465 (1985).

[5] D. R. Scifres, C. Lindstrom, R. D. Burnham, W. Streifer and T. L. Paoli, Elect. Lett., vol. 19, p. 169 (1983).

[6] A. Yariv, IEEE J. Quant. Elect., vol. QE-9, p. 919 (1973).

[7] C. P. Lindsey, P. Derry, S. Margalit and A. Yariv, paper #TuF1, presented at Conference on Lasers and Electro-Optics, Baltimore, Maryland, May 21-24, 1985.

[8] C. P. Lindsey, D. Mehuys and A. Yariv, 'Tailored-gain broad area semiconductor lasers," unpub.

[9] J. Salzman, T. Venkatesan, S. Margalit and A. Yariv, paper #ThV3, presented at Optical Society of America meeting, San Diego, California, Oct. 29-Nov. 1, 1984.

[10] M. Wada, K. Hamada, T. Shibutani, H. Shimizu, M. Kume, K. Itoh, G. Kano and I. Teramoto, IEEE J. Quant. Elect., vol. QE-21, p. 658 (1985).

[11] A. E. Siegman, Proc. IEEE, vol. 53, p. 277 (1965).

[12] J. Salzman, T. Venkatesan, R. Lang, M. Mittelstein and A. Yariv, Appl. Phys. Lett., vol. 46, p. 218 (1985).

[13] R. J. Lang, J. Salzman and A. Yariv, IEEE J. Quant. Elect., vol. QE-22, p. 463 (1986).

[14] J. Salzman, R. Lang and A. Yariv, Elect. Lett., vol. 21, p. 820 (1985).

[15] M. J. Smith, Appl. Opt., vol. 20, p. 4148 (1981).

[16] Yu. A. Anan'ev, Sov. J. Quant. Elect., vol. 1, p. 565 (1972).

[17] A. P. Bogatov, P. G. Eliseev, M. A. Man'ko, G. T. Mikaelyan and Yu. M. Popov, Sov. J. Quant. Elect., vol. 10, p. 620 (1980).

[18] M. Mittelstein, J. Salzman, T. Venkatesan, R. Lang and A. Yariv, Appl. Phys. Lett., vol. 46, pp. 923-925 (1985).

[19] R. R. Craig, L. W. Casperson, G. A. Evans and J. J. J. Yang, paper presented at Conference on Lasers and Electro-Optics, Anaheim, California, June 19-22, 1984.

[20] J. Salzman, R. Lang, A. Larsson and A. Yariv, "Confocal unstable resonator semiconductor laser," Opt. Lett., (1986), to be published.

[21] D. B. Rensch and A. N. Chester, Appl. Opt., vol. 12, p. 997 (1973).

[22] A. G. Fox and T. Li, Proc. IEEE, vol. 51, p. 80 (1963).

[23] J. L. Remo, Appl. Opt., vol. 19, p. 774 (1980).

[24] J. Salzman, R. Lang, S. Margalit and A. Yariv, Appl. Phys. Lett., vol. 47, pp. 9-11 (1985).

*

*

*

Chapter 3

Modal Analysis of Semiconductor Lasers with Non-Planar Mirrors

3.1 Introduction

Until recently, the theory of lateral mode structure in semiconductor lasers has concentrated on those devices that are homogeneous along their length and possess planar mirrors. This situation has persisted for two very good reasons. The first is that both the transverse and longitudinal dimensions can be eliminated from the problem, reducing it to a one-dimensional waveguide problem. The second, and perhaps more important reason, is that such devices were all that existed until recently.

The development of semiconductor lasers with non-planar mirrors calls for an analytical method of determining their lateral mode structure, and consequently, the gain of their various modes. The properties of lasers with non-planar mirrors and unstable resonators, in particular, have been described extensively in the literature. However, the application of such theory to semiconductor lasers encounters several problems that stem from the unique character of semiconductor lasers. Most theories [1-5] treat the resonator as consisting of two mirrors bounding a homogeneous medium; yet gain-guiding plays a substantial role in semiconductor lasers. Secondly, the finite size of the mirrors introduces effects due to edge diffraction that are lost in theories that assume infinite mirrors [1,6]. The two-dimensional nature of the semiconductor laser suggests many asymmetric configurations that would be impractical in a three-dimensional laser, and consequently, have not been analyzed. Also, the lossy material surrounding the pumped region absorbs the diffracted wave, which suggest that a real index waveguide in the lateral direction could increase the quantum efficiency of a URSL [4]. Finally, there are many geometries other than unstable resonators (e.g. a tilted-mirror resonator [7] or hybrid URSL/Fabry-Perot resonator [8]) that show promise of high power, yet have not been analyzed.

In this chapter, we present a general solution to the problem of determining the modes of such a structure. In section 3.2, we outline the mirror-coupled mode formalism. In section 3.3, we derive the complex waveguide modes to be used as a basis set and justify the truncation of the set to a finite size. In section 3.4, we calculate the coupling coefficients that characterize the mirrors and show how the nonlinear eigenvalue equation can be simplified to a linear eigenvalue problem. In section 3.5, we present results for three specific cases: a gain-guided URSL, an index-guided URSL, and a tilted-mirror resonator, and compare them to the experimental measurements made in the previous chapter. We conclude in section 3.6 by summarizing the important results of the analysis.

3.2 Outline of the Formalism

The device we are considering is shown schematically in Figure 3.1. It consists of a symmetric lateral waveguide with (complex) indices of refraction n_1 (cladding) and n_0 (core), terminated by nonplanar mirrors R_1 and R_2. We assume that all transverse (x axis) variation has been removed using an effective index approximation [9]. The electric field can be written in terms of the complete set of modes of the lateral waveguide as

$$E_y(y,z) = \sum_n a_n E_n(y) e^{-j\beta_n z} \tag{1}$$

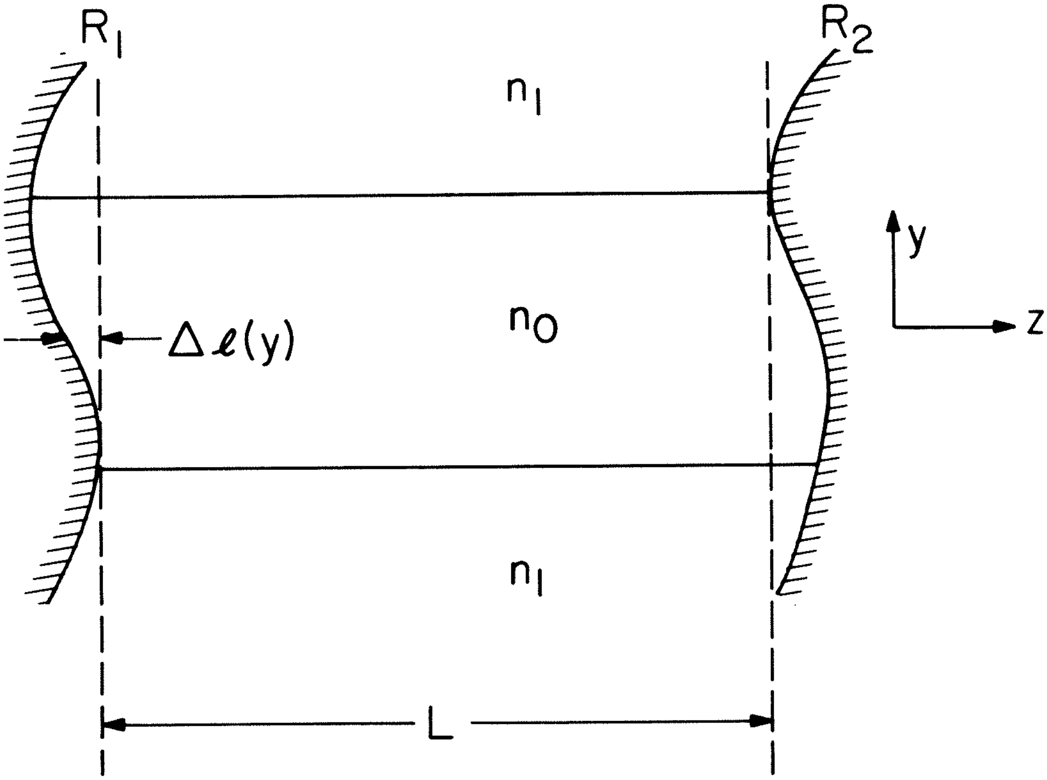

Figure 3.1: Schematic of a broad-area laser with non-planar mirrors and a lateral waveguide.

where the $\{a_n\}$ and $\{\beta_n\}$ are the complex mode amplitudes and propagation constants, respectively, of the (also complex) modes $\{E_n\}$ of the lateral waveguide. The sum in (1) is assumed to include the integration over continuum modes (radiation modes), which must be included for completeness. We can represent the field $E_y(y,z)$ by a column vector $\tilde{A}$ with components $\{a_n\}$; then the result of a propagation through a distance L within the waveguide can be expressed by left-multiplying by a propagation matrix

$$\overset{\approx}{P}(L) \equiv e^{-i\overset{\approx}{B}L} \tag{2}$$

where the n,m component of $\overset{\approx}{B}$ is $\delta_{nm}\beta_n$. We model each mirror by a complex reflectivity R(y), so that the field immediately after reflection is $R(y)E_y(y,z=L)$. Since the set of $\{E_n(y)\}$ is complete, we can expand the field after reflection in terms of the $\{E_n\}$; in particular, a mode $E_n(y)$ after reflection can be written

$$R(y)E_n(y) = \sum_m r_{nm}E_m(y) \tag{3}$$

where $\{r_{nm}\}$ are the elements of a mirror coupling matrix $\overset{\approx}{R}$ given by

$$r_{nm} \equiv (E_m'(y), R(y)E_n(y)) \tag{4}$$

$\{E_m'\}$ are the eigenmodes of the adjoint operator and "(,)" signifies the appropriate inner product.

The eigenmodes of the resonator are found by requiring that the lasing field reproduce itself after one round trip, i.e., that

$$\overset{\approx}{R}_2\overset{\approx}{P}(L)\overset{\approx}{R}_1\overset{\approx}{P}(L)\tilde{A} = \tilde{A} \tag{5}$$

This is in general a nonlinear eigenvalue problem. The free parameters (ω, the lasing frequency, and n, the threshold carrier density (or equivalently threshold gain)) are imbedded within the matrix $\overset{\approx}{P}(L)$ via the dependence of the propagation constants β_n upon ω and n, and to a lesser extent, within the reflectivity matrices due to the dependence of the modes themselves upon n. As it stands, the solution to (5) is not immediately forthcoming. Besides the nonlinearity, the matrices are infinite, and in places, continuous. In the next two sections, we will introduce and justify the approximations necessary to reduce the problem of solving (5) to a manageable task.

3.3 Lateral Waveguide Modes

Our first task is to truncate the set of lateral waveguide modes to some manageable number (according to some rational criterion) and to deal with the troublesome continuum modes. The modes of a symmetric real index waveguide are well known [10]; however, some complications occur when we open up the field to include a complex index of refraction (i.e. gain/loss). There is also the question of whether to include "leaky" modes (which diverge as $y \to \pm\infty$) in our basis. Furthermore, since we are dealing with a complex potential, the problem is non-self-adjoint, and the orthogonality condition between modes is different from that of real index-guided modes. We shall deal with all of these issues in one fell swoop by deriving the complex waveguide modes from the original equation. In the process, a simple picture of the analytic structure of the Green's function for the lateral mode eigenvalue equation will show which modes to keep and which we can safely discard. We begin with the Helmholtz equation for TE waves in the structure shown in figure 3.1.

$$\left[\nabla^2_{yz} + \frac{\omega^2 n^2(y)}{c^2}\right] E_y(y,z) = 0 \tag{6}$$

where ω is the oscillation frequency, c is the speed of light, and

$$n(y) \equiv \begin{cases} n_0 & |y| \le d \\ n_1 & |y| > d \end{cases} \tag{7}$$

We choose our time factor as $e^{j\omega t}$ and search for solutions of the form

$$E_y(y,z) = e^{-j\beta z} u(\zeta), \qquad \zeta \equiv y/d \tag{8}$$

and since we are looking for positive z-traveling waves, we stipulate

$$\mathrm{Re}(\beta) \ge 0. \tag{9}$$

We define

$$v(\zeta) \equiv \left[\frac{\omega dn(\zeta d)}{c}\right]^2, \quad v_0 \equiv \left[\frac{\omega dn_0}{c}\right]^2, \quad v_1 \equiv \left[\frac{\omega dn_1}{c}\right]^2, \quad \lambda \equiv -[\beta d]^2 \qquad (10)$$

to arrive at the nondimensional equation

$$\left[\frac{d^2}{d\zeta^2} + v(\zeta)\right]u(\zeta) + \lambda u(\zeta) = 0 \qquad (11)$$

The problem is fully specified when we include boundary conditions. It is convenient to work out even and odd fields separately (it is clear that any field can be decomposed into an even part and an odd part); so we can solve (11) on the interval $\zeta \in (0,\infty)$ with the boundary conditions

$$u'(0) = 0,\ u \text{ bounded at } \zeta = \infty \qquad (12)$$

for even modes, and

$$u(0) = 0,\ u \text{ bounded at } \zeta = \infty \qquad (13)$$

for odd modes.

A well-known result of spectral theory [11] is that the appropriate spectral representation for an operator L of the equation

$$Lu + \lambda u = 0 \qquad (14)$$

can be determined by integrating the Green's function for the operator on a great circle in the complex λ-plane. In this process, nonanalyticities give rise to the spectrum; poles generate a discrete spectrum; branch cuts, a continuous spectrum. The Green's function, of course, is the solution to

$$[L + \lambda]G(\zeta,\eta;\lambda) = \delta(\zeta-\eta) \qquad (15)$$

For the even modes, the Green's function is easily verified by direct substitution to be

$$G(\zeta,\eta;\lambda) = \frac{u_L(\zeta_<)u_R(\zeta_>)}{\sqrt{\lambda+v_0}\sin\sqrt{\lambda+v_0} - j\sqrt{\lambda+v_1}\cos\sqrt{\lambda+v_0}}$$

$$\text{with} \quad \begin{aligned}\zeta_< &\equiv \min(\zeta,\eta)\\ \zeta_> &\equiv \max(\zeta,\eta)\end{aligned}$$

$$u_L(\zeta) \equiv \begin{cases} \cos\zeta\sqrt{\lambda+v_0}, & \zeta \le 1 \\ \cos\sqrt{\lambda+v_0}\cos(\zeta-1)\sqrt{\lambda+v_1} - \sqrt{\dfrac{\lambda+v_1}{\lambda+v_0}}\sin(\zeta-1)\sqrt{\lambda+v_1}, & \zeta > 1 \end{cases}$$

$$u_R(\zeta) \equiv \begin{cases} \cos(\zeta-1)\sqrt{\lambda+v_0} - j\sqrt{\dfrac{\lambda+v_1}{\lambda+v_0}}\sin(\zeta-1)\sqrt{\lambda+v_0}, & \zeta\leq 1 \\ \exp-j(\zeta-1)\sqrt{\lambda+v_1}, & \zeta> 1 \end{cases} \tag{16}$$

Anticipating the great circle integral, we examine the analytic structure of G in the complex λ-plane. Clearly, there are poles wherever

$$\sqrt{\lambda+v_0}\sin\sqrt{\lambda+v_0} - j\sqrt{\lambda+v_1}\cos\sqrt{\lambda+v_0} = 0 \tag{17}$$

which will give rise to discrete modes. In addition, there is a branch cut emanating from $\lambda = -v_1$. (The quantity $\sqrt{\lambda+v_0}$ appears only in even powers; hence, no branch cut.) The direction of the branch cut can be inferred from the boundedness of u; this criterion, plus the last line of (16), implies

$$\mathrm{Im}\sqrt{\lambda+v_1}\leq 0, \text{ so } -2\pi\leq \arg(\lambda+v_1)\leq 0 \tag{18}$$

The analytic structure is illustrated in figure 3.2. Each nonanalyticity corresponds to a mode of the waveguide with a propagation constant β given by $\beta = d^{-1}\sqrt{-\lambda}$, Re $\beta \geq 0$. Near the negative real axis, a positive imaginary part of λ yields a negative imaginary part for β, implying a lossy mode. From this picture we can compare the losses of all of the waveguide modes using the qualitative rule up=loss, down=gain. To aid in the interpretation of the different modes, modes in different regions of the plane have been labeled in accordance with common usage.

Radiation modes (corresponding to the branch cut) present a special problem to a numerical solution of (5) because they are continuous. They can be dealt with by the following simple expedient;

We shall ignore all continuum modes. (19)

The question is, are we justified in doing so? The resonator modes we are interested in are those with the lowest loss; consequently our intuition suggests that we should use low-loss waveguide modes as a basis set. A closer examination shows that over the length of the laser, the continuum modes are strongly

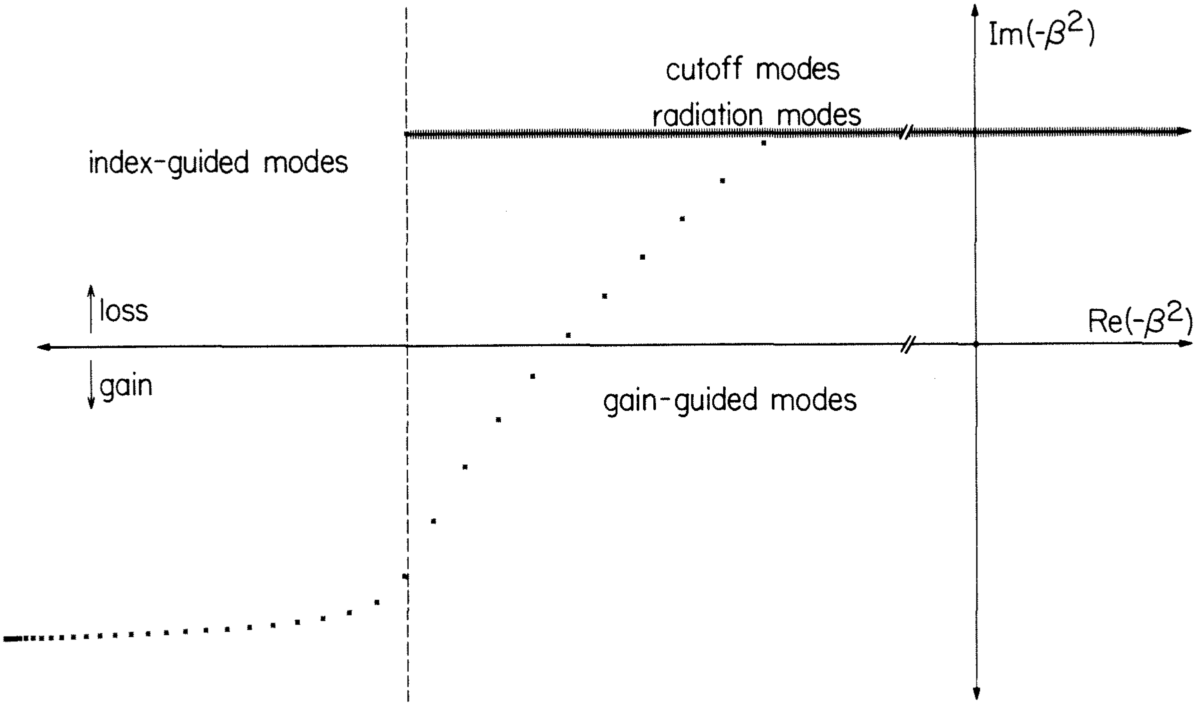

Figure 3.2: Analytic structure in the complex λ-plane of the Green's function for the even waveguide modes of a waveguide of width 20 μm; core: n=3.50, gain=50 cm^{-1}; cladding: n=3.40, loss=50 cm^{-1}. *'s are poles (corresponding to discrete modes) while the cross-hatched line indicates a branch cut (continuum modes).

attenuated compared to the lower-loss discrete modes; consequently, they make negligible contribution to the resonator mode after propagation and can, in fact, be ignored. Furthermore, any discrete modes lying above the branch cut have even higher loss than the continuum modes, so we gain nothing by including them in the basis set. Finally, although the "gain-guided" modes are beyond what is traditionally thought of as cut-off ($-\lambda < \text{Re } v_0$), their loss is comparable to the index-guided modes (if any exist) and should be included.

The validity of the above argument relies on the vertical separation between v_0 and v_1 in the λ-plane, that is, upon the high gain of the core and/or the high loss of the cladding. This pictorial representation indicates the validity of the approximation; for a low-gain medium (e.g., a gas laser) or purely real index guiding, both v_0 and v_1 lie on the real axis. There is no gain separation between continuum and discrete modes, and the theory breaks down. For semiconductor lasers, however, with gains on the order of 50 cm^{-1} or greater, the gain separation is large enough that neglecting continuum modes is a good approximation. (It should be noted that for high-loss resonators, the gain is necessarily much larger than for Fabry-Perot resonators, which strengthens the approximation.)

To summarize; we will use only those discrete modes that lie below the branch cut in figure 3.2. Carrying out the great circle integration yields

$$u_n(\zeta) \equiv \begin{cases} \cos\zeta\sqrt{\lambda_n+v_0}, & 0\leq |\zeta| \leq 1 \\ \cos\sqrt{\lambda_n+v_0}\, \exp -j(|\zeta|-1)\sqrt{\lambda_n+v_1}, & |\zeta| \geq 1 \end{cases} \tag{20}$$

with the orthogonality condition

$$\int_0^\infty d\zeta\, u_n(\zeta) u_m(\zeta) = \frac{1}{2}\delta_{nm}\left[1 + \frac{1}{j\sqrt{\lambda_n+v_1}}\right] \tag{21}$$

and the $\{\lambda_n\}$ satisfy

$$\begin{gathered} \sqrt{\lambda_n+v_0}\sin\sqrt{\lambda_n+v_0} - j\sqrt{\lambda_n+v_1}\cos\sqrt{\lambda_n+v_0}=0, \\ \text{Im}\,\lambda_n \leq \text{Im}\,-v_1, \quad -2\pi \leq \arg(\lambda_n+v_1) \leq 0 \end{gathered} \tag{22}$$

A similar procedure for the odd modes yields

$$u_n(\zeta) \equiv \begin{cases} \sin\zeta\sqrt{\lambda_n + v_0}, & 0 \leq |\zeta| \leq 1 \\ \sin\sqrt{\lambda_n + v_0}\exp -j(|\zeta| - 1)\sqrt{\lambda_n + v_0}, & |\zeta \geq 1 \end{cases}$$

where the $\{\lambda_n\}$ satisfy

$$\sqrt{\lambda_n + v_0}\cos\sqrt{\lambda_n + v_0} + j\sqrt{\lambda_n + v_1}\sin\sqrt{\lambda_n + v_0} = 0 \tag{23}$$

and the $\{u_n\}$ satisfy the same orthogonality condition. (Obviously any even mode is orthogonal to any odd mode.) A comparison of (20) and (23) with the standard theory of real dielectric waveguides reveals that they are precisely the dispersion relations for real index waveguides, extended into the complex plane.

3.4 Mirror Coupling and Diagonalization

Referring back to figure 3.1, we see that the mirror reflectivity R(y) is the reflectivity seen at a fixed reference plane. The common thin-lens approximation [12] is to model a nonplanar reflector as a complex phase shift of $-2j\beta\Delta l(y)$, where β is the material propagation constant and $\Delta l(y)$ is the distance from the mirror to the reference plane. The dielectric reflectivity and/or scattering can be included by an additional multiplying factor r(y). A single waveguide mode $u_n(\zeta)$ upon reflection can be reexpressed as a sum of waveguide modes

$$r(y)e^{-2j\beta(y)\Delta l(y)}u_n(\zeta) = \sum_m r_{nm}u_m(\zeta) \tag{24}$$

Multiplying by $u_m(\zeta)$ and integrating yields

$$r_{nm} = \left[1 + \frac{1}{j\sqrt{\lambda_m + v_1}}\right]^{-1} \int_{\text{mirror}} d\zeta\, r(\zeta d)u_m(\zeta)e^{-2j\sqrt{v(\zeta)}\Delta l(\zeta d)/d}u_n(\zeta) \tag{25}$$

where the relation $y = \zeta d$ has been used. Within the various regions of the waveguide, u_n and u_m consist of linear exponentials; most mirrors of interest are piecewise linear or (to a good approximation) quadratic; consequently, all of the mirror coupling coefficients are, at worst, sums of complex error functions, for which simple approximations are readily available [13]. For example, for a curved mirror of radius -R with unity reflectivity that extends only to the edge of the waveguide, we find

$$r_{nm} = \left[1 + \frac{1}{j\sqrt{\lambda_m + v_1}}\right]^{-1} \times$$

$$\int_{-1}^{+1} d\zeta \cos\left(\frac{t_m \pi}{2} - \zeta\sqrt{\lambda_m + v_0}\right) \cos\left(\frac{t_n \pi}{2} - \zeta\sqrt{\lambda_n + v_0}\right) e^{-j\sqrt{v_0}\zeta^2 d/R} \qquad (26)$$

where $t_i = 1$ if the ith mode is odd and 0 if it is even. (A more accurate model would include the spatial and angular variation of the reflectivity within the integral. We have assumed constant reflectivity throughout this work.)

We are left with the task of simplifying the frequency and gain dependence of the matrices. We perform a perturbation expansion around a fixed operating point

$$n \rightarrow \bar{n} + \Delta n, \qquad \omega \rightarrow \bar{\omega} + \Delta\omega \qquad (27)$$

and define

$$\Delta\beta_n \equiv \beta_0 - \beta_n \qquad (28)$$

so that $\Delta\omega$ and Δn become the new free parameters. Typically, $\bar{\omega}$ is the center of the gain spectrum and $\bar{n}$ is the approximate threshold carrier density. To lowest order, we can ignore the appearance of $\Delta\omega$ and Δn in the reflectivity matrices, but we must be more careful in the propagation matrix. We expand the diagonal elements of the matrix $\tilde{\tilde{B}}L$ in a Taylor series as

$$\beta_n(\omega, n)L = \beta_n(\bar{\omega}, \bar{n})L + \frac{\partial\beta_0}{\partial\omega}\Delta\omega L + \frac{\partial\beta_0}{\partial n}\Delta n L + \frac{\partial\Delta\beta_n}{\partial\omega}\Delta\omega L + \frac{\partial\Delta\beta_n}{\partial n}\Delta n L + \cdots \qquad (29)$$

The last two terms of (29) are typically much less than 1, and can be dropped entirely. This assumption is tantamount to assuming that all of the longitudinal modes of the resonator are degenerate. The second and third terms are common to all elements of $\tilde{\tilde{B}}L$ and may be pulled out as a product of a scalar and the identity $\tilde{\tilde{I}}$. The result is that the propagation matrix can be written as

$$\tilde{\tilde{P}}(\omega, n; L) \approx e^{-j\left[\frac{\partial\beta_0}{\partial\omega}\Delta\omega + \frac{\partial\beta_0}{\partial n}\Delta n\right]L} \tilde{\tilde{P}}(\bar{\omega}, \bar{n}; L) \qquad (30)$$

With this substitution, equation (5) can be written as

$$[\tilde{\tilde{R}}_2\tilde{\tilde{P}}(\overline{\omega},\overline{n};L)\tilde{\tilde{R}}_1\tilde{\tilde{P}}(\overline{\omega},\overline{n};L) - \gamma\tilde{\tilde{I}}]\tilde{A} = \tilde{0} \qquad (31)$$

where

$$\gamma \equiv e^{2j\left[\frac{\partial\beta_0}{\partial\omega}\Delta\omega + \frac{\partial\beta_0}{\partial n}\Delta n\right]L} \qquad (32)$$

Equation (31) is now a linear eigenvalue problem, which can be solved for γ by setting the determinant of the quantity in the square brackets equal to zero. This approximation is equivalent to that made by the Fox-Li iteration technique [5]; they both rely on the longitudinal cavity modes' degeneracy. From the form of (31), we see that $|\gamma|^2$ represents the fraction of energy left in the resonator after one round trip. In conventional unstable resonator theory, $|\gamma|^{-2}$ is the magnification M. For typical semiconductor lasers, the size of the matrix is around 100x100, which can be handled by most canned diagonalization routines. Often, only the few lowest-loss modes are desired, and one can use an approximate technique (e.g., the Prony method [14]) to find them without actually diagonalizing the entire matrix. In many cases (as we will show in the next section), the lowest-loss eigenvalues vary widely in magnitude, a property that increases the accuracy of such approximate techniques. The calculations presented in the remainder of this paper were performed on a VAX 11/780 using root-finding and matrix routines from the IMSL subroutine library.

3.5 Examples

A. Gain-Guided Unstable Resonator Semiconductor Laser

Recently, we reported the operation of an unstable resonator semiconductor laser with pure gain-guiding [5]. The near field, as calculated using our model, is shown in figure 3.3a, while an experimental plot is shown in figure 3.3b. The experimental and theoretical plots are both single-valued (nodeless) over

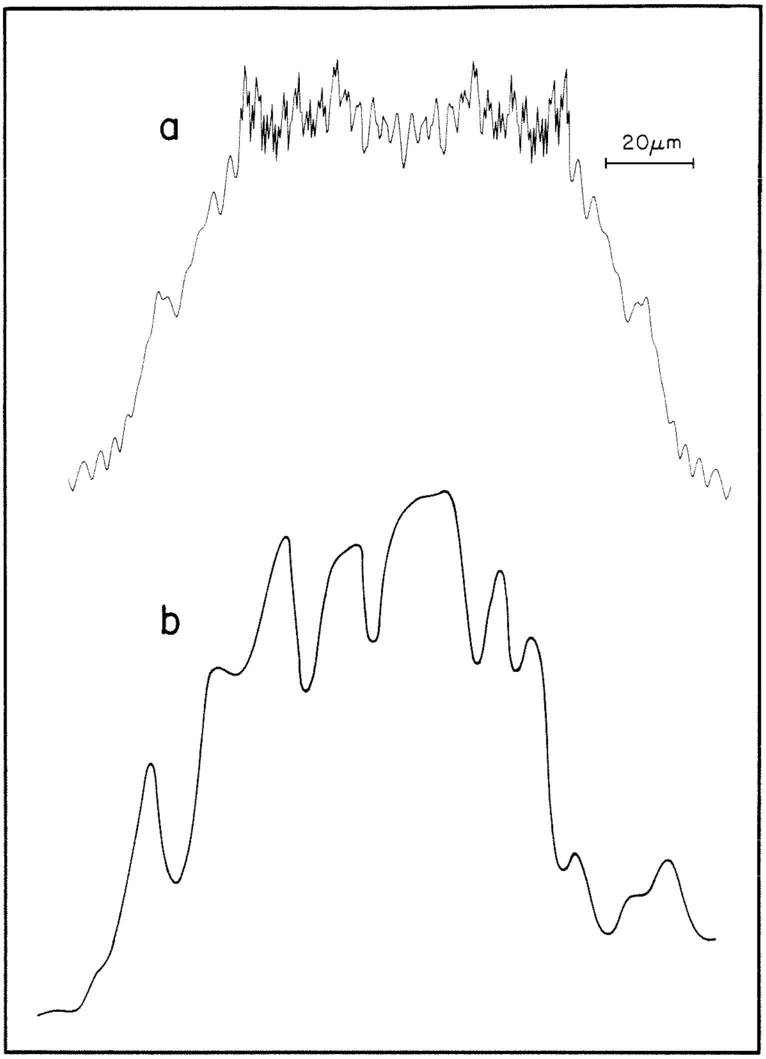

Figure 3.3: Near field of a purely gain-guided URSL of width 80 μm, length 200 μm, and two symmetric mirrors of radius 250 μm. a) theoretical, b) experimental.

the same width (which is to be expected, since the width is determined by the gain stripe). The large modulation visible on the experimental plot we attribute to imperfections in the output mirror, which scatter light and cause diffraction fringes. The round trip gain (normalized to that of plane wave propagation in the core material) was calculated to be $|\gamma| = .286$, $M^{½} = 3.5$. The geometric model of unstable resonators [1] for a symmetric, two-mirror resonator predicts

$$M^{½} = 1 + \frac{L}{R} + \left[\frac{L^2}{R^2} + \frac{2L}{R}\right]^{½} \tag{33}$$

For the laser of figure 3.3, $M^{½} = 3.3$ according to the geometrical model (which, of course, neglects diffraction and loss in the cladding). One interesting feature of unstable resonators is the large difference in round-trip losses between the lowest-loss and next lossy resonator lateral mode. For the laser of figure 3.3, the next lossy mode has $|\gamma| = .112$. In the absence of curved mirrors, the lateral waveguide modes are also the resonator modes, and an examination of the pole plot for this laser shows that there are well over 50 lateral waveguide modes with losses within a few percent of each other. The importance of large gain separation between the lowest-loss resonator modes becomes clear when one takes into account small perturbations from the ideal waveguide (for example, losses resulting from defects, or nonlinearities that appear at high pump currents). Consider a set of resonator modes $\{e_i(y,z)\}$ with eigenvalues $\{\gamma_i\}$. Any imperfection in the waveguide will cause some small scattering between the modes; the scattering can be characterized by matrix elements $\{\kappa_{ij}\}$ (calculated in the same way that the set of $\{r_{ij}\}$ were). For small scattering, we can use first-order perturbation theory [16] to calculate the effects on the modes;

$$e_i^{(1)} = e_i^{(0)} + \sum_{j=i} \frac{\kappa_{ij}}{\gamma_i - \gamma_j} e_j^{(0)} \tag{34}$$

As long as $\kappa_{ij} << \gamma_i - \gamma_k$, the lasing mode in the presence of the perturbation will closely resemble the calculated mode in the absence of the perturbation. On the other hand, if the coupling approaches the order of magnitude of the separation between the gains of the *i*th and *j*th modes, the modes will become mixed by the perturbation (also, the perturbation theory breaks down). Consequently, there is poor mode selection in flat-mirror broad lasers, and small perturbations in the optical cavity due to nonlinearities cause the laser to jump among mixtures of the nearly degenerate lateral modes. The strong coupling imposed by the curved mirrors of a URSL, however, breaks this degeneracy; the lowest-order mode is strongly preferred and is relatively insensitive to small perturbations to the cavity. This explains the stability of the single lateral resonator mode that was observed up to 4 times threshold.

Another feature of interest is the variation of mirror loss per bounce with numerical aperture. Figure 3.4 shows the loss per bounce as a function of waveguide width with all other parameters held fixed. As we vary the width, we are increasing the equivalent Fresnel number. The periodic mode crossings observed by Fox and Li [5] in open-walled unstable resonator structures are apparent.

B. Unstable Resonator with Lateral Waveguiding

One of the drawbacks to URSL's is that the lossy material in the cladding absorbs the diffraction losses of the resonator (which, in many other systems, are useful output) and degrades the external quantum efficiency. In fact, by extension of existing formulas one can show that the external quantum efficiency is given by [15,17]

$$\frac{1}{\eta_d} = \frac{1}{\eta_i}\left[1 + \frac{\alpha L}{\ln\frac{1}{R} + \ln\frac{1}{|\gamma|}}\right]\frac{1 - |\gamma|R}{1 - R} \qquad (35)$$

where α is the loss in the unpumped medium, R is the mirror reflectivity, and η_i

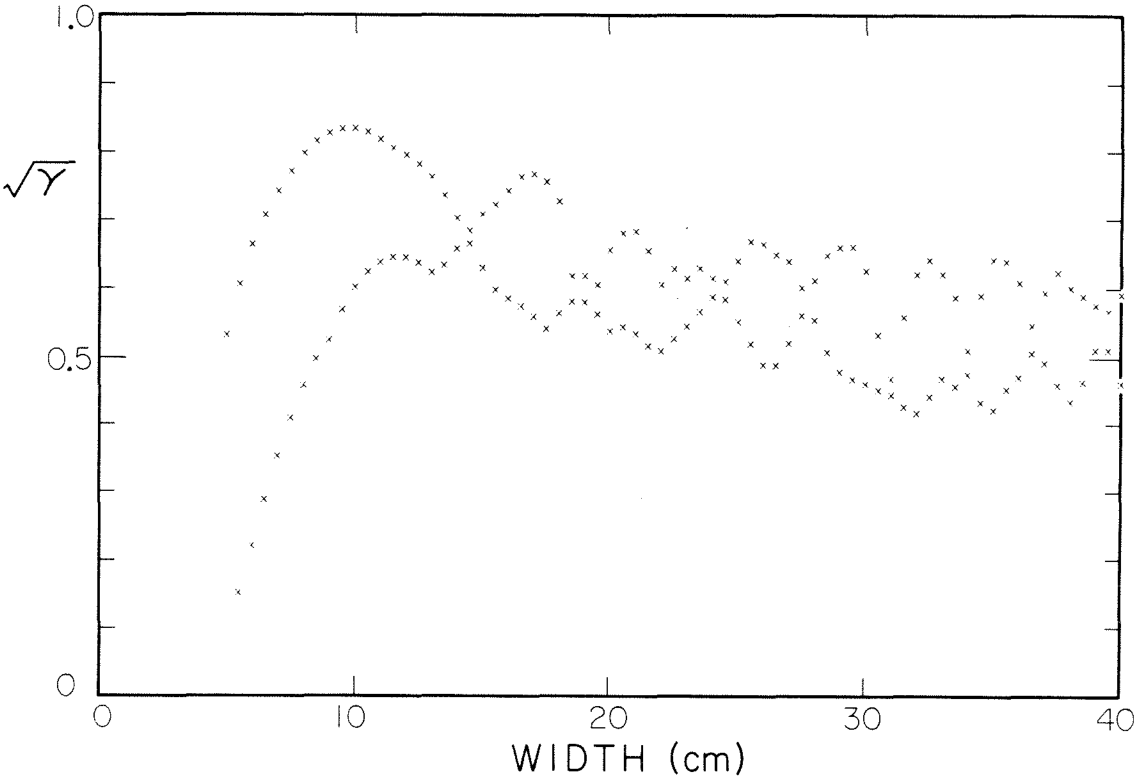

Figure 3.4: Amplitude loss per bounce ($\sqrt{\gamma}$) versus width for two lowest-loss modes of a symmetric gain-guided URSL of length 200 μm, mirror radius -250 μm. γ gives the round-trip amplitude loss, γ^2 gives the round-trip energy loss. Calculations performed at .5-μm intervals.

is the internal quantum efficiency. (In [15] a factor M is missing from the numerator of the equivalent expression.) One suggested method for increasing the quantum efficiency of a URSL is to add a real index step in the lateral direction to provide optical confinement [4]. Figures 3.5a and 3.5b show the calculated and measured near fields, respectively, of such a structure. As in the simple URSL, one gets a near field with an approximately constant average power density across the gain stripe; only in this case there is high-frequency, high-modulation-depth spatial modulation on the near field due to the interference of the reflections off of the confining walls. The spatial frequencies evident in the theoretical plot are greater due to the limited resolution of the experimental viewing system. This structure combines the advantages of a Fabry-Perot broad area laser and a purely gain-guided URSL, namely, the high quantum efficiency of the former and the stable near field of the latter. The results suggest that a larger index step is more desirable from the point of view of lowering losses, and in figure 3.6 we have plotted the losses of the two lowest-loss modes as a function of index step. Although the losses continue to improve with larger index step, the gain separation between the two lowest-loss modes decreases at the same time (also, the high spatial frequency ripples evident in figure 3.5 become larger and larger, which increases the sidelobes in the far field). Thus, there is an optimum index step that brings about low losses while maintaining high gain separation between modes.

C. Tilted-Mirror Resonators

Not all high-loss resonators possess circular mirrors. For example, two misaligned planar mirrors make up a tilted-mirror resonator. This geometry is interesting when viewed from the geometrical optics framework because, unlike classical unstable and stable resonators, there is no ray within the resonator

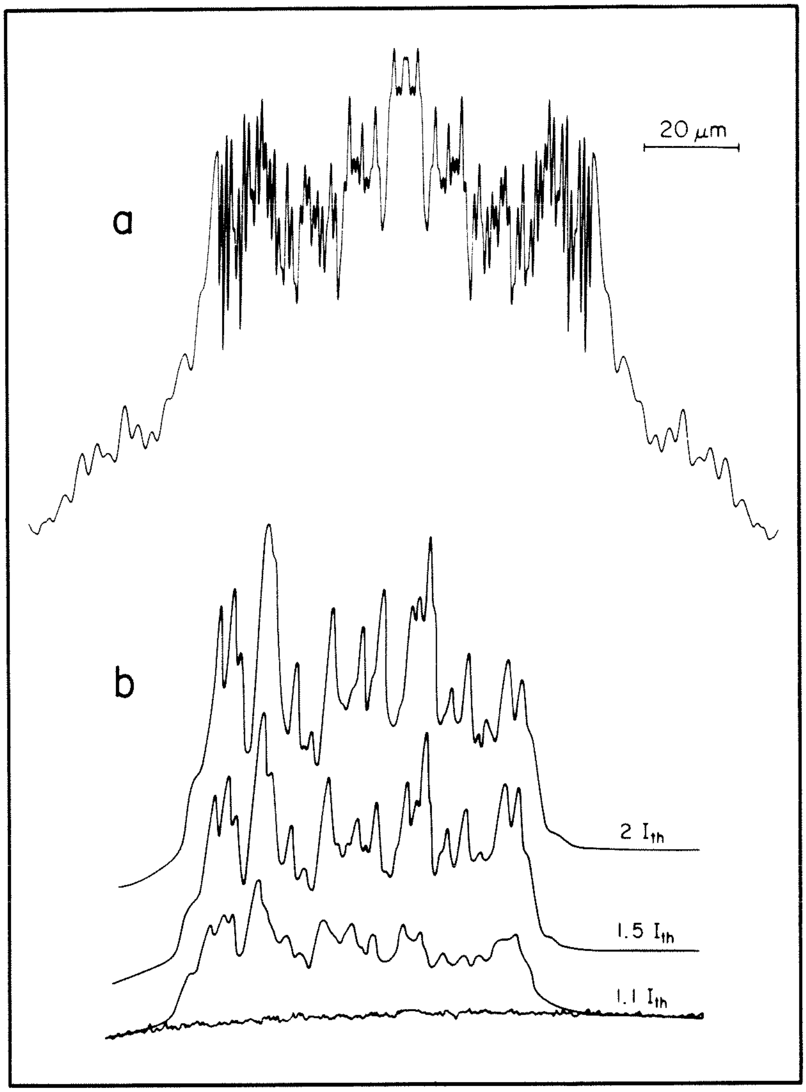

Figure 3.5: Near field of a index-guided URSL (same dimensions as figure 4) with a real index step of .03. a) theoretical, b) experimental.

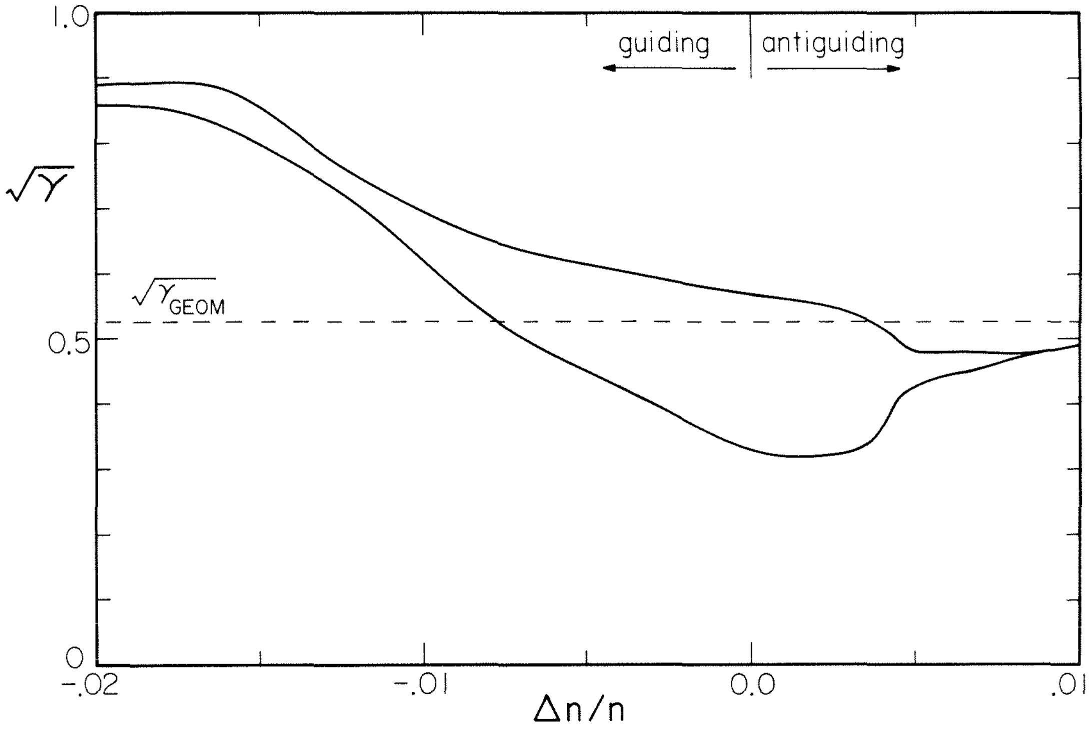

Figure 3.6: Round-trip losses for the two lowest-order modes as a function of real index step. Δn is the difference in index between the cladding and core, so that the left portion of the graph corresponds to a "guiding" waveguide, and the right portion corresponds to an "antiguiding" waveguide. The dotted line indicates the value of $\sqrt{\gamma}$ one would calculate using the geometric theory of unstable resonators.

that reproduces itself. This property suggests that incipient filaments within the resonator will also be unable to reproduce themselves. (It also suggests that the losses will be rather high.) Recently, we demonstrated operation of a tilted-mirror semiconductor laser [7]; the lowest-loss mode, calculated using the foregoing analysis (with $\Delta l(y) \equiv y\tan\vartheta$, $\vartheta \equiv \{$the tilt angle at one mirror$\}$), and an experimental near field measurement of the device are reproduced in figures 3.7a and 3.7b, respectively. In performing the calculation, use of a uniform gain distribution under the stripe contact yields two nearly degenerate resonator modes. However, we observed in the sub-threshold near field of a 0° laser that there was slightly higher gain at the edges of the stripe, which favored the theoretical mode shown in figure 3.7. One of the disadvantages of the tilted-mirror design is that the losses are quite high (since the only part of the resonator mode that reproduces itself comes from diffraction). Loss as a function of tilt angle is given in figure 3.8. The decrease in loss at large angle is interesting, since it suggests a region of low loss around 13−14° (unfortunately, the devices fabricated in [7] neatly bracketed this region--in fact, the losses at 0°, 5°, 10° and 15° all lie neatly on a straight line). Such a "loss window" was recently observed in calculations of tilt effects in CO_2 waveguide lasers [18].

3.6 Conclusions

We have performed an analysis of semiconductor lasers with non-planar mirrors that includes the effects of lateral gain/index guiding. We developed a criterion for truncation of the infinite set of waveguide modes based on the analytic structure of the Green's function for the waveguide problem. Then, using a thin-lens approximation, the mirrors were shown to couple the waveguide modes. We then reduced the nonlinear equation for frequency and gain to a linear eigenvalue problem, where the magnitude of the eigenvalues gave the

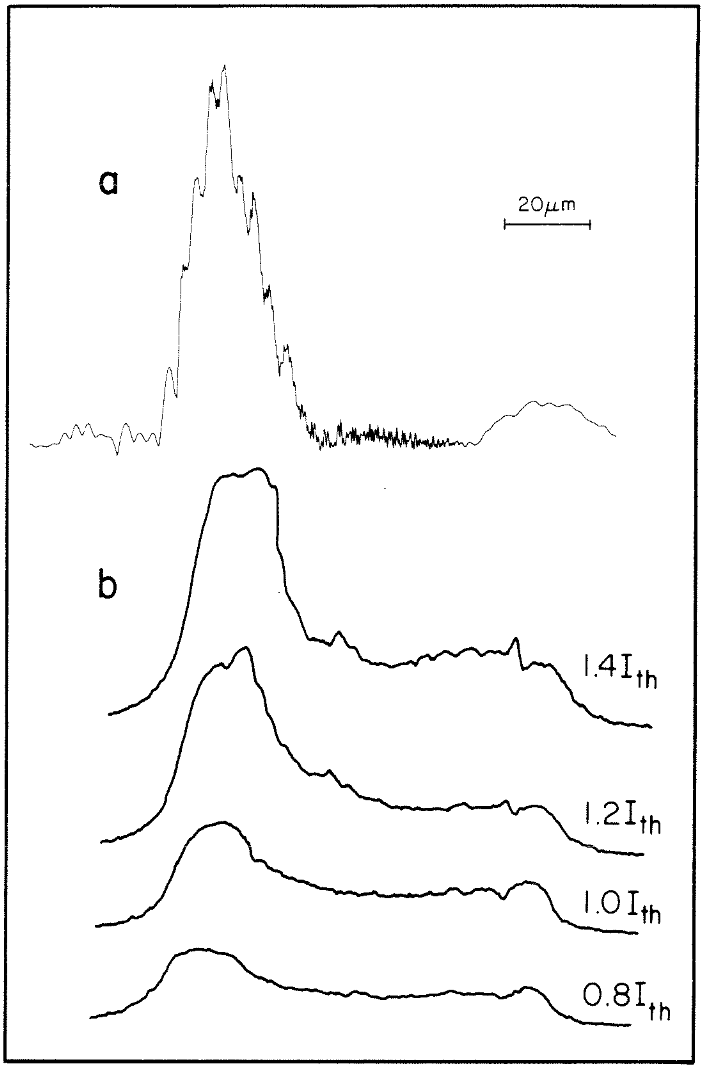

Figure 3.7: Near field of a tilted-mirror laser of width 100 μm, length 300 μm, tilt angle 10^0. a) theoretical, b) experimental.

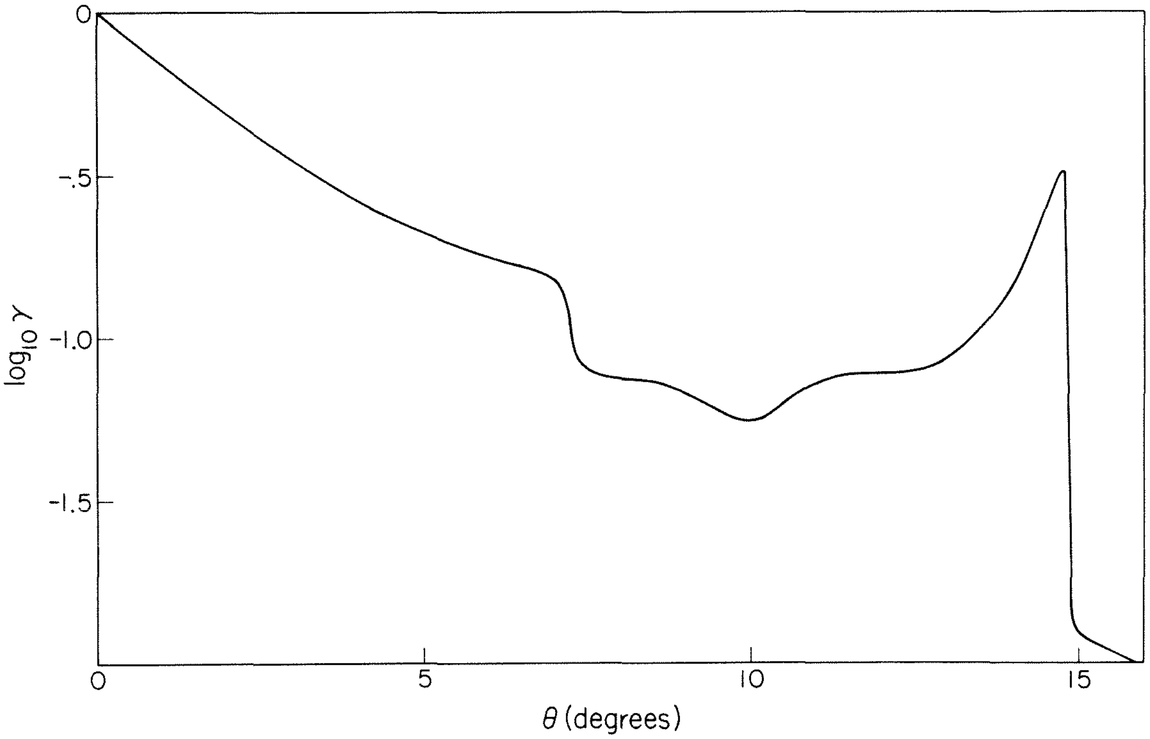

Figure 3.8: Round-trip energy loss as a function of tilt angle for a tilted-mirror resonator of the same dimensions as figure 3.7.

cold-cavity losses. We applied the analysis to three cases of interest--a gain-guided URSL, an index-guided URSL, and a gain-guided tilted-mirror resonator. The calculated near fields agreed with those of measured devices. We also showed that URSL's possess high gain separation between the lowest-loss modes. The addition of a lateral index waveguide can reduce the losses while maintaining gain separation and resistance to filamentation, at the expense of degrading the smoothness of the near field. Tilted-mirror resonators were shown to possess well-defined modes, and the variation of loss with tilt angle was presented.

References

[1] A. E. Siegman, Proc. IEEE., vol. 53, pp. 277-287 (1965).

[2] P. Horwitz, J. Opt. Soc. Am., vol. 63, pp. 1528-1543 (1983).

[3] L-W. Chen and L. B. Felsen, IEEE J. Quant. Elect., vol. QE-9, pp. 1102-1113 (1973).

[4] J. Salzman, R. Lang, M. Mittelstein and A. Yariv, Appl. Phys. Lett., vol. 47, pp. 445-447 (1985).

[5] A. G. Fox and T. Li, Bell Syst. Tech. J., vol. 40, pp. 453-488 (1961).

[6] L. Bergstein, Appl. Opt., vol. 7, pp. 495-504 (1968).

[7] J. Salzman, R. Lang, S. Margalit and A. Yariv, Appl. Phys. Lett., vol. 47, pp. 9-11 (1985).

[8] A. P. Bogatov, P. G. Eliseev, M. A. Man'ko, G. T. Mikaelyan and Yu. M. Popov, Sov. J. Quant. Elect., vol. 10, pp. 620-622 (1980).

[9] W. Streifer and E. Kapon, Appl. Opt., vol. 18, pp. 3724-3725 (1979).

[10] D. Marcuse, *Theory of Dielectric Optical Waveguides* (Academic Press, New York, 1974) p. 1.

[11] B. Freidman, *Principles and Techniques of Applied Mathematics*, (Wiley, New York, 1956) p. 214.

[12] J. W. Goodman, *Introduction to Fourier Optics*, (McGraw-Hill, New York, 1968) p. 77.

[13] M. Abramowitz and I. A. Stegun, *Handbook of Mathematical Functions*, (National Bureau of Standards, Washington, D.C., 1964) p. 295.

[14] A. E. Siegman and H. Y. Miller, Appl. Opt., vol. 9, pp. 2729-2736 (1970).

[15] J. Salzman, T. Venkatesan, R. Lang, M. Mittlestein, and A. Yariv, Appl. Phys. Lett., vol. 46, pp. 218-220 (1985).

[16] C. Cohen-Tannoudji, B. Diu, F. Laloe, *Quantum Mechanics vol. II*, (Wiley, New York, 1977) p. 1108.

[17] J. Salzman, R. Lang and A. Yariv, Elect. Lett., vol. 21, pp. 821-823 (1985).

[18] C. A. Hill and D. R. Hall, presented at Conference on Lasers and Electro-Optics, Baltimore, Maryland, May 21-24, 1985.

*

*

*

Chapter 4

Laterally Coupled-Cavity Semiconductor Lasers

4.1 Introduction

In the previous two chapters we have concentrated our efforts upon lateral mode control. However, longitudinal mode control is also an issue in semiconductor lasers. The gain spectrum in a semiconductor laser is inhomogeneously broadened--that is, the gain at a given photon energy comes from transitions between different k-states, and consequently, spectral hole burning should cause the laser to naturally lase in multiple longitudinal modes. However, the intraband relaxation rate is much, much faster than the interband relaxation rate (i.e, stimulated emission)--femtoseconds compared to nanoseconds--so that an incident field effectively saturates the entire inversion uniformly. Hence, the laser *behaves* as if it were homogeneously broadened, and thus should run in a single longitudinal mode. Unfortunately, it doesn't. The gain is so high that the cavity can (and for low threshold currents, should be) extremely lossy; this means that a large fraction of the spontaneous emission can couple into the lasing modes, and the non-lasing modes as well. Furthermore, nonlinearities in the semiconductor laser are rather high, and spatial hole burning, as well as some general distortion of the gain curve, tend to saturate the gain seen by the primary lasing mode. The result is that left to its own devices, a semiconductor laser will run multi-longitudinal mode.

This behavior is undesirable for a laser in a communications system. If the laser is used to transmit information over an optical fiber, one of the limits to system performance is fiber dispersion, and the spectrum of a multimode signal is far wider than it need be; the signal undergoes pulse spreading after propagation through a lossy fiber. Secondly, multimode lasers are noisier than their single-mode counterparts due to partition noise. Thirdly, coherent communications systems require single-mode operation for simple and efficient heterodyning of the optical signal.

More complicated laser structures than the simple two-mirror Fabry-Perot resonator have been proposed that would discriminate between the longitudinal modes. They include distributed feedback lasers [1] and distributed Bragg reflectors [2], in which a corrugated grating of period approximately half of the optical wavelength has been incorporated. They suffer from difficulties in fabrication due to the need to bury a very fine structure underneath GaAs. The other direction of research has been coupled-cavity lasers [3] in which more than one Fabry-Perot resonator have been coupled together. These last are of particular interest since they are relatively simple to fabricate and offer the potential of FM operation [4], linewidth reduction, and modulation speed enhancement [5-7] as well as single-mode operation.

To date, the most common geometry of coupled-cavity laser has been longitudinal; that is, the two lasers are butted up against each other, end-to-end. In this geometry, the gap between the two lasers plays a crucial role in the laser operation. For best gain selectivity, it must be a (small) integral number of half-wavelengths [8]. Unfortunately, accurate control over the gap requires mechanical adjustment, which is undesirable from the system point of view.

An alternative is to monolithically fabricate two lasers side-by-side, and to allow the coupling to occur via the evanescent fields of the individual lasers. If the lasers are of different lengths, then the longitudinal spectra of the two lasers differ, and one would expect low thresholds only where the longitudinal modes of the two lasers coincide. In this chapter we analyze the theory of a laterally coupled-cavity laser and present experimental results of such a device. In section 4.2, we outline the theory of operation and calculate some representative threshold gain curves that illustrate the gain discrimination. In section 4.3, we present the experimental measurements on the device. In section 4.4, we summarize the important points of the chapter.

4.2 Theory of Operation

The device under consideration is illustrated in figure 4.1. It consists of two lasers of length L_1 and L_2, characterized by propagation constants β_1 and β_2, respectively. We should like to calculate what the modes of such a structure are and what threshold gains are required to bring each mode to lasing threshold. Our intuition suggests the following; each cavity is on resonance when the optical path length seen by a field as it traverses the cavity becomes an integral number of wavelengths. Only for a select few frequencies will both cavities simultaneously see an integral number of wavelengths. In fact, the situation is more complicated than this simplistic picture. In the region of the laser where the two lasers are side-by-side, a field cannot propagate in one cavity alone, due to the coupling between the two cavities. The appropriate description of the system is in terms of the *supermodes*, that is, the modes of the twin waveguide.

Any field at a fixed position in the cavity can be written either as a sum of the supermodes of the cavity, or as a sum of the modes of the individual channels. Since the laser contains portions where each cavity is by itself and portions where the two cavities are coupled, we will need a means to switch back and forth from the supermode representation (SM) to a channel mode (CM)

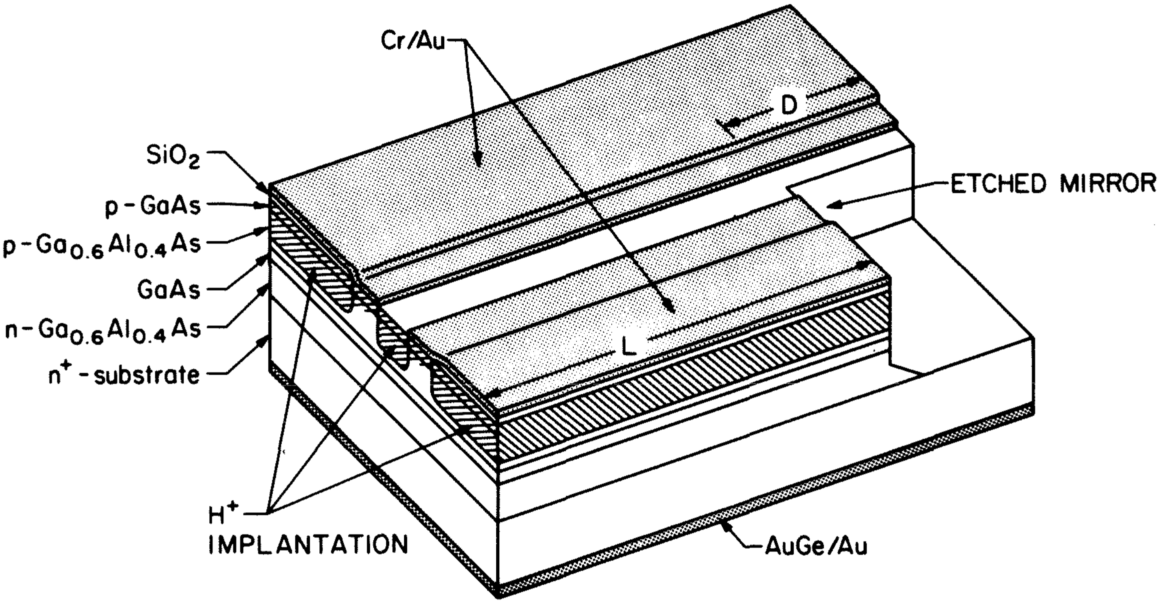

Figure 4.1: Schematic drawing of a laterally coupled cavity semiconductor laser.

representation. We first define the propagation constants of the isolated channels.

$$\beta_{1,2} \equiv \frac{\omega\mu_0}{c} + (\alpha + j)\frac{\gamma_{1,2}}{2} \tag{1}$$

where the subscript 1,2 refers to the channel, ω is the lasing frequency, μ_0 is the nonresonant refractive index, $\gamma_{1,2}$ is the gain supplied to each channel, and α is the linewidth enhancement factor relating changes in the real and imaginary index. When these two cavities are coupled together, standard coupled-mode theory gives us a good approximation to the propagation constants and fields by assuming that the supermodes are composed of a linear combination of the channel modes. We define coupling coefficents by overlap integrals of the channel mode fields

$$\begin{aligned} \kappa_{12} &\equiv \frac{\omega\mu_0^2}{c}\int \Delta\mu_1^2 E_1(x)E_2(x)\,dx \\ \kappa_{21} &\equiv \frac{\omega\mu_0^2}{c}\int \Delta\mu_2^2 E_2(x)E_1(x)\,dx \end{aligned} \tag{2}$$

where $\Delta\mu_{1,2}$ is the perturbation in index seen by one channel mode due to the other channel. Then, if we make the definitions

$$\begin{aligned} \bar{\beta} &\equiv \frac{\beta_1 + \beta_2}{2} \\ \Delta\beta &\equiv \frac{\beta_1 - \beta_2}{2} \\ S &\equiv \sqrt{\kappa_{21}\kappa_{12} + \Delta\beta^2} \end{aligned} \tag{3}$$

then the propagation constants of the two supermodes are given by

$$\sigma_{1,2} = \bar{\beta} \pm S \tag{4}$$

Furthermore, any field that is represented by a linear sum of the channel mode fields can be written as a linear sum of the supermode fields and vice versa. If we represent the amplitudes of the two channel modes by a column vector $\tilde{A} \equiv \begin{pmatrix} a_1 \\ a_2 \end{pmatrix}_{CM}$, where a_1 and a_2 are the amplitudes of the two channel modes, then the amplitudes b_1 and b_2 of the two supermodes' fields can be written as

$$\tilde{B} \equiv \begin{bmatrix} b_1 \\ b_2 \end{bmatrix}_{SM} = \tilde{\tilde{V}} \begin{bmatrix} a_1 \\ a_2 \end{bmatrix}_{CM} \tag{5}$$

where the square matrix $\tilde{\tilde{V}}$ is given by

$$\tilde{\tilde{V}} \equiv \begin{bmatrix} p_1 & -p_2 \\ p_2 & p_1 \end{bmatrix} \tag{6}$$

and $p_{1,2} \equiv \dfrac{1 \pm \Delta\beta/S}{2}$. We point out that as so defined, $\tilde{\tilde{V}}$ is unitary; that is, $\tilde{\tilde{V}}^{-1} = \tilde{\tilde{V}}^{T}$.

Obviously, then, $\tilde{A} = \tilde{\tilde{V}}^{-1}\tilde{B}$. We can write the effects of any linear operation upon the fields as a square matrix *within a given representation*; for example, in the channel mode representation, the field after an encounter with a mirror of reflectivity R_0 would be

$$\tilde{A}_{(after)} = \begin{bmatrix} r_0 & 0 \\ 0 & r_0 \end{bmatrix} \tilde{A}_{(before)} \tag{7}$$

However, to write the appropriate operator for a supermode vector, we must transform the operator to the new representation. This we accomplish with the matrix $\tilde{\tilde{V}}$. For an operator T, if we denote the channel mode representation of this operator by $\tilde{\tilde{T}}_{CM}$ and the supermode representation by $\tilde{\tilde{T}}_{SM}$, the two matrices are related by

$$\tilde{\tilde{T}}_{SM} = \tilde{\tilde{V}}\tilde{\tilde{T}}_{CM}\tilde{\tilde{V}}^{-1}, \quad \tilde{\tilde{T}}_{CM} = \tilde{\tilde{V}}^{-1}\tilde{\tilde{T}}_{SM}\tilde{\tilde{V}} \tag{8}$$

The reason for introducing all this rigamarole is that some operations are easier to write in one representation than in the other. Let us choose an arbitrary field in the supermode representation $\tilde{B}_{SM}$ at $z = 0$ in figure 4.2, and calculate the matrix that propagates it through one round trip of the resonator. We do this by composing a matrix for each portion of the journey and appending it to the left side of the initial matrix, the identity matrix.

We begin by propagating from $z = 0$ to $z = L$. That matrix, in the supermode representation, is given by inspection; it is

$$\tilde{\tilde{P}}_{SM} \equiv \begin{bmatrix} e^{-j\sigma_1 L} & 0 \\ 0 & e^{-j\sigma_2 L} \end{bmatrix} \tag{9}$$

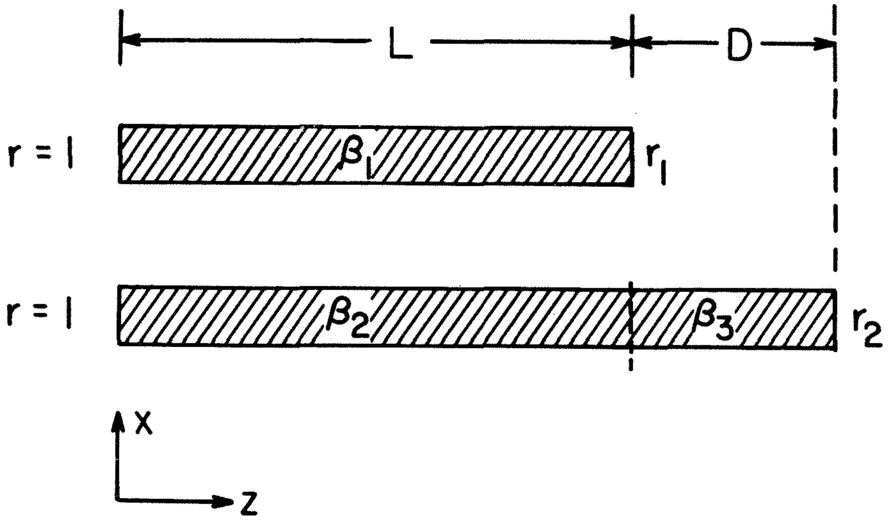

Figure 4.2: Schematic representation of an idealized laterally coupled cavity laser.

since each supermode merely gains a phase factor. At L, we must switch over to a channel mode representation, by multiplying by a factor $\tilde{\tilde{V}}^{-1}$. The field in channel 1 sees a reflectivity r_1, while the field in channel 2 propagates on further for a distance D, is reflected by reflectivity r_1, and then propagates back to z=L. This matrix can be written as

$$\tilde{\tilde{R}}_{CM}^{(R)} \equiv \begin{bmatrix} r_1 & 0 \\ 0 & r_2 e^{-j\beta_2 D} \end{bmatrix} \tag{10}$$

Now we transfer back to the supermode representation, by multiplying by $\tilde{\tilde{V}}$. We propagate back to $z = 0$ with the matrix $\tilde{\tilde{P}}_{SM}$, and reflect off of the left mirror. It turns out that for uniform reflectivity on the left, the representation doesn't matter;

$$\tilde{\tilde{R}}_{CM}^{(L)} = \tilde{\tilde{R}}_{SM}^{(L)} = \begin{bmatrix} r_0 & 0 \\ 0 & r_0 \end{bmatrix} \tag{11}$$

So, our round-trip matrix $\tilde{\tilde{T}}_{SM}$ is given by

$$\tilde{\tilde{T}}_{SM} = \tilde{\tilde{R}}_{SM}^{(L)} \tilde{\tilde{P}}_{SM} \tilde{\tilde{V}} \tilde{\tilde{R}}_{CM}^{(R)} \tilde{\tilde{V}}^{-1} \tilde{\tilde{P}}_{SM} \tag{12}$$

The lasing condition, that a field $\tilde{B}_{SM}$ reproduce itself exactly after one round trip, can be expressed as

$$\tilde{\tilde{T}}_{SM} \tilde{B}_{SM} = \tilde{B}_{SM} \tag{13}$$

We recognize this as an eigenvalue problem; to have a non-trivial solution for $\tilde{B}_{SM}$, the matrix $\tilde{\tilde{T}}_{SM} - \tilde{\tilde{I}}$ must be singular. If we define

$$\begin{aligned} r_{1\text{eff}} &\equiv p_1^2 r_1 + p_2^2 r_2 e^{-2j\beta_2 D} \\ r_{2\text{eff}} &\equiv p_2^2 r_1 + p_1^2 r_2 e^{-2j\beta_2 D} \\ r_\Delta &\equiv p_1 p_2 (r_1 - r_2 e^{-2j\beta_2 D}) \end{aligned} \tag{14}$$

then the secular equation associated with the preceding matrix can be written as

$$\left[r_{1\text{eff}} e^{-2j\sigma_1 L} - 1\right]\left[r_{2\text{eff}} e^{-2j\sigma_2 L} - 1\right] = r_\Delta^2 e^{-2j(\sigma_1+\sigma_2)L} \tag{15}$$

The roots to equation (15) implicitly define the threshold gains γ_i and lasing frequency ω of the different modes. This becomes more apparent when we recall than the propagation constants $\beta_{1,2}$, and consequently the supermode propagation constants $\sigma_{1,2}$, depended explicitly upon the gains in the two channels.

In figure 4.3 we have plotted the threshold gains for 11 adjacent longitudinal modes of a representative LC^2 laser consisting of two phase-matched ($|\beta_1-\beta_2|^2 << |\kappa_{21}\kappa_{12}|$) channels of lengths 200 and 240 μm (for this set of cavity lengths, the longitudinal mode spectrum possesses 11-fold periodicity). The mirror reflectivites of the two cavities were taken to be .55 and .1, respectively, the latter number reflecting imperfections in the etched mirror [11]. On the same graph, we have plotted the threshold gains for the same set of modes when the coupling disappears (independent lasers, or phase-mismatched channels). When the channels are mismatched, the supermodes are localized on one channel or the other; consequently, the longitudinal modes of the resonator are just the longitudinal modes of the individual cavities, which are degenerate. Thus, the horizontal and vertical dashed lines in figure 4.2 correspond to 6 and 5 modes, respectively. And, of course, where the two lines cross, all 11 modes are degenerate.

There are several features of interest to be gleaned from this graph. The first is the broken degeneracy of the longitudinal modes, as seen by the spread nature of the solid curves in figure 4.3. As will be explained in greater detail in chapter 6, the only accessible region of the γ_1-γ_2 plane is the unsullied region in the lower right portion of the graph (below threshold) and the locus of sections of threshold curves that makes up the boundary of that region (corresponding to laser operation). The gain differences between adjacent modes is related to the spacing between the first mode to lase (the first line encountered as one moves out from the origin) and subsequent modes. This spacing is shaded in figure 4.3. We see that the greatest spacing, and hence, the greatest mode discrimination, arises when γ_2 is large and γ_1 is small, or when we pump the

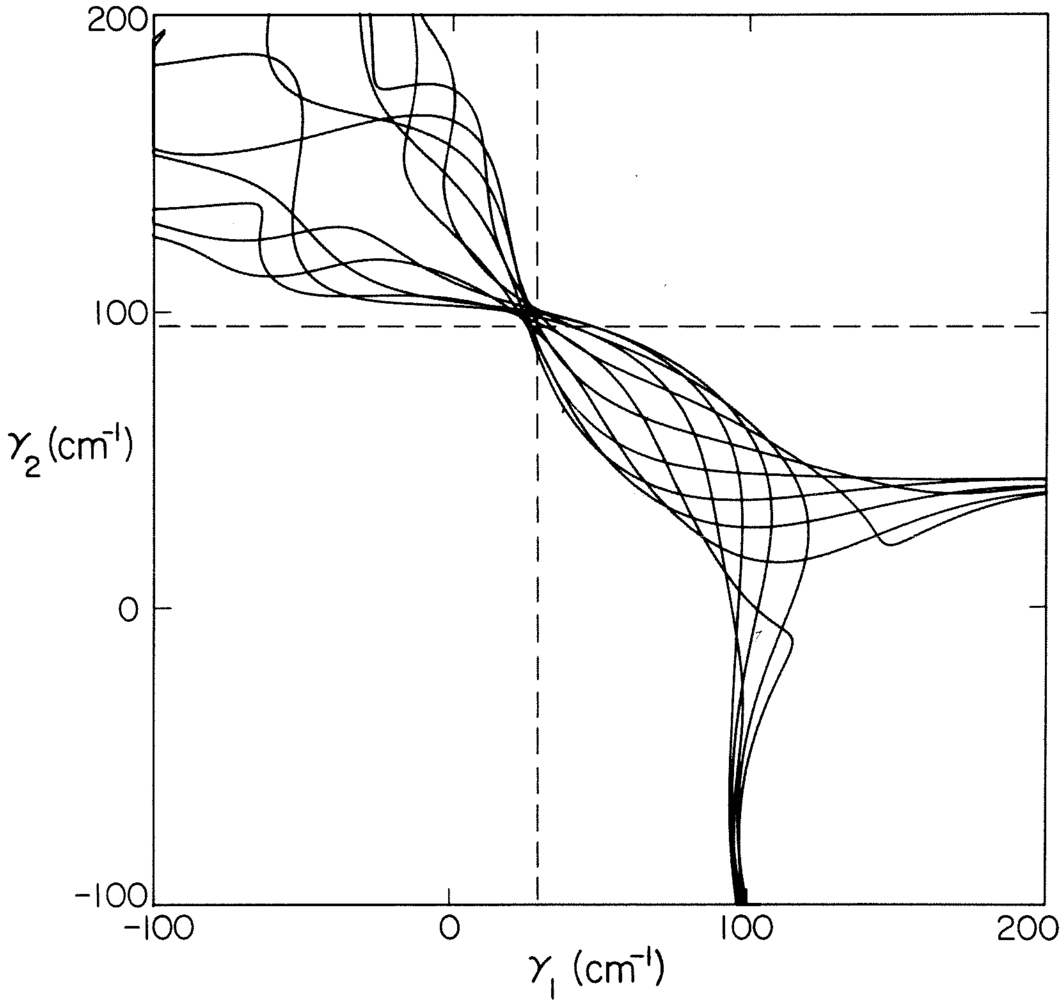

Figure 4.3: Threshold gain in the (γ_1,γ_2)-plane for an LC^2 laser consisting of two segments of lengths 200 and 240 μm, and intercavity coupling coefficient κ = 10 cm^{-1}. Dashed lines indicate threshold gains of the individual lasers in the absence of coupling.

lossy laser hard. Another feature to observe is that the plot of γ_{1th} vs γ_{2th} contains several ripples, due to the changes in optical path length with gain via the α-parameter. Finally, we see from the formulas that the distance that controls the periodicity of the structure is D, the difference in length. The only thing that remains to be seen is whether a real device exhibits any of this behavior.

4.3 Experimental Measurements

The devices were fabricated upon GaAlAs double heterostructures grown by liquid phase epitaxy (LPE). Twin gain stripes 4 μm wide with center-to-center separations of 9 μm were defined by proton implantation at 70 keV. CrAu contacts were evaporated on the surface, and the mirror of the shorter laser was etched using techniques similar to those used in chapter 2. The devices were lapped down to 75-100 μm and AuGe contacts were evaporated on the bottom and annealed. The devices were then cleaved into varying lengths with varying differences in cavity length.

One feature that became apparent immediately was that short cavity lengths were better for getting single-mode operation. As the model suggests, the difference in cavity lengths determines the periodicity of the longitudinal mode spectrum. The spectrum of a device with a fairly long difference is shown in figure 4.4, with a sinusoid of period $c/2\mu D$ superimposed over it. Also shown is the spectrum of the two devices when operated independently. This shows another feature that is common to coupled cavities but has not been adequately explained; when two or more cavities are coupled together to reduce the number of longitudinal modes, there is invariably a shift to longer wavelength operation. One possible explanation is that the losses of coupled cavity geometries that have exhibited this phenomenon (see, for example, [13]) are larger than in the uncoupled case (see figure 4.3) and the increased loss necessitates harder

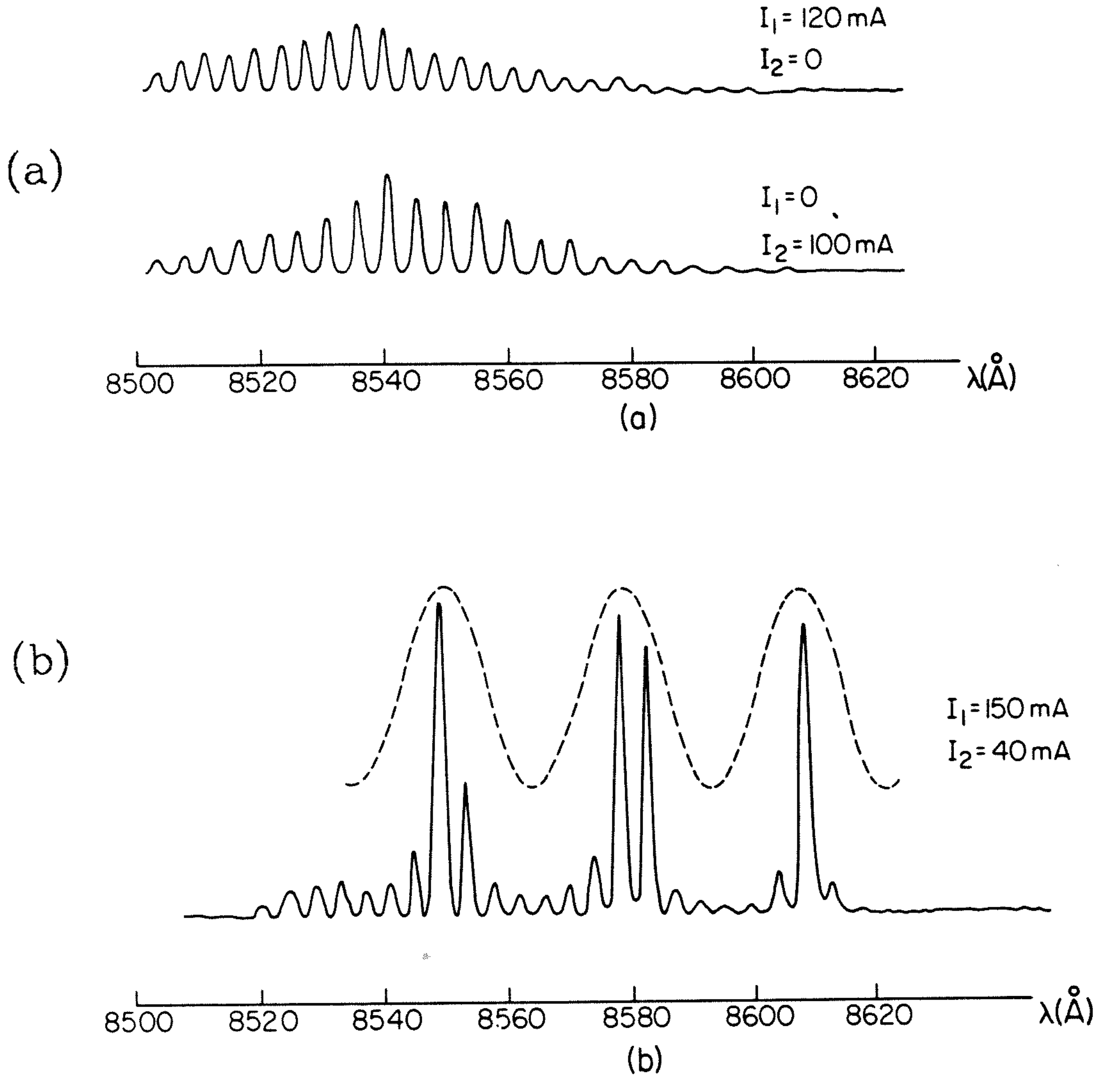

Figure 4.4: Longitudinal mode spectrum for a laser of length L = 450 μm, path difference D = 60 μm. (a) Spectrum when lasers are operated separately. (b) Spectrum of the composite structure with superimposed periodicity of the gap.

pumping and shifts the gain curve. The shift in optical path length with carrier density can be seen in figure 4.5 where cavity number 2 is pumped successively harder, thus increasing the carrier density in the additional section of length D and shifting the longitudinal modes.

Shorter cavity lengths demonstrate other phenomena. Figure 4.6 shows the threshold currents (proportional to the threshold gains) required by the two cavities for a $D = 3 \pm 1$ μm device, illustrating the ripples from interference. This particular device lased in a single longitudinal mode from threshold up to a current level of twice threshold for asymmetric pumping (figure 4.7). Yet another device ($D = 10$ μm) shows single mode operation over limited current ranges of about 20% of threshold, and shows a mode hop between single modes, again showing the shift to longer wavelength and a periodicity controlled by the difference in cavity lengths (figure 4.8).

4.4 Conclusions

In conclusion, we have presented a device capable of single-longitudinal mode operation that is easily fabricated monolithically, a laterally coupled cavity laser. We note that for optoelectronic integration, it will be desirable to etch all mirrors of the laser, and the scheme of etching one laser shorter than the other fits neatly within this plan. Despite the operation of this laser under pulsed conditions and the fact that the modes were gain-guided (which means that the coupling coefficients change somewhat with pump current), large regimes of single-mode operation were obtained. This success indicates that a laterally coupled-cavity laser designed for CW operation (e.g., a twin buried heterostructure) may well be suitable for use in single-mode laser systems.

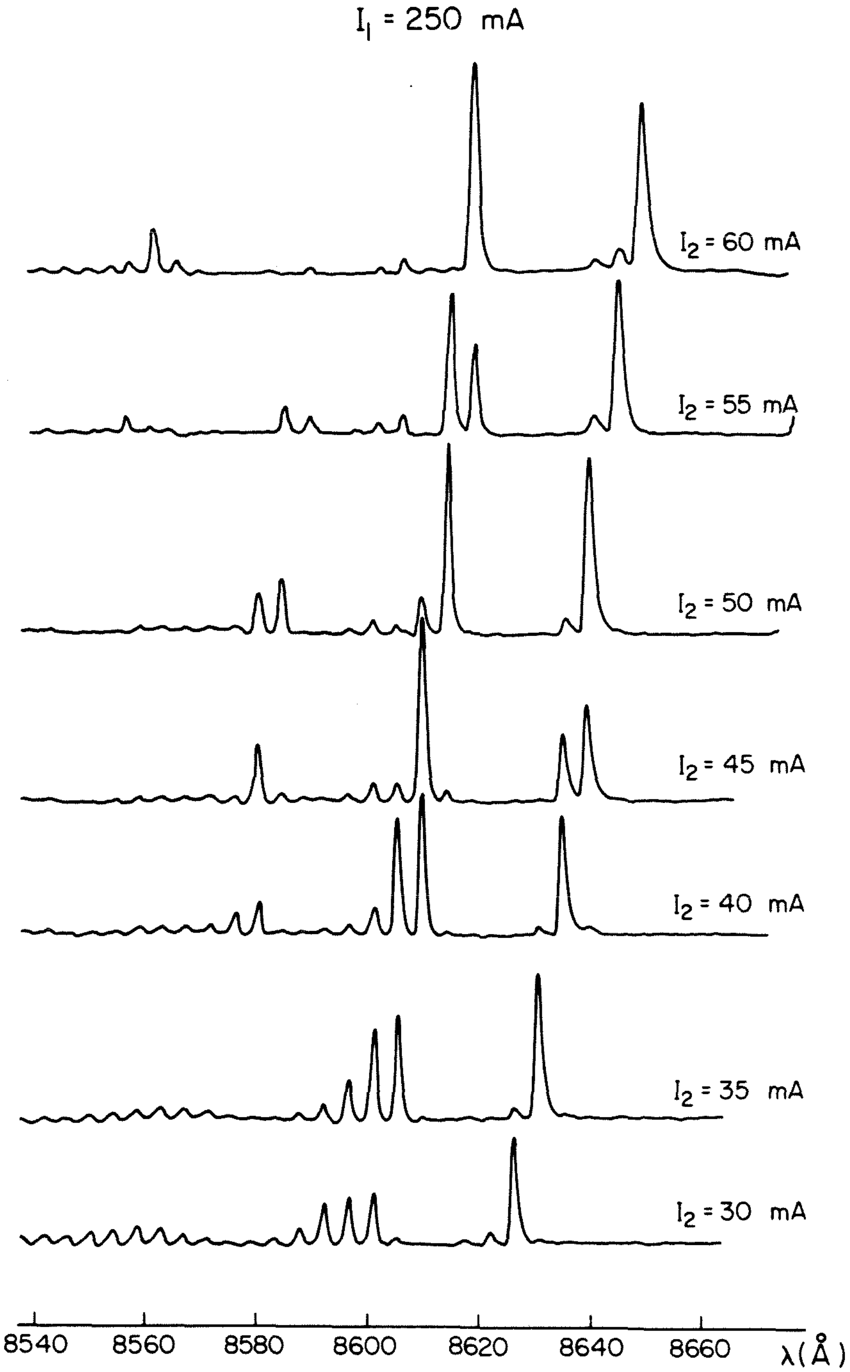

Figure 4.5: Longitudinal mode spectrum of the device of figure 4.4 as a function of tuning current in cavity 2 (the long cavity).

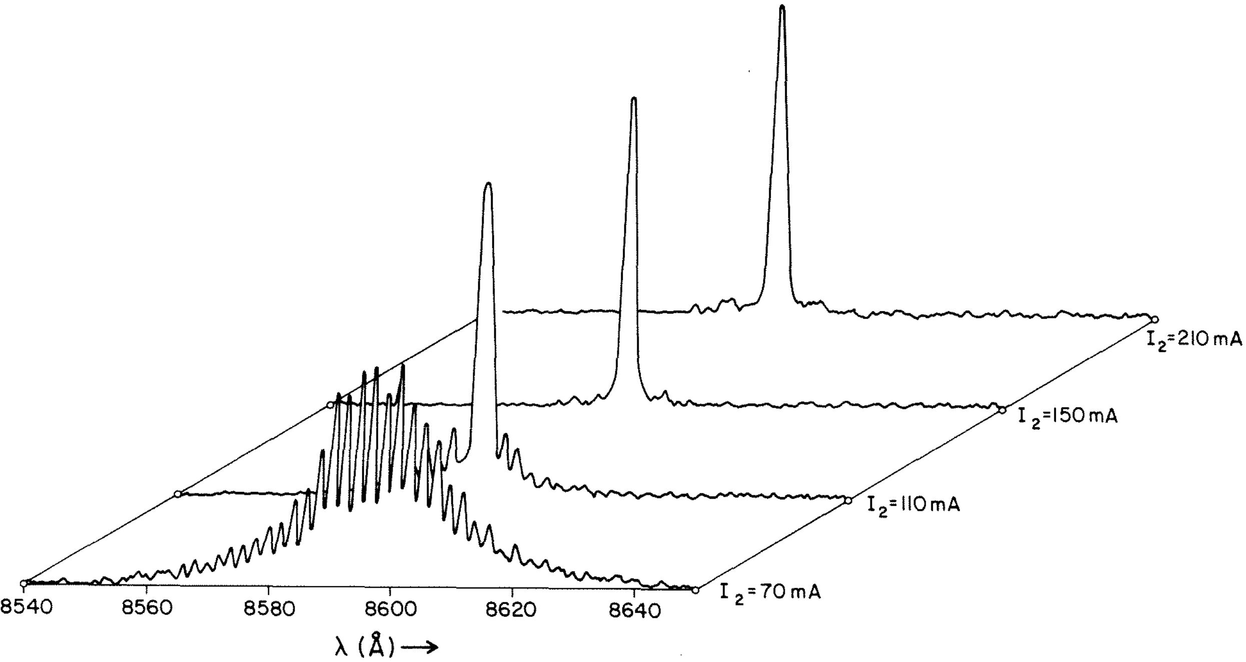

Figure 4.6: Spectra of a device with D ≈ 3 μm for different currents supplied to the short cavity (not to the same vertical scale).

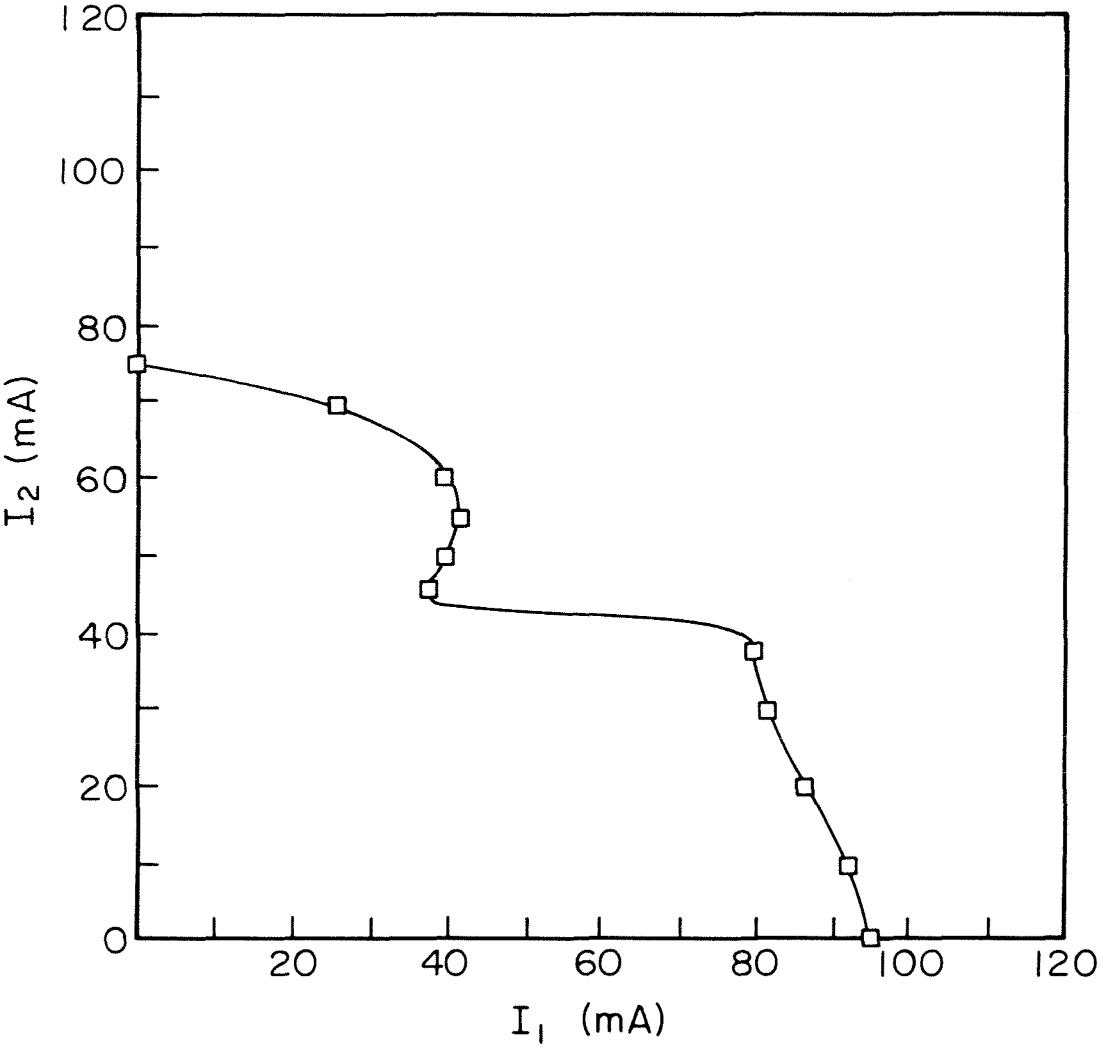

Figure 4.7: Threshold gains for the device of figure 4.6.

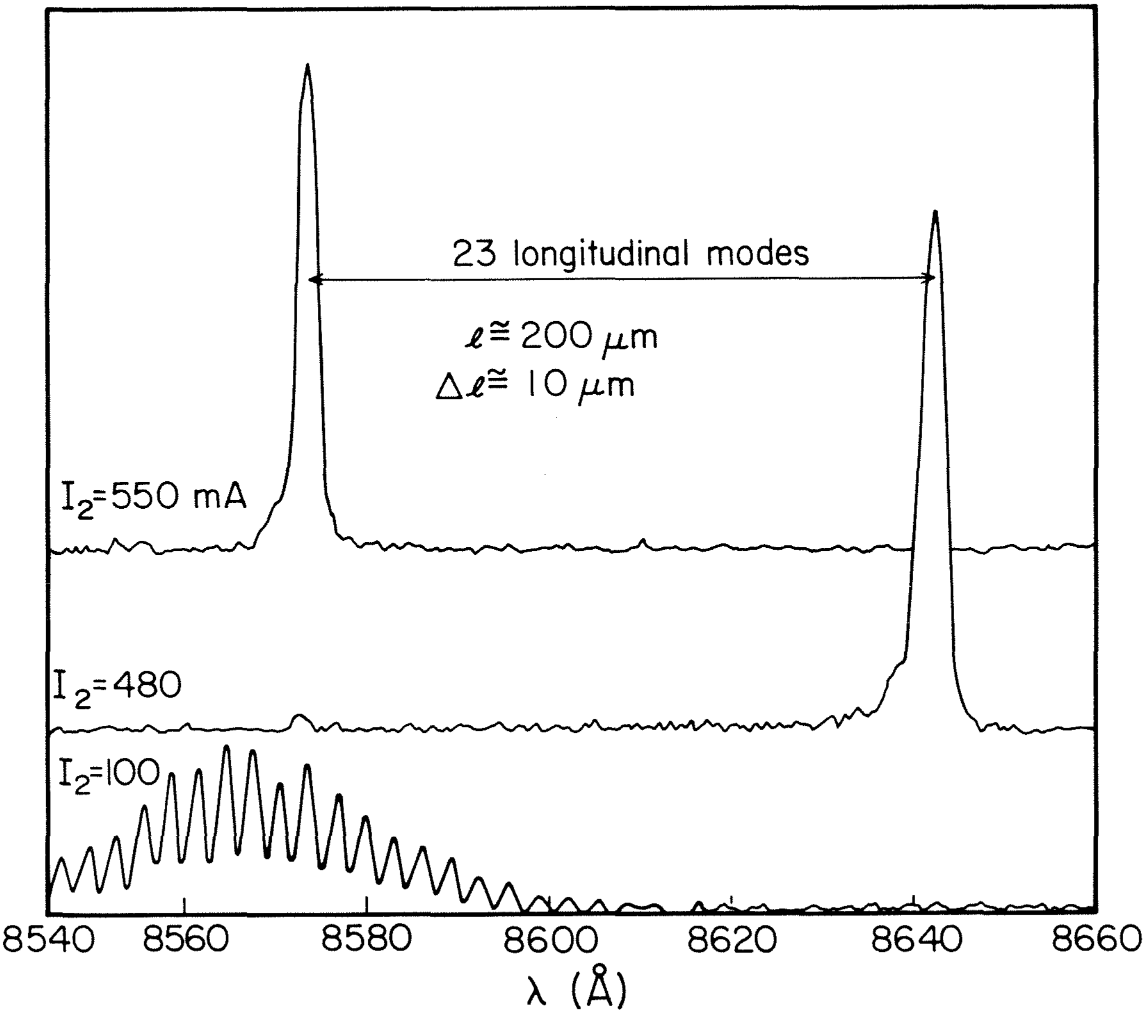

Figure 4.8: Spectrum of a D = 10 μm device showing a mode hop and the periodicity of the path difference.

References

[1] M. Nakamura, K. Aiki, J-I Umeda, A. Yariv, H. W. Yen and T. Morkawa, Appl. Phys. Lett., vol. 25, p. 487 (1985).

[2] H. W. Yen, W. Ng, I. Samid and A. Yariv, Opt. Comm., vol. 17, p. 213 (1985).

[3] W. T. Tsang and N. A. Olsson, Appl. Phys. Lett., vol. 42, p. 650 (1983).

[4] W. Streifer, D. Yevick, T. L. Paoli and R. D. Burnham, paper #ThO4 presented at Optical Society of America meeting, San Diego, California, 1984.

[5] K. Vahala and A. Yariv, Appl. Phys. Lett., vol. 45, p. 501 (1984).

[6] K. Vahala, J. Paslaski and A. Yariv, Appl. Phys. Lett., vol. 46, p. 1025 (1985).

[7] R. J. Lang and A. Yariv, IEEE J. Quant. Elect., vol. QE-22, p. 436 (1986).

[8] C. H. Henry and R. F. Kazarinov, IEEE J. Quant. Elect., vol. QE-20, p. 733 (1984).

[9] J. Salzman, R. Lang and A. Yariv, Appl. Phys. Lett., vol. 47, p. 195 (1985).

[10] A. Yariv, *Introduction to Optical Electronics*, 2nd ed. (Holt, Rinehart and Winston, 1976) p. 365.

[11] J. Salzman, T. Venkatesan, S. Margalit and A. Yariv, J. Appl. Phys., vol. 57, p. 2948 (1985).

[12] R. J. Lang and A. Yariv, paper #WD33, presented at Optical Instabilities Conference, Rochester, New York, June 1985.

[13] K. K. Anderson, R. H. Rediker and L. J. Van Ruyven, paper #ThCC3, presented at Integrated and Guided Wave Optics Conference, Atlanta, Georgia, February 26-28, 1986.

Chapter 5

Dynamic Analysis of Multielement Semiconductor Lasers

5.1 Introduction

The analysis of multielement laser structures is considerably more difficult than that of a simple Fabry-Perot cavity. The steady-state analysis is fairly well codified, albeit complicated. The steady-state lasing frequency can be analyzed by performing a round-trip analysis of each element of the system, including intercavity coupling [1-8]. The result of such analyses is typically a nonlinear equation that implicitly defines the lasing frequency ω; the equation depends upon the gain and refractive indices (and hence, carrier density) of the various cavities, and the requirement that ω be real (for steady-state operation) imposes a constraint on the set of carrier densities.

However, the full time evolution under large-signal modulation must include the (also nonlinear) carrier rate equations for the different active elements in the system, as well as rate equation(s) for the optical field. In one approach, the electric field in each section of the laser is taken as a dynamical variable, and rate equations for both the electric field and carrier densities are solved for a transient excitation [2,5,8]. In the other approach, a single field equation that describes a mode of the composite resonator is used [3]. The latter treatment has the advantage of including fewer dynamical variables. In either case, the rate equations are strongly nonlinear, due to the nonlinear dependence of characteristic parameters (e.g., lasing frequency, photon lifetime, carrier lifetime) on the dynamical variables. Generally, the only way to solve them is numerically.

Recently Agrawal [8] presented numerical solutions from a small-signal analysis of a two-active-element laser in which the photon density and carrier densities of each cavity, and the relative phase between the two cavities, were taken as the dynamical variables. The small-signal modulation response, however, can be solved *analytically* using the modes of the composite resonator. Not only does this approach give analytic expressions for the small-signal modulation (useful in their own right), but it enables us to see immediately what physical quantities are important and how they effect such things as the relaxation resonance or linewidth enhancement factor. Furthermore, while a smooth, chirpless small-signal response does not guarantee the same large-signal response, a poor small-signal response pretty much rules out the possibility of a reasonable large-signal response. Finally, pathologies in the small-signal response (e.g. singularities, negative differential gain) can indicate the presence of other properties of interest (e.g., bistability).

In this chapter, we derive an analytic solution to the dynamic response for a general multielement semiconductor laser. To do this, we must develop a "resonator-independent" formalism that can be applied to *any* single-mode laser. In section 5.2, we develop the formalism from a mutimode theory and show that the dynamic behavior of the optical field can be obtained from an analytic continuation of the steady-state eigenvalue equation to complex frequency. The relevant parameters that characterize the modulation can then be written in terms of partial derivatives of the steady-state equation. In section 5.3, we develop the relevant rate equations for carriers. These equations yield complete expressions for the amplitude- and frequency fluctuations under current modulation. In section 5.4 we apply the formalism to the case of a two-element semiconductor laser and explicitly calculate the modulation response as a function of modulation frequency, in terms of the effective gain, α-parameter, and relaxation resonance frequency. We show that frequency modulation (chirping) is generally present in the two-section laser (and in fact, in any laser of more than two sections); however, it can be eliminated if the operating point is chosen such that the effective α-parameters of the two cavities are equal [9] or by appropriate splitting of the modulation current [10]. In section 5.5 we summarize the important points of the analysis. In appendix A we calculate an important relation explicitly linking the dynamic complex frequency, material gain and instantaneous cavity loss rate.

5.2 Optical Field

The theory of this chapter and the two that follow relies on the fact that any fluctuations that occur take place on a timescale long compared to a single optical cycle. This observation not only allows us to use volume-average rate equations for the carriers, but to model the field by a single scalar quantity as well. Under dynamic modulation, however, the spatial properties of the electric field change in coupled-cavity lasers. It is not entirely clear just what the scalar field should represent. Under steady-state operation it is taken to be the amplitude of the lasing mode. Under dynamic modulation, the concept of a "mode" is no longer well-defined; however, we will make use of it to develop a powerful tool for treating the dynamics of semiconductor lasers by performing a perturbation expansion in powers of the ratio between optical and fluctuation timescales.

In keeping with the spirit of the semiclassical approximation, we begin with the scalar wave equation derived from Maxwell's equations for a charge-free time-varying medium:

$$\nabla^2 E(\mathbf{x},t) - \frac{1}{c^2}\frac{\partial^2}{\partial t^2}[\mu^2(\mathbf{x},\tau)\ E(\mathbf{x},t)] = 0 \tag{1}$$

where $E(\mathbf{x},t)$ is the electric field and $\mu(\mathbf{x},\tau)$ is the index of refraction varying on a timescale $\tau = \varepsilon t$, $\varepsilon << 1$, i.e., much more slowly than optical frequencies. We shall carry ε around through the analysis to facilitate asymptotic expansions and then drop it at the end. The presence of material gain and loss can be accommodated by allowing complex μ if the loss is approximately constant as a function of frequency. We will use a variation upon the standard separation of variables technique. We first solve the Helmholtz equation with parametric τ

$$\nabla^2 A_i(\mathbf{x},\tau) + \frac{\omega_i^2(\tau)\mu^2(\mathbf{x},\tau)}{c_2} A_i(\mathbf{x},\tau) = 0 \tag{2}$$

The set of $\{A_i(\mathbf{x},\tau)\}$ form an orthonormal basis that spans Euclidean 3-space for *any* τ, that is,

$$\int_V \mu^2(\mathbf{x},\tau)A_i(\mathbf{x},\tau)A_j(\mathbf{x},\tau)\,dV = \delta_{ij} \tag{3}$$

Therefore, we can write without loss of generality

$$E(\mathbf{x},t) = \sum_i f_i(t)A_i(\mathbf{x},\tau) \tag{4}$$

for some set of $\{f_i\}$. Insert (4) into (1) and use (2) to obtain

$$\sum_i -\omega_i^2(\tau)\mu^2(\mathbf{x},\tau)f_i(t)A_i(\mathbf{x},\tau) \equiv \sum_i \frac{\partial^2}{\partial t^2}(\mu^2(\mathbf{x},\tau)f_i(t)A_i(\mathbf{x},\tau)) \tag{5}$$

Now we multiply both sides of the equation by $A_j(\mathbf{x},\tau)$ and integrate over all space. The orthogonality of the $A_i(\mathbf{x},\tau)$ helps in several places; we get

$$\frac{d^2}{dt^2}f_j(t) + \omega_j^2 f_j(t) =$$

$$-\sum_i \int_V \left[2\frac{df_i(t)}{dt}\frac{\partial}{\partial t}(\mu^2(\mathbf{x},\tau)A_i(\mathbf{x},\tau)) + f_i(t)\frac{\partial^2}{\partial t^2}(\mu^2(\mathbf{x},\tau)A_i(\mathbf{x},\tau))\right]A_j(\mathbf{x},\tau)\,dV \tag{6}$$

So far, all is rigorous. Now we make the perturbation expansion by converting time derivatives $\frac{\partial}{\partial t}$ into $\varepsilon\frac{\partial}{\partial \tau}$. As is common in perturbed frequency problems, a more accurate expansion develops if we expand the phase of the unknown variable in a series, rather than the variable itself. Let

$$f_j(t) \equiv e^{j\psi_j},\ \ j\psi_j \equiv \varphi_{j0}(\tau) + \varepsilon\varphi_{j1}(\tau) + O(\varepsilon^2) \tag{7}$$

Plugging this definition into (6) gives

$$\begin{gathered}(\varphi_{j0}^2 + 2\varepsilon\varphi_{j0}(\tau)\varphi_{j1}(\tau) + O(\varepsilon^2) + \omega_j^2)f_j(t) = \\ -\sum_i \int_V 2f_i(t)\varepsilon\varphi_{i0}\frac{\partial}{\partial\tau}(\mu^2(\mathbf{x},\tau)A_i(\mathbf{x},\tau))A_j(\mathbf{x},\tau)\,dV + O(\varepsilon^2)\end{gathered} \tag{8}$$

Solving this by orders gives the zeroth-order solution

$$\varphi_{j0}^2(\tau) = -\omega_j^2(\tau) \text{ so } \varphi_{j0}(\tau) = j\omega_j(\tau) \tag{9}$$

and the first-order correction

$$\varphi_{j1}(\tau) = -\sum_i f_i(t)\int_V \frac{\partial}{\partial\tau}(\mu^2(\mathbf{x},\tau)A_i(\mathbf{x},\tau))A_j(\mathbf{x},\tau)\,dV \tag{10}$$

If we truncate the series representation for $f_j(t)$ at these two terms, we can combine these with the definition of equation (7) to get a first-order differential equation for the time evolution of $f_i(t)$:

$$\dot{f}_j = j\omega_j(t)f_j - \sum_i f_i\int_V \frac{\partial}{\partial t}(\mu^2(\mathbf{x},t)A_i(\mathbf{x},t))A_j(\mathbf{x},t)\,dV \tag{11}$$

where we have finally dropped the ε's and discontinued the distinction between τ and t.

As it turns out, we can frequently drop the summation on the right-hand side of (11) for a variety of reasons, including:

Homogeneous gain--If the gain fluctuations are homogeneous over the lasing mode, then the time derivative in the integral separates, and the orthogonality of the set of $A_j(\mathbf{x},\tau)$ makes all the terms with $i \neq j$ vanish.

Single-mode--If the laser is running single-mode, then all of the $f_i(t)$ are zero except for the lasing mode.

Quasi-steady-state--In quasi-steady-state operation, the time derivative of anything in the integral will be negligibly small.

We would still be left with one term, the self-coupling term:

$$\dot{f}_j(t) \equiv \left[j\omega_j(t) - \int_V \frac{\partial}{\partial t}(\mu^2(\mathbf{x},t)A_j(\mathbf{x},t))A_j(\mathbf{x},t)\,dV\right]f_j(t) \tag{12}$$

But if we make an estimate of the size of the integral in the brackets, we find that since the $\{A_i\}$ are normalized, it is approximately

$$\frac{\partial}{\partial t}\left(\frac{\Delta\mu_{avg}}{\mu}\right) \tag{13}$$

Since $\Delta\mu/\mu$ is typically on the order of .005, we find that the error in dropping this term entirely is less than a percent of the transform limit. Consequently, for the rest of the analysis, we will use the simple (and intuitive) equation of motion

$$\dot{f}(t) = j\omega(t)f(t) \tag{14}$$

or the equivalent

$$\dot{\psi}(t) = \omega(t) \tag{15}$$

Of course, a solution for ψ requires an expression for the steady-state ω, and as mentioned previously, for multielement SL's, ω is generally defined implicitly in a nonlinear equation of the form

$$F(\omega, n_1, \cdots n_N) = 0 \tag{16}$$

for an N-active-element laser with carrier densities $\{n_i\}$. (Note that the number of "elements" in this analysis refers to the number of active elements. The presence of passive sections of the laser complicates the resonance function F but does not increase the number of dynamical variables. Thus, an external-cavity laser is a one-active-element laser; a C^3 laser is a two-active-element laser). It is not the point of this section to derive the steady-state equation; that has been done in numerous works for various structures, including two-element axially coupled lasers [3-8], multielement axially coupled lasers [2]; in the previous chapter, two-element laterally coupled lasers [1], and in chapters 7 and 9, axially coupled lasers. We note, however, that such an equation, although solved for a fixed, real ω, is formally equivalent to a solution of (3) for the instantaneous freqency $\omega(t)$; consequently, we need not return to first principles to find the dynamic response of a multielement device. We may simply analytically continue the DC resonance equation to complex ω and use equation (16) as an instantaneous definition of $\omega(t)$ in terms of the independent variables $\{n_i\}$.

We shall also require a set of fill factors, defined by

$$\Gamma_i \equiv \frac{p_i \sum_k V_k}{\sum_k p_k V_k} \tag{17}$$

where p_k is the photon density in the *k*th cavity and V_k is the volume of the *k*th cavity; the summation includes both active and passive elements. In general, $\Gamma_i \neq 1$ (as noted by [2]), and in fact Γ_i can (and does) vary under modulation. We note that while the Γ's so defined will depend explicitly upon both ω and the $\{n_i\}$, ω is already defined in terms of the independent $\{n_i\}$ by equation (16).

We now have all of the machinery to carry out the small-signal analysis of the optical field. We linearize (15) and (16) about a steady-state operating point

$$\dot{\psi} \equiv \omega_0 + \Delta\omega(t) - j\dot{\rho}(t)$$
$$n_i \equiv n_{i0} + \nu_i(t)$$
$$(\Delta\omega - j\dot{\rho})\frac{\partial F}{\partial \omega}\Big|_{\omega_0, n_{i0}} + \sum_i \nu_i \frac{\partial F}{\partial n_i}\Big|_{\omega_0, n_{i0}} = 0 \tag{18}$$

Divide by $\partial F/\partial\omega$ and take real and imaginary parts to get

$$\dot{\rho} = \sum_i g'_{ieff}\nu_i, \qquad \Delta\omega = -\sum_i m'_{ieff}\nu_i \tag{19}$$

where

$$g'_{ieff} \equiv \mathrm{Im}\left[\frac{\partial F/\partial n_i}{\partial F/\partial\omega}\right], \qquad m'_{ieff} \equiv \mathrm{Re}\left[\frac{\partial F/\partial n_i}{\partial F/\partial\omega}\right]$$

We call g'_{ieff} and m'_{ieff} the effective differential gain and index constants, respectively. It is clear from the above relations that they have the correct units; it remains to be shown that they in fact play the same role as the corresponding parameters in single-cavity lasers.

5.3 Carrier Dynamics

Each section of the laser can be treated as an independent carrier pool, described by a volume-averaged rate equation

$$\dot{n}_i = \frac{J_i}{qd} - \frac{n_i}{\tau_s} - g_i(n_i)\Gamma_i(n_1, \cdots n_N)p \qquad (20)$$

where J_i is the ith pump current density, q is the charge on a single carrier, d is the active layer thickness, τ_s is the spontaneous lifetime, g_i is the gain constant, Γ_i is the fill factor mentioned above, and p is the average power density (so that p is proportional to $|\exp j\psi|^2$). We linearize this set of equations in the same way we did in equation (18):

$$J_i \equiv J_{i0} + qd \cdot e_i(t)$$

$$\dot{\nu}_i = e_i - \left[\frac{1}{\tau_s} + g'_i\Gamma_i p\right] - 2g_i\Gamma_i p\rho - \sum_k g_i p \frac{d\Gamma_i}{dn_k}\nu_k \qquad (21)$$

where g'_i is the material (as opposed to the effective) differential gain constant, and the total derivatives of Γ_i are given by

$$\frac{d\Gamma_i}{dn_k} = \frac{\partial\Gamma_i}{\partial n_k} - m'_{keff}\frac{\partial\Gamma_i}{\partial \mathrm{Re}(\omega)} - g'_{keff}\frac{\partial\Gamma_i}{\partial \mathrm{Im}(\omega)} \qquad (22)$$

The distinction between Re(ω) and Im(ω) must be made here because the fill factor is not an analytic function of ω. We have also made use of the relations

$$\mathrm{Re}\frac{\partial\omega}{\partial n_k} = \frac{\partial \mathrm{Re}\omega}{\partial n_k}, \qquad \mathrm{Im}\frac{\partial\omega}{\partial n_k} = \frac{\partial \mathrm{Im}\omega}{\partial n_k}$$

We now Fourier transform equations (19) and (22). The operator $\partial/\partial t$ becomes a factor $j\Omega$, and the equations become

$$j\Omega\tilde{\rho} = \sum_i g'_{ieff}\tilde{\nu}_i, \qquad \Delta\tilde{\omega} = \sum_i m'_{ieff}\tilde{\nu}_i \qquad (23)$$

$$j\Omega\tilde{\nu}_i = \tilde{e}_i - \left[1/\tau_s + g'_i\Gamma_i p\right]\tilde{\nu}_i - 2g_i\Gamma_i p\tilde{\rho} - \sum_k g_i p\frac{d\Gamma_i}{dn_k}\tilde{\nu}_k \qquad (24)$$

where a tilde indicates a transformed variable. It is convenient to make some definitions of parameters;

$$\frac{1}{\tau_i} \equiv \frac{1}{\tau_s} + g'_i\Gamma_i p, \qquad \omega_{ieff}^2 \equiv 2g_i\Gamma_i p g'_{ieff}, \qquad \alpha_{ieff} \equiv m'_{ieff}/g'_{ieff}$$

$$d_i \equiv (j\Omega + \frac{1}{\tau_i}), \quad c_{ik} \equiv pg_i \frac{d\Gamma_i}{dn_k} \tag{25}$$

with these definitions, equations (23) and (24) can be put into matrix form

$$\begin{bmatrix} j\Omega & 0 & -g'_{1eff} & \cdots & -g'_{Neff} \\ 0 & 1 & -\alpha_{1eff}g'_{1eff} & \cdots & -\alpha_{Neff}g'_{Neff} \\ \dfrac{\omega_{1eff}^2}{g'_{1eff}} & 0 & c_{11}+d_1 & \cdots & c_{1N} \\ \vdots & \vdots & \vdots & & \vdots \\ \dfrac{\omega_{Neff}^2}{g'_{Neff}} & 0 & c_{N1} & \cdots & c_{NN}+d_N \end{bmatrix} \begin{bmatrix} \tilde{\rho} \\ \Delta\tilde{\omega} \\ \tilde{\nu}_1 \\ \vdots \\ \tilde{\nu}_N \end{bmatrix} = \begin{bmatrix} 0 \\ 0 \\ \tilde{e}_1 \\ \vdots \\ \tilde{e}_N \end{bmatrix} \tag{26}$$

This matrix system can be solved by Cramer's rule to yield

$$\tilde{\rho}(\Omega) = \frac{\begin{vmatrix} 0 & -g'_{1eff} & \cdots & -g'_{Neff} \\ \tilde{e}_1 & c_{11}+d_1 & \cdots & c_{1N} \\ \vdots & \vdots & & \vdots \\ \tilde{e}_N & c_{N1} & \cdots & c_{NN}+d_N \end{vmatrix}}{\begin{vmatrix} j\Omega & -g'_{1eff} & \cdots & -g'_{Neff} \\ \dfrac{\omega_{1eff}^2}{g'_{1eff}} & c_{11}+d_1 & \cdots & c_{1N} \\ \vdots & \vdots & & \vdots \\ \dfrac{\omega_{Neff}^2}{g'_{Neff}} & c_{N1} & \cdots & c_{NN}+d_N \end{vmatrix}} \tag{27a}$$

$$\Delta\tilde{\omega}(\Omega) = \frac{\begin{vmatrix} j\Omega & 0 & -g'_{1eff} & \cdots & -g'_{Neff} \\ 0 & 0 & -\alpha_{1eff}g'_{1eff} & \cdots & -\alpha_{Neff}g'_{Neff} \\ \dfrac{\omega_{1eff}^2}{g'_{1eff}} & \tilde{e}_1 & c_{11}+d_1 & \cdots & c_{N1} \\ \vdots & \vdots & \vdots & & \vdots \\ \dfrac{\omega_{Neff}^2}{g'_{Neff}} & \tilde{e}_N & c_{N1} & \cdots & c_{NN}+d_N \end{vmatrix}}{\begin{vmatrix} j\Omega & -g'_{1eff} & \cdots & -g'_{Neff} \\ \dfrac{\omega_{1eff}^2}{g'_{1eff}} & c_{11}+d_1 & \cdots & c_{1N} \\ \vdots & \vdots & & \vdots \\ \dfrac{\omega_{Neff}^2}{g'_{Neff}} & c_{N1} & \cdots & c_{NN}+d_N \end{vmatrix}} \tag{27b}$$

$$\tilde{\nu}_i(\Omega) = \frac{\begin{vmatrix} j\Omega & -g'_{1\mathrm{eff}} & \cdots & -g'_{(i-1)\mathrm{eff}} & 0 & \cdots & -g'_{N\mathrm{eff}} \\ \frac{\omega^2_{1\mathrm{eff}}}{g'_{1\mathrm{eff}}} & c_{11}+d_1 & \cdots & c_{1(i-1)} & \tilde{e}_1 & \cdots & c_{1N} \\ \vdots & \vdots & & \vdots & \vdots & & \vdots \\ \frac{\omega^2_{N\mathrm{eff}}}{g'_{N\mathrm{eff}}} & c_{N1} & \cdots & c_{N(i-1)} & \tilde{e}_N & \cdots & c_{NN}+d_N \end{vmatrix}}{\begin{vmatrix} j\Omega & -g'_{1\mathrm{eff}} & \cdots & -g'_{N\mathrm{eff}} \\ \frac{\omega^2_{1\mathrm{eff}}}{g'_{1\mathrm{eff}}} & c_{11}+d_1 & \cdots & c_{1N} \\ \vdots & \vdots & & \vdots \\ \frac{\omega^2_{N\mathrm{eff}}}{g'_{N\mathrm{eff}}} & c_{N1} & \cdots & c_{NN}+d_N \end{vmatrix}} \tag{27c}$$

In many cases, the optical power density in an individual element is desired (e.g., the power emitted from one of the exit facets); in this case the photon density in the ith cavity p_i is given by (17) to be

$$p_i = \Gamma_i p \tag{28}$$

which yields the modulation response

$$\tilde{p}_i(\Omega) = \Gamma_i \tilde{p}(\Omega) + \sum_k \frac{d\Gamma_i}{dn_k} \tilde{\nu}_k(\Omega) \tag{29}$$

with the total derivatives $\frac{d\Gamma_i}{dn_k}$ defined by (22).

5.4 Applications

We shall first check the formalism by applying it to the well-known case of a single-cavity, simple Fabry-Perot resonator. In this case, c_{11} can be absorbed into the term $1/\tau_1$ (in practice, it can be neglected entirely) and equations (27) become

$$\tilde{p}(\Omega) = \tilde{e}_1(\Omega) \frac{\frac{g'_{1\mathrm{eff}}}{j\Omega + 1/\tau_1}}{j\Omega + \frac{\omega^2_{1\mathrm{eff}}}{j\Omega + 1/\tau_1}}, \qquad \Delta\tilde{\omega}(\Omega) = \tilde{e}_1(\Omega) \cdot j\Omega\, \alpha_{1\mathrm{eff}} \frac{\frac{g'_{1\mathrm{eff}}}{j\Omega + 1/\tau_1}}{j\Omega + \frac{\omega^2_{1\mathrm{eff}}}{j\Omega + 1/\tau_1}} \tag{30}$$

Equation (30) is exactly the frequency response one derives from the more familiar theory [11], exhibiting a relaxation resonance at frequency $\omega_{1\mathrm{eff}}$ and residual phase modulation that goes to zero at zero frequency. Furthermore, we can check the values of $g'_{1\mathrm{eff}}$, $\omega_{1\mathrm{eff}}$, and $\alpha_{1\mathrm{eff}}$ by direct calculation from the simple eigenvalue equation for the lasing frequency:

$$F(\omega,n_1) \equiv \frac{1}{R^2}\exp\left[(\gamma(n_1)-\gamma_0)L-\frac{2j\omega\mu(n_1)L}{c}\right]-1=0 \tag{31}$$

where $\gamma(n_1)$ is the power gain per unit length, γ_0 is the loss, L is the length of the laser, $\mu(n_1)$ is the index of refraction, and R is the mirror reflectivity. Applying equations (19) to (31), we find

$$g'_{1\mathrm{eff}}=\frac{\gamma' c}{2\mu},\quad m'_{1\mathrm{eff}}=-\frac{\omega\mu'}{\mu},\quad \alpha_{1\mathrm{eff}}=-\frac{2\omega\mu'}{\gamma' c} \tag{32}$$

which we recognize as being precisely the material differential gain constant, differential index, and linewidth enhancement factor. Similarly, $\omega^2_{1\mathrm{eff}}$ is the relaxation resonance familiar from McCumber's theory [12].

Thus reassured, we now turn to uncharted territory and analyze the response of a two-element laser. We shall not here calculate the effective modulation quantities; the algebra is straightforward given $F(\omega,n_1,n_2)$, but the exact form of F depends on the particular configuration chosen. As above, the diagonal elements c_{ii} can be absorbed into the term $1/\tau_i$ of (25), i.e.,

$$\frac{1}{\tau_1}\equiv\frac{1}{\tau_s}+g'_i\Gamma_i p+g_i p\frac{d\Gamma_i}{dn_i}$$

Then, evaluating (27) for a two-active element laser yields

$$\tilde{\rho}(\Omega)=\tilde{e}_1(\Omega)\left\{\frac{\dfrac{g'_{1\mathrm{eff}}-g'_{2\mathrm{eff}}\dfrac{c_{21}}{j\Omega+1/\tau_1}}{j\Omega+1/\tau_2}}{j\Omega+\dfrac{\omega^2_{1\mathrm{eff}}}{j\Omega+1/\tau_1}+\dfrac{\omega^2_{2\mathrm{eff}}}{j\Omega+1/\tau_2}}\right\}+$$

$$\tilde{e}_2(\Omega)\left\{\frac{\dfrac{g'_{2\mathrm{eff}}-g'_{1\mathrm{eff}}\dfrac{c_{12}}{j\Omega+1/\tau_2}}{j\Omega+1/\tau_1}}{j\Omega+\dfrac{\omega^2_{1\mathrm{eff}}}{j\Omega+1/\tau_1}+\dfrac{\omega^2_{2\mathrm{eff}}}{j\Omega+1/\tau_2}}\right\} \tag{33}$$

$$\Delta\tilde{\omega}(\Omega) = \tilde{e}_1(\Omega)\left\{\frac{\dfrac{g'_{1\mathrm{eff}}}{j\Omega+1/\tau_1}\left[j\Omega\left(\alpha_{1\mathrm{eff}}-\alpha_{2\mathrm{eff}}\dfrac{g'_{2\mathrm{eff}}}{g'_{1\mathrm{eff}}}\dfrac{c_{21}}{j\Omega+1/\tau_2}\right)+\dfrac{(\alpha_{1\mathrm{eff}}-\alpha_{2\mathrm{eff}})\omega^2_{2\mathrm{eff}}}{j\Omega+1/\tau_2}\right]}{j\Omega+\dfrac{\omega^2_{1\mathrm{eff}}}{j\Omega+1/\tau_1}+\dfrac{\omega^2_{2\mathrm{eff}}}{j\Omega+1/\tau_2}}\right\}+$$

$$\tilde{e}_2(\Omega)\left\{\frac{\dfrac{g'_{2\mathrm{eff}}}{j\Omega+1/\tau_2}\left[j\Omega\left(\alpha_{2\mathrm{eff}}-\alpha_{1\mathrm{eff}}\dfrac{g'_{1\mathrm{eff}}}{g'_{2\mathrm{eff}}}\dfrac{c_{12}}{j\Omega+1/\tau_1}\right)+\dfrac{(\alpha_{2\mathrm{eff}}-\alpha_{1\mathrm{eff}})\omega^2_{1\mathrm{eff}}}{j\Omega+1/\tau_1}\right]}{j\Omega+\dfrac{\omega^2_{1\mathrm{eff}}}{j\Omega+1/\tau_1}+\dfrac{\omega^2_{2\mathrm{eff}}}{j\Omega+1/\tau_2}}\right\} \tag{34}$$

The expressions for $\tilde{\nu}_i(\Omega)$ are similarly obtainable (and equally formidable); however, the relations simplify somewhat if $c_{ij}\tau_i << 1$ for all off-diagonal elements c_{ij} (which has been suggested, for example, for the laterally coupled cavity laser [1]). In this case, there is no difference between $\tilde{\rho}(\Omega)$ and $\tilde{\rho}_i(\Omega)$, and (33), (34) reduce to

$$\tilde{\rho}(\Omega) = \tilde{e}_1(\Omega)\left\{\frac{\dfrac{g'_{1\mathrm{eff}}}{j\Omega+1/\tau_1}}{j\Omega+\dfrac{\omega^2_{1\mathrm{eff}}}{j\Omega+1/\tau_1}+\dfrac{\omega^2_{2\mathrm{eff}}}{j\Omega+1/\tau_2}}\right\}+\tilde{e}_2(\Omega)\left\{\frac{\dfrac{g'_{2\mathrm{eff}}}{j\Omega+1/\tau_2}}{j\Omega+\dfrac{\omega^2_{1\mathrm{eff}}}{j\Omega+1/\tau_1}+\dfrac{\omega^2_{2\mathrm{eff}}}{j\Omega+1/\tau_2}}\right\} \tag{35}$$

$$\Delta\omega(\Omega) = \tilde{e}_1(\Omega)\left\{\frac{\dfrac{g'_{1\mathrm{eff}}}{j\Omega+1/\tau_1}\left[j\Omega\,\alpha_{1\mathrm{eff}}+\dfrac{(\alpha_{1\mathrm{eff}}-\alpha_{2\mathrm{eff}})\omega^2_{2\mathrm{eff}}}{j\Omega+1/\tau_2}\right]}{j\Omega+\dfrac{\omega^2_{1\mathrm{eff}}}{j\Omega+1/\tau_1}+\dfrac{\omega^2_{2\mathrm{eff}}}{j\Omega+1/\tau_2}}\right\}+$$

$$\tilde{e}_2(\Omega)\left\{\frac{\dfrac{g'_{2\mathrm{eff}}}{j\Omega+1/\tau_2}\left[j\Omega\,\alpha_{2\mathrm{eff}}+\dfrac{(\alpha_{2\mathrm{eff}}-\alpha_{1\mathrm{eff}})\omega^2_{1\mathrm{eff}}}{j\Omega+1/\tau_1}\right]}{j\Omega+\dfrac{\omega^2_{1\mathrm{eff}}}{j\Omega+1/\tau_1}+\dfrac{\omega^2_{2\mathrm{eff}}}{j\Omega+1/\tau_2}}\right\} \tag{36}$$

In figures 5.1 and 5.2 we have plotted $\tilde{\rho}(\Omega)$ and $\Delta\tilde{\omega}(\Omega)$ as a function of frequency for a particular set of effective modulation constants with the c_{ij} taken to be zero. The first feature to note is the presence of two resonance terms in the denominators. They combine to give a single resonance at the Pythagorean sum of the two resonance frequencies (as can be seen from the figures. The resonant frequencies are proportional to $g'_{i\mathrm{eff}}$; consequently, any increase in $g'_{i\mathrm{eff}}$ over the

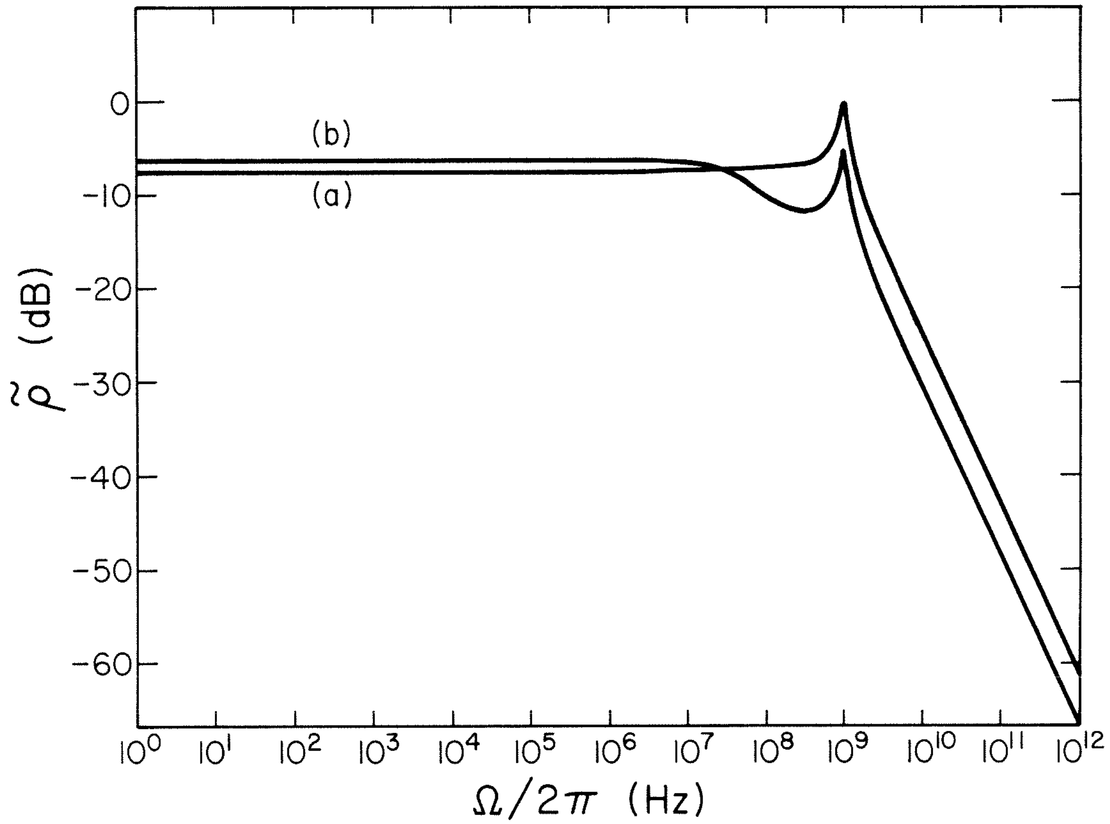

Figure 5.1: Amplitude modulation response for parameters $\omega_{1\mathrm{eff}} = 6.\cdot 10^9$ rad/sec, $\omega_{2\mathrm{eff}} = 1.\cdot 10^9$ rad/sec, $\tau_1 = 10^{-9}$ sec, $\tau_2 = 5\cdot 10^{-9}$ sec, $g'_{1\mathrm{eff}} = 1.2\cdot 10^{-5}$ cm^3/sec, $g'_{2\mathrm{eff}} = 3.0\cdot 10^{-6}$ cm^3/sec, $\alpha_{1\mathrm{eff}} = 5.01$, $\alpha_{2\mathrm{eff}} = 5.00$.

(a) Amplitude modulation response (arbitrary zero) for $\tilde{e}_2 = 0$. (b) Amplitude modulation response (same zero) for $\tilde{e}_1 = 0$.

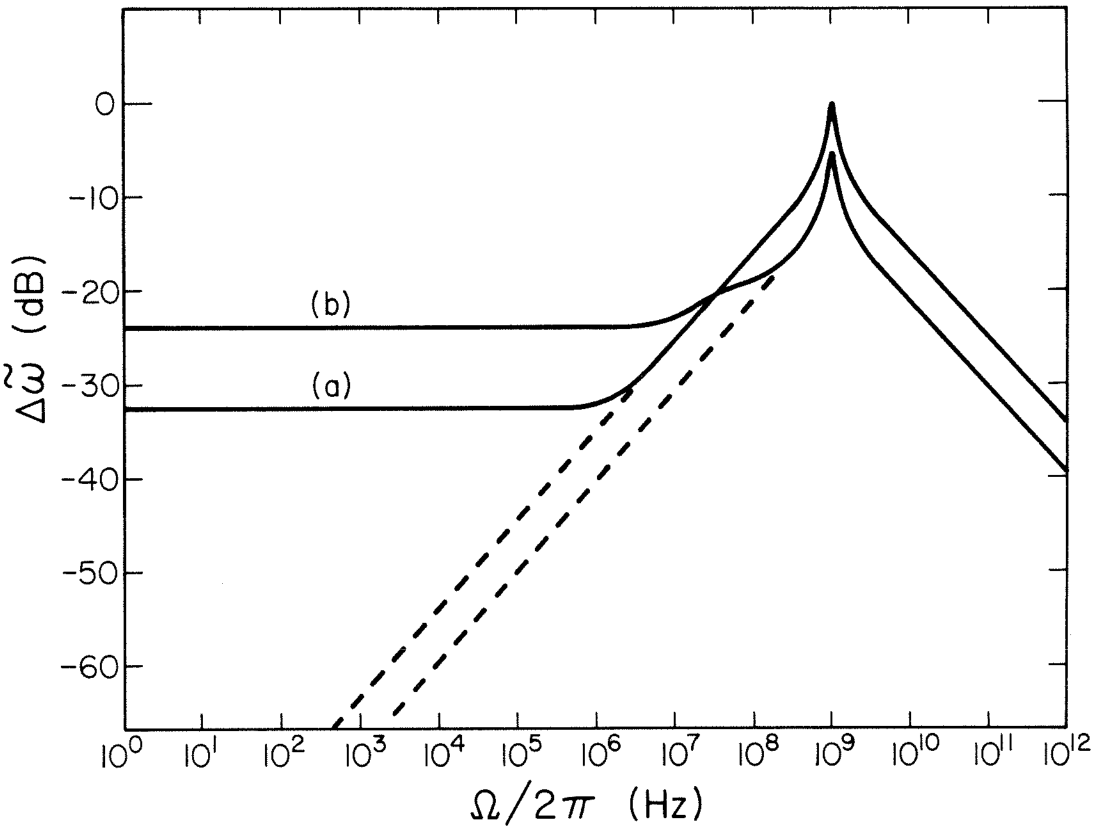

Figure 5.2: Frequency modulation response for the same parameters as in figure 5.1. (a) $\tilde{e}_2 = 0$, (b) $\tilde{e}_1 = 0$. Dashed lines indicate the residual phase modulation present in single-cavity lasers.

material g'_i will result in an enhanced modulation bandwidth. Such behavior has been demonstrated in passive-active coupled cavities [9].

Another feature of interest is the fact that the frequency modulation does not go to zero as $\Omega \rightarrow 0$. In fact, while the first term in the square brackets in (36) is simply the residual FM found in any single-cavity semiconductor laser, which disappears at zero frequency, the second term causes the frequency response to level off at low frequencies (in fact, it can be seen from equation (36) that if the difference in the effective α-parameters is of order 1, the frequency response is flat up to the relaxation resonance). This results in an undesirable FM response under modulation. It should be noted that for multielement lasers, the effective linewidth enhancement factor is generally not equal to the material enhancement factor (the corresponding quantity for the single-element laser)--it depends strongly on the particular operating point selected. So, if an operating point is chosen such that the effective α-parameters for the two lasers are equal, the low-frequency FM modulation disappears. Alternatively, it may be nulled out by splitting the current modulation such that

$$\frac{\tilde{e}_1}{g_1\Gamma_1} = \frac{\tilde{e}_2}{g_2\Gamma_2} \tag{37}$$

as was done in ref. [10]. (It is also equally possible to null out the AM response to obtain a purely FM laser, although the regime of linear operation (and hence validity of the small-signal response) is rather small [13].) It is clear from equation (36) that for structures with more than two elements, there will generally be some frequency modulation. While in some structures the elements of the $\{c_{ij}\}$ matrix are negligible (e.g. the aforementioned laterally coupled laser), in many they are not (e.g. a C^3 laser); for such geometries equations (29), (33), and (34) must be used and the structure of the response is somewhat more complicated than that displayed in the two figures.

5.5 Conclusions

In summary, we have presented the first analytic expressions for the dynamic response of multielement semiconductor lasers. In the process, we derive effective differential gains, indexes, and α-parameters that play the role of the corresponding material quantities in single-element semiconductor lasers. We have verified the general formalism in the single-element case and applied it to a special case of a two-element semiconductor laser. We have shown that frequency chirping is generally present even at zero frequency in two-element lasers, yet it can be avoided either by modulating at an operating point where the effective α-parameters for the two cavities are equal, or alternatively, by driving the currents to both cavities in a fixed relationship.

Appendix A—Dynamic Gain-Loss Relations

It would be helpful to identify some physical mechanisms with the imaginary part of the complex instantaneous frequency used in this chapter. In this appendix, we briefly derive a relation linking three functions of the instantaneous frequency and the quasi-mode and identify them with measurable quantities.

We begin with the well-posed problem

$$\left[\nabla^2 + \frac{\omega^2(t)\mu^2(\mathbf{x},t)}{c^2}\right]E(\mathbf{x},t) = 0 \text{ in domain D} \tag{38}$$

$$\frac{dE}{dn} + AE = 0 \text{ on S} \tag{39}$$

where S is the boundary of domain D, $\mathbf{n}$ is the surface normal, A is an arbitrary coefficient and ω, μ, and E are complex. Green's identity gives us

$$\int_V E\nabla^2 E^* + \nabla E \cdot \nabla E^* \, dV = \oint_S E \frac{dE^*}{dn} dS \tag{40}$$

Subtracting equation 40 from its complex conjugate gives

$$\int_V (E\nabla^2 E^* - E^*\nabla^2 E)\,dV = \oint_S \left(E\frac{dE^*}{dn} - E^*\frac{dE}{dn}\right) dS \qquad (41)$$

Use equations (38) and (39) to get

$$\int_V \left[(\omega\mu)^2 - (\omega^*\mu^*)^2\right] EE^*\,dV = c^2\oint_S (A - A^*)EE^*\,dS \qquad (42)$$

Now we split ω and μ into real and imaginary parts:

$$\omega = \omega_r + j\omega_i,\quad \mu = \mu_r + \mu_i,\quad \omega_i << \omega_r,\quad \mu_i << \mu_r$$

to get (to lowest order in the imaginary parts),

$$\int_V 4j\omega_r\mu_r(\omega_r\mu_i + \omega_i\mu_r)EE^*\,dV = c^2\oint_S (A - A^*)EE^*\,dS \qquad (43)$$

If we recognize the energy density $U(\mathbf{x}) \equiv \mu_r^2 EE^*$, then this can be written as

$$\int_V \frac{2\omega_r\mu_i}{\mu_r} U(\mathbf{x})\,dV + \int_V 2\omega_i U(\mathbf{x})\,dV = \frac{c^2}{2j\omega_r}\oint_S \frac{A - A^*}{\mu_r^2} U(S)\,dS \qquad (44)$$

Now, let's specialize to the case of a semiconductor laser, where the boundary S is a dielectric interface with a medium of index μ_e. Then the appropriate boundary coefficient is

$$A = j\beta\frac{\mu_r}{\mu_e} \text{ where } \beta = \frac{\omega_r\mu_r}{c} \qquad (45)$$

Furthermore, the imaginary part of the index is related to the linear gain by

$$\mu_i = \frac{1}{2}\frac{\gamma c}{\omega_r} \qquad (46)$$

or, recognizing the gain coefficient

$$g(\mathbf{x}) = \frac{\gamma c}{\mu_r} \qquad (47)$$

we have

$$\int_V 2\omega_i U(\mathbf{x})\,dV + \int_V g(\mathbf{x})U(\mathbf{x})\,dV - \frac{c}{\mu_e}\oint_S U(S)\,dS = 0 \qquad (48)$$

We define the total energy in the optical mode by

$$U_{tot} \equiv \int_V U(\mathbf{x})\,dV \qquad (49)$$

The 'fill factor'' Γ is then recognizeable as

$$\Gamma g = \frac{1}{U_{tot}}\int_V g(\mathbf{x})U(\mathbf{x})\,dV \qquad (50)$$

where g is some representative or average gain in the active region. The last integral over the boundary gives the energy loss by transmission out of the medium; we can identify it with the photon lifetime

$$1/\tau_p \equiv \frac{c}{\mu_e}\oint_S U(S)\,dS \tag{51}$$

And so we can identify the components of the imaginary parts of the instantaneous frequency as arising from the instantaneous gain and mirror losses, or

$$2\omega_i(t) + \Gamma(t)g(t) - \frac{1}{\tau_p(t)} = 0. \tag{52}$$

References

[1] J. Salzman, R. Lang and A. Yariv, Appl. Phys. Lett., vol. 47, pp. (1985).

[2] K. J. Ebeling and L. A. Coldren, J. Appl. Phys., vol. 54, p. 2962 (1983).

[3] D. Marcuse and T-P. Lee, IEEE J. Quant. Elect., vol. QE-20, p. 166 (1984).

[4] H. K. Choi, K-L. Chen and S. Wang, IEEE J. Quant. Elect., vol. QE-20, p. 385 (1984).

[5] L. Coldren and T. L. Koch, IEEE J. Quant. Elect., vol. QE-20, p. 659 (1984).

[6] W. Streifer, D. Yevick, T. L. Paoli and R. D. Burnham, IEEE J. Quant. Elect., vol. QE-20, p. 754 (1984).

[7] C. H. Henry and R. F. Kazarinov, IEEE J. Quant. Elect., vol. QE-20, p. 733 (1984).

[8] G. Agrawal, IEEE J. Quant. Elect., vol. QE-21, p. 255 (1985).

[9] K. Vahala, J. Paslaski and A. Yariv, Appl. Phys. Lett., vol. 46, p. 1025 (1985).

[10] L. A. Coldren, G. D. Boyd, J. E. Bowers and C.A. Burrus, Appl. Phys. Lett., vol. 46, p. 125, (1985).

[11] K. Y. Lau, N. Bar-Chaim, I. Ury, Ch. Harder and A. Yariv, Appl. Phys. Lett., vol. 43, p. 1 (1983).

[12] D. E. McCumber, Phys. Rev., vol. 141, p. 306 (1966).

[13] W. Streifer, D. Yevick, T. L. Paoli, and R. D. Burnham, paper #ThO4 presented at OSA, San Diego, California, October 29-November 2, 1984.

*

*

*

Chapter 6

Intermodal Stability of a Coupled-Cavity Laser

6.1 Introduction

As we have seen, coupled-cavity lasers are interesting devices because of their potential for single-mode operation under high-speed current operation [1,2]. In addition, they, like many other two-element lasers [3], have been shown to exhibit bistable behavior. Such behavior makes them suitable for digital optical read/write operations or candidates for elements of an optical logic system [4]. Although there have been several analyses of longitudinally coupled-cavity lasers (e.g., a C^3 laser) at varying levels of approximation [5-8], none have treated the problems associated with operation near a mode boundary. Yet, when the current supplied to one of the two cavities is modulated, crossing a mode boundary is almost inevitable [8]. Recently, in a steady-state analysis, Henry and Kazarinov made the claim that there existed regimes of operation near a mode boundary where no steady-state solutions were stable (although they left open the question of what happened in such a regime). In this paper, we analyze the behavior of a two-element coupled-cavity laser near a mode boundary. Although we choose the specific geometry of a longitudinally coupled pair of cavities, the nondimensional equations of motion are equally applicable to any two-element laser (e.g., a laterally coupled cavity [9]). In section 6.2, we give a brief development of the equations of motion of the laser, using the slowly-varying complex frequency approximation of the previous chapter [10].

In section 6.3, we expand around a mode hop in the carrier density plane and develop a set of nondimensional equations that describes the dynamical behavior of the laser. We solve for the DC solutions of the equations and perform a stability analysis upon the solutions. We show that in all regimes of operation there exists at least one stable solution, sometimes two; we identify a sufficiency condition for bistable behavior, and solve for the lines of instability on which a bistable transition occurs. In section 6.4, we summarize the important results of the analysis.

6.2 Equations of Motion

We begin by deriving the eigenvalue equation for the modes of a longitudinally coupled-cavity laser illustrated schematically in figure 6.1. It consists of two cavities of length L_1 and L_2, separated by a small gap D. Although in actual practice one would control the currents j_1 and j_2 supplied to each of the two sections, for the purposes of analysis it is more convenient to treat the carrier densities n_1 and n_2 as free parameters, solve for the lasing frequency ω, and then find the currents necessary to support that operating point at a given power level. We choose our time factor as $e^{j\omega t}$. Then a round-trip self-reproduction condition imposed upon the field in the laser yields the secular equation [5]

$$\left[\frac{e^{-\gamma_1(n_1)L_1 + 2j\omega\mu_1(n_1)L_1/c}}{R_1} - 1\right]\left[\frac{e^{-\gamma_2(n_2)L_2 + 2j\omega\mu_2(n_2)L_2/c}}{R_2} - 1\right] - K_s = 0 \qquad (1)$$

where $\gamma_i(n_i)$ is the linear gain constant for the *i*th cavity, $\mu_i(n_i)$ is the index of refraction, R_i is the reflectivity of the outside mirrors, and K_s is a coupling factor that characterizes the gap (taking into account the length and reflectivity of the mirrors bounding the gap) [5]. Equation (1) can be considered [10] an implicit equation for complex ω as a function of n_1 and n_2. For any fixed pair (n_1, n_2), there exist an infinite number of complex ω solutions; each solution

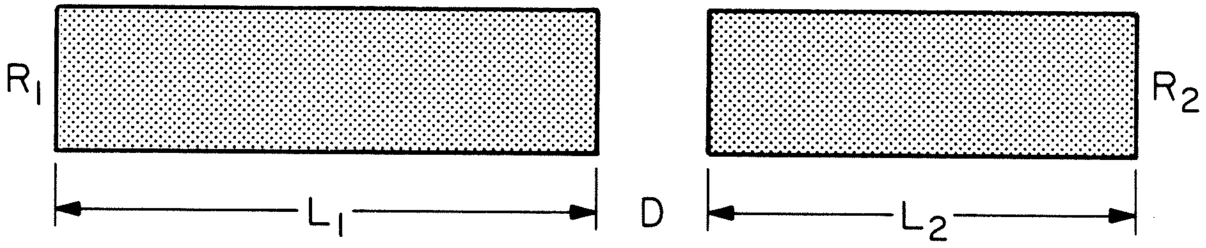

Figure 6.1: Schematic of a longitudinally coupled-cavity laser.

corresponds to a different spatial (longitudinal) mode of the structure. We are not interested in the phase of the optical field, so we can ignore the real part of ω, but the dynamics of the power depend upon the imaginary part. By adapting our equations of motion from the last chapter (we discard the intermodal coupling coefficients since we consider only quasi-steady-state operation) we can construct the multimode equations of motion. The time evolution of the average photon density p_i in the *i*th mode obeys

$$\dot{p}_i = -2\mathrm{Im}(\omega_i)p_i + \frac{1}{\tau_s}\sum_j \beta_{ij} n_j \tag{2}$$

where n_j is the carrier density in the *j*th cavity, τ_s is the spontaneous lifetime, and β_{ij} are coefficients representing the fraction of spontaneous emission coupled into the *i*th mode from the *j*th cavity. For a single mode, the line determined by the requirement $\mathrm{Im}(\omega) = 0$ (figure 6.2) corresponds to a quasi-steady-state mode which neither grows nor decays in time (that is, a true steady-state mode). For $\mathrm{Im}(\omega) < 0$, the quasi-steady-state mode grows without limit, and for $\mathrm{Im}(\omega) > 0$, it decays to zero. When spontaneous emission (which was not included in equation (1)) is considered, the carrier densities of the laser are clamped just to the left of the $\mathrm{Im}(\omega) = 0$ line (in the absence of spontaneous emission, they are clamped onto it).

As we said, there are an infinite number of solutions $\mathrm{Im}(\omega) = 0$ to (1), each corresponding to a different longitudinal mode; we plot a set of them in figure 6.3. Consider a point well to the left of any of the lines, e.g., point A in figure 6.3. Then $\mathrm{Im}(\omega) > 0$ for all the modes in the set; any excitation will decay away and no lasing state exists for that pair of carrier densities. On the other hand, a point on the curve's leftmost boundary (point B) is on the steady-state curve for one mode and in the $\mathrm{Im}(\omega) > 0$ region for the rest; consequently the one mode will lase (and since $\mathrm{Im}(\omega)=0$, neither grow nor decay) while all others decay away. An operating point at the intersection of two curves (point C) could conceivably

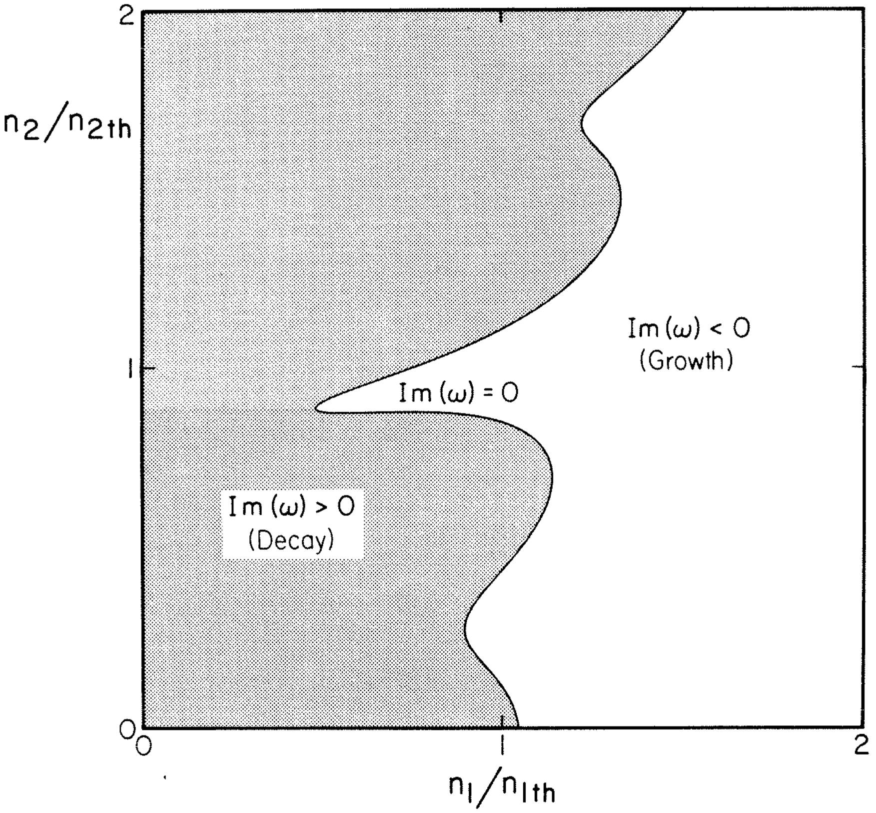

Figure 6.2: Plot of the line Im(ω) = 0 for a single mode in the carrier density plane (normalized to threshold values for the uncoupled lasers), for a laser with L_1 = 200 μm, L_2 = 20μm, D = 1.5 wavelengths.

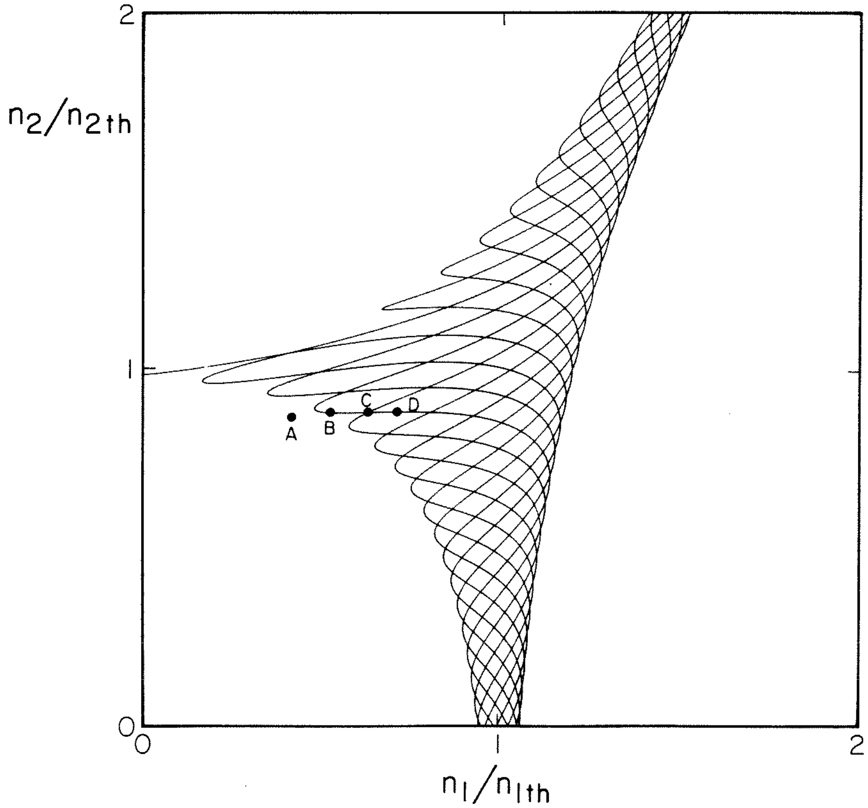

Figure 6.3: Plot of 10 modes in the carrier density plane.

have two lasing modes. However, a point to the right of *any* of the mode curves (point D) does not correspond to a physically realizable steady state. It is in the $\mathrm{Im}(\omega) < 0$ regime for one or more modes, and those modes will thus grow exponentially without limit. This region is, of course, accessible on a transient basis--but if one drives the device into the $\mathrm{Im}(\omega) < 0$ region for a particular mode, the optical power in that mode will build up over time and saturate the gain back down to a point somewhere on the lowest curve. These arguments justify the division of the (n_1, n_2) plane into regions below and above threshold as in figure 6.4. Between any two cusps, the curve corresponds to the $\mathrm{Im}(\omega) = 0$ line of the lowest-lying mode. The cusps correspond to mode hopping. Above lasing threshold, the carrier density is clamped onto the threshold line (although it is free to shift along the line).

In practice, one controls the currents supplied to the two sections, not the carrier densities. The question of multistability refers to the existence of multiple operating points (n_1, n_2) for the same pump current densities (j_1, j_2). We must also consider the carrier density equations

$$\dot{n}_i = \frac{j}{qd} - \frac{n_i}{\tau_s} - g_i(n_i)\sum_j \Gamma_{ij} p_j \tag{3}$$

where q is the electronic charge, d is the thickness of the active layer, $g_i(n_i)$ is the gain constant, and Γ_{ij} are fill factors defined by

$$\Gamma_{ij} \equiv \left\{ \text{the proportion of optical power of the jth mode in the ith cavity} \right\}$$

In steady-state, we can write this equation as

$$\frac{j_i}{qd} = \frac{n_i}{\tau_s} + g_i(n_i)\sum_j \Gamma_{ij} p_j \tag{4}$$

Thus, for a given operating point (n_1, n_2) and a given set of photon densities p_j, the currents are exactly determined. As we have seen, for all operating points well away from a mode boundary, only a single mode lases, so we can set the photon density for that mode equal to the total power density and set all of the

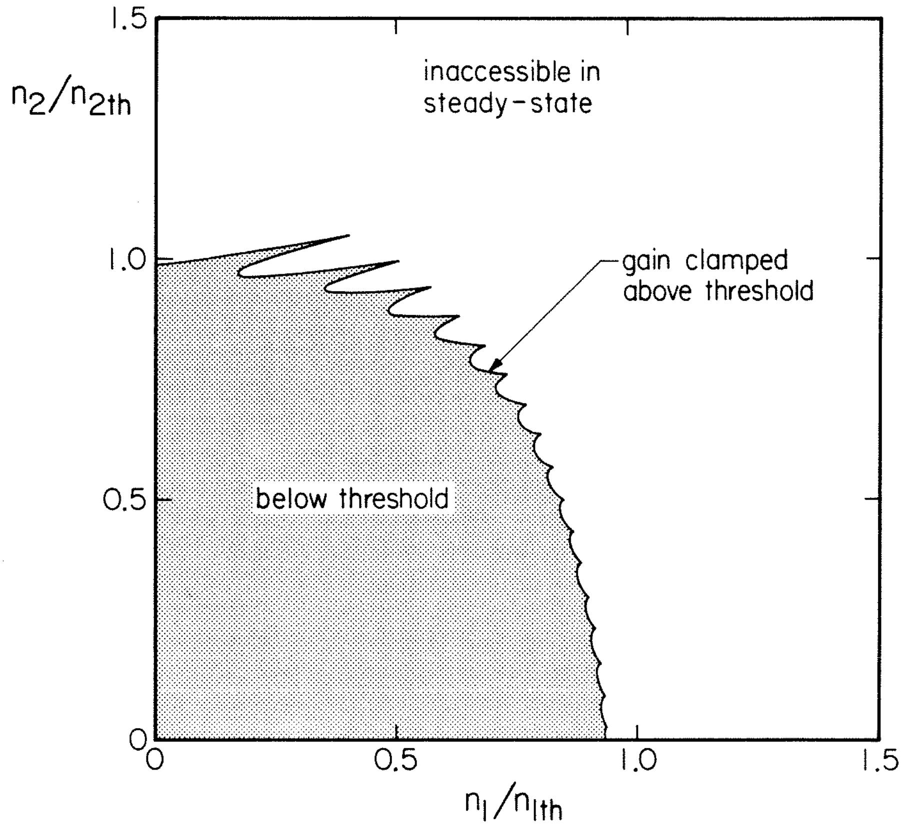

Figure 6.4: Accessible regions of the carrier density plane. Above threshold, the carrier density is clamped onto the threshold carrier density line. Each cusp on the curve indicates a mode hop.

other photon densities to 0. For $p_{tot} = 0$, the allowable currents are precisely equal to the threshold carrier densities (with a scaling factor of qd/τ_s), and for $p_{tot} > 0$, we can use equations (4) to replot the carrier density curves at any desired power level.

A modification occurs when we are at a cusp, since two lasing modes are possible. Let the two modes have power levels

$$p_1 = xp_{tot}, \quad p_2 = (1-x)p_{tot} \tag{5}$$

so that x is the relative fraction of optical power in mode 1; then the current relations can be written as

$$\frac{j_i}{qd} = \frac{n_i}{\tau_s} + g_i(n_i)[x\Gamma_{i1} + (1-x)\Gamma_{i2}]p_{tot} \tag{6}$$

It is clear from equation (6) that as x varies from 0 to 1, the current (and mode) changes linearly from that of purely mode 1 to that of purely mode 2. Hence as we increase the power, the cusps that exist at threshold move out into the current plane and become straight line segments that join the single-mode curves. There are two qualitatively different ways in which this situation manifests itself, both illustrated in figure 6.5 for a constant p_{tot} (they usually do not occur together; both are shown on the same graph for illustrative purposes only). The line segment labeled "modes 1&2" is one of a family that fills the region of the current plane claimed [5] to possess no stable solution. The segment labeled "modes 2&3," which completes the loop, shows that multiple (in this case, three) steady-state solutions exist (the three solutions at three different power levels for the same (j_1,j_2) are shown explicitly in figure 6.6). A steady-state analysis cannot tell us anything about the stability of such states, however. In the next section, we will transform the equations of motion near the mode hop to a simple system of nonlinear ordinary differential equations that incorporate all of the relevant physics, yet allow simple analytic solutions and thus an unmistakable interpretation of the physics of the device.

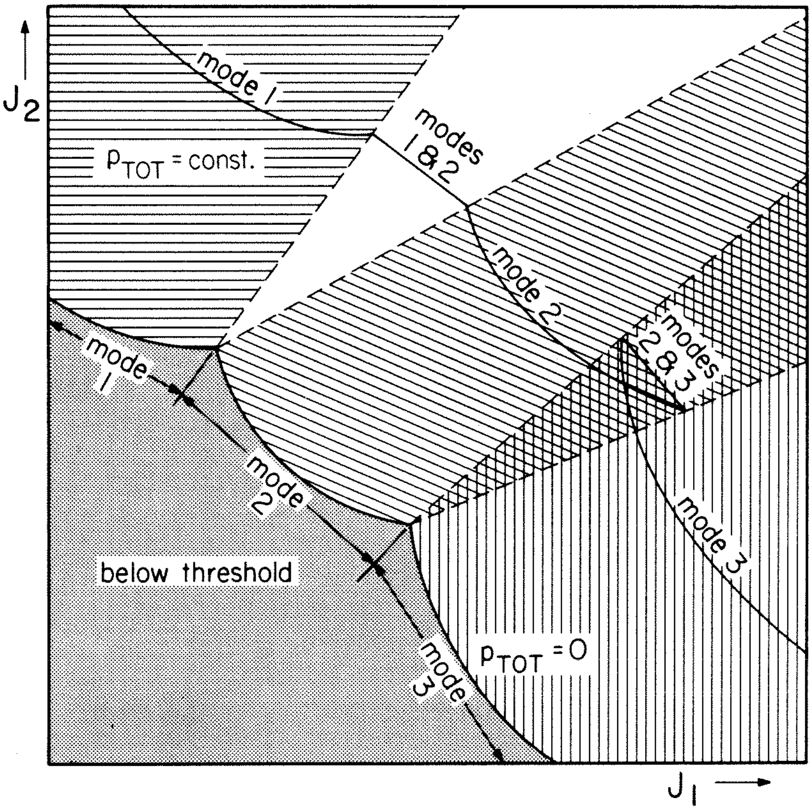

Figure 6.5: Schematic of constant power curves in the current plane (arbitrary units). The $p_{tot} = 0$ curve is identical to the threshold gain curve in the (n_1, n_2) plane (within a scaling factor). The straight line segments joining the curves for fixed $p_{tot} \geq 0$ are the mixed state (two simultaneously oscillating modes).

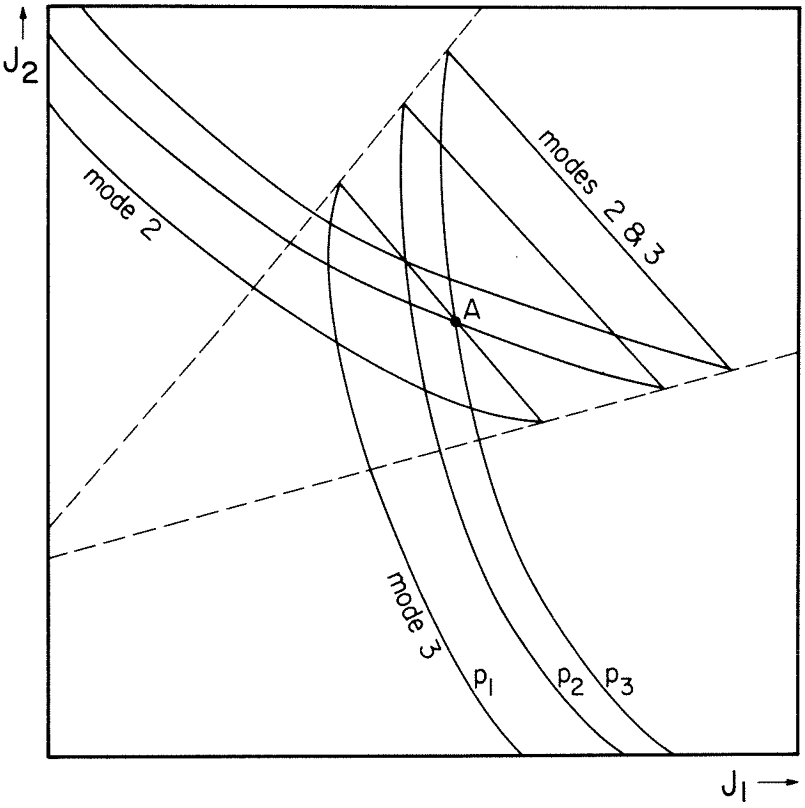

Figure 6.6: Illustration of a single point in the current plane that possesses three steady-state solutions at different power levels (multimode at p_1, mode 2 at p_2, mode 3 at p_3).

6.3 Nondimensional Equations and Stability

The problem as posed is strongly nonlinear; in particular, the variation of $\mathrm{Im}(\omega_j)$ with n_i must be analyzed numerically. However, we can put equations (2) and (3) into nondimensional form valid near a mode boundary, which carries all physical information, without recourse to numerical techniques. The results we derive will be applicable to any two-element laser and not exclusively to a longitudinally coupled-cavity laser.

The algebra is simplified if we put equations (3) and (2) in matrix form.

$$\dot{\tilde{N}} = \frac{1}{qd}\tilde{J} - \frac{1}{\tau_s}\tilde{N} - \overset{\approx}{G}(\tilde{N})\overset{\approx}{\Gamma}\tilde{P} \tag{7}$$

$$\dot{\tilde{P}} = \overset{\approx}{W}\tilde{P} + \overset{\approx}{B}\tilde{N} \tag{8}$$

The *i*th element of $\tilde{N}$ is $\{n_i\}$; the elements of $\tilde{J}$ are $\{j_i\}$; the elements of $\overset{\approx}{\Gamma}$ are $\{\Gamma_{ij}\}$; the elements of $\overset{\approx}{W}$ are $\{\delta_{ij}\mathrm{Im}(\omega_i)\}$; the elements of $\overset{\approx}{B}$ are $\{\beta_i\delta_{ij}/\tau_s\}$; the elements of $\tilde{P}$ are $\{p_i\}$. We now transform to the coordinate system $\tilde{M}$ illustrated in figure 6.7. If we linearize the mode lines about the mode crossing, then there exists a transformation matrix $\overset{\approx}{R}$ such that

$$\tilde{M} = \overset{\approx}{R}(\tilde{N} - \tilde{N}^{(0)}) \tag{9}$$

where the elements of $\tilde{N}^{(0)}$ are $\{n_i^{(0)}\}$, the coordinates of the mode crossing. (Note that $\overset{\approx}{R}$ is only unique to within a constant scaling matrix $\begin{bmatrix} a & 0 \\ 0 & b \end{bmatrix}$ with $a,b > 0$; this ambiguity does not affect the analysis.) To lowest order, the system of matrix equations becomes

$$\dot{\tilde{M}} = \frac{1}{qd}\overset{\approx}{R}\left(\tilde{J} - \frac{qd}{\tau_s}\tilde{N}^{(0)}\right) - \frac{1}{\tau_s}\tilde{M} - \overset{\approx}{R}\overset{\approx}{G}(\tilde{N}^{(0)})\overset{\approx}{\Gamma}\tilde{P} \tag{10}$$

$$\dot{\tilde{P}} = \overset{\approx}{K}\overset{\approx}{M}\tilde{P} + \overset{\approx}{B}\tilde{N}^{(0)} \tag{11}$$

where the elements of $\overset{\approx}{K}$ are $\left\{-2\frac{\partial \mathrm{Im}(\omega_i)}{\partial m_j}\right\}$ and $\overset{\approx}{M}$ is the 2x2 matrix with the elements of $\tilde{M}$ on the diagonal. The virtue of choosing the axes $\{m_i\}$ is that (to the

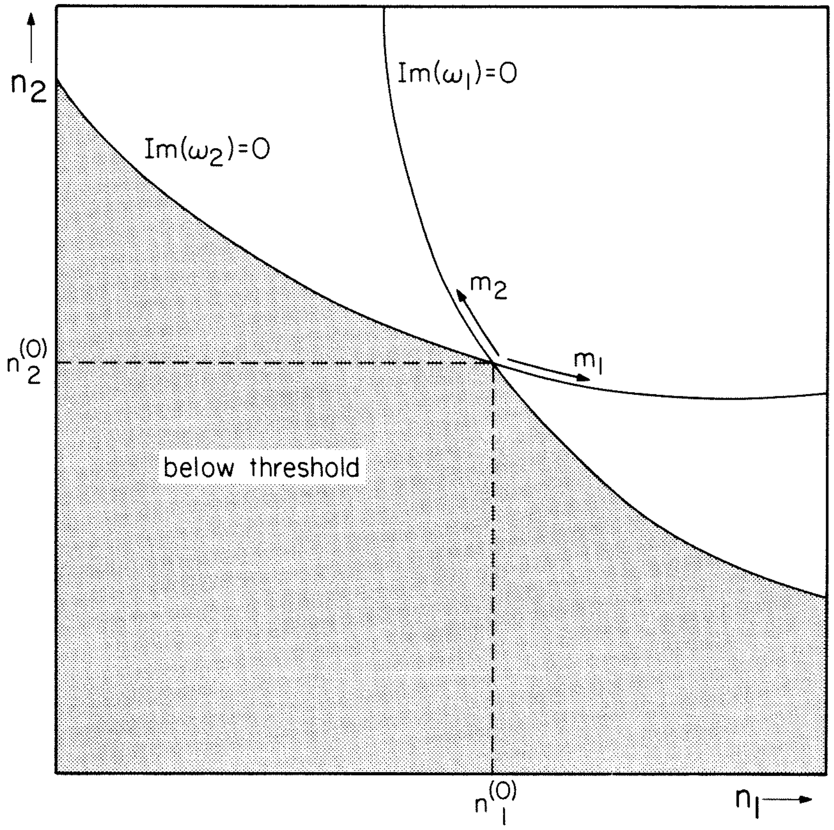

Figure 6.7: Schematic of a single mode crossing in the carrier density plane (arbitrary units). The transformed variables $\{m_i\}$ are measured along the two intersecting mode lines.

same order of approximation as the linearization), $\overset{\approx}{K}$ is diagonal. It is also important to note that with the axes so defined, det $\overset{\approx}{R} > 0$ (if the axes were reversed, the sign would change). Now, we define dimensionless variables by taking

$$t \equiv \tau_s \cdot \tau, \quad \tau \text{ is the new time variable,} \tag{12a}$$

$$\tilde{E} \equiv \overset{\approx}{K}\tilde{M} \tag{12b}$$

$$\tilde{I} \equiv \frac{\tau_s}{qd}\overset{\approx}{K}\overset{\approx}{R}\tilde{J} - \overset{\approx}{K}\overset{\approx}{R}\tilde{N}^{(0)} \tag{12c}$$

$$\overset{\approx}{H} \equiv \overset{\approx}{K}\overset{\approx}{R}\overset{\approx}{G}(\tilde{N}^{(0)})\overset{\approx}{\Gamma} \tag{12d}$$

$$\overset{\approx}{D} \equiv \overset{\approx}{B}\tilde{N}^{(0)} \tag{12e}$$

which reduces (10) and (11) to the simple system

$$\begin{aligned} \dot{\tilde{E}} &= \tilde{I} - \tilde{E} - \overset{\approx}{H}\tilde{P} \\ \dot{\tilde{P}} &= \overset{\approx}{E}\tilde{P} + \tilde{D} \end{aligned} \tag{13}$$

In component form,

$$\dot{e}_i = i_i - e_i - \sum_j h_{ij} p_j \tag{14}$$

$$\dot{p}_j = e_j p_j + d_j \tag{15}$$

Equations (14) and (15) are several levels removed from the original system, so it is helpful to review the terms in each equation and identify them with a physical mechanism. $\{e_i\}$ are carrier densities, $\{i_i\}$ are pump currents, $\{p_i\}$ are the modal power densities, $\{h_{ij}\}$ are the fill factors (the proportion of mode j in carrier pool i) and $\{d_j\}$ are the spontaneous emission rates. Thus the three terms on the right side of (14) correspond to pump current, spontaneous emission, and stimulated emission, respectively; the two terms on the right of (15) are stimulated emission and spontaneous emission, respectively. Examination of (12d) reveals that det H is of the same sign as det Γ (because the determinants of all of the intervening matrices are positive). This is indicative of the fact that in transforming from the $\{n_i\}$ representation to the $\{e_i\}$ representation, we "stretched" the axes, but didn't flip them over. Also, we note that the spontaneous emission rate is typically quite small ($\beta_i \approx 10^{-4}$) so that $\{d_i\}$ are also of the same small order.

The steady-state solutions of (14) and (15) are plotted in the current plane for a fixed p_{tot} in figure 6.8 (subject to the physical constraint $p_i \geq 0$). The solutions in the absence of spontaneous emission ($d_i = 0$) are apparent by inspection (one virtue of the dimensionless system of equations). They are

$$\begin{cases} p_1 = 0, \ e_2 = 0, \ e_1 \text{ free} \end{cases}$$

or

$$\begin{cases} p_2 = 0, \ e_1 = 0, \ e_2 \text{ free} \end{cases}$$

or

$$\begin{cases} e_1 = e_2 = 0, \ p_2 = p_{tot} - p_1, \ p_1 \text{ free} \end{cases} \tag{16}$$

If we include spontaneous emission and define x as the free parameter (restricted to $x \in [0,1]$), the solutions are

$$\begin{cases} p_1 = x p_{tot}, \ p_2 = (1-x) p_{tot}, \ e_1 = \dfrac{-d_1}{x p_{tot}}, \ e_2 = \dfrac{-d_2}{(1-x) p_{tot}} \end{cases} \tag{17}$$

(17) is more exact than (16); however, the shape of the curves is not as obvious from the equations.

With or without spontaneous emission, we still must prove that these steady-state solutions are stable. We do this by performing a second linearization of (14) and (15) and determining the boundedness of the response of the homogeneous system to a perturbation.

$$e_i \rightarrow e_i + \varepsilon_i, \qquad p_i \rightarrow p_i + \rho_i \tag{18}$$

giving

$$\begin{aligned} \dot{\varepsilon}_i &= -\varepsilon_i - \sum_j h_{ij} \rho_j \\ \dot{\rho}_j &= \varepsilon_j p_j + e_j \rho_j \end{aligned} \tag{19}$$

These can be put into matrix form as

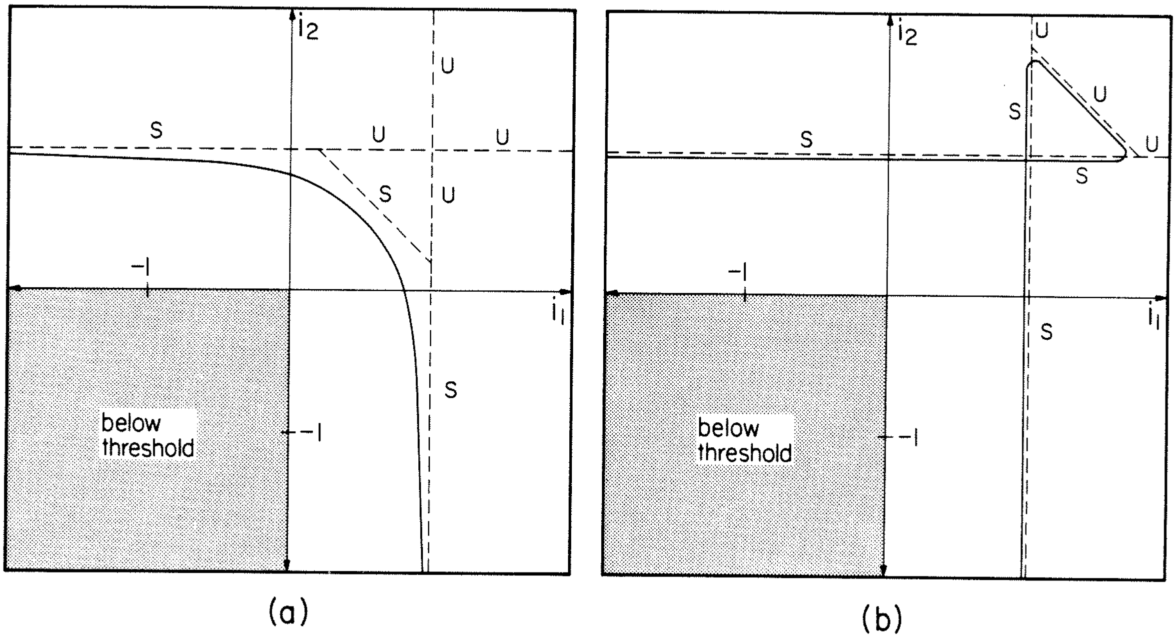

Figure 6.8: Steady-state modes in the transformed current plane for fixed total output power $p_{tot} = 1$. Dotted lines are solutions in the absence of spontaneous emission ($d_i \equiv 0$); solid lines are solutions including spontaneous emission ($d_1 = d_2 = 0.05$). a) $h_{11} = h_{22} = 1$, $h_{12} = h_{21} = .2$, so det $H \geq 0$; b) $h_{11} = h_{22} = 1$, $h_{12} = h_{21} = 1.8$, so det $H \leq 0$.

$$\begin{bmatrix}\varepsilon_1\\ \varepsilon_2\\ \rho_1\\ \rho_2\end{bmatrix}^{\cdot} = \begin{bmatrix}-1 & 0 & -h_{11} & -h_{21}\\ 0 & -1 & -h_{12} & -h_{22}\\ p_1 & 0 & e_1 & 0\\ 0 & p_2 & 0 & e_2\end{bmatrix}\begin{bmatrix}\varepsilon_1\\ \varepsilon_2\\ \rho_1\\ \rho_2\end{bmatrix} \qquad (20)$$

The solution to (20) is bounded only if all of the eigenvalues of the square matrix have nonpositive real parts. The secular equation for the eigenvalue λ is

$$(\lambda+1)^2(\lambda-e_1)(\lambda-e_2)+(\lambda+1)(\lambda-e_2)p_1h_{11}+(\lambda+1)(\lambda-e_1)p_2h_{22}+p_1p_2\det H=0 \qquad (21)$$

We shall first solve for the case with no spontaneous emission.

Case I. $e_2 = p_1 = 0$ *(only mode 2 lasing).*

Equation (21) reduces to

$$(\lambda+1)(\lambda-e_1)[\lambda(\lambda+1) + p_2h_{22}] = 0 \qquad (22)$$

The roots are $\lambda = -1$, $\lambda = e_1$, $\lambda = -\frac{1}{2}\pm[\frac{1}{4}-p_2h_{22}]^{½}$, so the solution is stable if $e_1 \leq 0$.

Case II. $e_1 = p_2 = 0$ *(only mode 1 lasing).*

By switching indices, we see that $e_2 \leq 0$ is necessary for stability.

Case III. $e_1 = e_2 = 0$ *(multimode state).*

$$(\lambda+1)^2\lambda^2 + (p_1h_{11}p_2h_{22})\lambda(\lambda+1) + p_1p_2\det H = 0 \qquad (23)$$

Define $x \equiv \lambda(\lambda+1)$. Then

$$\lambda=-\frac{1}{2}\pm[\frac{1}{4}+x]^{½} \qquad (24)$$

so x must have a negative real part for stability. The equation for x is

$$x^2 + (p_1h_{11}+p_2h_{22})x + p_1p_2\det H = 0 \qquad (25)$$

From inspection we can see that x has a negative real part only if $\det H \geq 0$. In figure 6.8 we have plotted representative cases in the (i_1,i_2) plane for the two possible signs of det H. Case I yields the vertical dashed lines, case II yields horizontals, and case III yields the diagonal line; $\det H \geq 0$ in figure 6.8a, $\det H \leq 0$ in figure 6.8b. Thus, the multimode state (case II) is stable in figure 6.8a, while it is unstable in figure 6.8b. All of the steady-state solutions in figure 6.8 are labeled

(S=stable, U=unstable) according to these rules. While one can numerically work out the roots for the case including spontaneous emission, there is no need; as the spontaneous emission goes to zero, the solution lines and the roots of (21) must collapse onto those of no spontaneous emission. Therefore, the labelings are valid for the curves that include spontaneous emission.

One important point is that the portions of the single-mode curves in figure 6.8b that overlap each other (and consequently yield multiple solutions) are stable; bistable transitions can only occur at their endpoints (where they become unstable). Furthermore, we have proven the stability of the mixed state of figure 6.8a. It remains to relate this nondimensional problem to the physical problem we started with. This is accomplished by noting that the point $(e_1,e_2) = (0,0)$ is the crossing of the two mode lines in figure 6.5. Since (as we pointed out earlier) det H and det Γ have the same sign, the stability criterion for the mixed state is that det $\Gamma \geq 0$. The different states and their stability are summarized in figure 6.9. The current plane will, in general, divide into regions of single-mode operation; the boundaries will either consist of bimodal regions (two simultaneous lasing modes) where det $\Gamma \geq 0$, or bistable regions (two possible single-mode states) where det $\Gamma \leq 0$. This is contrary to the assertions of reference [5]. One final point of interest; the stable mixed state (figure 6.8a) is a multimode state that persists in the absence of spontaneous emission. This is to be contrasted with the more usual multimode behavior, where the intensity of side modes is proportional to the spontaneous emission rate. (It should be pointed out that with insufficient selectivity between modes, any laser--including coupled-cavity--will run multimode, due to the spontaneous emission).

There are several features of this behavior that would be of interest from a systems viewpoint. Every point in the bimodal region corresponds to the same set of carrier densities $\left\{e_1 = e_2 = 0\right\}$. Therefore, the carrier density is fixed, and

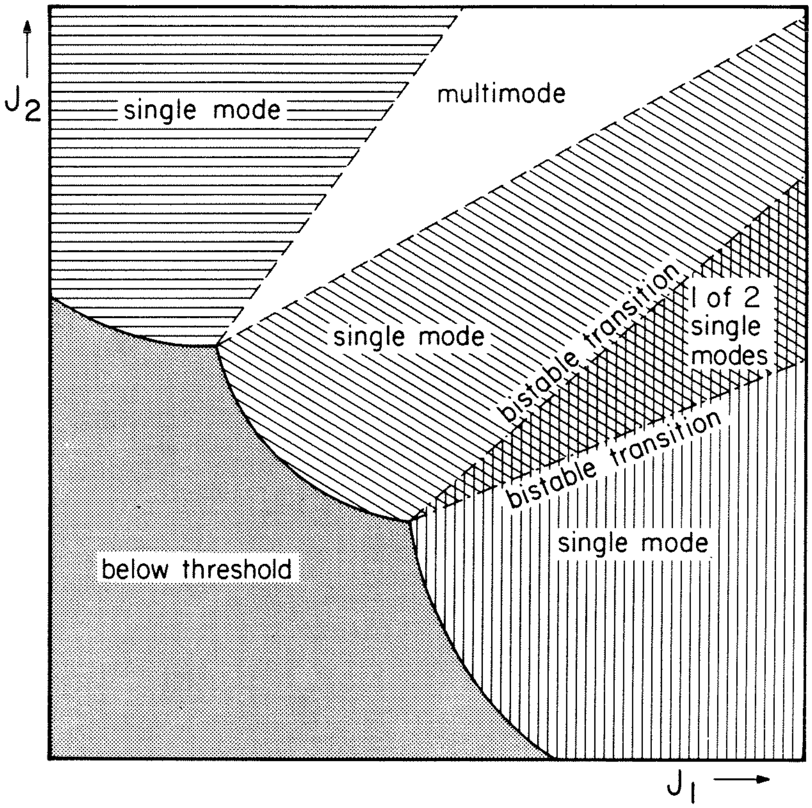

Figure 6.9: Division of the current plane into regions of sub-threshold, lasing, multimode operation, single-mode operation and bistable operation. Lines of instability on which bistable transitions take place are indicated.

so the gain and resonant refractive index are effectively clamped (which is *not* the case in a single mode region). Consequently, if one modulates the laser entirely within the multimode region, there is no direct frequency modulation of either of the two modes. With the addition of a notch filter to remove one of the two modes from the optical output, the device becomes a chirpless modulator. Also, the response time of a laser diode is dependent upon the total optical power present. By modulating the diode in the bimodal region, the optical power is merely switched from one mode to another (as in a push-pull amplifier); consequently, even though the amplitude of the desired mode may approach zero, the *total* power present remains constant and the response time of the device remains short.

On the other hand, if the cavity were tuned such that det $\Gamma \leq 0$ at the mode hop, the device possesses electrical bistability and the inherent noise immunity associated with bistability. Examination of equation (4) shows that an external beam of light impinging upon one of the cavities shifts the entire set of tuning curves up and down (or side to side) in the current plane. Hence, all-optical bistability is equally feasible.

6.4 Conclusions

In summary, we have analyzed the steady-state operation of a two-element coupled-cavity semiconductor laser near a mode boundary. We showed how the equations of motion for a specific system of a longitudinally coupled-cavity laser can be reduced to a non-dimensional set of nonlinear differential equations that describe the behavior of a general two-element coupled-cavity laser near a mode boundary. We showed that a multimode state that was previously unexplained exists whenever the determinant of the matrix of fill-factor coefficients is nonzero. The multimode state varies continuously between the two involved single modes regardless of the level of spontaneous emission. If the determinant is greater than zero, the multimode state is stable. Otherwise, it is unstable, but there are two stable single-mode states. Bistable transitions occur on the boundaries of the unstable multimode state. Large bistabilities are desirable from the point of optical storage and hysteretic devices; consequently, the relation between the bistable region and the size of the determinant of the fill factor matrix is a useful design criterion for such devices.

References

[1] W. T. Tsang and N. A. Olsson, Appl. Phys. Lett., vol. 42, pp. 650-652 (1983).

[2] K. J. Ebeling, L. A. Coldren, B. I. Miller and J. A. Rentschler, Appl. Phys. Lett., vol. 42, pp. 6-8 (1983).

[3] I. H. White, J. E. Carroll and R. G. Plumb, IEE Proc., vol. 129, pp. 291-293 (1982).

[4] Ch. Harder, K. Y. Lau and A. Yariv, Appl. Phys. Lett., vol. 40, pp. 124-126 (1982).

[5] C. H. Henry and R. F. Kazarinov, IEEE J. Quant. Elect., vol. QE-20, pp. 733-744 (1984).

[6] D. Marcuse and T-P Lee, IEEE J. Quant. Elect., vol. QE-20, pp. 166-176 (1984).

[7] K. J. Ebeling and L. A. Coldren, J. Appl. Phys., vol. 54, pp. 2962-2969 (1983).

[8] W. Streifer, D. Yevick, T. L. Paoli and R. D. Burnham, J. Quant. Elect., vol. QE-20, pp. 754-764 (1984).

[9] J. Salzman, R. Lang and A. Yariv, Appl. Phys. Lett., vol. 47, pp. 195-197 (1985).

[10] R. J. Lang and A. Yariv, IEEE J. Quant. Elect., vol. QE-21, pp. 1683-1688 (1985).

Chapter 7

Semiclassical Theory of Noise in Multielement Semiconductor Lasers

7.1 Introduction

We have seen how multielement lasers, while desirable for use as transmitters in fiber optic systems because of their potential for high-speed modulation and narrow spectrum, are generally more difficult to analyze regarding threshold gain and dynamic properties than their simpler single-element counterparts. They often exhibit qualitatively different behavior from the two-mirror Fabry-Perot lasers. For example, as we saw in chapter 5, many of the laser geometries are plagued by chirping, or FM, under current modulation[1,2], while in chapter 6 we showed that bimodal and bistable behavior was possible. While chirping may be desirable for an FM modulation system, in AM systems it broadens the spectrum of the modulated laser. Recently it has been demonstrated that chirping in two-section lasers can be reduced by splitting the modulation current between the two sections [1] or by judicious selection of the bias point [2]; we showed this analytically in chapter 5 [4], when we derived analytic expressions for both the frequency and amplitude responses of a general multielement semiconductor laser in terms of the bias point quantities. The knowledge of which physical quantities affect the chirp, resonance frequency, etc., allow one to design multielement lasers with a minimum of chirp under modulation.

The fundamental limit to the linewidth of the laser, however, is the noise associated with the process of spontaneous emission and quantization of the carriers and photons. In the past five years, the noise properties of semiconductor lasers have been the subject of scrutiny, and several anomalous features have been observed and explained, including a spiking resonance in the intensity spectrum [5,6] and frequency fluctuation spectrum [7], a linewidth some 30 times greater than that predicted by the modified Schawlow-Townes theory [8,9], power-independent linewidth components [10], asymmetry in the field spectrum [7], and excess noise at low frequencies in both the intensity and frequency fluctuation spectrum [11-14].

However, just as the dynamic properties of multielement lasers were more difficult to determine than those of two-mirror lasers, the noise properties are similarly difficult. In fact, to date there have been no attempts at analyzing the noise properties of semiconductor lasers with multiple active elements. Recently, it was observed [15,16] that phase noise could be reduced in a passive-active laser by varying the coupling between the cavities, and it seems likely that such would be the case in an active-active cavity. On the other hand, coupled-cavity lasers are known to possess an FM response to current fluctuations, which may increase the fundamental linewidth even in the absence of modulation. A theory of multielement laser noise would be useful in evaluating multielement lasers for systems applications.

In fact, the extension of the theory from the last chapter to include noise comes almost as a corollary to the formalism we developed there. A common technique for analyzing noise properties is to model the noise by a Langevin (white) source with an appropriate normalization that drives the rate equations of the system in question [4,17-20]. In this paper, we apply the Langevin theory to small-signal rate equations to calculate the spectra of a multielement laser.

In section 7.2, we follow the formalism of chapter 5 to develop the small-signal linear rate equations from the nonlinear equations describing the dynamics of the laser and introduce the Langevin driving sources. In section 7.3, we normalize the Langevin sources and calculate their correlations and spectra. In section 7.4, we combine the results of the previous two sections to produce general formulas for the relative intensity spectra, frequency fluctuation spectra, and field spectra of an arbitrary multielement semiconductor laser. In addition, we evaluate some of the formulas for several specific cases. In section 7.5, we summarize the important results of the analysis.

7.2 Rate Equations

The system we are considering is a semiconductor laser consisting of N active elements (and an arbitrary number of passive elements). For each active element, the carrier dynamics can be described by volume-averaged rate equations as

$$\dot{n}_i = \frac{J_i}{qd} - \frac{n_i}{\tau_s} - g_i(n_i)p_i \tag{1}$$

where n_i is the carrier density in the ith cavity, J_i is the pump current density, q is the charge on an electron, d is the active layer thickness, τ_s is the spontaneous lifetime, $g_i(n_i)$ is the gain constant (as a function of the carrier density), and p_i is the photon density in the ith cavity.

The DC operation of the resonator (threshold carrier density and lasing frequency) is governed by a dispersion relation of the form

$$F(\omega, n_1, \cdots n_N) = 0 \tag{2}$$

particular to the geometry under consideration. The derivation of equation (2) has been carried out for several geometries of interest [20-26], and is generally straightforward. In section 7.4 we will derive the dispersion function F for those systems we consider in detail, but for now we will assume it exists and is known. We will also require a set of fill factors defined by

$$\Gamma_i(\omega, n_1, \cdots n_N) \equiv \frac{p_i}{p} \tag{3}$$

where p is the average photon density in the composite cavity, and ω in equation (3) is implicitly defined by equation (2) as a complex function of the carrier densities $\{n_i\}$.

As we saw, if one takes the electric field amplitude to be of the form $e^{i\psi(t)}$ then the dispersion equation (equation (2)) is an instantaneously valid description of the dynamics of the system if we replace ω by $\dot{\psi}$. The result is a first-order nonlinear differential equation for the field amplitude and phase [4]. We substitute (3) in (1) and linearize (1) and (2) about a steady-state operating point:

$$\begin{gathered} J_i \equiv J_{i0} + qd \cdot e_i(t) \\ n_i \equiv n_{i0} + \nu_i(t) \\ \dot{\psi} \equiv \omega_0 + \Delta\omega(t) - j\rho(t) \end{gathered} \tag{4}$$

which yields

$$\dot{\rho} = \sum_i g'_{ieff} \nu_i \tag{5}$$

$$\Delta\omega = -\sum_i m'_{ieff} \nu_i \tag{6}$$

$$\dot{\nu}_i = e_i - \left[\frac{1}{\tau_s} + g'_i \Gamma_i p\right] \nu_i - 2 g_i \Gamma_i p \rho - \sum_k g_i p \frac{d\Gamma_i}{dn_k} \nu_k \tag{7}$$

where

$$g'_{ieff} \equiv \operatorname{Im} \frac{\partial F / \partial n_i}{\partial F / \partial \omega}, \qquad m'_{ieff} \equiv \operatorname{Re} \frac{\partial F / \partial n_i}{\partial F / \partial \omega} \tag{8}$$

$$\frac{d\Gamma_i}{dn_k} = \frac{\partial \Gamma_i}{\partial n_k} - m'_{keff} \frac{\partial \Gamma_i}{\partial \operatorname{Re}(\omega)} - g'_{keff} \frac{\partial \Gamma_i}{\partial \operatorname{Im}(\omega)} \tag{9}$$

and all derivatives are evaluated at the operating point. Equations (5)-(7) are now a set of linear differential equations giving the response to a small modulation.

We Fourier transform equations (5)-(7) (so that the operator d/dt becomes a factor $j\Omega$), and we denote transformed dynamical variables by a tilde. We make the following definitions:

$$\frac{1}{\tau_i} \equiv \frac{1}{\tau_s} + g'_i\Gamma_i p, \quad \omega_{i\mathrm{eff}}^2 \equiv 2g'_{i\mathrm{eff}}g_i\Gamma_i p, \quad \alpha_{i\mathrm{eff}} \equiv m'_{i\mathrm{eff}}/g'_{i\mathrm{eff}}$$

$$d_i \equiv j\Omega + \frac{1}{\tau_i}, \quad c_{ik} \equiv pg_i\frac{d\Gamma_i}{dn_k} \tag{10}$$

The transformed equations, now linear algebraic, can be put into matrix form as

$$\begin{pmatrix} j\Omega & 0 & -g'_{1\mathrm{eff}} & \cdots & -g'_{N\mathrm{eff}} \\ 0 & 1 & \alpha_{1\mathrm{eff}}g'_{1\mathrm{eff}} & \cdots & \alpha_{N\mathrm{eff}}g'_{N\mathrm{eff}} \\ \dfrac{\omega_{1\mathrm{eff}}^2}{g'_{1\mathrm{eff}}} & 0 & c_{11}+d_1 & \cdots & c_{N1} \\ \vdots & \vdots & \vdots & & \vdots \\ \dfrac{\omega_{N\mathrm{eff}}^2}{g'_{N\mathrm{eff}}} & 0 & c_{N1} & \cdots & c_{NN}+d_N \end{pmatrix} \begin{pmatrix} \tilde{\rho} \\ \Delta\tilde{\omega} \\ \tilde{\nu}_1 \\ \vdots \\ \tilde{\nu}_N \end{pmatrix} = \begin{pmatrix} 0 \\ 0 \\ \tilde{e}_1 \\ \vdots \\ \tilde{e}_N \end{pmatrix} \tag{11}$$

Equation (11) defines the small-signal response of the field amplitude ($\tilde{\rho}$), frequency ($\Delta\tilde{\omega}$) and carrier densities ($\tilde{\nu}_i$) to fluctuations in the pump current ($\tilde{e}_i$). Had we some physical mechanism for directly driving the amplitude or phase, that, too, could be incorporated into the right side of (11). In the next section, we develop the appropriate Langevin sources for insertion into (11).

7.3 Langevin Sources

When several systems of particles interact with each other and/or with external baths through random particle interactions, there are fluctuations associated with each interaction. Such fluctuations can be accounted for by including appropriately normalized Langevin sources into the equations of motion. This approach can also be used with variables that vary continuously (e.g. temperature, phase [14]) but the normalization procedure is not as clear-cut as it is for particulate variables. In the latter case, each independent number variable $\{A\}$ will have associated with it a fluctuation source $\{a\}$ that satisfies

$$< a(t)a(t')> \; = \; < \frac{dA}{dt} > \delta(t-t') \tag{12}$$

where $< \; >$ denotes ensemble average. The source $\{a\}$ is then used to drive the rate equation for the fluctuations in $\{A\}$. If there are more than one independent mechanism creating particle fluxes into or out of the number variable pool, there will be a driving source associated with each transition rate. Alternatively, the various sources may be lumped into a single source whose autocorrelation is the sum of the individual sources (as is done here).

In our system, the number variables are total photon number in the optical mode, and carrier number in each cavity. Thus, for the photon number, the appropriate Langevin source possesses the autocorrelation

$$< s(t)s(t')> \; \equiv \; \left[\sum_i (R_i^{STE} + R_i^{STA} + \beta R_i^{SPE}) + R^{CAV}\right]\delta(t-t') \tag{13}$$

where R_i^{STE} is the stimulated emission rate from cavity *i*, R_i^{STA} is the stimulated absorption rate, R_i^{SPE} is the spontaneous emission rate, R^{CAV} is the cavity loss rate, and β is the fraction of spontaneous emission rate coupled into the optical mode. For carrier number in cavity *i*, we have

$$< c_i(t)c_i(t')> \; \equiv \; \left[R_i^{STE} + R_i^{STA} + R_i^{SPE} + R_i^{PMP}\right]\delta(t-t') \tag{14}$$

where R_i^{PMP} is the pump rate into cavity *i*.

Since $\beta \approx 10^{-4}$, we can drop it from equation (13); in addition, balancing input and output flows from the particle pools yields the relations

$$R^{CAV} = \sum_i R_i^{STE} - R_i^{STA}, \qquad R_i^{PMP} = R_i^{STE} - R_i^{STA} \tag{15}$$

Also, if we introduce the spontaneous emission factors

$$\eta_i \equiv \frac{R_i^{STE}}{R_i^{STE} - R_i^{STA}} \tag{16}$$

we can relate all of these rates to the variables in the rate equations

$$R_i^{STE} - R_i^{STA} = V_i g_i \Gamma_i p, \qquad R_i^{SPE} = n_i / \tau_s \tag{17}$$

The Langevin sources possess non-zero cross correlations whenever an event changes two variables at once (which stimulated emission and absorption do; spontaneous emission does also but the cross-correlation is on the order of β and can safely be ignored). The cross-correlations of interest are:

$$\begin{aligned} \langle s(t)c_i(t') \rangle &= -(R_i^{STE} + R_i^{STA})\delta(t-t') \\ \langle c_i(t)c_j(t') \rangle &= 0 \text{ for } i \neq j. \end{aligned} \tag{18}$$

We should now convert these Langevin sources appropriate for number variables to sources appropriate for the variables in our system--namely, relative amplitude and carrier density. If we define the sources as Δ for relative amplitude and Ξ_i for carrier density, then

$$s = 2pV\Delta, \quad c_i = V_i\Xi_i \tag{19}$$

where V is the total volume of the optical mode and V_i is the volume of the *i*th active element. The phase, too, is subject to random fluctuations due to spontaneous emission. Being a continuous variable, the correlations of its Langevin source Φ are not as immediately obvious as those of the amplitude and carrier sources. Using a model discussed by Henry [9], Vahala et al. have shown [16] that the Langevin source driving the phase has the same autocorrelation as that of the source driving the amplitude fluctuations, but is uncorrelated with any other source. (Although they were considering only a single-element laser, their argument is independent of the number of separate active regions.) Using equations (15)-(17) to put the transition rates in terms of the rate equation variables, we can summarize the relevant correlations for the amplitude Langevin source Δ, the phase source Φ, and the carrier sources Ξ as

$$\langle \Delta(t)\Delta(t') \rangle = \langle \Phi(t)\Phi(t') \rangle = \frac{1}{2pV^2}\sum_i \eta_i g_i \Gamma_i V_i \delta(t-t') \tag{20}$$

$$\langle \Xi_i(t)\Xi_j(t') \rangle = \frac{2}{V_i}\left[\frac{n_i}{\tau_s} + \eta_i g_i \Gamma_i p\right]\delta_{ij}\delta(t-t') \tag{21}$$

$$\langle \Delta(t)\Xi_i(t') \rangle = -\frac{g_i\Gamma_i}{2V}(2\eta_i - 1)\delta(t-t') \tag{22}$$

All other cross-correlations are zero. Equation (11) is in terms of transformed variables, so it is convenient to cast (19)-(22) in the same manner, particularly since we are interested in spectral functions $W_{fg}(\Omega)$, which are themselves transformed quantities. Mathematical problems arise when one attempts to transform a stationary signal, however; to be rigorous, one must use finite-domain Fourier transforms defined as follows:

$$\tilde{f}_T(\omega) \equiv \int_{\frac{-T}{2}}^{\frac{+T}{2}} dt\, f(t)e^{-j\omega t}, \quad \tilde{g}_T(\omega) \equiv \int_{\frac{-T}{2}}^{\frac{+T}{2}} dt\, g(t)e^{-j\omega t}, \tag{23}$$

Then one can calculate the spectral quantities defined by the Wiener-Khintchine relations as

$$W_{fg}(\Omega) \equiv \int d\tau < f(t)g(t+\tau) > e^{-j\Omega\tau} \tag{24}$$

from the finite-domain transforms by

$$W_{fg}(\Omega) = \lim_{T\to\infty} \frac{< \tilde{f}_T(\Omega)\tilde{g}_T(-\Omega) >}{T} \tag{25}$$

Strictly speaking, the relations that make the Fourier transform useful (transformation of differential operators) do not hold so long as the object of the transform is finite at the limits of integration; for example, the derivative transforms as

$$\int_{\frac{-T}{2}}^{\frac{+T}{2}} dt\, \frac{df}{dt} e^{-j\omega t} = f(t)e^{-j\omega t}\Big|_{\frac{-T}{2}}^{\frac{T}{2}} + j\omega\tilde{f}_T(\omega) \tag{26}$$

However, the first term on the right in (26) (and others like it) drop out after ensemble averaging and dividing by T in (25). Therefore, we will continue to use properties of infinite-domain transforms with the understanding that at some point down the line, we will perform the average and limit of equation (25). Questions of validity and existence aside, we can calculate the spectra of the Langevin sources in (19)-(22) directly from (24). They are

$$W_{\Delta\Delta}(\Omega) = W_{\Phi\Phi}(\Omega) = \frac{1}{2pV^2}\sum_i \eta_i g_i \Gamma_i V_i \tag{27}$$

$$W_{\Xi_i \Xi_j}(\Omega) = \frac{2}{V_i}\left[\frac{n_i}{\tau_s} + \eta_i g_i \Gamma_i p\right]\delta_{ij} \tag{28}$$

$$W_{\Xi_i\Delta}(\Omega) = W_{\Delta\Xi_i}(\Omega) = -\frac{g_i\Gamma_i}{2V}(2\eta_i - 1) \tag{29}$$

All spectra of Langevin sources are white; all other spectra between sources are zero.

7.4 Fluctuation Spectra

A. General Formulas

At this point, we insert our appropriately normalized Langevin sources into the driving term of the small-signal equations, that is, the right side of (11). In the absence of external modulation ($\tilde{e}_i \equiv 0$), the result is

$$\begin{pmatrix} j\Omega & -g'_{1\mathrm{eff}} & \cdots & -g'_{N\mathrm{eff}} \\ 0 & \alpha_{1\mathrm{eff}}g'_{1\mathrm{eff}} & \cdots & \alpha_{N\mathrm{eff}}g'_{N\mathrm{eff}} \\ \dfrac{\omega^2_{1\mathrm{eff}}}{g'_{1\mathrm{eff}}} & c_{11}+d_1 & \cdots & c_{N1} \\ \vdots & \vdots & & \vdots \\ \dfrac{\omega^2_{N\mathrm{eff}}}{g'_{N\mathrm{eff}}} & c_{N1} & \cdots & c_{NN}+d_N \end{pmatrix} \begin{pmatrix} \tilde{p} \\ \Delta\tilde{\omega} \\ \tilde{\nu}_1 \\ \vdots \\ \tilde{\nu}_N \end{pmatrix} = \begin{pmatrix} \tilde{\Delta} \\ \tilde{\Phi} \\ \tilde{\Xi}_1 \\ \vdots \\ \tilde{\Xi}_N \end{pmatrix} \tag{30}$$

recognizing, as we said, that the transforms exist only for finite intervals. Now the formulation is complete; by inverting equation (30), we can write each response $\{\tilde{p}, \Delta\tilde{\omega}, \tilde{\nu}_i\}$ as a linear combination of the Langevin sources $\{\tilde{\Delta}, \tilde{\Phi}, \tilde{\Xi}_i\}$, and consequently write spectral functions of the response elements (e.g. $W_{pp}(\Omega)$) as linear combinations of the previously defined spectra of the Langevin sources (e.g. $W_{\Delta\Delta}$).

Equation (30) can be solved using Cramer's rule, yielding

$$\tilde{\rho}(\Omega) = \frac{\begin{vmatrix} \tilde{\Delta} & -g'_{1\mathrm{eff}} & \cdots & -g'_{N\mathrm{eff}} \\ \tilde{\Xi}_1 & c_{11}+d_1 & \cdots & c_{1N} \\ \vdots & \vdots & & \vdots \\ \tilde{\Xi}_N & c_{N1} & \cdots & c_{NN}+d_N \end{vmatrix}}{\begin{vmatrix} j\Omega & -g'_{1\mathrm{eff}} & \cdots & -g'_{N\mathrm{eff}} \\ \frac{\omega^2_{1\mathrm{eff}}}{g'_{1\mathrm{eff}}} & c_{11}+d_1 & \cdots & c_{1N} \\ \vdots & \vdots & & \vdots \\ \frac{\omega^2_{N\mathrm{eff}}}{g'_{N\mathrm{eff}}} & c_{N1} & \cdots & c_{NN}+d_N \end{vmatrix}} \tag{31}$$

$$\Delta\tilde{\omega} = \frac{\begin{vmatrix} j\Omega & \tilde{\Delta} & -g'_{1\mathrm{eff}} & \cdots & -g'_{N\mathrm{eff}} \\ 0 & \tilde{\Phi} & \alpha_{1\mathrm{eff}}g'_{1\mathrm{eff}} & \cdots & \alpha_{N\mathrm{eff}}g'_{N\mathrm{eff}} \\ \frac{\omega^2_{1\mathrm{eff}}}{g'_{1\mathrm{eff}}} & \tilde{\Xi}_1 & c_{11}+d_1 & \cdots & c_{1N} \\ \vdots & \vdots & \vdots & & \vdots \\ \frac{\omega^2_{N\mathrm{eff}}}{g'_{N\mathrm{eff}}} & \tilde{\Xi}_N & c_{N1} & \cdots & c_{NN}+d_N \end{vmatrix}}{\begin{vmatrix} j\Omega & -g'_{1\mathrm{eff}} & \cdots & -g'_{N\mathrm{eff}} \\ \frac{\omega^2_{1\mathrm{eff}}}{g'_{1\mathrm{eff}}} & c_{11}+d_1 & \cdots & c_{1N} \\ \vdots & \vdots & & \vdots \\ \frac{\omega^2_{N\mathrm{eff}}}{g'_{N\mathrm{eff}}} & c_{N1} & \cdots & c_{NN}+d_N \end{vmatrix}} \tag{32}$$

$$\tilde{\nu}_i = \frac{\begin{vmatrix} j\Omega & -g'_{1\mathrm{eff}} & \cdots & -g'_{(i-1)\mathrm{eff}} & \tilde{\Delta} & \cdots & -g'_{N\mathrm{eff}} \\ \frac{\omega^2_{1\mathrm{eff}}}{g'_{1\mathrm{eff}}} & c_{11}+d_1 & \cdots & c_{1(i-1)} & \tilde{\Xi}_i & \cdots & c_{1N} \\ \vdots & \vdots & & \vdots & \vdots & & \vdots \\ \frac{\omega^2_{N\mathrm{eff}}}{g'_{N\mathrm{eff}}} & d_{N1} & \cdots & c_{N(i-1)} & \tilde{\Xi}_N & \cdots & c_{NN}+d_N \end{vmatrix}}{\begin{vmatrix} j\Omega & -g'_{1\mathrm{eff}} & \cdots & -g'_{N\mathrm{eff}} \\ \frac{\omega^2_{1\mathrm{eff}}}{g'_{1\mathrm{eff}}} & c_{11}+d_1 & \cdots & c_{1N} \\ \vdots & \vdots & & \vdots \\ \frac{\omega^2_{N\mathrm{eff}}}{g'_{N\mathrm{eff}}} & c_{N1} & \cdots & c_{NN}+d_N \end{vmatrix}} \tag{33}$$

So, a spectral term $W_{fg}(\Omega)$ is given by

$$W_{fg}(\Omega) = \lim_{T\to\infty} \frac{<\tilde{f}(\Omega)\tilde{g}(-\Omega)>}{T} \tag{34}$$

and we can produce this by multiplying the expressions for $\tilde{f}(\Omega)$ and $\tilde{g}(-\Omega)$

together and replacing each product of Langevin sources (e.g., $\tilde{\Delta}\tilde{\Delta}$) by the associated spectral quantity (e.g., $W_{\Delta\Delta}$). In this manner one can produce any desired spectral quantity. We shall not carry this process out in full generality (although the prescription is here for anyone so inclined). Instead, we shall spend the rest of this chapter deriving spectra for some specific devices of interest.

B. Single-Element Fabry-Perot Laser

To begin to get a feel for how to use equations (27)-(29) and (31)-(33) to calculate spectra, let us first rederive the noise spectra for a single-element, simple two-mirror resonator. As pointed out previously, the term c_{11} can be absorbed into $1/\tau_1$, so that when we evaluate (31) and (32) we get

$$\tilde{\rho}(\Omega) = \frac{\left(j\Omega + 1/\tau_1\right)\tilde{\Delta} + g'_{1\mathrm{eff}}\tilde{\Xi}_1}{\omega_{1\mathrm{eff}}^2 - \Omega^2 + j\Omega/\tau_1} \tag{35}$$

$$\Delta\tilde{\omega}(\Omega) = \tilde{\Phi} + \alpha_{1\mathrm{eff}}\frac{\omega_{1\mathrm{eff}}^2\tilde{\Delta} - j\Omega\, g'_{1\mathrm{eff}}\tilde{\Xi}_1}{\omega_{1\mathrm{eff}}^2 - \Omega^2 + j\Omega/\tau_1} \tag{36}$$

which leads to the relative intensity spectrum

$$W_{\rho\rho}(\Omega) = \frac{(\Omega^2 + 1/\tau_1^2)W_{\Delta\Delta} + 2g'_{1\mathrm{eff}}W_{\Delta\Xi_1}/\tau_1 + {g'_{1\mathrm{eff}}}^2 W_{\Xi_1\Xi_1}}{(\omega_{1\mathrm{eff}}^2 - \Omega^2)^2 + \Omega^2/\tau_1^2} \tag{37}$$

and the frequency fluctuation spectrum

$$W_{\omega\omega}(\Omega) = W_{\Phi\Phi} + \alpha_{1\mathrm{eff}}^2 \frac{\omega_{1\mathrm{eff}}^4 W_{\Delta\Delta} + \Omega^2 {g'_{1\mathrm{eff}}}^2 W_{\Xi_1\Xi_1}}{(\omega_{1\mathrm{eff}}^2 - \Omega^2)^2 + \Omega^2/\tau_1^2} \tag{38}$$

Now we substitute in the normalizations for the Langevin sources:

$$W_{\rho\rho}(\Omega) =$$

$$\frac{1}{2pV}\frac{(\Omega^2 + 1/\tau_1^2)\left[\eta_1 g_1 \Gamma_1 \frac{V_1}{V}\right] + 4g'_{1\mathrm{eff}}p\frac{V}{V_1}\left[\frac{n_1}{\tau_s} + \eta_1 g_1 \Gamma_1 P\right] - (2\eta_1 - 1)\omega_{1\mathrm{eff}}^2/\tau_1}{(\omega_{1\mathrm{eff}}^2 - \Omega^2)^2 + \Omega^2/\tau_1^2} \tag{39}$$

$$W_{\omega\omega}(\Omega) = \frac{\eta_1 g_1 \Gamma_1}{2pV}\left[1 + \alpha_{1\mathrm{eff}}^2 \frac{\omega_{1\mathrm{eff}}^4}{(\omega_{1\mathrm{eff}}^2 - \Omega^2)^2 + \Omega^2/\tau_1^2}\right]$$

$$+ \frac{2}{V}\frac{\alpha_{1\mathrm{eff}}^2 \Omega^2 {g'_{1\mathrm{eff}}}^2 \left[\frac{n_1}{\tau_s} + \eta_1 g_1 \Gamma_1 p\right]}{(\omega_{1\mathrm{eff}}^2 - \Omega^2)^2 + \Omega^2/\tau_1^2} \tag{40}$$

We recognize the above as the relative intensity and frequency fluctuation spectrum of a simple single-cavity, two-mirror laser [16]. Of particular interest is the contribution of the frequency fluctuation spectrum to the linewidth. If amplitude fluctuations are negligible or suppressed in measurement, then the field spectrum $W_\varepsilon(\omega_0+\omega)$ (where ω is the deviation from the lasing frequency ω_0) is [17]

$$W_\varepsilon(\omega+\omega_0) = \frac{1}{2}E_0^2 \operatorname{Re}\int_{-\infty}^{+\infty} d\tau e^{-j\omega\tau} \exp\left[\frac{-\tau^2}{2\pi}\int_0 d\Omega\, W_{\omega\omega}(\Omega)\left(\frac{\sin\Omega\tau/2}{\Omega\tau/2}\right)^2\right] \qquad (41)$$

in which E_0 is the field amplitude. If $W_{\omega\omega}$ is a sum of several components, then the field spectrum is the convolution of the spectrum computed individually from each of the components. While high-frequency structure in the spectrum of $W_{\omega\omega}$ is responsible for structure in the field spectrum (e.g., sidebands at the relaxation resonance [16]), the dominant contribution to linewidth comes from the $\Omega = 0$ component of $W_{\omega\omega}$. It in fact produces a Lorentzian with linewidth equal to $W_{\omega\omega}(0)$ [17]. Examination of equation (40) shows that the linewidth of a single-element laser is

$$W_{\omega\omega}(0) = \frac{\eta_1 g_1 \Gamma_1}{2pV}(1+\alpha_{1\text{eff}}^2) \qquad (42)$$

that is, the enhanced modified Schawlow-Townes linewidth [9]. To calculate $\alpha_{1\text{eff}}$, we recall that the dispersion equation for a single-element, two-mirror laser is

$$F(\omega,n_1) \equiv \frac{1}{R^2}\exp\left[(\gamma_1(n_1)-\gamma_0)L_1 - \frac{2j\omega\mu_1(n_1)L_1}{c}\right] - 1 = 0 \qquad (43)$$

where $\gamma_1(n_1)$ is the power gain per unit length, γ_0 is the loss, L_1 is the length of the laser, $\mu_1(n_1)$ is the index of refraction, and R is the mirror reflectivity. Applying relations (8) and (10) to (43), we get

$$g'_{1\text{eff}} = \frac{\gamma'_1 c}{2\mu_1}, \quad m'_{1\text{eff}} = \frac{\omega\mu'_1}{\mu_1}, \quad \alpha_{1\text{eff}} = \frac{2\omega\mu'_1}{\gamma'_1 c} \qquad (44)$$

where a prime on a material parameter denotes differentiation with respect to the carrier density. So, for this configuration, the effective modulation quantities are equal to the material modulation quantities, which is in fact what we expect from the conventional theory.

C. Passive-Active Coupled Cavity

The above situation (effective parameters=material parameters) does not always hold, even for single-active-element cavities. The addition of a passive element to the resonator (e.g., an external cavity) changes the dispersion equation, and consequently alters the effective modulation parameters; their values end up depending upon the relative tuning of the two cavities. We shall now treat the case of an active element coupled to a passive cavity, illustrated in figure 7.1. Two cavities of length L_1 and L_2 are coupled via an effective mirror (e.g. an air gap; the length of the gap may be zero as long as the discontinuity remains) with transmission and reflection coefficients T_2 and R_2, respectively. (In all calculations and graphs that follow, we will assume the following material parameters: loss $\gamma_0 = 80\ \mathrm{cm}^{-1}$, nonresonant refractive index $\mu_{\mathrm{GaAs}} = 3.5$, and linewidth enhancement factor $\alpha_{\mathrm{GaAs}} = -5$.) The resonance condition is determined by requiring that the field reproduce itself after one round trip through the composite structure. Following the approach of Henry [26], we find that the field E'_1 at the coupler results from reflection of E_1 and transmission of E_2;

$$E'_1 = R_2E_1 + T_2E_1 \tag{45}$$

while the round trip through cavity 1 results in

$$E_1 = R_1\exp\Big[(\gamma_1-\gamma_0)L_1 - 2j\omega\mu_1L_1/c\Big]E'_1 \tag{46}$$

A similar pair of equations holds for E'_2 and E_2. To minimize the algebra, let us define

$$\varphi_1(\omega,n_1) \equiv -(\gamma_1-\gamma_0)L_1 + 2j\omega\mu_1L_1/c - \ln R_1R_2, \qquad \varphi_2(\omega) \equiv 2j\omega\mu_2L_2/c - \ln R_3R_2$$

$$K^{1/2} \equiv \frac{T_2}{R_2} \tag{47}$$

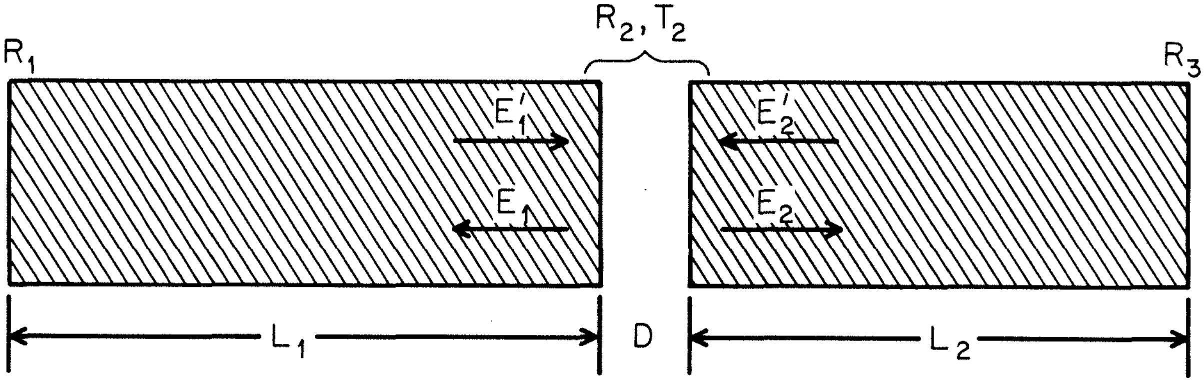

Figure 7.1: Schematic of a longitudinally coupled-cavity laser. Cavity 2 may be either passive or active. E'_1 and E'_2 are the fields incident upon a gap of width D. L_1 and L_2 are the lengths of cavities 1 and 2, respectively.

Then equations (45) and (46) and their companion equations for cavity 2 yield

$$\left[e^{\varphi_1} - 1\right]E_1 = K^{1/2}E_2, \qquad \left[e^{\varphi_2} - 1\right]E_2 = K^{1/2}E_1 \tag{48}$$

Eliminating the field variables yields the dispersion equation

$$F(\omega, n_1) \equiv \left[e^{\varphi_1} - 1\right]\left[e^{\varphi_2} - 1\right] - K = 0 \tag{49}$$

If the gain per unit length is not too large, then it is a good approximation to take the photon density in the *i*th cavity as proportional to $|E_i|^2$. (More exact results can be obtained by integrating the fields in each cavity, but in the interest of obtaining maximum information for minimum algebra, we shall use the approximate results.) Manipulation of (48) gives the fill factor

$$\Gamma_1 = \frac{\left|e^{\varphi_1} - 1\right|(L_1 + L_2)}{\left|e^{\varphi_1} - 1\right|L_2 + \left|e^{\varphi_2} - 1\right|L_1} \tag{50}$$

The effective modulation quantities $g'_{1\mathrm{eff}}$, $m'_{1\mathrm{eff}}$, and $\alpha_{1\mathrm{eff}}$ are determined by equations (18) in terms of partial derivatives of (49), evaluated at the operating point. Unfortunately, (49) is a transcendental equation that must be solved numerically. We can find approximate solutions for weak coupling between the cavities, however, (that is, $K \ll 1$) by doing a perturbation series in K.

For small coupling, we can treat the passive resonator as providing a frequency-dependent load on the other; we expand ω in a perturbation series

$$\omega \equiv \omega_0 + \omega_1 + O(K^2) \tag{51}$$

where ω_1 is $O(K)$. The zeroth order equation is

$$\left[e^{\varphi_1(\omega_0)} - 1\right]\left[e^{\varphi_2(\omega_0)} - 1\right] = 0 \tag{52}$$

If cavity 2 posesses no gain, then the right bracket of (52) cannot be zero near threshold. Thus, we take the left bracket equal to zero.

$$\left[e^{\varphi_1(\omega_0)} - 1\right] = 0 \quad \rightarrow \quad \omega_0 = \frac{c}{\mu_1 L_1}\left\{k\pi + \frac{1}{2j}\left[(\gamma_1 - \gamma_0)L_1 + \ln R_1 R_2\right]\right\} \tag{53}$$

where k is an arbitrary integer, chosen such that ω_0 is close to the peak of the gain spectrum. The next order of the perturbation sequence is

$$\omega_1 = K\frac{c}{\mu_1 L_1}\left[e^{\varphi_2(\omega_0)} - 1\right]^{-1} \tag{54}$$

ω_1 represents the effect of the detuned loading upon the resonance ω_0. The imaginary part of ω_1 changes the threshold gain and provides gain selectivity between modes, while the real part pulls the resonance frequency. Explicitly evaluating $\varphi_2(\omega_0)$, we find

$$\varphi_2(\omega_0) = \frac{\mu_2 L_2}{\mu_1 L_1}2jk\pi + \frac{\mu_2 L_2}{\mu_1 L_1}(\gamma_1 - \gamma_0)L_1 + \frac{\mu_2 L_2}{\mu_1 L_1}\ln R_1 R_2 - \ln R_2 R_3 \tag{55}$$

We use the expression for ω_0 and ω_1 with equation (51) to formulate a new, approximate dispersion equation:

$$F(\omega, n_1) \equiv \omega - \frac{c}{\mu_1 L_1}\left\{k\pi + \frac{(\gamma_1 - \gamma_0)L_1 + \ln R_1 R_2}{2j} + \frac{K}{2j}\left[e^{\varphi_2(\omega_0)} - 1\right]^{-1}\right\} = 0 \tag{56}$$

Now we can use this approximate equation to find the steady-state lasing frequency $\overline{\omega}$ and threshold gain $\gamma_1(n_{1th})$, and subsequently the effective modulation parameters g'_{1eff}, m'_{1eff}, and α_{1eff} to order K.

$$\overline{\omega} = \frac{c}{\mu_1 L_1}\left\{k\pi + \frac{1}{2}\mathrm{Im}\frac{K}{\left[e^{\varphi_2(\omega_0)} - 1\right]}\right\} \tag{57}$$

$$\gamma_1(n_{1th}) = \left[\gamma_0 - \frac{1}{L_1}\ln R_1 R_2\right] - \frac{1}{L_1}\mathrm{Re}\frac{K}{\left[e^{\varphi_2(\omega_0)} - 1\right]} \tag{58}$$

(Since μ_1 depends upon n_{1th}, the way to evaluate (57) and (58) is this: use the zeroth-order part of (58) to calculate n_{1th}, and then use this value to find $\mu_1(n_{1th})$ for use in the first-order equations for $\overline{\omega}$ and γ_1.) In a passive-active resonator, the most conveniently tunable parameter is the length of the passive cavity L_2, so we have plotted the threshold gain and lasing frequency, respective for K=−.4 in figures 7.2 and 7.3 and for K=+.4 in figures 7.4 and 7.5.

The effective modulation parameters are given by equations (8) to be

$$\begin{Bmatrix} g'_{1eff} \\ m'_{1eff} \end{Bmatrix} = \begin{Bmatrix} \mathrm{Im} \\ \mathrm{Re} \end{Bmatrix}\left(\frac{\overline{\omega}\mu'_1}{\mu_1} - \frac{1}{2j}\frac{\gamma'_1 c}{\mu_1}\right)\left[1 + K\frac{\mu_2 L_2}{\mu_1 L_1}\frac{e^{\varphi_2(\omega_0)}}{\left[e^{\varphi_2(\omega_0)} - 1\right]^2}\right] \tag{59}$$

Recall that the material parameters g'_1 and m'_1 were given by

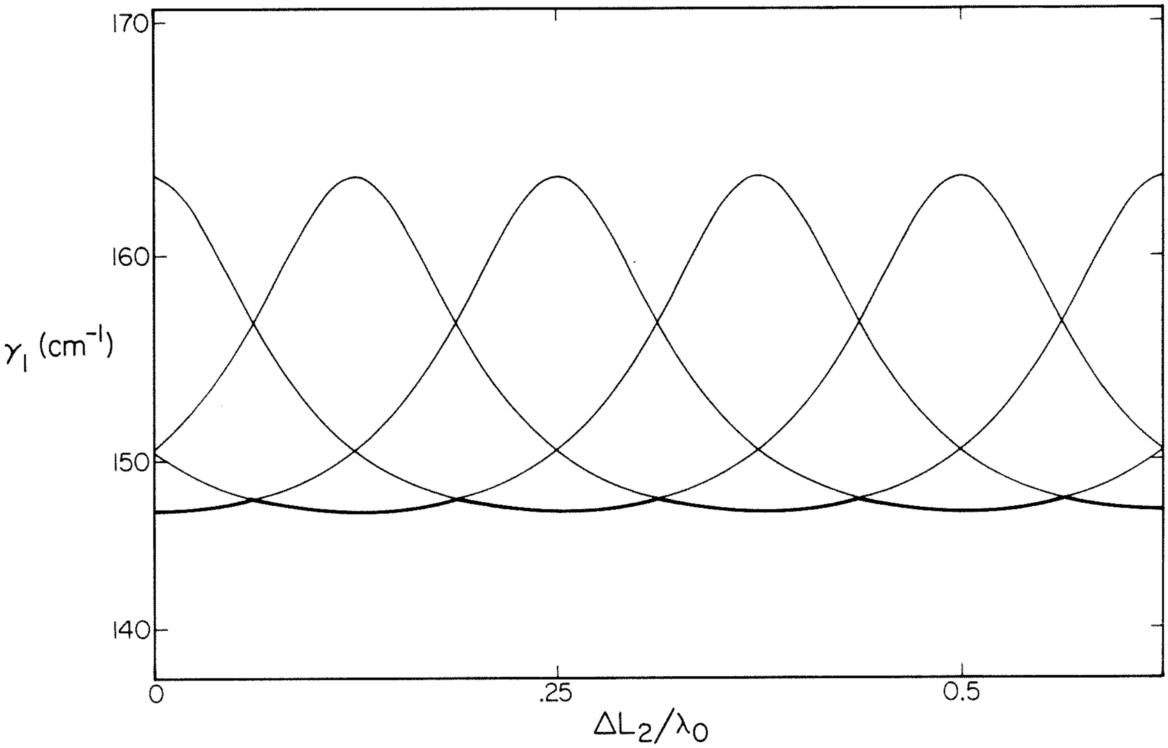

Figure 7.2: Threshold gain for several modes as a function of passive cavity length in a (200 μm$-$175 μm) active-passive laser, with a coupling factor K=$-$.4. Heavy lines indicate the lasing mode, i.e., the mode with the lowest threshold gain.

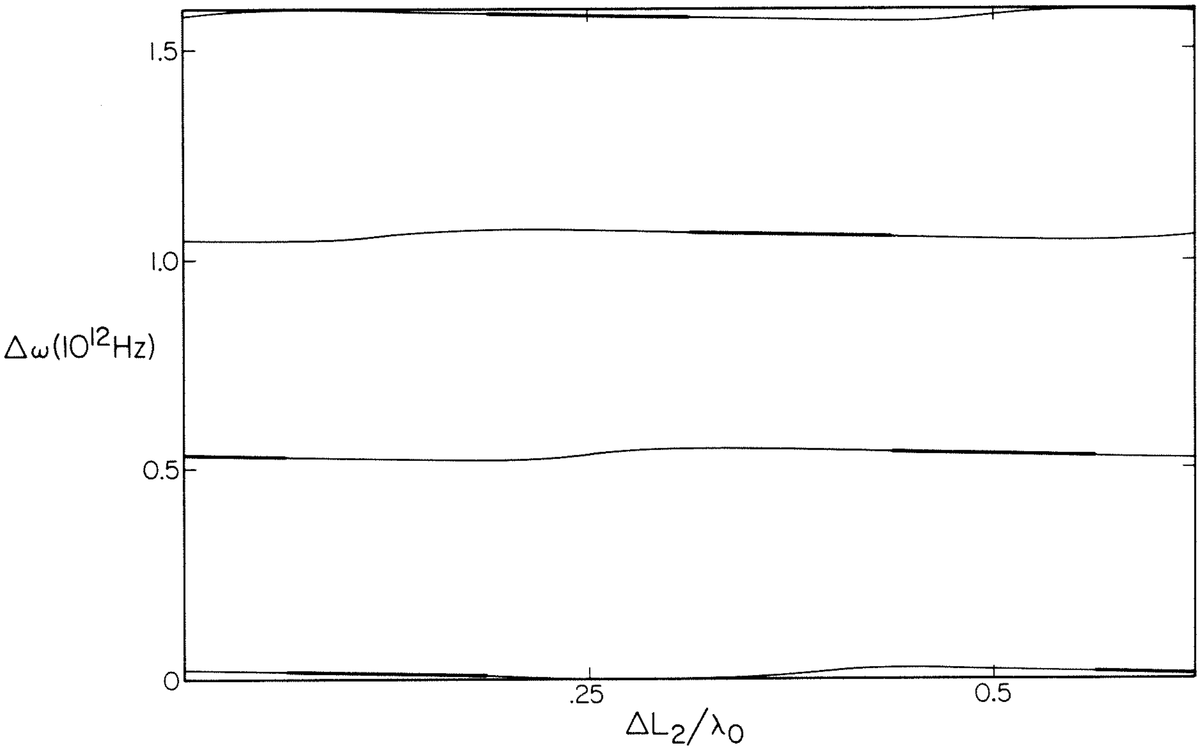

Figure 7.3: Lasing frequency versus cavity length for the device of figure 7.2, showing the effects of frequency pulling on each mode. As in figure 7.2, the heavy line indicates the lasing mode.

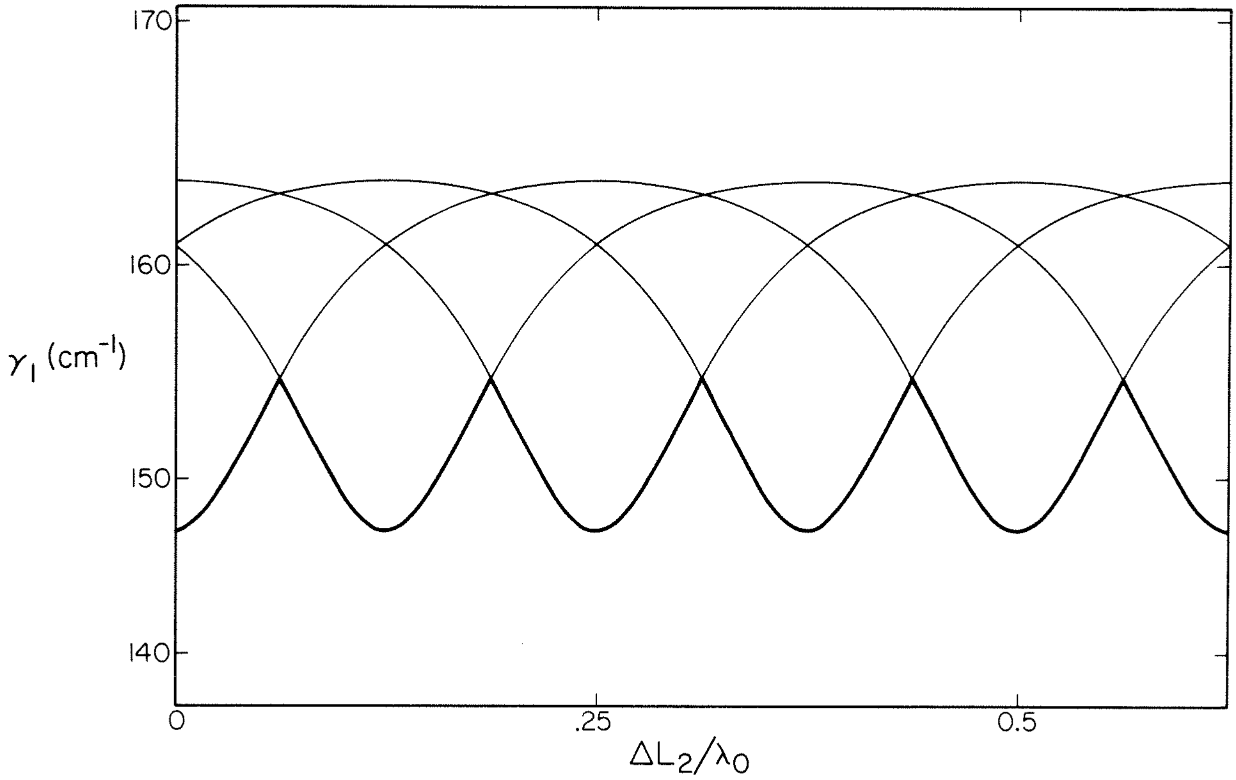

Figure 7.4: Threshold gain for several modes of a passive-active laser with coupling factor K=+.4.

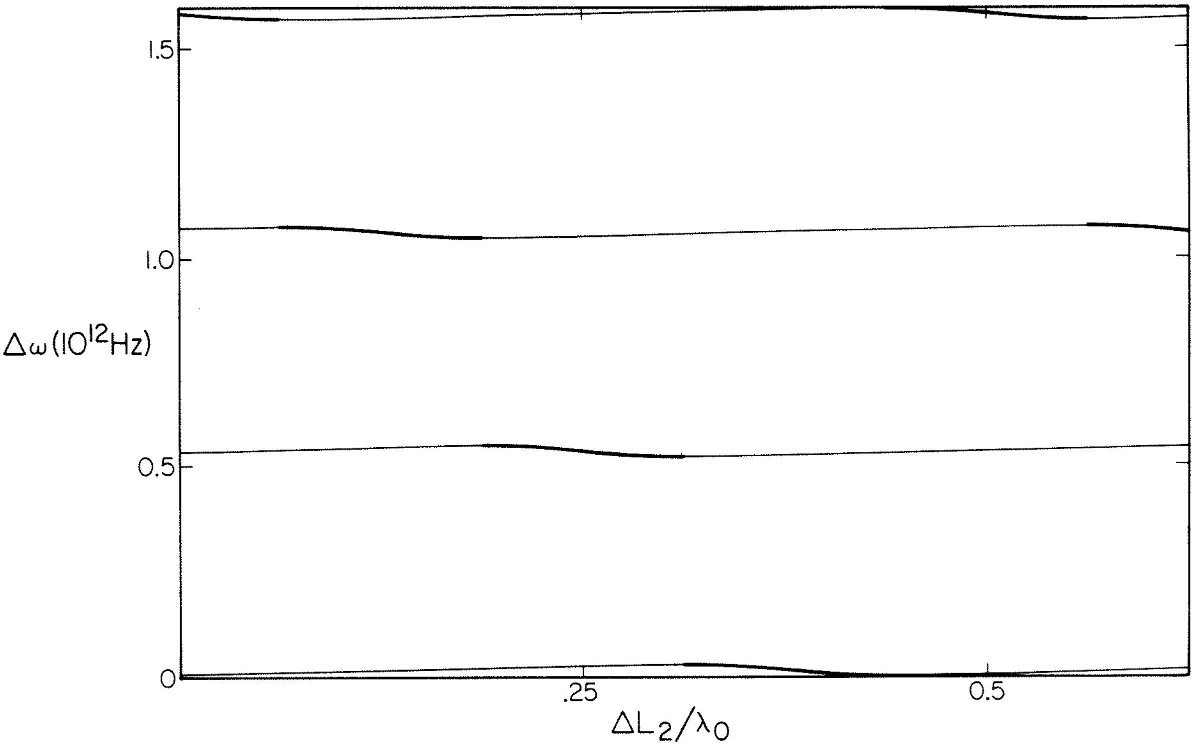

Figure 7.5: Lasing frequency versus cavity length for the device of figure 7.4.

$$g'_1 \equiv \frac{\gamma'_1 c}{2\mu_1}, \quad m'_1 \equiv \frac{\bar{\omega}\mu'_1}{\mu_1} \tag{60}$$

and define the complex quantity

$$\upsilon \equiv K\frac{\mu_2 L_2}{\mu_1 L_1}\frac{e^{\varphi_2(\omega_0)}}{\left[e^{\varphi_2(\omega_0)} - 1\right]^2} \tag{61}$$

Then, denoting real and imaginary parts of υ by an r and i subscript, respectively, the effective modulation parameters are given by

$$g'_{1\mathrm{eff}} = g'_1(1+\upsilon_r) + \upsilon_i m'_1, \quad m'_{1\mathrm{eff}} = m'_1(1+\upsilon_r) - \upsilon_i g'_1 \tag{62}$$

From (62) we see that the effect of the passive cavity is to "mix" the material differential gain and index to produce the effective quantities. For negative imaginary values of υ_i, we get a simultaneous increase in $g'_{1\mathrm{eff}}$ (and related quantities, like the relaxation resonance frequency) and a decrease in $m'_{1\mathrm{eff}}$ (and the phase modulation). In figures 7.6 (K> 0) and 7.7 (K< 0) we plot trajectories of $g'_{1\mathrm{eff}}$ and $m'_{1\mathrm{eff}}$ in the (g',m') plane that illustrate this mixing. The effective α-parameter, which determines the linewidth, can be written in terms of the coupling quantities and the material parameter α_1 as

$$\alpha_{1\mathrm{eff}} \equiv \frac{m'_{1\mathrm{eff}}}{g'_{1\mathrm{eff}}} = \frac{\alpha_1(1+\upsilon_r) - \upsilon_i}{(1+\upsilon_r) + \alpha_1\upsilon_i} \tag{63}$$

In figures 7.8 and 7.9 we plot $\alpha_{1\mathrm{eff}}$ versus L_2 for the same set of parameters as in figures 7.2 and 7.4. It is clear that by varying the tuning of the laser $\alpha_{1\mathrm{eff}}$ can be reduced, and since (with only one active element) equation (42) still applies, the linewidth may be reduced (or increased). A comparison of figures 7.8 and 7.9 shows that the potential for linewidth alteration is much greater for the K> 0 case than for K< 0; conveniently, that is also the case in which the gain selectivity between modes is highest (compare figures 7.2 and 7.4). If the coupling element between the active and passive cavity is lossless (e.g., a single mirror) then K is always negative. We see from figures 7.2 and 7.4, however, that the widest range of variation in $\alpha_{1\mathrm{eff}}$ occurs for K> 0 (which occurs, for example, when the coupling is a gap of half-integral-wavelength spacing [26]). This result then

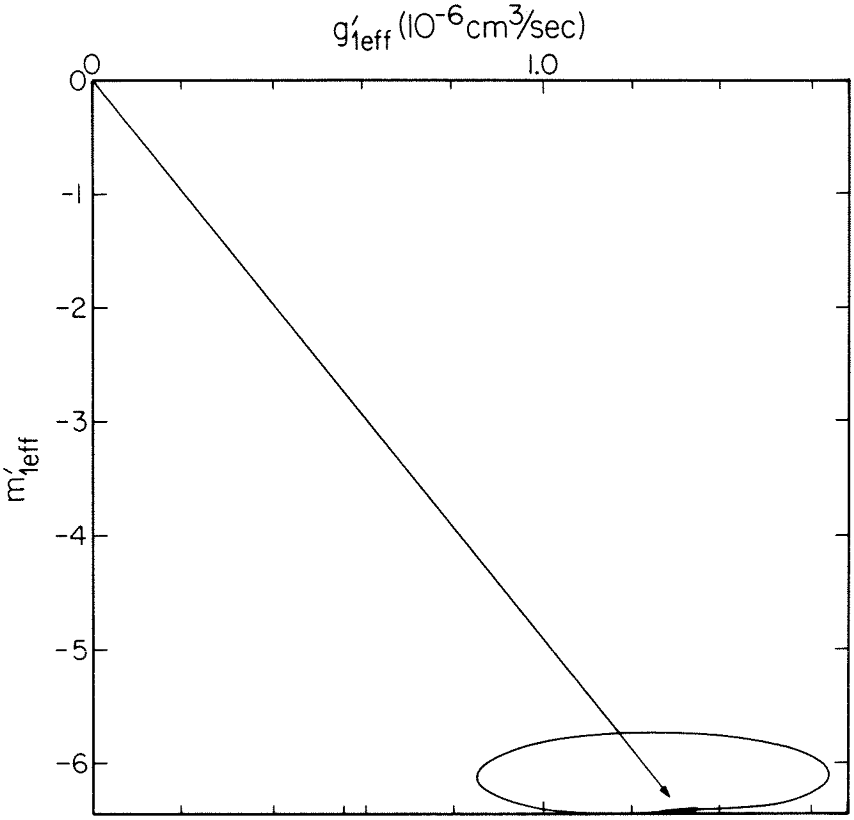

Figure 7.6: Trajectory of $g'_{1\text{eff}}, m'_{1\text{eff}}$ in the g',m' plane for the device of figure 7.2. The slope of a vector from the origin to a point on the tuning curve gives the effective α-parameter. The vector connecting the origin to the point in the interior of the trajectory corresponds to the material quantities g',m'.

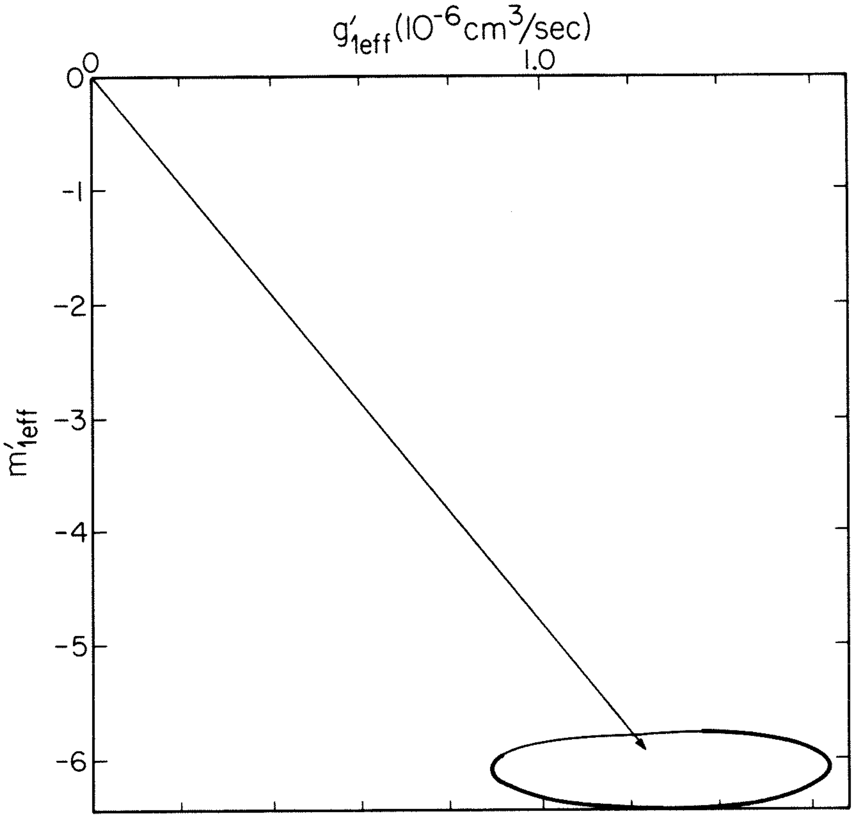

Figure 7.7: Trajectory of g'_{1eff}, m'_{1eff} for the device of figure 7.4.

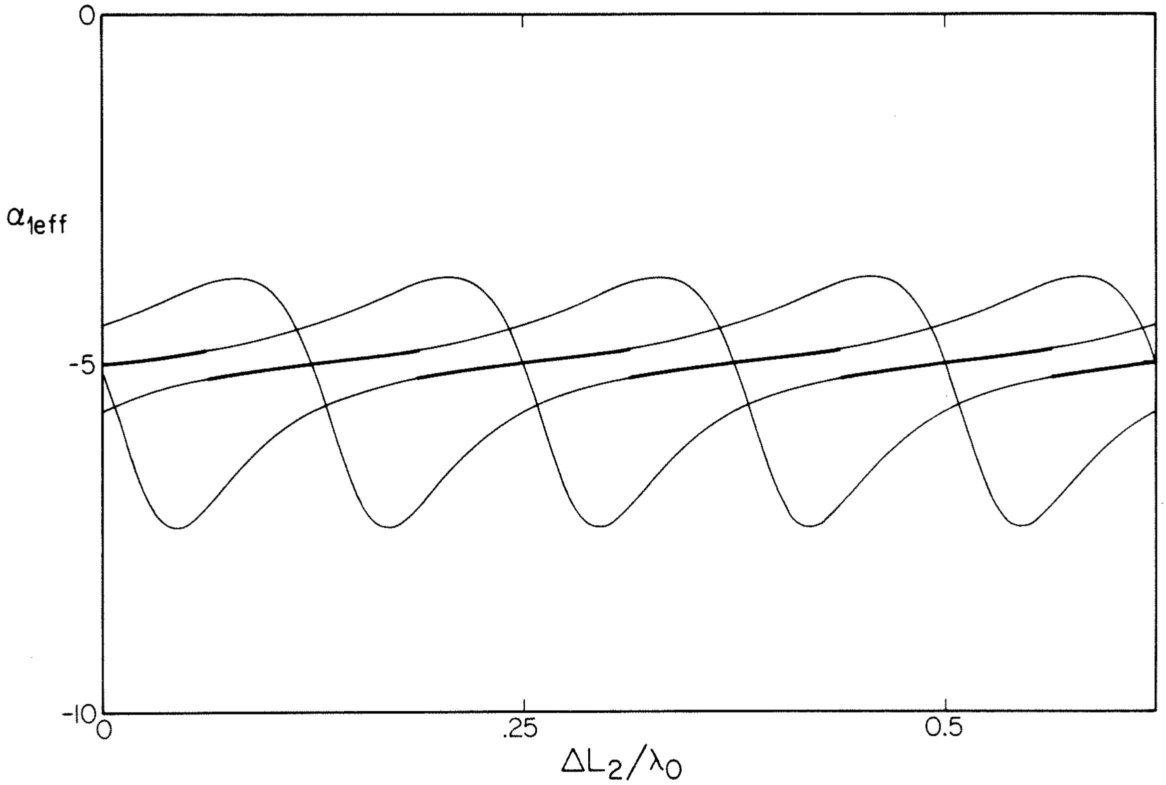

Figure 7.8: Linewidth enhancement factor α_{1eff} versus cavity length for the device of figure 7.2.

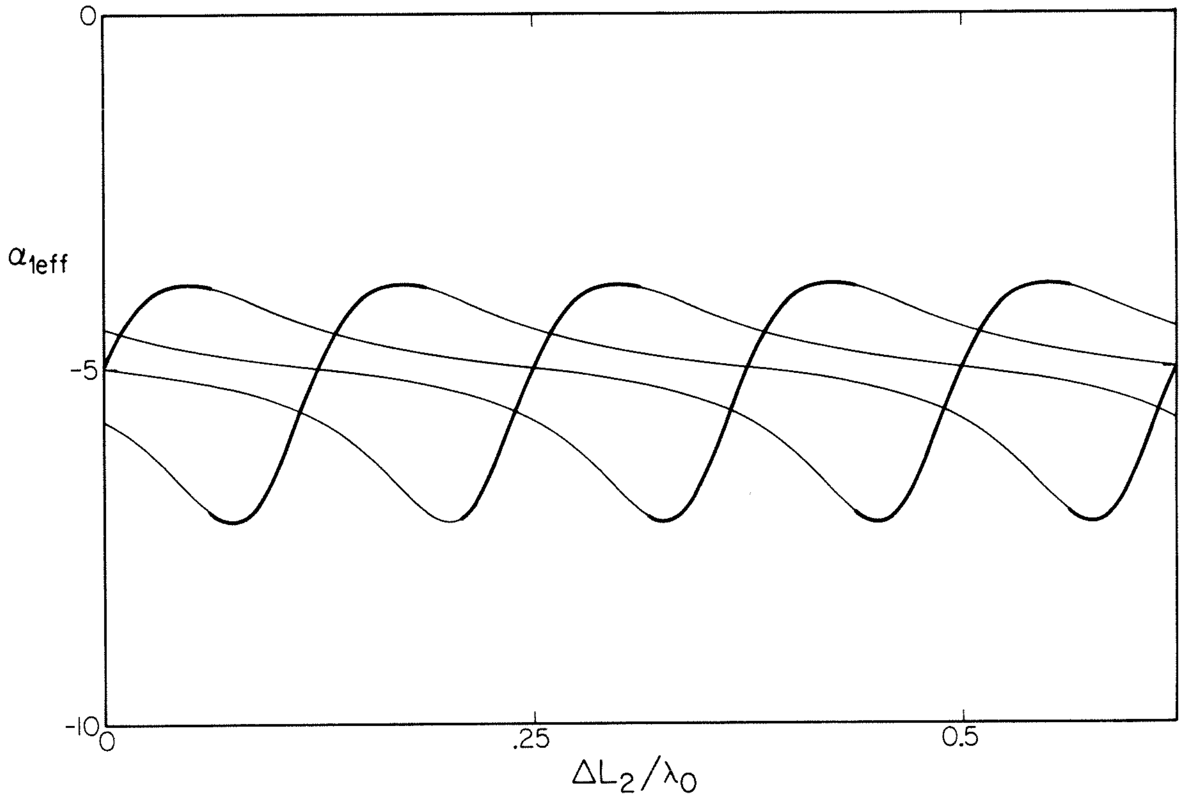

Figure 7.9: Linewidth enhancement factor α_{1eff} for the device of figure 7.4.

suggests that by suitably coating the output facet of a passive-active resonator with a thick, lossy coating, the linewidth could be reduced well below that which is otherwise attainable. It should be noted that such linewidth reduction predicted [15] and subsequently observed [16] by Vahala et al, and was explained in terms of a detuned loading mechanism, where the passive cavity became a frequency-dependent load upon the active one, and our $v_{r,i}$ play the same role as the $\beta_{1,2}$ in their treatment. If the second cavity becomes active, however, then such a description is no longer applicable. The "load" becomes both frequency- and intensity-dependent, and it introduces noise of its own into the system. In the next section, we derive the relative intensity and frequency fluctuation spectra for a general two-active-element laser in terms of the effective modulation parameters, and explicitly evaluate them for a system consisting of two weakly coupled active cavities (e.g., a C^3 laser with a large air gap).

D. Active-Active Coupled Cavity

Let us first restrict ourselves to the case in which the fill factors Γ_i do not change appreciably under modulation; that is, we assume $c_{ij}\tau_i << 1$ for all ij pairs. This assumption will not qualitatively alter the physics, but it cuts down on the algebra considerably and renders the rather formidable expressions for the spectra somewhat more tractable. Then equations (31) and (32) give the responses to the Langevin sources

$$\tilde{\rho}(\Omega) = \frac{\tilde{\Delta} + \frac{g'_{1\mathrm{eff}}}{j\Omega + 1/\tau_1}\tilde{\Xi}_1 + \frac{g'_{2\mathrm{eff}}}{j\Omega + 1/\tau_2}\tilde{\Xi}_2}{j\Omega + \frac{\omega_{1\mathrm{eff}}^2}{j\Omega + 1/\tau_1} + \frac{\omega_{2\mathrm{eff}}^2}{j\Omega + 1/\tau_2}} \tag{64}$$

$$\Delta\tilde{\omega}(\Omega) = \tilde{\Phi} + \tilde{\Delta}\frac{\alpha_{1\mathrm{eff}}\frac{\omega_{1\mathrm{eff}}^2}{j\Omega + 1/\tau_1} + \alpha_{2\mathrm{eff}}\frac{\omega_{2\mathrm{eff}}^2}{j\Omega + 1/\tau_2}}{j\Omega + \frac{\omega_{1\mathrm{eff}}^2}{j\Omega + 1/\tau_1} + \frac{\omega_{2\mathrm{eff}}^2}{j\Omega + 1/\tau_2}}$$

$$
- \tilde{\Xi}_1 \frac{\dfrac{g'_{1\mathrm{eff}}}{j\Omega + 1/\tau_1}\left[j\Omega\, \alpha_{1\mathrm{eff}} + \dfrac{(\alpha_{1\mathrm{eff}} - \alpha_{2\mathrm{eff}})\omega_{2\mathrm{eff}}^2}{j\Omega + 1/\tau_2} \right]}{j\Omega + \dfrac{\omega_{1\mathrm{eff}}^2}{j\Omega + 1/\tau_1} + \dfrac{\omega_{2\mathrm{eff}}^2}{j\Omega + 1/\tau_2}}
- \tilde{\Xi}_2 \frac{\dfrac{g'_{2\mathrm{eff}}}{j\Omega + 1/\tau_2}\left[j\Omega\, \alpha_{2\mathrm{eff}} + \dfrac{(\alpha_{2\mathrm{eff}} - \alpha_{1\mathrm{eff}})\omega_{1\mathrm{eff}}^2}{j\Omega + 1/\tau_1} \right]}{j\Omega + \dfrac{\omega_{1\mathrm{eff}}^2}{j\Omega + 1/\tau_1} + \dfrac{\omega_{2\mathrm{eff}}^2}{j\Omega + 1/\tau_2}}
\tag{65}
$$

The relative intensity and field fluctuation spectra are then

$$
W_{\rho\rho}(\Omega) = \frac{W_{\Delta\Delta} + \dfrac{{g'_{1\mathrm{eff}}}^2 W_{\Xi_1\Xi_1} + (2/\tau_1) g'_{1\mathrm{eff}} W_{\Delta\Xi_1}}{\Omega^2 + 1/\tau_1^2} + \dfrac{{g'_{2\mathrm{eff}}}^2 W_{\Xi_2\Xi_2} + (2/\tau_2) g'_{2\mathrm{eff}} W_{\Delta\Xi_2}}{\Omega^2 + 1/\tau_2^2}}{\left| j\Omega + \dfrac{\omega_{1\mathrm{eff}}^2}{j\Omega + 1/\tau_1} + \dfrac{\omega_{2\mathrm{eff}}^2}{j\Omega + 1/\tau_2} \right|^2}
\tag{66}
$$

$$
\begin{aligned}
W_{\omega\omega}(\Omega) = {} & W_{\Phi\Phi} + W_{\Delta\Delta} \left| \frac{\alpha_{1\mathrm{eff}} \dfrac{\omega_{1\mathrm{eff}}^2}{j\Omega + 1/\tau_1} + \alpha_{2\mathrm{eff}} \dfrac{\omega_{2\mathrm{eff}}^2}{j\Omega + 1/\tau_2}}{j\Omega + \dfrac{\omega_{1\mathrm{eff}}^2}{j\Omega + 1/\tau_1} + \dfrac{\omega_{2\mathrm{eff}}^2}{j\Omega + 1/\tau_2}} \right|^2 \\
& + W_{\Xi_1\Xi_1} \left| \frac{g'_{1\mathrm{eff}}}{j\Omega + 1/\tau_1} \, \frac{\left[j\Omega\, \alpha_{1\mathrm{eff}} + \dfrac{(\alpha_{1\mathrm{eff}} - \alpha_{2\mathrm{eff}})\omega_{2\mathrm{eff}}^2}{j\Omega + 1/\tau_2} \right]}{j\Omega + \dfrac{\omega_{1\mathrm{eff}}^2}{j\Omega + 1/\tau_1} + \dfrac{\omega_{2\mathrm{eff}}^2}{j\Omega + 1/\tau_2}} \right|^2 \\
& + W_{\Xi_2\Xi_2} \left| \frac{g'_{2\mathrm{eff}}}{j\Omega + 1/\tau_2} \, \frac{\left[j\Omega\, \alpha_{2\mathrm{eff}} + \dfrac{(\alpha_{2\mathrm{eff}} - \alpha_{1\mathrm{eff}})\omega_{1\mathrm{eff}}^2}{j\Omega + 1/\tau_1} \right]}{j\Omega + \dfrac{\omega_{1\mathrm{eff}}^2}{j\Omega + 1/\tau_1} + \dfrac{\omega_{2\mathrm{eff}}^2}{j\Omega + 1/\tau_2}} \right|^2 \\
& + 2W_{\Delta\Xi_1} \frac{\mathrm{Re}\left(\alpha_{1\mathrm{eff}} \dfrac{\omega_{1\mathrm{eff}}^2}{j\Omega + 1/\tau_1} + \alpha_{2\mathrm{eff}} \dfrac{\omega_{2\mathrm{eff}}^2}{j\Omega + 1/\tau_2} \right)\left(\dfrac{g'_{1\mathrm{eff}}}{j\Omega + 1/\tau_1} \left[j\Omega\, \alpha_{1\mathrm{eff}} + \dfrac{(\alpha_{1\mathrm{eff}} - \alpha_{2\mathrm{eff}})\omega_{2\mathrm{eff}}^2}{j\Omega + 1/\tau_2} \right] \right)}{\left| j\Omega + \dfrac{\omega_{1\mathrm{eff}}^2}{j\Omega + 1/\tau_1} + \dfrac{\omega_{2\mathrm{eff}}^2}{j\Omega + 1/\tau_2} \right|^2} \\
& + 2W_{\Delta\Xi_2} \frac{\mathrm{Re}\left(\alpha_{2\mathrm{eff}} \dfrac{\omega_{2\mathrm{eff}}^2}{j\Omega + 1/\tau_2} + \alpha_{1\mathrm{eff}} \dfrac{\omega_{1\mathrm{eff}}^2}{j\Omega + 1/\tau_1} \right)\left(\dfrac{g'_{2\mathrm{eff}}}{j\Omega + 1/\tau_2} \left[j\Omega\, \alpha_{1\mathrm{eff}} + \dfrac{(\alpha_{2\mathrm{eff}} - \alpha_{1\mathrm{eff}})\omega_{1\mathrm{eff}}^2}{j\Omega + 1/\tau_1} \right] \right)}{\left| j\Omega + \dfrac{\omega_{1\mathrm{eff}}^2}{j\Omega + 1/\tau_1} + \dfrac{\omega_{2\mathrm{eff}}^2}{j\Omega + 1/\tau_2} \right|^2}
\end{aligned}
\tag{67}
$$

A fundamental quantity of interest is the $\Omega = 0$ component of $W_{\omega\omega}$, since it gives the major contribution to the linewidth. We define for convenience the dimensionless ratios

$$x_1 \equiv \frac{\omega_{1\mathrm{eff}}^2\tau_1}{\omega_{1\mathrm{eff}}^2\tau_1 + \omega_{2\mathrm{eff}}^2\tau_2}, \quad x_2 \equiv \frac{\omega_{2\mathrm{eff}}^2\tau_2}{\omega_{1\mathrm{eff}}^2\tau_1 + \omega_{2\mathrm{eff}}^2\tau_2} \tag{68}$$

and produce from (67)

$$\begin{aligned} W_{\omega\omega}(\Omega=0) &= W_{\Phi\Phi} + W_{\Delta\Delta}(\alpha_{1\mathrm{eff}}x_1 + \alpha_{2\mathrm{eff}}x_2)^2 \\ &+ W_{\Xi_1\Xi_1}[g'_{1\mathrm{eff}}\tau_1(\alpha_{1\mathrm{eff}}-\alpha_{2\mathrm{eff}})x_2]^2 + W_{\Xi_2\Xi_2}[g'_{2\mathrm{eff}}\tau_2(\alpha_{2\mathrm{eff}}-\alpha_{1\mathrm{eff}})x_1]^2 \\ &+ 2W_{\Delta\Xi_1}(\alpha_{1\mathrm{eff}}x_1 + \alpha_{2\mathrm{eff}}x_2)[g'_{1\mathrm{eff}}\tau_1(\alpha_{1\mathrm{eff}}-\alpha_{2\mathrm{eff}})x_2] \\ &+ 2W_{\Delta\Xi_2}(\alpha_{2\mathrm{eff}}x_2 + \alpha_{1\mathrm{eff}}x_1)[g'_{2\mathrm{eff}}\tau_2(\alpha_{2\mathrm{eff}}-\alpha_{1\mathrm{eff}})x_1] \end{aligned} \tag{69}$$

If we also make the assumption that $1/\tau_s << 1/\tau_{1,2}$, that is, that we are well above threshold, then these relations simplify when we insert the normalizations for the Langevin spectra. The cross-correlation terms $W_{\Delta\Xi_1}$ and $W_{\Delta\Xi_2}$ cancel each other out, and we are left with

$$\begin{aligned} W_{\omega\omega}(0) &= \frac{\eta_1 g_1\Gamma_1 V_1 + \eta_2 g_2 \Gamma_2 V_2}{2pV^2}\left[1 + (\alpha_{1\mathrm{eff}}x_1 + \alpha_{2\mathrm{eff}}x_2)^2\right] \\ &+ \frac{\eta_1 g_1 \Gamma_1 V_2 + \eta_2 g_2 \Gamma_2 V_1}{p\Gamma_1\Gamma_2 V_1 V_2} 2x_1x_2\left(\frac{g'_{1\mathrm{eff}}}{g'_1}\right)\left(\frac{g'_{2\mathrm{eff}}}{g'_2}\right)(\alpha_{1\mathrm{eff}}-\alpha_{2\mathrm{eff}})^2 \end{aligned} \tag{70}$$

as the linewidth of a two-active element laser. The first part arises from optical fluctuations; in fact, it looks exactly like the enhanced Schawlow-Townes formula

$$W_{\omega\omega}(0) = \frac{\eta g}{2pV}(1+\alpha^2) \tag{71}$$

where the material parameter α has been replaced by a weighted average of the effective $\alpha_{i\mathrm{eff}}$'s. The second part arises from the $W_{\Xi\Xi}$'s, and represents direct FM due to carrier fluctuations. It is proportional to the square of the difference in the effective α's. Consequently, were we to attempt to utilize detuned loading to change the effective α's and shrink the linewidth, we should not only seek to reduce the effective α's, but at the same time to minimize their difference. Both contributions to the linewidth vary with inverse power. Equation (70) holds for any two-active-element laser--C^3, axially groove-coupled, or laterally coupled cavity. The evaluation of $\alpha_{1\mathrm{eff}}$ and $\alpha_{2\mathrm{eff}}$ depends on the exact configuration, however, so we will now evaluate them for the case of two weakly coupled active cavities. We can adapt some of our results from the passive-active case by making cavity 2 of figure 7.1 an active one, with gain γ_2 and index μ_2 both dependent upon the carrier density n_2 in cavity 2. Equations (49) and (50) remain valid if we redefine

$$\begin{aligned} \varphi_1(\omega) &\equiv -(\gamma_1-\gamma_0)L_1 + 2j\omega\mu_1 L_1/c - \ln R_1R_2, \\ \varphi_2(\omega) &\equiv -(\gamma_2-\gamma_0)L_2 + 2j\omega\mu_2 L_2/c - \ln R_3R_2 \end{aligned} \tag{72}$$

As with the passive-active case, the resonance equation is transcendental. For weak coupling, we can again perform a perturbation series in K, although it is not clear whether our zeroth order equation should be

$$\left[e^{\varphi_1(\omega_0)} - 1\right] = 0 \quad \text{or} \quad \left[e^{\varphi_2(\omega_0)} - 1\right] = 0 \tag{73}$$

For weak coupling, there will be two families of modes, one associated with each of the two equations in (73). So, we will consider only the modes in which cavity 1 is dominant, and cavity 2 assumes the role of the frequency-dependent loss. There is still one degree of freedom left unaccounted for (in a two-element laser, the gain is clamped onto a line in the (γ_1,γ_2)-plane, rather than a point [9]), so we will take γ_2 as the free parameter. If we use the following as the definition of $\varphi_2(\omega_0)$,

$$\varphi_2(\omega_0) = 2j\frac{\mu_2 L_2}{\mu_1 L_1}k\pi - (\gamma_2-\gamma_0)L_2 + \frac{\mu_2 L_2}{\mu_1 L_1}(\gamma_1-\gamma_0)L_1 + \frac{\mu_2 L_2}{\mu_1 L_1}\ln R_1R_2 - \ln R_2R_3 \tag{74}$$

then equations (53)-(54) and (56)-(59) give the correct results for $\overline{\omega}$, $\gamma_1(n_{1th})$, g'_{1eff} and m'_{1eff}. Differentiating (56) with respect to n_2 yields

$$\begin{Bmatrix} g'_{2eff} \\ m'_{2eff} \end{Bmatrix} = \begin{Bmatrix} \mathrm{Im} \\ \mathrm{Re} \end{Bmatrix} \left(\frac{\overline{\omega}\mu'_2}{\mu_2} - \frac{1}{2j}\frac{\gamma'_2 c}{2\mu_2} \right) \left(K\frac{\mu_2 L_2}{\mu_1 L_1} \frac{e^{\varphi_2(\omega_0)}}{\left[e^{\varphi_2(\omega_0)} - 1\right]^2} \right) \tag{75}$$

or, recognizing υ of equation (61) (using the appropriate $\varphi_2(\omega_0)$, of course) and the material quantities

$$g'_2 \equiv \frac{\gamma'_2 c}{2\mu_2}, \qquad m'_2 \equiv \frac{\overline{\omega}\mu'_2}{\mu_2}$$

The effective differential quantities are given by

$$g'_{2\mathrm{eff}} = g'_2 \upsilon_r + m'_2 \upsilon_i, \qquad m'_{2\mathrm{eff}} = m'_2 \upsilon_r - g'_2 \upsilon_i \tag{76}$$

Consequently, the effective linewidth enhancement factors that enter into equation (71) are given by

$$\alpha_{1\mathrm{eff}} = \frac{\alpha_1(1+\upsilon_r) - \upsilon_i}{(1+\upsilon_r) + \alpha_1 \upsilon_i}, \qquad \alpha_{2\mathrm{eff}} = \frac{\alpha_2 \upsilon_r - \upsilon_i}{\upsilon_r + \alpha_2 \upsilon_i} \tag{77}$$

In a two-active-element laser both L_1 and L_2 are fixed, and what varies the tuning is the gain and index γ_2 and μ_2. In figures 7.10-7.13 and 7.14-7.17 we plot the gain, lasing frequency, effective α's and linewidth versus γ_2 for $K=\pm .4$, respectively. A cursory inspection of figure 7.12b and equation (76) shows that it is quite possible for $g'_{2\mathrm{eff}}$ to go to zero, in which case $\alpha_{2\mathrm{eff}} \to \infty$, and the linewidth would seem to diverge as well. However, there are $g'_{2\mathrm{eff}}$-dependent terms in (70) (e.g. x_2) which remove the apparent singularity. In this case, the direct FM contribution to linewidth can be written as

$$W_{\omega\omega}^{FM}(0) = \frac{2}{p}\left(\frac{\eta_1 g_1}{\Gamma_2 V_2} + \frac{\eta_2 g_2}{\Gamma_1 V_1}\right)\left(\frac{g_2}{g_1}\right)\left(\frac{m'_{2\mathrm{eff}}}{m'_2}\right)^2 \alpha_2^2 \tag{78}$$

where α_2 is the material α for cavity 2. The chirp (direct FM under modulation) in an active-active coupled-cavity laser has been shown to be proportional to the difference in effective α's [4]; in equation (70), we showed that there is a component of the linewidth that scales with this difference. Consequently, it would be desirable to reduce both the chirp and linewidth by tuning the α's to be equal. Assuming that the material α's are equal (and denoting them by α devoid of subscript), the difference in the effective α's is given by

$$(\alpha_{1\mathrm{eff}} - \alpha_{2\mathrm{eff}}) = \frac{\alpha(1+\upsilon_r) - \upsilon_i}{(1+\upsilon_r) + \alpha \upsilon_i} - \frac{\alpha \upsilon_r - \upsilon_i}{\upsilon_r + \alpha \upsilon_i} = \frac{\upsilon_i(1+\alpha^2)}{[(1+\upsilon_r) + \alpha \upsilon_i][\upsilon_r + \alpha \upsilon_i]} \tag{79}$$

So when $\upsilon_i = 0$, the cavity is tuned at the chirpless bias point. At that point, however, we see from (77) that $\alpha_{1\mathrm{eff}} = \alpha_{2\mathrm{eff}} = \alpha$, the material linewidth enhancement factor. The upshot of this result is that while we can eliminate chirp in two-active element lasers by selection of bias point, we give up the potential for linewidth reduction using the detuned loading mechanism that was possible with

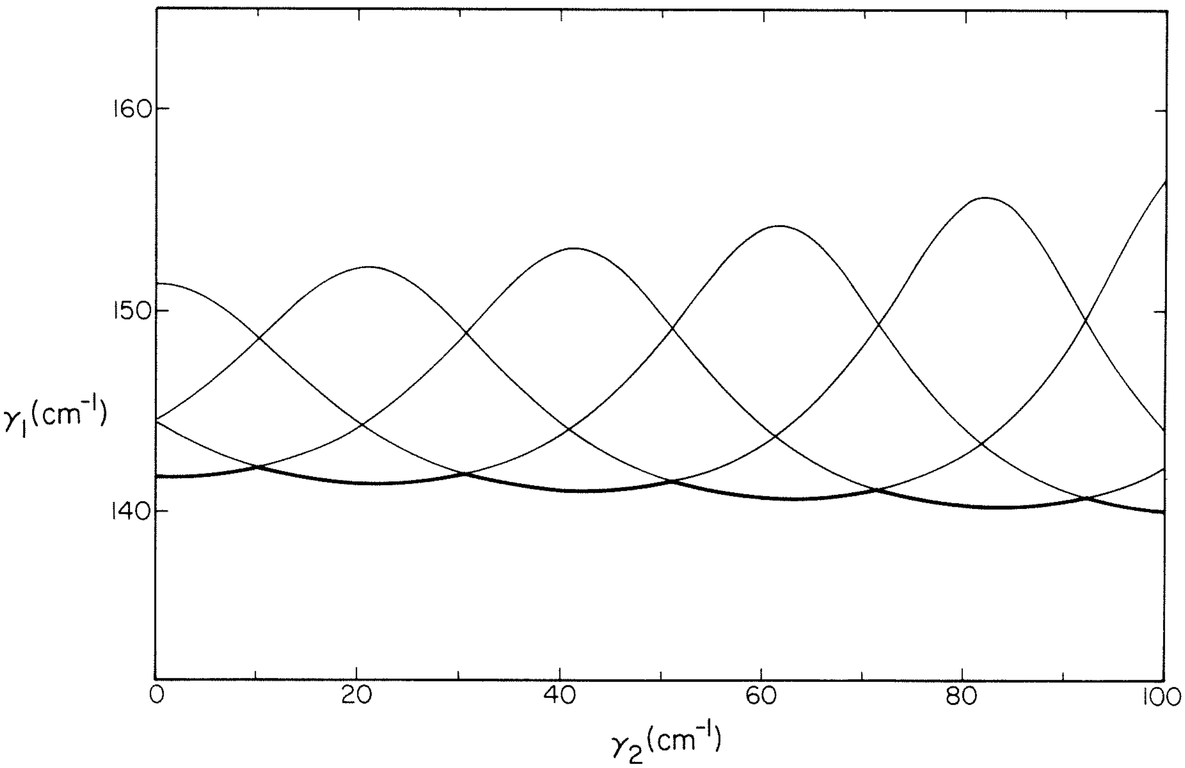

Figure 7.10: Threshold gain for several modes of a (200 μm$-$50 μm) active-active laser versus gain γ_2 in cavity 2, with a coupling factor K=$-$.4.

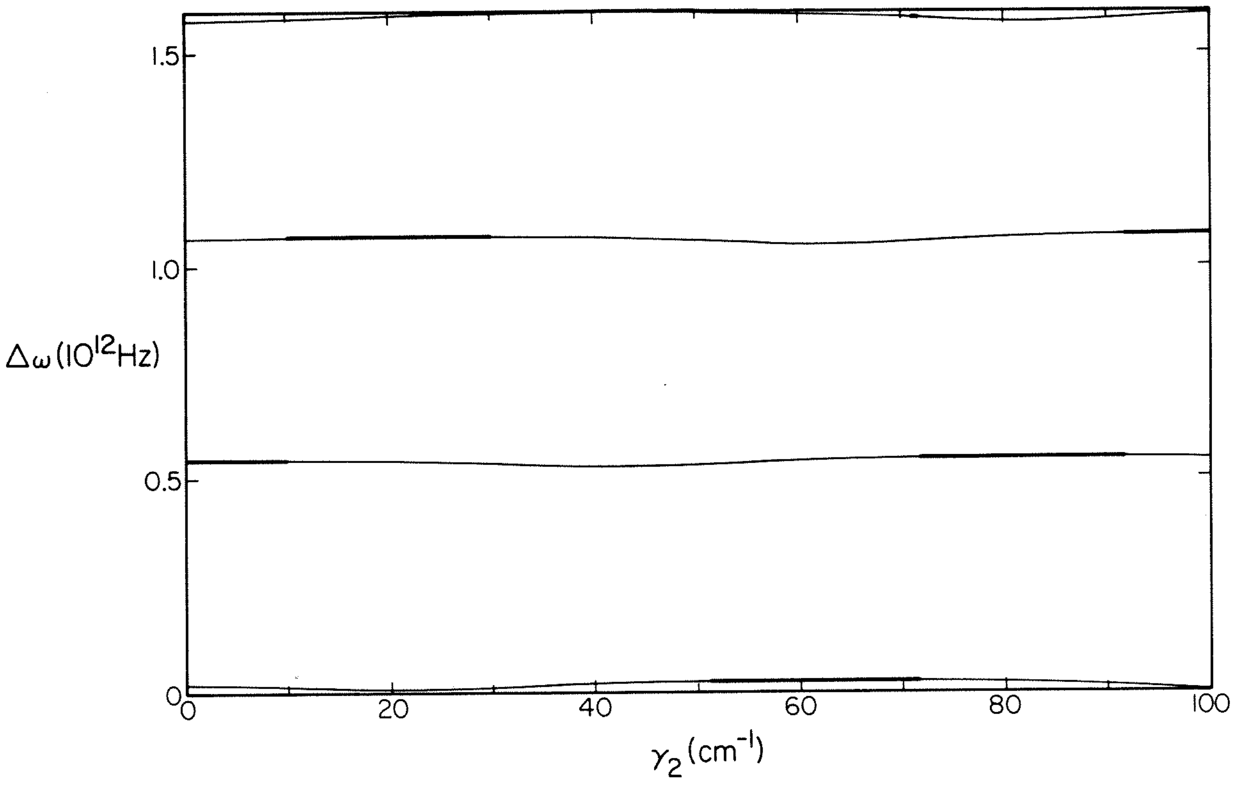

Figure 7.11: Lasing frequency versus γ_2 for the device of figure 7.10.

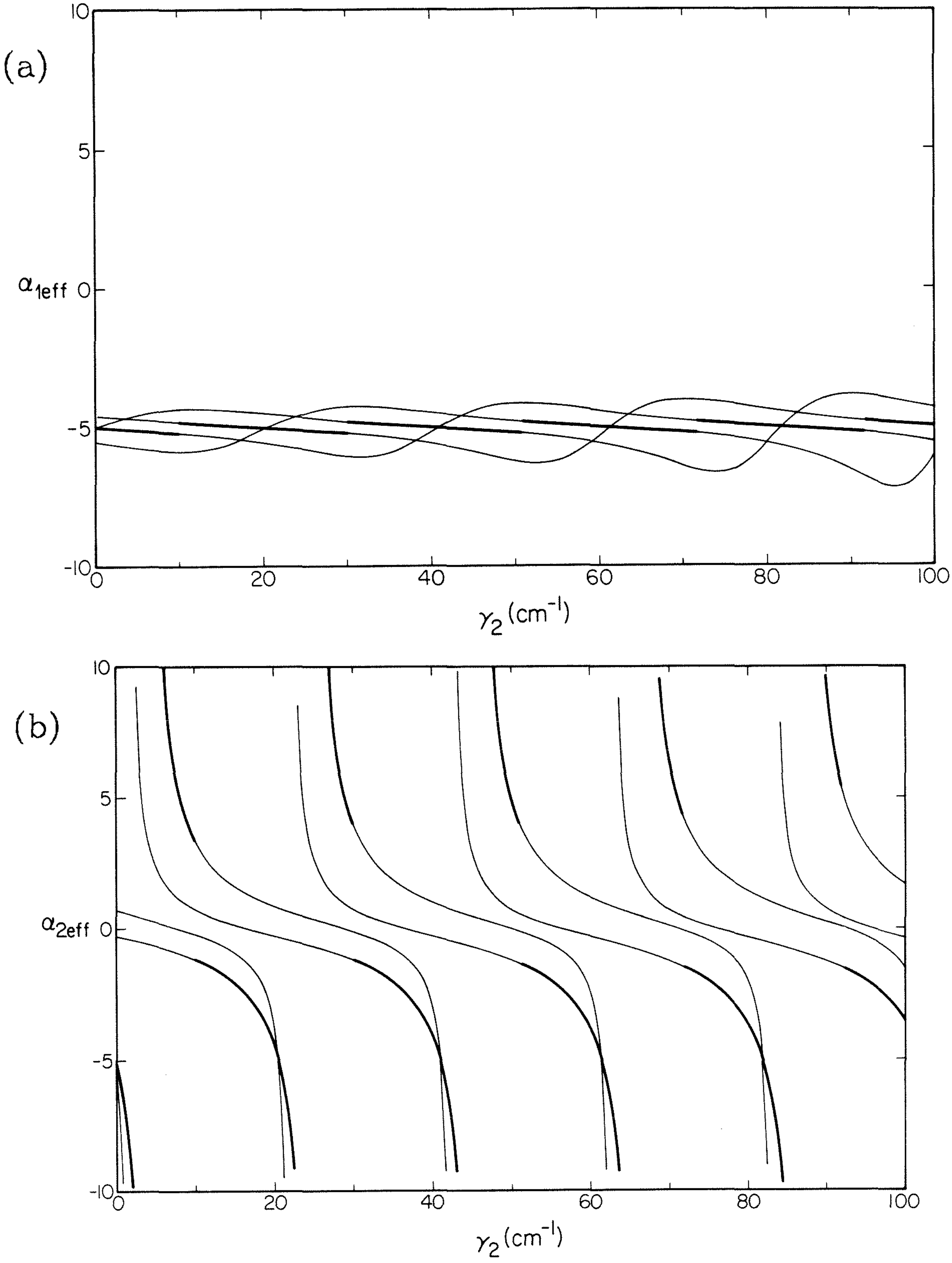

Figure 7.12: Effective α-parameters for the device of figure 7.10. (a) $\alpha_{1\mathrm{eff}}$, (b) $\alpha_{2\mathrm{eff}}$.

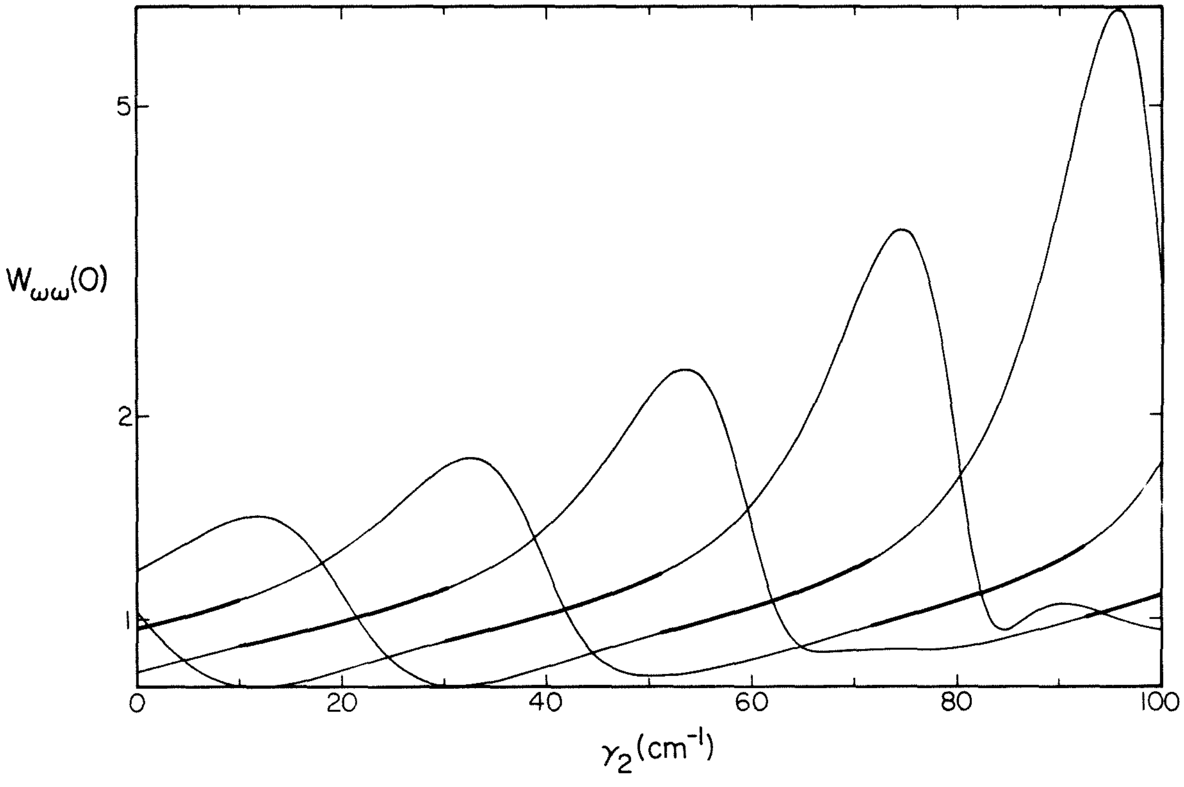

Figure 7.13: Linewidth of the device of figure 7.10 as a function of γ_2 (logarithmic scale) relative to that of a single-element cavity of length 250 μm, reflectivities R_1,R_3 at the end mirrors.

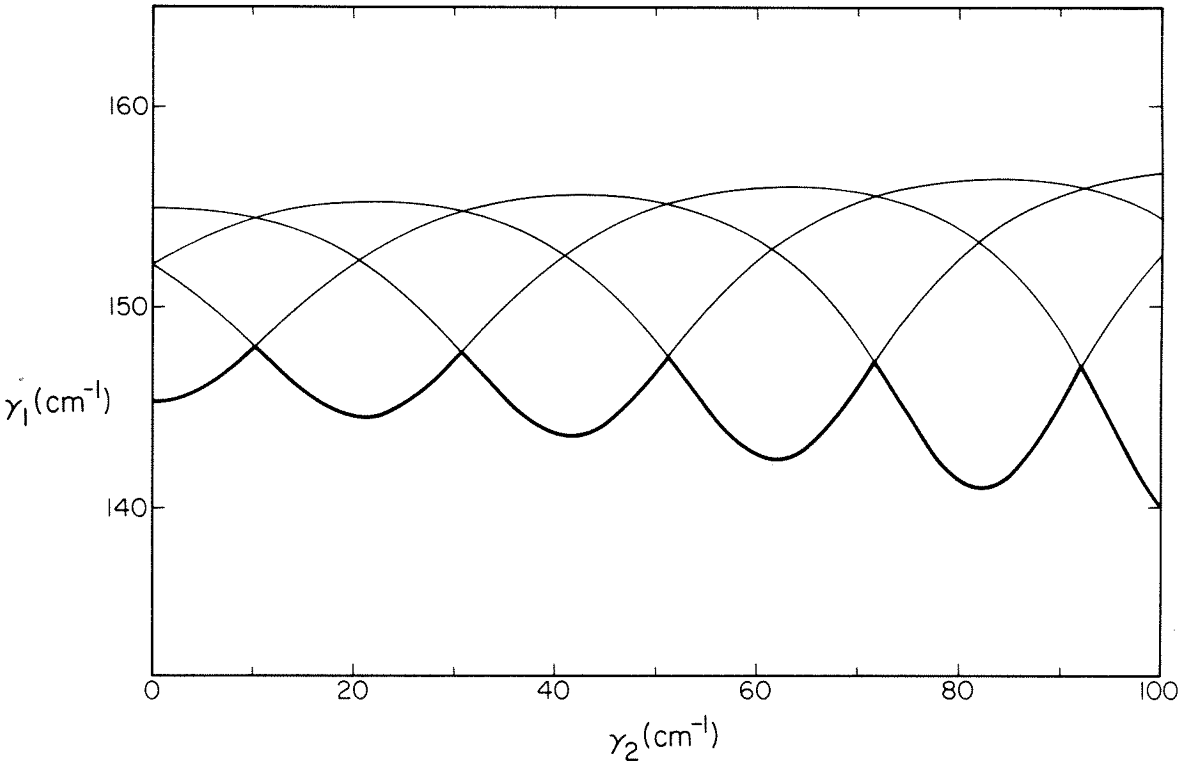

Figure 7.14: Threshold gain for an active-active cavity versus γ_2 for a coupling factor K=+.4.

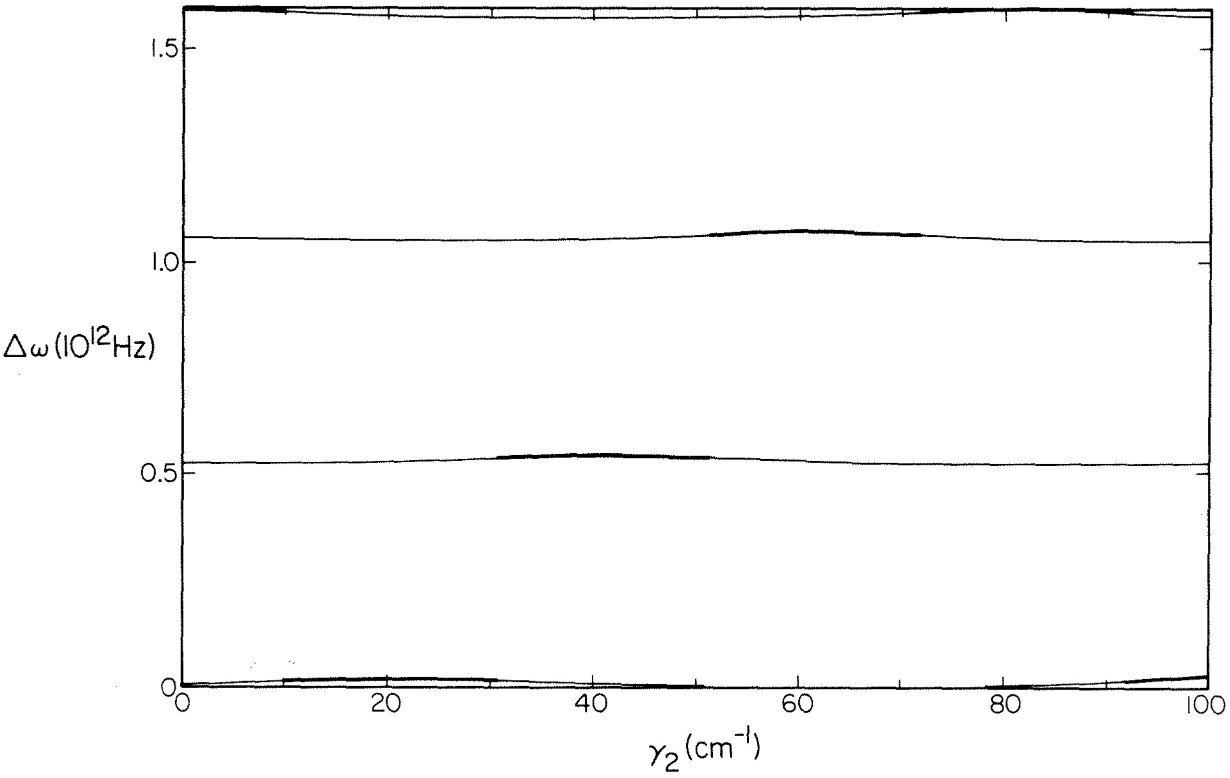

Figure 7.15: Lasing frequency versus γ_2 for device of figure 7.14.

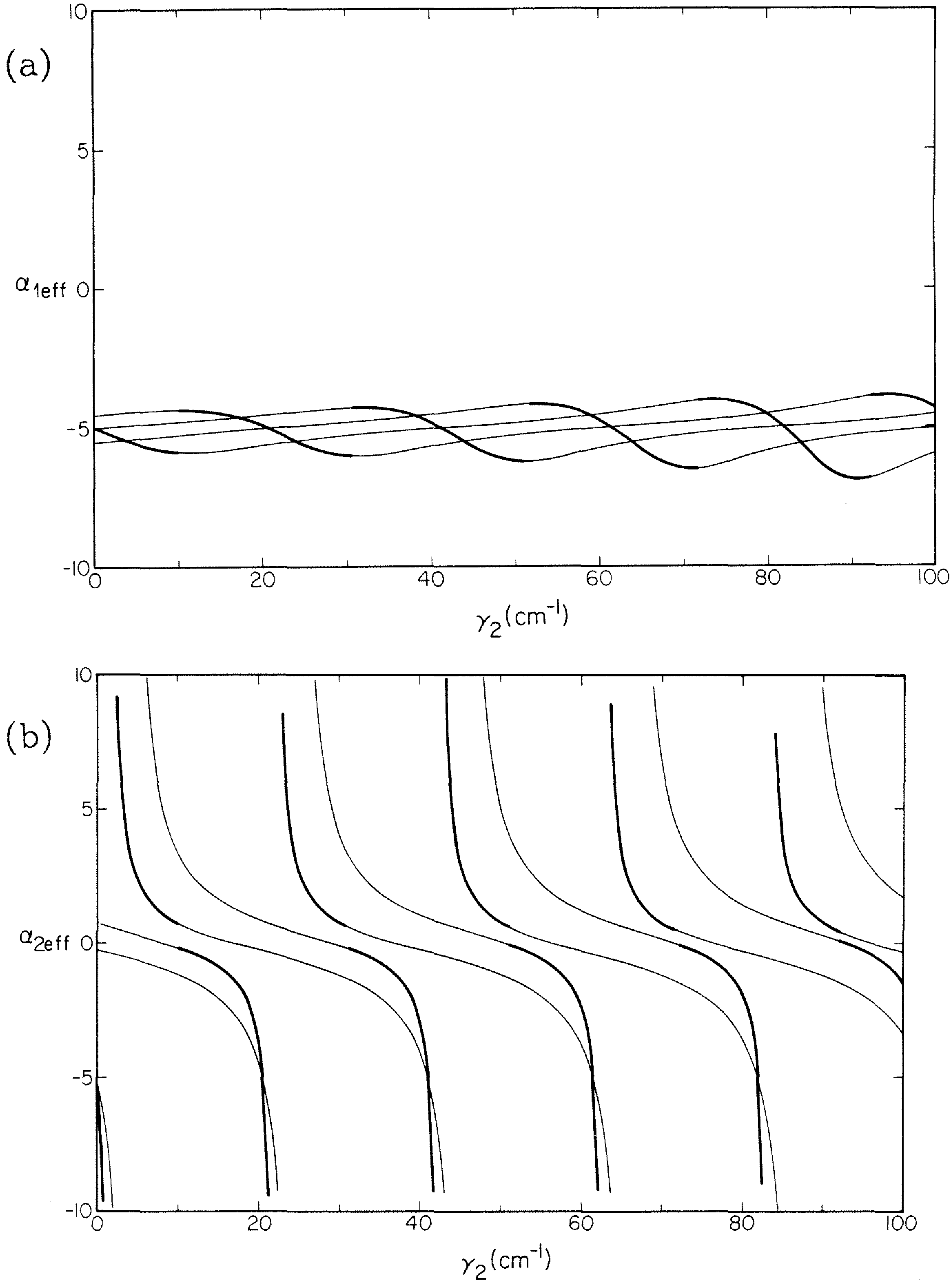

Figure 7.16: Effective α-parameters for device of figure 7.14. (a) α_{1eff}, (b) α_{2eff}.

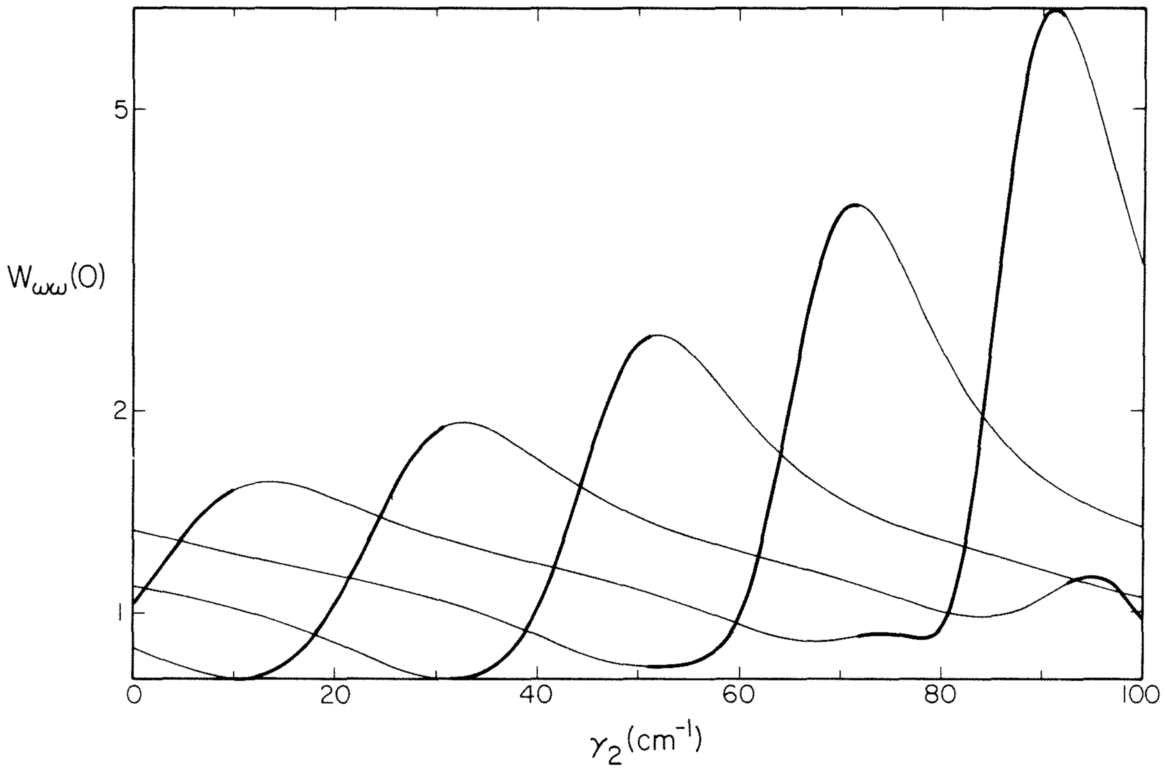

Figure 7.17: Linewidth of the device of figure 7.14 relative to that of an equivalent single-element laser (logarithmic scale).

the passive-active cavity. Conversely, any attempt to reduce the linewidth through detuned loading will result in a chirp under modulation. Another feature is that the largest linewidth excursions occur near a mode hop, so that the mode selectivity is likely to be low when tuned to a narrow linewidth. On the other hand, one could locate the narrow-linewidth regions by tuning to the vicinity of a mode hop. Although it has been shown that away from the zero-chirp bias point, the chirp may be reduced by driving both of the cavities with a fixed amplitude relationship [1], this modulation will not affect the noise properties. Consequently, the linewidth of the laser may still be larger than that at the zero-chirp point due to the FM contribution. It must be noted that equations (76)-(79) are based on the assumption of weakly coupled cavities; for two strongly coupled cavities, one must numerically solve the transcendental dispersion equation for the threshold gain and lasing frequency (although once in possession of those quantities, equations (8) may be evaluated directly for the effective modulation parameters). We expect, however, that the results of the perturbation analysis will still hold qualitatively. With strong coupling, the modulation quantities should vary even more widely from their material values, yielding larger excursions of the linewidth and other functions of noise (as well as dynamic quantities, like the relaxation resonance). The formalism presented in this section is easily applicable to larger ensembles of coupled cavities since the matrices in (30)-(33) are general and the dispersion function $F(\omega, n_1, \cdots n_n)$ is usually straightforward to derive. However, the complexity and large number of degrees of freedom in such a device will likely limit its technological significance. Perhaps of more importance, the "cavity-independent" nature of the formalism allows it to also be applied to cavities with frequency-dependent mirrors, e.g., DFB lasers.

7.5 Conclusions

In summary, we have provided a formalism for calculating any spectral function of an arbitrary multielement semiconductor laser. We carried out the analysis for a single-active element laser and showed that the spectra obtained were identical to those calculated from the more conventional theory. When a passive element is added to the system, the material differential gain and index constants are replaced by effective quantities that can be calculated from the dispersion equation. For the case of a passive resonator weakly coupled to an active one, we found approximate solutions for the lasing frequency, threshold, and effective modulation quantitites consistent with prior results. The effective parameters were shown to be mixtures of the material parameters, with the relative contributions determined by the relative tuning of the two cavities.

We then calculated expressions for the relative intensity and frequency fluctuation spectra of a device with two active elements, e.g. a C^3 laser. We derived formulas that defined the effective modulation parameters, and for the special case of a sub-threshold cavity ("modulator") weakly coupled to another active cavity we produced approximate solutions for the gain and lasing frequency as a function of carrier density in the modulator cavity. We also gave simple expressions for the effective modulation quantities in terms of the material parameters and a single complex constant that determines the amount of mixing. For the weakly coupled geometry, the cavities can be adjusted so that there is no chirp under modulation, but in that case, it is not possible to reduce the linewidth below the enhanced Schawlow-Townes limit with detuned loading. On the other hand, if the laser is not biased to the zero-chirp condition, the linewidth may be increased or decreased beyond that given by the enhanced Schawlow-Townes formula, depending upon the tuning of the cavity.

References

[1] L. A. Coldren, G. D. Boyd, J. E. Bowers and C.A. Burrus, Appl. Phys. Lett., vol. 46, p. 125 (1985).

[2] W. Streifer, D. Yevick, T. L. Paoli, and R. D. Burnham, paper #ThO4 presented at OSA, San Diego, California, October 29-November 2, 1984.

[3] G. Agrawal, IEEE J. Quant. Elect., vol. QE-21, p. 255 (1985).

[4] R. J. Lang and A. Yariv, IEEE J. Quant. Elect., vol. QE-21, p. 1683 (1985).

[5] T. L. Paoli and J. E. Ripper, Phys. Rev., vol. 2, p. 2551 (1970).

[6] D. E. McCumber, Phys. Rev. vol. 141, p. 306 (1966).

[7] K. Vahala, Ch. Harder and A. Yariv, Appl. Phys. Lett., vol. 42, p. 211 (1983).

[8] M. Fleming and A. Mooradian, Appl. Phys. Lett., p. 511 (1981).

[9] C. H. Henry, IEEE J. Quant. Elect., vol. QE-18, p. 259 (1982).

[10] D. Welford and A. Mooradian, Appl. Phys. Lett., vol. 40, p. 560 (1982).

[11] G. Tenchio, Elect. Lett., vol. 12, p. 562 (1976).

[12] G. Tenchio, Elect. Lett., vol. 13, p. 614 (1977).

[13] A. Dandridge and A. B. Tveten, Appl. Phys. Lett., vol. 39, p. 530 (1981).

[14] R. Lang, K. Vahala and A. Yariv, IEEE J. Quant. Elect., vol. QE-21, p. 443 (1985).

[15] K. Vahala and A. Yariv, Appl. Phys. Lett., vol. 45, p. 501 (1984).

[16] K. Vahala, J. Paslaski and A. Yariv, Appl. Phys. Lett., vol. 46, p. 1025 (1985).

[17] K. Vahala and A. Yariv, IEEE J. Quant. Elect., vol. QE-19, p. 1102 (1983).

[18] M. Lax, Phys. Rev., vol. 145, p. 110 (1965).

[19] H. Haug and H. Haken, Z. Phys., vol. 204, p. 262 (1967).

[20] J. Salzman, R. Lang and A. Yariv, Appl. Phys. Lett., vol. 47, p. 195 (1985).

[21] J. Katz, E. Kapon, C. Lindsey, S. Margalit, U. Shreter and A. Yariv, Appl. Phys. Lett., vol. 43, pp. 521-523 (1983).

[22] D. Marcuse and T-P. Lee, IEEE J. Quant. Elect., vol. QE-20, p. 166 (1984).

[23] H. K. Choi, K-L. Chen and S. Wang, IEEE J. Quant. Elect., vol. QE-20, p. 385 (1984).

[24] L. Coldren and T. L. Koch, IEEE J. Quant. Elect., vol. QE-20, p. 659 (1984).

[25] W. Streifer, D. Yevick, T. L. Paoli and R. D. Burnham, IEEE J. Quant. Elect., vol. QE-20, p. 754 (1984).

[26] C. H. Henry and R. F. Kazarinov, IEEE J. Quant. Elect., vol. QE-20, p. 733 (1984).

Chapter 8

The Effect of Spatially Dependent Temperature and Carrier Fluctuations on Noise in Semiconductor Lasers

8.1 Introduction

The theory of semiconductor laser noise has proven to be spectacularly successful at explaining noise phenomena at frequencies above about 1 MHz. The anomalous features observed in the noise spectra of laser diodes include a spiking resonance in the intensity spectrum [1] and the frequency fluctuation spectrum [2], a linewidth some thirty times greater than that predicted by the modified Schawlow-Townes theory [3], power-independent linewidth components [4,5], asymmetry in the field spectrum [2] and excess noise at low frequencies in both the intensity and frequency fluctuation spectrum [5-8]. Several theoretical models, both semiclassical and quantum mechanical, have explained many of these features. Early work by McCumber [9] explained the spiking resonance in the intensity spectrum as a result of photon-inversion dynamics using a Langevin approach; treatments by Lax [10] and Haug and Haken [11] also noted this effect and in addition provided a quantum-mechanical treatment. More recently, gain spectrum detuning has been invoked by several authors to explain linewidth enhancement, the asymmetrical field spectrum, and resonance structure in the frequency fluctuation spectrum [12,13]. Other theoretical and experimental works have corroborated these results [15]. To date, however, there has been no satisfactory explanation of the observed rise in both intensity and frequency noise below approximately 1 MHz.

Most theories, including those of the last chapter, either assume *a priori* or quickly reduce to spatially independent sets of equations. This approach offers the distinct advantage of reducing a multi-dimensional set of partial differential equations to a one-dimensional set of ordinary differential equations, and the assumption's validity is justified by the large number of effects predicted or explained by such theories. Still, there are features of the laser dynamics that are lost; implicit in such treatments are the assumptions that averages of products are equal to the product of the averages, and any fluctuations in spatial distributions are lost in the averaging process [16].

Diffusion, for example, plays no role in a spatially independent treatment, yet diffusion both damps out spatial fluctuations and introduces fluctuations of its own. Voss and Clarke [17] and van Vliet and Mehta [14,18] have proposed diffusion noise as a major source of low-frequency transport noise in semiconductors. Using a Langevin approach, they calculated carrier and temperature fluctuations in different geometries, and from those, current and voltage noise.

The analysis of a semiconductor laser is somewhat different from that of the bulk semiconductor, however, because of the additional coupling between carriers, temperature distribution, and the optical field. In this paper, we shall solve the spatially varying equations of motion for the carrier density, temperature distribution, and lasing field. The results of the analysis will show that spatially varying temperature fluctuations contribute significantly to the low-frequency noise in both the intensity and frequency fluctuation spectra, and that diffusion controls the precise structure of the spectra. Carrier fluctuations, while present, are shown to contribute minimally to the two spectra. In section 8.2, we set up transport equations for the photon field, carrier density, and temperature distribution with Langevin sources; we linearize them, and transform the small-signal equations to spatial and temporal frequency-space. In section 8.3, we normalize the Langevin sources to the dynamical variables and relate them to the macroscopic transition rates in the laser. In section 8.4, we derive expressions for relative intensity, frequency, and field fluctuation spectra, including simplified results for the low-frequency limit; we present numerical examples of the results, and compare them with experimental observations. We conclude in section 8.5 by summarizing several important results of the analysis.

8.2 Equations of Motion

A. Transport Equations

The starting point for the analysis is the set of equations describing the time evolution of the carrier density, temperature, and laser mode amplitude. The equations are, respectively, for carriers:

$$\dot{N} = D_E \nabla^2 N - \frac{\varepsilon_0}{2\hbar}\chi_i(N,T)\,|E_n|^2 - R_s(N) + R(\mathbf{x}) + \Xi \tag{1}$$

where $N(\mathbf{x})$ is the carrier density, D_E is the electronic diffusivity, R_s is the spontaneous emission rate per unit volume, $R(\mathbf{x})$ is the pump rate, Ξ is a Langevin source, and $\chi_i(N,T)$ is the imaginary part of the susceptibility. For temperature:

$$\dot{T} = D_T \nabla^2 T + \Theta \tag{2}$$

where $T(\mathbf{x})$ is the temperature, D_T is the thermal diffusivity, and Θ is a Langevin source. For the electric field, the short (picosecond) round-trip time of the cavity lets one treat the lasing mode as effectively seeing all parts of the cavity at once, so that the optical field responds to integrals over the lasing volume. The field equation is [15]:

$$\ddot{E}_n + \frac{1}{\tau_p}\dot{E}_n + \omega_n^2 E_n = \frac{-1}{\varepsilon_0 \mu^2 V}\int d^3\mathbf{x}\,\ddot{\mathbf{P}}\cdot\mathbf{e}_n(\mathbf{x}) + \Delta e^{j\omega_m t} \tag{3}$$

where E_n is the electric field amplitude of the *n*th mode, ω_n is the *n*th resonant frequency of the unpumped cavity, τ_p is the photon lifetime, μ is the non-resonant contribution to refractive index, $\mathbf{P}(\mathbf{x})$ is the induced polarization, Δ is a Langevin source, ω_m is the actual lasing frequency, and $\{\mathbf{e}_n(\mathbf{x})\}$ are the normalized *n*th spatial modes of the unpumped resonator, where

$$\int d^3\mathbf{x}\ |\mathbf{e}_n(\mathbf{x})|^2 = V$$

and V is the volume of the lasing mode.

These equations are then linearized about operating points

$$\begin{aligned} N(\mathbf{x}) &\equiv N_0(\mathbf{x}) + \nu(\mathbf{x},t) \\ R_s(N) &\equiv R_s(N_0) + \omega_s \cdot \nu \\ E_n(t) &\equiv A_0(1+\rho(t))e^{j(\omega_m t+\varphi(t))} \\ T(\mathbf{x}) &\equiv T_0(\mathbf{x}) + \tau(\mathbf{x},t) \\ \chi(N,T) &\approx \chi(N_0,T_0) + \zeta\nu + \eta\tau \end{aligned} \tag{4}$$

where

$$\zeta \equiv \left.\frac{\partial\chi}{\partial N}\right|_{N=N_0,T=T_0} \text{and } \eta \equiv \left.\frac{\partial\chi}{\partial T}\right|_{N=N_0,T=T_0}$$

and

$$\omega_s \equiv \left.\frac{\partial R_s}{\partial N}\right|_{N=N_0,T=T_0}$$

is the differential spontaneous emission rate per unit volume. If the laser is assumed to be running in a single mode, then

$$\mathbf{P}(\mathbf{x}) = \varepsilon_0\chi(N,T)\mathbf{E}(\mathbf{x}) = \varepsilon_0\chi(N,T)E_n\mathbf{e}_n(\mathbf{x})$$

so that

$$\begin{gathered} \frac{1}{\varepsilon_0\mu^2 V}\int d^3\mathbf{x}\ \ddot{\mathbf{P}}(\mathbf{x})\cdot\mathbf{e}_n(\mathbf{x}) \approx \\ \left[\frac{1}{\varepsilon_0\mu^2 V}\int d^3\mathbf{x}\ \varepsilon_0(\chi(N_0,T_0) + \zeta\nu + \eta\tau)E_n\,|e_n(\mathbf{x})|^2\right]^{\cdot\cdot} \end{gathered} \tag{5}$$

We can define an "effective susceptibility" as

$$\chi_\Gamma \equiv \frac{1}{V}\int_V d^3\mathbf{x}\ \chi(N_0,T_0)\,|e_n(\mathbf{x})|^2 \tag{6}$$

Substitute definitions (4)-(6) into equations (1)-(3), neglecting terms of second order or less to get

$$\dot{\nu} = D_E \nabla^2 N_0 + D_E \nabla^2 \nu - \frac{\varepsilon_0}{2\hbar}\left[\chi_i(N_0)A_0^2(1+2\rho) + \zeta_i \nu A_0^2\right] - R_s(N_0) - \omega_s \nu + R + \Xi \quad (7)$$

$$\dot{\tau} = D_T \nabla^2 T_0 + D_T \nabla^2 \tau + \Theta \quad (8)$$

$$2j\omega_m A_0(\dot{\rho}+j\dot{\varphi}) - \frac{\omega_m^2 A_0}{\mu^2 V}\int_V d^3\mathbf{x}\,(\zeta\nu + \eta\tau)\,|e_n|^2 +$$
$$(\omega_n^2 - \omega_m^2 + j\frac{\omega_m}{\tau_p} - \frac{\omega_m^2}{\mu^2}\chi_\Gamma)A_0 = \Delta e^{-j\varphi(t)}. \quad (9)$$

Here r and i subscripts on ζ, η, χ, and Δ denote the real and imaginary parts, respectively, of the quantities that bear them.

The zeroth-order terms in equations (7)-(9) establish the operating point for the laser; the first-order terms describe the small-signal response to the Langevin driving terms. Since (a) we are only interested in the second moment of Δ, and (b) Δ is approximately white over the laser line, we can drop the $e^{-j\varphi}$ on the right side of (9); separating real and imaginary parts of (9) and taking out the zeroth order terms gives

$$\dot{\rho} - \frac{\omega_m}{2\mu^2 V}\int d^3\mathbf{x}\,(\zeta_i\nu + \eta_i\tau)\,|e_n|^2 = \frac{1}{2\omega_m A_0}\Delta_i \quad (10)$$

$$\dot{\varphi} + \frac{\omega_m}{2\mu^2 V}\int d^3\mathbf{x}\,(\zeta_r\nu + \eta_r\tau)\,|e_n|^2 = \frac{-1}{2\omega_m A_0}\Delta_r \quad (11)$$

$$\dot{\nu} - D_E \nabla^2 \nu + \frac{1}{\tau_R}\nu + \frac{\varepsilon_0 \chi_i(N_0, T_0) A_0^2}{\hbar}\rho = \Xi \quad (12)$$

$$\dot{\tau} - D_T \nabla^2 \tau = \Theta \quad (13)$$

where $\frac{1}{\tau_R} \equiv \omega_s + \frac{\varepsilon_0 A_0^2 \zeta_i(\mathbf{x})}{2\hbar}$. Equations (10)-(13) comprise the fluctuation equations describing the small-signal behavior of the relative amplitude ($\rho(t)$), phase ($\varphi(t)$), carrier density ($\nu(\mathbf{x},t)$), and temperature ($\tau(\mathbf{x},t)$) of a single-mode semiconductor laser.

B. Fourier Analysis

Equations (12) and (13) are partial differential equations involving spatial derivatives in the Laplacian operator. An exact solution must take into account the spatial variation of $1/\tau_R$ and the boundary conditions, the latter of which are in general mixed and/or inhomogeneous. Unfortunately, configurations for which closed-form solutions exist are few and far between. We will make three simplifying assumptions: (1) ζ_i, ζ_r, and ω_s (and thus $1/\tau_R$) are constant over the active region. (2) the carriers are confined to the active region so that the normal derivative of ν vanishes on the boundary (e.g., an ideal buried heterostructure). We can include structures with no lateral confinement (e.g., gain-guided) by allowing the lateral confinement direction to approach infinity. (3) The temperature profile is subject to fictitious boundary conditions; all functions and derivatives are continuous across the boundary of the device (i.e., we neglect variations in material parameters resulting from compositional shifts from GaAs to AlGaAs).

We now define Fourier transforms. For quantities that vary in time,

$$\tilde{f}(\omega) \equiv \int dt\, f(t)e^{-j\omega t} \ , \ f(t) \equiv \frac{1}{2\pi}\int d\omega\, \tilde{f}(\omega)e^{j\omega t} \tag{14}$$

For quantities that vary in space and have fictitious boundary conditions,

$$\tilde{g}(\mathbf{k}) \equiv \int d^3\mathbf{x}\, g(\mathbf{x})e^{j\mathbf{k}\cdot\mathbf{x}} \ , \ g(\mathbf{x}) = \frac{1}{(2\pi)^3}\int d^3\mathbf{k}\, \tilde{g}(\mathbf{k})e^{-j\mathbf{k}\cdot\mathbf{x}} \tag{15}$$

For carrier fluctuations confined to a region $S_1 \times S_2 \times S_3$ with volume $V_A = S_1S_2S_3$, the finite domain gives rise to a discrete spectrum with eigenfunctions defined as

$$g(\mathbf{n},\mathbf{x}) \equiv \begin{cases} \cos q_1(x_1 - \frac{S_1}{2})\cos q_2(x_2 - \frac{S_2}{2})\cos q_3(x_3 - \frac{S_3}{2}) & \text{for } x_i \in \left[\frac{-S_i}{2}, \frac{S_i}{2}\right] \\ 0 & \text{otherwise} \end{cases} \tag{16}$$

having index vector $\mathbf{n}$; the wavevector $\mathbf{q}(\mathbf{n})$ is defined by

$$q_i(\mathbf{n}) \equiv \frac{n_i\pi}{S_i}$$

The associated spectral representation is

$$\tilde{h}(\mathbf{n}) \equiv \int_{V_A} d^3\mathbf{x}\, h(\mathbf{x}) g(\mathbf{n},\mathbf{x}) \quad , \quad h(\mathbf{x}) = \sum_{\mathbf{n}} \frac{\gamma(\mathbf{n})}{V_A} \tilde{h}(\mathbf{n}) g(\mathbf{n},\mathbf{x}) \tag{17}$$

In this expression, the $\{n_i\}$ can take on integer values from 0 to ∞, and $\gamma(\mathbf{n})$ is a normalization factor equal to 1, 2, 4, or 8, depending on how many of the n_i's are zero (0, 1, 2, or 3, respectively). Then the operators in (10)-(13) transform as

$$\frac{\partial}{\partial t} \rightarrow j\omega \quad , \quad \nabla^2 \rightarrow -k^2 \text{ or } -q^2(\mathbf{n}) \tag{18}$$

We make use of the identity

$$\int d^3\mathbf{x}\, f(\mathbf{x}) g(\mathbf{x}) = \frac{1}{(2\pi)^3} \int d^3\mathbf{k}\, \tilde{f}(\mathbf{k}) \tilde{g}(-\mathbf{k}) \tag{19}$$

define

$$\Gamma(\mathbf{k}) \equiv \frac{1}{(2\pi)^3} \int d^3\mathbf{x}\, |e_n(\mathbf{x})|^2 e^{-j\mathbf{k}\cdot\mathbf{x}} \tag{20}$$

and approximate

$$\tilde{\eta}_{i,r}(\mathbf{k}) \approx \bar{\eta}_{i,r} \cdot (2\pi)^3 \Gamma(-\mathbf{k}) \tag{21}$$

(which is tantamount to assuming that η is constant over the optical mode) so that the fluctuation equations, transformed in both space and time, become

$$\begin{aligned} j\omega\tilde{\rho}(\omega) - \frac{\omega_m}{2\mu^2 V} \int d^3\mathbf{x}\, |e_n(\mathbf{x})|^2 \zeta_i \sum_{\mathbf{n}} \frac{\gamma(\mathbf{n})}{V_A} \tilde{\nu}(\mathbf{n},\omega) g(\mathbf{n},\mathbf{x}) \\ - \frac{\omega_m}{2\mu^2 V} \int d^3\mathbf{k}\, \bar{\eta}_i \Gamma(\mathbf{k}) \tilde{\tau}(\mathbf{k},\omega) = \frac{1}{2\omega_m A_0} \tilde{\Delta}_i(\omega) \end{aligned} \tag{22}$$

$$\begin{aligned} j\omega\tilde{\varphi}(\omega) + \frac{\omega_m}{2\mu^2 V} \int d^3\mathbf{x}\, |e_n(\mathbf{x})|^2 \zeta_r \sum_{\mathbf{n}} \frac{\gamma(\mathbf{n})}{V_A} \tilde{\nu}(\mathbf{n},\omega) g(\mathbf{n},\mathbf{x}) \\ + \frac{\omega_m}{2\mu^2 V} \int d^3\mathbf{k}\, \bar{\eta}_r \Gamma(\mathbf{k}) \tilde{\tau}(\mathbf{k},\omega) = \frac{-1}{2\omega_m A_0} \tilde{\Delta}_r(\omega) \end{aligned} \tag{23}$$

$$\left[j\omega + D_E q^2(\mathbf{n}) + \frac{1}{\tau_R} \right] \tilde{\nu}(\mathbf{n},\omega) + \frac{\varepsilon_0 \tilde{\chi}_i(\mathbf{n}) A_0^2}{\hbar} \tilde{\rho}(\omega) = \tilde{\Xi}(\mathbf{n},\omega) \tag{24}$$

$$\left[j\omega + D_T k^2 \right] \tilde{\tau}(\mathbf{k},\omega) = \tilde{\Theta}(\mathbf{k},\omega) \tag{25}$$

Elimination of carrier density ($\tilde{\nu}$) and temperature distribution ($\tilde{\tau}$) from equations (22)-(25) gives

$$\begin{aligned} \tilde{\rho}(\omega) = R(\omega) \Bigg[\frac{\omega_m}{2\mu^2 V} \sum_{\mathbf{n}} \Lambda(\mathbf{n}) \zeta_i \frac{\tilde{\Xi}(\mathbf{n},\omega)}{j\omega + D_E q^2(\mathbf{n}) + \frac{1}{\tau_R}} \\ + \frac{\omega_m}{2\mu^2 V} \int d^3\mathbf{k}\, \Gamma(\mathbf{k}) \bar{\eta}_i \frac{\tilde{\Theta}}{j\omega + D_T k^2} + \frac{1}{2\omega_m A_0} \tilde{\Delta}_i \Bigg] \end{aligned} \tag{26}$$

$$
\begin{aligned}
j\omega\tilde{\varphi}(\omega) &= \left[\frac{\zeta_r}{\zeta_i}(1-j\omega R)-\frac{\bar{\eta}_r}{\bar{\eta}_i}\right]\int d^3\mathbf{k}\,\Gamma(\mathbf{k})\bar{\eta}_i\frac{\Theta(\mathbf{k},\omega)}{j\omega+D_T k^2} \\
&- j\omega R\frac{\zeta_r}{\zeta_i}\sum_{\mathbf{n}}\Lambda(\mathbf{n})\zeta_i\frac{\tilde{\Xi}(\mathbf{n},\omega)}{j\omega+D_E q^2(\mathbf{n})+\frac{1}{\tau_R}}-\frac{1}{2\omega_m A_0}\tilde{\Delta}_r+\frac{\zeta_r}{\zeta_i}(1-j\omega R)\frac{1}{2\omega_m A_0}\tilde{\Delta}_i \qquad (27)
\end{aligned}
$$

where

$$\Lambda(\mathbf{n}) \equiv \frac{\gamma(\mathbf{n})}{V_A}\int d^3\mathbf{x}\,|e_n(\mathbf{x})|^2 g(\mathbf{n},\mathbf{x}) \qquad (28)$$

$$\frac{1}{R(\omega)} \equiv j\omega + \sum_{\mathbf{n}}\frac{\omega_m\zeta_i\varepsilon_0\tilde{\chi}_i(\mathbf{n})\Lambda(\mathbf{n})A_0^2}{2\mu^2\hbar V}\left[j\omega+D_E q^2(\mathbf{n})+\frac{1}{\tau_R}\right]^{-1} \qquad (29)$$

C. Relaxation Resonance

If either $\chi_i(\mathbf{x})$ or $|e_n(\mathbf{x})|$ are constant over the active region then the only non-zero $\tilde{\chi}_i(\mathbf{n})$ or $\Lambda(\mathbf{n})$ is the $\mathbf{n} = (0,0,0)$ term. In this situation, $R(\omega)$ reduces to McCumber's relaxation resonance [9]

$$R(\omega) = \frac{j\omega+\frac{1}{\tau_R}}{\omega_R^2-\omega^2+\frac{j\omega}{\tau_R}}\ , \quad \omega_R^2 \equiv \frac{\omega_m\zeta_i\varepsilon_0\chi_i\Lambda A_0^2}{2\mu^2\hbar} \qquad (30)$$

where Λ is the fill factor. However, if both $\chi_i(\mathbf{x})$ and $|e_n(\mathbf{x})|$ vary over the active region, then there are non-zero values for $\tilde{\chi}_i(\mathbf{n})$ and $\Lambda(\mathbf{n})$, which contribute additional terms to the resonance expression. Physically, this is a demonstration of the fact that there is a considerable diffusive flow of carriers if the carrier density is not uniform, and the phase lag between the diffusion process and the normal carrier-photon dynamics alters the frequency response [19]. For typical dimensions and distributions, the result is a damping of both the intensity resonance $|R(\omega)|^2$ and the frequency resonance $|1-j\omega R(\omega)|^2$. Figures 8.1 and 8.2 illustrate the damping for several different configurations. It is interesting to note that if any of the products $\tilde{\chi}_i(\mathbf{n})\Lambda(\mathbf{n})$ are negative, they can have the effect of sharpening the resonance; however, such terms decrease the overlap between the gain and the optical mode, degrading the performance of the laser and mak-

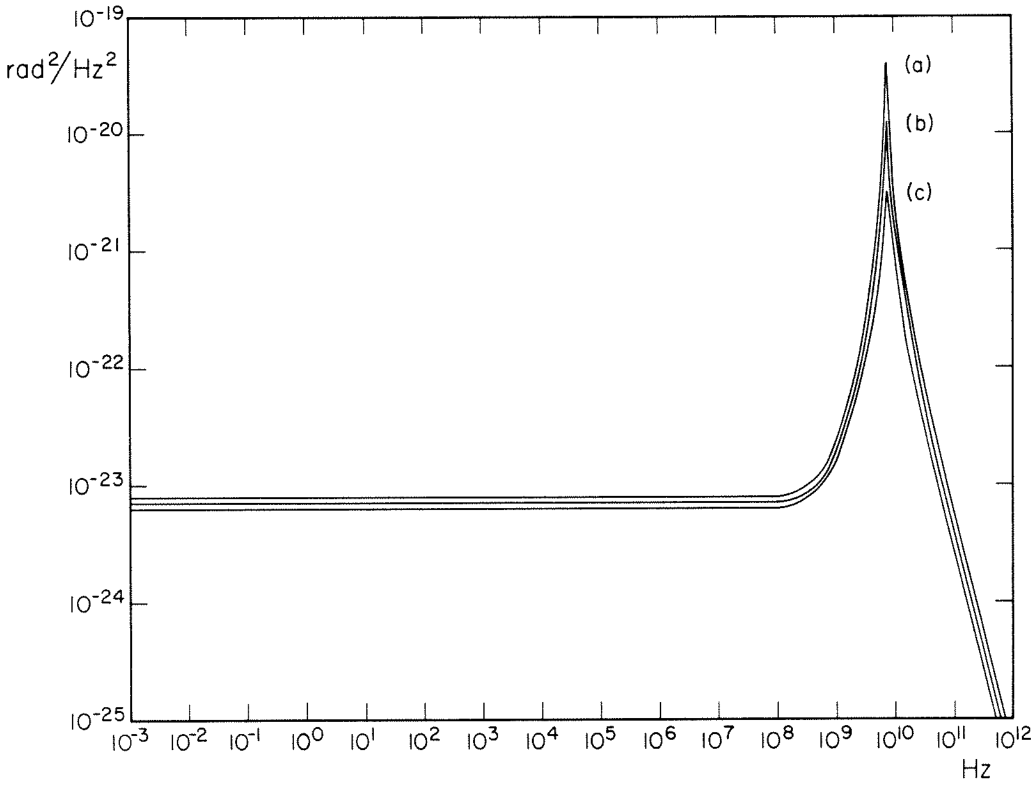

Figure 8.1: Effect of inhomogeneities in carrier density and optical field on relaxation resonance $|R(\Omega)|^2$ in the intensity noise spectrum. The optical field distribution is taken to be $\frac{1}{2}\left[1+\cos\frac{2\pi x_i}{S_i}\right]$ in the lateral direction and susceptibility is taken to be proportional to $\frac{1}{1+\varepsilon}\left[1+\varepsilon\cos\frac{2\pi x_i}{S_i}\right]$ in the lateral direction. Transverse variation contributes negligibly to the resonance, so for a symmetric structure, the dominant damping comes from the **n** = (0,2,0) term. (a) $\varepsilon = 0$; (b) $\varepsilon = .5$, $S_2 = 2.0\ \mu$m; (c) $\varepsilon = .5$, $S_2 = 4.0\ \mu$m.

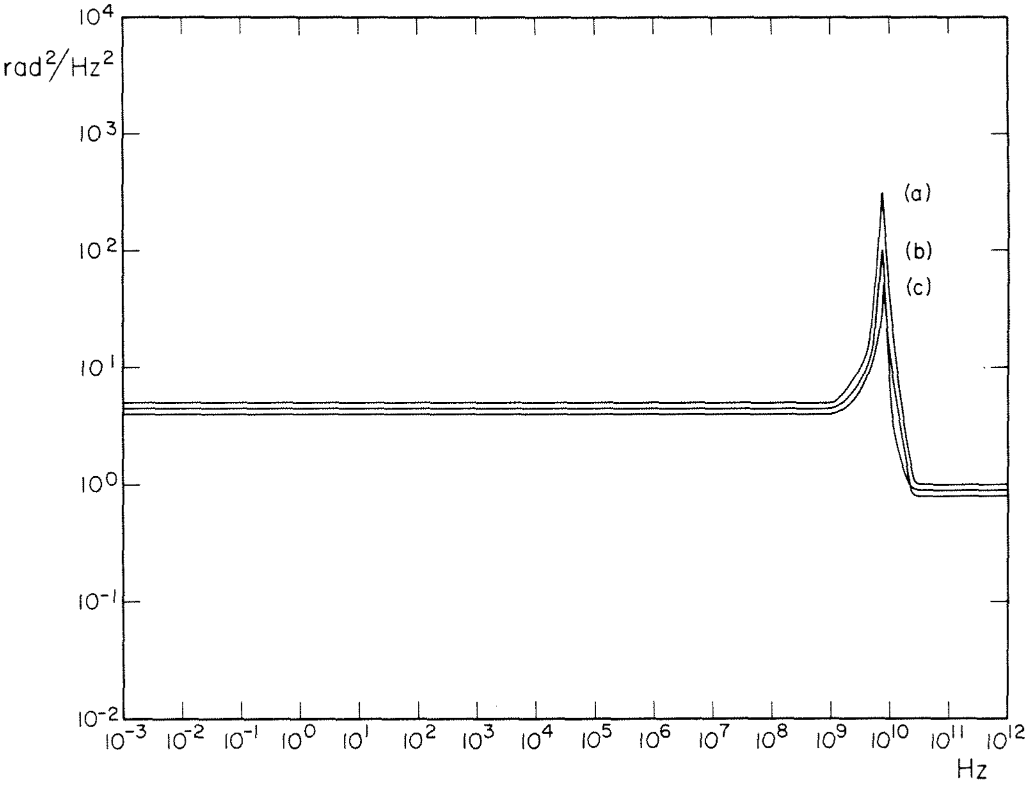

Figure 8.2: Same parameters for frequency fluctuation resonance $1 + \alpha_N^2 |1 - j\Omega R|^2$.

ing it unlikely that such a mode would be the preferred mode of oscillation.

8.3 Langevin Sources

A. Rate Normalization

When several systems of particles interact with each other and/or with external baths through random particle interactions, there are fluctuations associated with each interaction. Such fluctuations can be accounted for by including appropriately normalized Langevin sources into the equations of motion. This approach can be used with systems that vary continuously (e.g., temperature) if the interaction being characterized by a Langevin source is particulate (that is, the interaction occurs in discrete units, such as photon absorption or nonradiative recombination). Each independent number variable {A} will have associated with it a fluctuation source {a} that satisfies

$$< a(t)a(t')> \; = \; < \frac{dA}{dt} > \delta(t-t') \tag{31}$$

where < > denotes ensemble average. For a number variable which varies in space as well, one has the modified relation

$$< a(\mathbf{x},t)a(\mathbf{x}',t')> \; = \; < \frac{dA(\mathbf{x},t)}{dt} > \delta(t-t')\delta^3(\mathbf{x}-\mathbf{x}') \tag{32}$$

There are additional fluctuations associated with the microscopic kinetics of carrier and thermal diffusion, however. These have a different spatial correlation than the previous sources. Van Vliet and Mehta [18] have shown that the sources obey

$$< \xi_D(\mathbf{x},t)\xi_D(\mathbf{x}',t')> \; = 2D_E\nabla_{\mathbf{x}}\cdot\nabla_{\mathbf{x}'}[N_0(\mathbf{x})\delta^3(\mathbf{x}-\mathbf{x}')]\delta(t-t') \tag{33}$$

for carrier diffusion, and

$$< \vartheta_D(\mathbf{x},t)\vartheta_D(\mathbf{x}',t')> \; = \frac{2D_Tk_BT_0^2}{\kappa}\nabla_{\mathbf{x}}\cdot\nabla_{\mathbf{x}'}\delta^3(\mathbf{x}-\mathbf{x}')\delta(t-t') \tag{34}$$

for thermal diffusion where κ is the specific heat per unit volume and k_B is

Boltzmann's constant.

We can then split $\Xi = \xi_D + \xi_E$, $\Theta = \vartheta_D + \vartheta_E$ into diffusion-related and particle-related fluctuation terms; the particle terms, after normalizing to number rates, give the following correlations [13]:

$$< \Delta_i(t)\Delta_i(t')> \; = \; < \Delta_r(t)\Delta_r(t')> \; = \left[\frac{2\hbar\omega_m^2}{\varepsilon V A_0}\right]^2 R_0\delta(t-t') \qquad (35)$$

where R_0 is the sum of all rates that change photon number.

$$< \xi_E(\mathbf{x},t)\xi_E(\mathbf{x}',t')> \; = R_2(\mathbf{x})\delta^3(\mathbf{x}-\mathbf{x}')\delta(t-t') \qquad (36)$$

where R_2 is the rate per unit volume of events that change carrier density.

$$< \vartheta_E(\mathbf{x},t)\vartheta_E(\mathbf{x}',t')> \; = \left[\frac{E_{NR}}{\kappa}\right]^2 R_3(\mathbf{x})\delta^3(\mathbf{x}-\mathbf{x}')\delta(t-t') \qquad (37)$$

where E_{NR} is the mean thermal energy dissipated in a non-radiative (or absorptive) event and R_3 is the event rate per unit volume.

In addition, there are several non-zero off-diagonal correlations, reflecting the fact that many events change more than one system at a time. They are as follows:

$$< \xi_E(\mathbf{x},t)\Delta_i(t')> \; = \left[\frac{2\hbar\omega_m^2}{\varepsilon V A_0}\right] R_1(\mathbf{x})\delta(t-t') \qquad (38)$$

where $R_1(\mathbf{x})$ is the rate of stimulated transitions.

$$< \vartheta_E(\mathbf{x},t)\Delta_i(t')> \; = \left[\frac{2\hbar^2\omega_m^3}{\varepsilon V A_0 \kappa}\right] R_4(\mathbf{x})\delta(t-t') \qquad (39)$$

where R_4 is the rate of heat-generating absorptions.

$$< \vartheta_E(\mathbf{x},t)\xi_E(\mathbf{x}',t')> \; = \left[\frac{E_{NR}}{\kappa}\right] R_5(\mathbf{x})\delta^3(\mathbf{x}-\mathbf{x}')\delta(t-t') \qquad (40)$$

where R_5 is the rate of non-radiative carrier recombination. All other possible off-diagonal terms are negligible or zero, including $< \Delta_i\Delta_r>$ [13].

B. Langevin Sources in the Transform Plane

Equations (28) and (29) are in terms of transformed variables, so it is convenient to cast (33)-(40) in the same manner, particularly since we will eventually be interested in spectral functions $W_{fg}(\Omega)$, which are themselves transformed quantities. Mathematical problems arise when one attempts to take the Fourier transform of a stationary signal, however. (While it is always possible to solve the equations by Laplace transform, the complications due to the initial conditions make the calculation somewhat tedious.) To be rigorous, one must use finite-domain Fourier transforms defined as follows:

$$\tilde{f}_T(\omega) \equiv \int_{\frac{-T}{2}}^{\frac{+T}{2}} dt\, f(t)e^{-j\omega t} \ , \ \tilde{g}_T(\omega) \equiv \int_{\frac{-T}{2}}^{\frac{+T}{2}} dt\, g(t)e^{-j\omega t} \tag{41}$$

then, calculate the spectral term defined by the Wiener-Khintchine relations as

$$W_{fg}(\Omega) \equiv \int d\tau < f(t)g(t+\tau)> e^{-j\Omega t}. \tag{42}$$

In terms of the transforms (41),

$$W_{fg}(\Omega) = \lim_{T\to\infty} \frac{< \tilde{f}_T(\Omega)\tilde{g}_T(-\Omega)>}{T} \tag{43}$$

Strictly speaking, the relations that make the Fourier transform useful (e.g., transformation of differential operators) are not exact so long as the object of the transform is finite at the limits of integration. However, as $T\to\infty$, the results of the spectral calculation become valid. In deference to our use of properties of the infinite-domain transform, we will drop the $\tilde{f}_T$ notation and continue to use $\tilde{f}$.

We are also interested in spatial Fourier transforms of the Langevin sources in the same way that we defined transforms for the dynamical variables in equations (15) and (16). The calculations are somewhat simplified if we make the assumption that all carrier rates are uniform over the active region. The transformed (33)-(40) are

$$\tilde{\tilde{W}}_{\xi_D\xi_D}(\mathbf{n},\mathbf{n}',\Omega) \approx \frac{D_E\gamma(\mathbf{n})}{4}\delta_{\mathbf{n},\mathbf{n}'}\overline{M} \tag{44}$$

where $\overline{\mathrm{M}} \equiv \int_{V_A} d^3\mathbf{x} -[\nabla^2 N_0(\mathbf{x})]$

$$\tilde{\tilde{W}}_{\vartheta_D\vartheta_D}(\mathbf{k},\mathbf{k}',\Omega) = \frac{-2D_T k_B T_0^2}{\kappa}\mathbf{k}\cdot\mathbf{k}'(2\pi)^3\delta^3(\mathbf{k}+\mathbf{k}') \tag{45}$$

$$W_{\Delta_1\Delta_1}(\Omega) = W_{\Delta_r\Delta_r}(\Omega) = \left(\frac{2\hbar\omega_m^2}{\varepsilon V A_0}\right)^2 R_0 \tag{46}$$

$$\tilde{\tilde{W}}_{\xi_E\xi_E}(\mathbf{n},\mathbf{n}',\Omega) = \frac{\gamma(\mathbf{n})}{8} V_A R_2 \delta_{\mathbf{n},\mathbf{n}'} \tag{47}$$

$$\tilde{\tilde{W}}_{\vartheta_E\vartheta_E}(\mathbf{k},\mathbf{k}',\Omega) = \left(\frac{E_{NR}}{\kappa}\right)^2 \tilde{R}_3(\mathbf{k}+\mathbf{k}') \tag{48}$$

$$\tilde{W}_{\Delta_1\xi_E}(\mathbf{n},\Omega) = \tilde{W}_{\xi_E\Delta_1}(\mathbf{n},\Omega) = \left(\frac{2\hbar\omega_m^2}{\varepsilon V A_0}\right) R_1 \delta_{\mathbf{n},0} \tag{49}$$

$$\tilde{W}_{\Delta_1\vartheta_E}(\mathbf{k},\Omega) = \tilde{W}_{\vartheta_E\Delta_1}(\mathbf{k},\Omega) = \left(\frac{2\hbar^2\omega_m^3}{\varepsilon V A_0 \kappa}\right) \tilde{R}_4(\mathbf{k}) \tag{50}$$

$$\tilde{\tilde{W}}_{\vartheta_E\xi_E}(\mathbf{k},\mathbf{n},\Omega) = \tilde{\tilde{W}}_{\xi_E\vartheta_E}(\mathbf{k},\mathbf{n},\Omega) =$$
$$\left(\frac{E_{NR}}{\kappa}\right) R_5 \frac{V_A}{8} \prod_{i=1}^{3} \left[e^{\frac{-iq_i(\mathbf{n})S_i}{2}} \operatorname{sinc}\frac{(k_i+q_i(\mathbf{n}))S_i}{2} + e^{\frac{+iq_i(\mathbf{n})S_i}{2}} \operatorname{sinc}\frac{(k_i-q_i(\mathbf{n}))S_i}{2} \right] \tag{51}$$

where $\operatorname{sinc}(x) \equiv \frac{\sin(x)}{x}$ and $\delta_{\mathbf{n},\mathbf{n}'}$ is the Kronecker delta.

None of the Langevin spectra have any frequency dependence, which is as it should be; the nature of the Langevin approach is that the sources are Markoffian [16] and therefore, white.

8.4 Fluctuation Spectra

A. Relative Intensity and Frequency Fluctuation Spectra

The relative intensity fluctuation spectrum is defined as

$$W_{\rho\rho}(\Omega) \equiv \lim_{T\to\infty} \frac{<\tilde{\rho}(\Omega)\tilde{\rho}(-\Omega)>}{T} \tag{52}$$

while the frequency fluctuation spectrum is

$$W_{\Delta\omega}(\Omega) \equiv \lim_{T\to\infty} \frac{<\tilde{\varphi}(\Omega)\tilde{\varphi}(-\Omega)>}{T} = \lim_{T\to\infty} \frac{<[j\Omega\,\tilde{\varphi}(\Omega)][-j\Omega\,\tilde{\varphi}(\Omega)]>}{T} \tag{53}$$

We make use of equations (28) and (29) for $\tilde{\rho}$ and $j\Omega\,\tilde{\varphi}$, and relations (44)-(51) for the Langevin spectra. The tedium of the algebra is somewhat relieved if we note that the off-diagonal driving terms (e.g., $W_{\Delta_i\xi_E}$) are of importance only near a crossing of the associated diagonal spectra (e.g., $W_{\Delta_i\Delta_i}$, $W_{\xi_E\xi_E}$); while a full solution must contain the off-diagonal terms, we lose very little by ignoring them for the rest of the analysis. Define $\alpha_N \equiv \zeta_r/\zeta_i$ and $\alpha_T \equiv \bar{\eta}_r/\bar{\eta}_i$; the relative intensity fluctuation spectrum including photon, carrier, and temperature noise sources, is

$$W_{\rho\rho}(\Omega) = |R(\Omega)|^2\left(\frac{\omega_m}{2\mu^2V}\right)^2\left\{\sum_{\mathbf{n}}\Lambda^2(\mathbf{n})\zeta_i^2\frac{\gamma(\mathbf{n})}{8}\frac{2D_E\overline{M}}{\Omega^2+\left(D_Eq^2(\mathbf{n})+\frac{1}{\tau_R}\right)^2}\right. \tag{54a}$$

$$+\sum_{\mathbf{n}}\Lambda^2(\mathbf{n})\zeta_i^2\frac{\gamma(\mathbf{n})}{8}\frac{V_AR_2}{\Omega^2+\left(D_Eq^2(\mathbf{n})+\frac{1}{\tau_R}\right)^2} \tag{54b}$$

$$+\int d^3\mathbf{k}d^3\mathbf{k}'\ \Gamma(\mathbf{k})\Gamma(\mathbf{k}')\bar{\eta}_i^2\frac{\frac{-2D_Tk_BT_0^2}{\kappa}\mathbf{k}\cdot\mathbf{k}'(2\pi)^3\delta^3(\mathbf{k}+\mathbf{k}')}{\left(j\Omega+D_Tk^2\right)\left(-j\Omega+D_Tk'^2\right)} \tag{54c}$$

$$\left.+\int d^3\mathbf{k}d^3\mathbf{k}'\ \Gamma(\mathbf{k})\Gamma(\mathbf{k}')\bar{\eta}_i^2\frac{\left(\frac{E_{NR}}{\kappa}\right)^2\tilde{R}_3(\mathbf{k}+\mathbf{k}')}{\left(j\Omega+D_Tk^2\right)\left(-j\Omega+D_Tk'^2\right)}\right\} \tag{54d}$$

$$+|R(\Omega)|^2\left(\frac{\hbar\omega_m}{\varepsilon VA_0^2}\right)^2R_0 \tag{54e}$$

The frequency fluctuation spectrum is

$$W_{\Delta\omega}(\Omega) = \alpha_n^2\Omega^2|R(\Omega)|^2\left(\frac{\omega_m}{2\mu^2V}\right)^2\left\{\sum_{\mathbf{n}}\Lambda^2(\mathbf{n})\zeta_i^2\frac{\gamma(\mathbf{n})}{8}\frac{2D_E\overline{M}}{\Omega^2+\left(D_Eq^2(\mathbf{n})+\frac{1}{\tau_R}\right)^2}\right. \tag{55a}$$

$$\left.+\sum_{\mathbf{n}}\Lambda^2(\mathbf{n})\zeta_i^2\frac{\gamma(\mathbf{n})}{8}\frac{V_AR_2}{\Omega^2+\left(D_Equ^2(\mathbf{n})+\frac{1}{\tau_R}\right)^2}\right\} \tag{55b}$$

$$+|\alpha_n(1-j\Omega R)-\alpha_T|^2\left(\frac{\omega_m}{2\mu^2V}\right)^2$$

$$\cdot\left\{\int d^3\mathbf{k}d^3\mathbf{k}'\ \Gamma(\mathbf{k})\Gamma(\mathbf{k}')\bar{\eta}_i^2\frac{\frac{-2D_tk_BT_0^2}{\kappa}\mathbf{k}\cdot\mathbf{k}'(2\pi)^3\delta^3(\mathbf{k}+\mathbf{k}')}{\left(j\Omega+D_Tk^2\right)\left(-j\Omega+D_Tk'^2\right)}\right. \tag{55c}$$

$$+\int d^3\mathbf{k}d^3\mathbf{k}'\ \Gamma(\mathbf{k})\Gamma(\mathbf{k}')\bar{\eta}_i^2 \frac{\left(\frac{E_{NR}}{\kappa}\right)\tilde{R}_3(\mathbf{k}+\mathbf{k}')}{\left(j\Omega + D_T k^2\right)\left(-j\Omega + D_T k'^2\right)}\Bigg\} \tag{55d}$$

$$+[1+\alpha_N^2|1-j\Omega R|^2]\left(\frac{\hbar\omega_m}{\varepsilon V A_0^2}\right)^2 R_0 \tag{55e}$$

Equations (54a-e) and (55a-e) are plotted in figures 8.3a-e and 8.4a-e, respectively, for a typical laser with parameters listed in table 8.1. There are several features of interest in the equations and graphs. Equations (54e) and (55e) are the familiar expressions one derives using the standard volume-averaged rate equation analysis [13]. They contain a relaxation resonance in the intensity noise [9] and the same resonance in the frequency noise, along with the linewidth enhancement factor α_N [12,13]. The remaining expressions are those that are lost in the volume-averaged treatment. We can see from the graphs that both the diffusion-driven carrier fluctuations (54a,55a) and the spontaneous emission-driven carrier fluctuations (54b,55b) make negligible contributions to the intensity noise and frequency fluctuation spectra (figures 8.3b,8.4b). Closer examination of the summations in (54b) and (55b) will show why this is so. Each term makes a contribution with a corner frequency of $\Omega_0 = D_E q^2(\mathbf{n}) + 1/\tau_R$; this is an indication of diffusion damping above Ω_0. Below Ω_0, where diffusion is less effective, however, the carrier lifetime τ_R is responsible for damping the perturbation. In other words, spatial perturbations to the carrier density are damped out before they can make a substantial low-frequency contribution to the noise spectrum. Additional carrier noise sources (for example, noise in the pump current) can be similarly treated by inclusion into the Ξ Langevin source.

The fluctuations due to temperature diffusion (c) are, by themselves, greater than the noise produced by spontaneous emission (e); they are, however, themselves masked by the noise from event-driven thermal fluctuations (d).

$\alpha_N = -2.2$
$\alpha_T = 0.90$
$\omega_m = 2.2 \cdot 10^{15}$ rad/sec
$\omega_s = 10^9$ sec^{-1}
$N_0 = 10^{18}$ cm^{-3}
$\tau_p = 2 \cdot 10^{-12}$ sec
$S_1 = 0.2$ μm
$S_2 = 2.0$ μm
$S_3 = 200$ μm
$V = V_A = 8.0 \cdot 10^{-11}$ cm^3
$\zeta_i = 7.3 \cdot 10^{-21}$ cm^3
$\eta_i = 4.7 \cdot 10^{-4}$ $^\circ\text{K}^{-1}$
$P_0 = 5.0 \cdot 10^{-3}$ W
$\tau_R = 1.9 \cdot 10^{-10}$ sec
$\omega_R = 4.6 \cdot 10^{10}$ rad/sec
$R_0 = 4.2 \cdot 10^{17}$ sec^{-1}
$R_2 = 5.3 \cdot 10^{27}$ $\text{cm}^{-3}\text{sec}^{-1}$
$R_3 = 1.3 \cdot 10^{27}$ $\text{cm}^{-3}\text{sec}^{-1}$
$\overline{M} = 5.0 \cdot 10^{16}$ cm^{-2}
$E_{NR} = 2.3 \cdot 10^{-19}$ J
$\kappa = 1.9$ $\text{J}^\circ\text{K}^{-1}\text{cm}^{-3}$
$D_E = 220$ cm^2/sec
$D_T = .24$ cm^2/sec

Table 8.1: Laser parameters assumed in the graphs of figures 8.3 and 8.4.

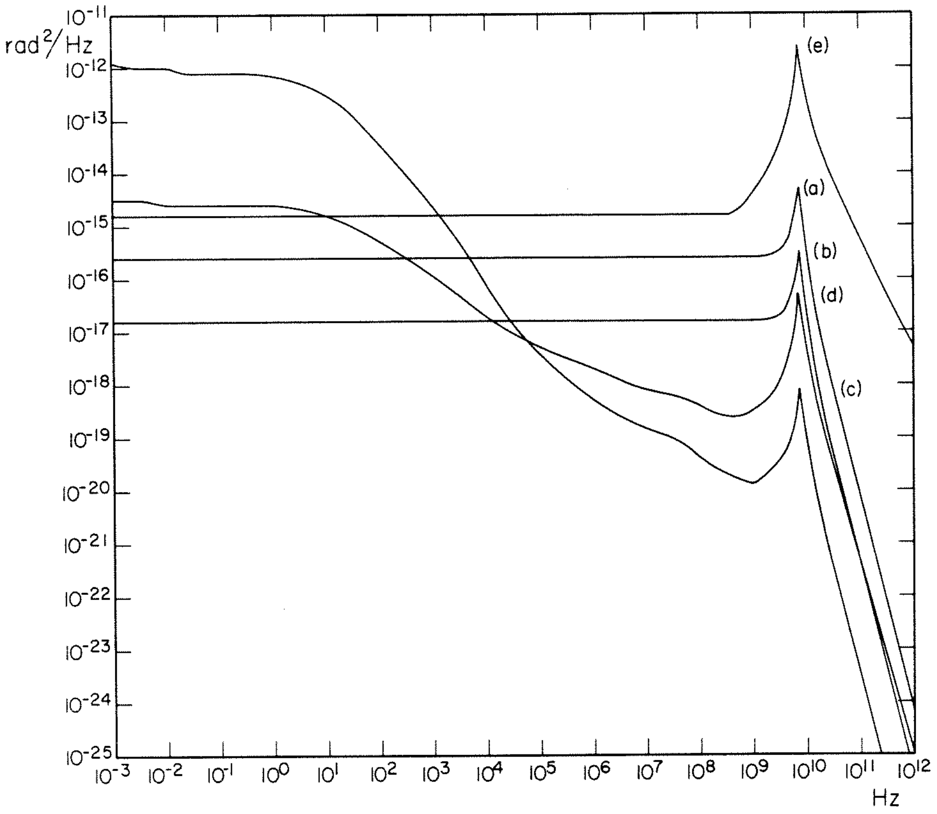

Figure 8.3: Noise terms in the intensity noise spectrum (eqn. (54a-e)) for the parameters listed in table 8.1. (a) carrier diffusion; (b) carrier creation/annihilation; (c) temperature diffusion; (d) non-radiative recombination/absorption temperature fluctuations; (e) spontateous emission.

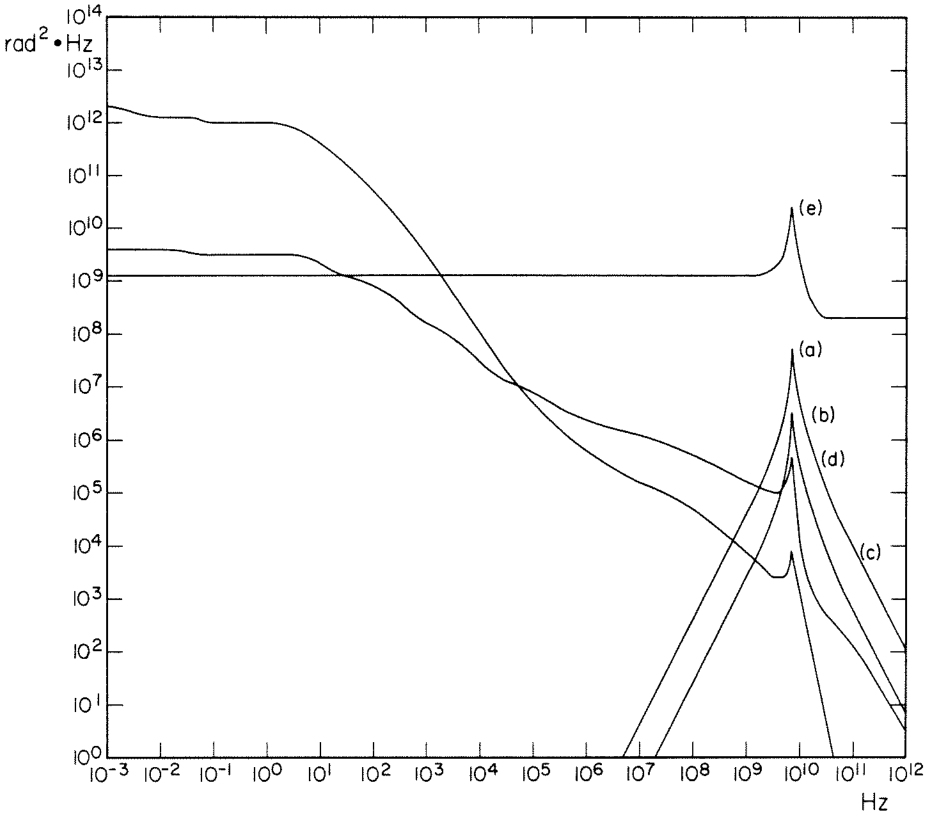

Figure 8.4: Noise terms in the frequency fluctuation spectrum (eqn. (55a-e) for the parameters listed in table 8.1. (a) carrier diffusion; (b) carrier creation/annihilation; (c) temperature diffusion; (d) non-radiative recombination/absorption temperature fluctuations; (e) spontaneous emission.

Two major contributors to this noise source are non-radiative recombination and optical absorption. These produce delta-like impulses of heat (Voss and Clarke's P-source revived [17]). Since there is no thermal lifetime (the equivalent of $1/\tau_R$), the temperature fluctuations extend to very low frequency before leveling off due to the finite volume of the lasing region. The fluctuations couple to the amplitude via gain dependence upon temperature, and to the phase via the refractive index dependence. It is instructive to compare the photon and temperature noise in the intensity spectrum with the corresponding noise in the frequency spectrum. The noise terms are substantially the same (aside from the leading $|R(\Omega)|^2$), but the photon noise in the frequency spectrum is enhanced by a factor $1+\alpha_N^2$ over its counterpart in the intensity spectrum, and exhibits a resonance. This is due to the amplitude-phase coupling through carrier dynamics [12,13,15] and was observed by Fleming and Mooradian [3]. The temperature fluctuation-driven noise in the frequency spectrum is enhanced by a factor $(\alpha_N-\alpha_T)^2$. Here α_T is a new coupling parameter; it represents amplitude-phase fluctuations coupled through the temperature dependence of gain and index. α_N has been measured and calculated [20,21] to be approximately -2 to -4, while α_T is approximately .5 to 1. Since they are of opposite sign, the two effects reinforce one another. The frequency dependence of this noise source is of the form $1/f^\alpha$, $\alpha \approx 1$ for several decades, which is in agreement with experimental measurements from several sources [5-8,22-24,27]. The noise should exhibit the relaxation resonance before falling off as $1/f^2$ at high frequency; this behavior, however, is in practice masked by other processes.

B. Field Spectrum and Linewidth

The field spectrum of the laser diode is given by

$$< E_n(t+\tau)E_n^*(t)> \; = A_0^2 < (1+\rho(t+\tau))e^{j\varphi(t+\tau)}(1+\rho(t))e^{j\varphi(t)} > e^{j\omega_m\tau} \qquad (56)$$

If amplitude fluctuations are negligible or suppressed in the measurement process (as, for example, was done in [22]) then the field spectrum can be put in terms of the frequency fluctuation spectrum [25] as

$$W_\varepsilon(\omega+\omega_m) = \frac{1}{2}A_0^2 \mathrm{Re}\int_{-\infty}^{+\infty} d\tau \, e^{-j\omega\tau} \exp\left[\frac{-\tau^2}{2\pi}\int_0^\infty d\Omega \;\; W_{\Delta\omega}(\Omega)\left(\frac{\sin\frac{\Omega\tau}{2}}{\frac{\Omega\tau}{2}}\right)^2\right] \qquad (57)$$

where ω is the deviation from the lasing frequency ω_m. In the case where $W_{\Delta\omega}$ is a sum of several terms, then W_ε will be the convolution of the individual W_ε's calculated from each of the terms of $W_{\Delta\omega}$. So, for example, a DC component of $W_{\Delta\omega}$ results in a Lorentzian line

$$W_\varepsilon(\omega+\omega_m) = \frac{A_0^2}{4\pi}\frac{W_{\Delta\omega}^{DC}(0)}{\omega^2 + \left(\frac{W_{\Delta\omega}^{DC}(0)}{2}\right)^2} \qquad (58)$$

This has a linewidth of $W_{\Delta\omega}^{DC}(0)$, namely $(1+\alpha_N^2)\left(\frac{\hbar\omega}{\varepsilon V A_0^2}\right)R_0$, the enhanced Schawlow-Townes linewidth. To include the contribution of the recombination noise, we note from Figure 8.3 that the spectrum at low frequency is approximately $\frac{1}{f}$-like with a corner frequency near 1 Hz: we model it as

$$W_{\Delta\omega}^{NR}(\Omega) = \frac{\omega_0^2}{\Omega + \omega_1} \qquad (59)$$

This leads to an approximate lineshape of

$$\frac{1}{2\pi}\int_{-\infty}^{+\infty} d\tau \, e^{-j\omega\tau} \exp\left\{\frac{-\tau^2\omega_0^2}{2\pi}\ln\left(1 + \frac{2}{\omega_1|\tau|}\right)\right\} \qquad (60)$$

This is not an easy Fourier transform to evaluate, but we can pick out the contribution to linewidth by exploiting the Fourier uncertainty relationship, that

$$\Delta\tau\Delta\omega \approx 2 \qquad (61)$$

so that the linewidth $\Delta\omega$ satisfies the implicit relation

$$\Delta\omega \approx \omega_0 \left[\ln\left(\frac{\Delta\omega}{\omega_1} \right) \right]^{\frac{1}{2}} \tag{62}$$

For the laser with parameters given in figure 8.3, we have $\omega_0^2 \approx 3 \cdot 10^{12}$ rad^2/sec^2, $\omega_1 \approx 3$ rad^2/sec, which gives $\Delta\omega \approx 6.6 \cdot 10^6$rad/sec and $\Delta f \approx 1.1$ MHz. This is comparable to the power-independent linewidth observed by Welford, Mooradian, and Harrison [4,26] and Kikuchi and Okoshi [5]. While carrier fluctuations are strongly damped by the carrier lifetime τ_R at low frequency, and, as can be seen from figure 8.4, make minimal contributions to the frequency fluctuation spectrum (and hence, linewidth), temperature-induced index/gain variations are not similarly damped. A primary source for these fluctuations is nonradiative recombination, which is a function of carrier density, and therefore is constant above threshold. Hence, the resulting contribution to linewidth is power-independent.

8.5 Conclusions

In this chapter we have derived the fluctuation spectra of a single-mode semiconductor laser that result from spatially dependent fluctuations in carrier density and temperature distribution. We have shown that the relaxation resonance that appears in both the intensity noise and frequency fluctuation spectra is damped more effectively than that predicted by spatially independent models; and, that carrier and temperature fluctuations are most important at low frequencies, where some of them mask the flat inverse power spectra reported elsewhere. Carrier fluctuations are damped by the short carrier lifetime; perturbations to the carrier density do not persist long enough to make significant low-frequency contributions, while at higher frequencies they are damped by diffusion. Temperature fluctuations, subject to no such low-frequency damping, play a major role in low-frequency fluctuations. Events that produce isolated rises in temperature (e.g., nonradiative recombination, absorption) give rise to a spectrum that increases at low frequencies, contains decades of 1/f-like behavior and levels off below 1 Hz. The frequency spectrum displays an enhancement due to the detuned nature of the gain spectrum; the enhancement factor contains both the carrier-related amplitude-phase coupling coefficient and a new, temperature-related amplitude-phase coupling coefficient. One additional prediction of the theory is a power-independent linewidth comparable to that which has been observed experimentally.

References

[1] T. L. Paoli and J. E. Ripper, Phys. Rev., vol.2, p. 2551 (1970).

[2] K. Vahala, Ch. Harder, and A. Yariv, Appl. Phys. Lett., vol. 42, p. 211 (1983).

[3] M. Fleming and A. Mooradian, Appl. Phys. Lett., vol. 38, p. 511 (1981).

[4] D. Welford and A. Mooradian, Appl. Phys. Lett., vol. 40, p. 560 (1982).

[5] K. Kikuchi and T. Okoshi, Elect. Lett., vol. 19, p. 812 (1983).

[6] G. Tenchio, Elect. Lett., vol. 12, p. 562, (1976).

[7] G. Tenchio, Elect. Lett., vol. 13, p. 614, (1977).

[8] A. Dandridge and A. B. Tveten, Appl. Phys. Lett., vol. 39, p. 530 (1981).

[9] D. E. McCumber, Phys. Rev., vol. 141, p. 306 (1966).

[10] M. Lax, IEEE J. Quant. Elect., vol. QE-3, p. 37 (1967).

[11] H. Haug and H. Haken, Z Physik, vol. 203, p. 262 (1967).

[12] C. H. Henry, IEEE J. Quant. Elect., vol. QE-18, p. 259 (1982).

[13] K. Vahala and A. Yariv, IEEE J. Quant. Elect., vol. QE-19, p. 1102 (1983).

[14] K. M. van Vliet, J. Math. Phys., vol. 12, p. 1981 (1971).

[15] K. Vahala and A. Yariv, IEEE J. Quant. Elect., vol. QE-19, p. 1096 (1983).

[16] J. B. Moreno, J. Appl. Phys., vol. 48, p. 4152 (1977).

[17] R. F. Voss and J. Clarke, Phys. Rev. B, vol. 13, p. 556 (1976).

[18] K. M. van Vliet and H. Mehta, Phys. Stat. Solidi (b), vol. 106, p. 11 (1981).

[19] G. H. B. Thompson, *Physics of Semiconductor Laser Devices*, (John Wiley & Sons, Ltd., 1980) p. 424.

[20] Ch. Harder, K. Vahala, and A. Yariv, Appl. Phys. Lett., vol. 42, p. 328 (1983).

[21] K. Vahala, L. C. Chiu, S. Margalit, and A. Yariv, Appl. Phys. Lett., vol. 42, p. 631 (1983).

[22] F. G. Walther and J. E Kaufmann, paper #TUJ5 presented at Optical Fiber Conference, New Orleans, Louisiana, 1983.

[23] M. J. O'Mahony and I. D. Henning, Elect. Lett., vol. 19, p. 1000 (1983).

[24] M. Ohtsu and S. Kotajima, Japan. J. Appl. Phys., vol. 23, p. 760 (1984).

[25] K. Vahala and A. Yariv, 'Power, frequency, and field spectra for single and multimode semiconductor lasers," unpub.

[26] J. Harrison and A. Mooradian, Appl. Phys. Lett., vol. 45, p. 318 (1983).

[27] T. K. Yee, paper #TUH3 presented at Conference on Lasers and Electro-Optics, Baltimore, Maryland, 1983.

*

*

*

Chapter 9

Local Field Rate Equations for Coupled Optical Resonators

9.1 Introduction

The springboard for the analysis of almost any laser's dynamics--modulation response, noise properties, or even a simple stability analysis--is the rate equation describing the optical field in terms of material parameters and other dynamical quantities (e.g., gain). While the ultimate arbiter of the field's behavior must be Maxwell's equations, the set of second-order partial differential wave equations that follows from Maxwell's does not lend itself to a simple solution in the face of fluctuating coefficients in the equation. Fortunately, in almost all cases, a sufficient description is provided by a set of first-order ordinary differential equations in which the field is characterized by a small number of variables, e.g., the spatial average of the field amplitude over different regions of the resonator. In fact, for many systems, even complicated sets of coupled resonators, the field dependence can be adequately described by a single variable, the amplitude of the lasing mode of the composite cavity [1]. We used such a formalism in the last four chapters to analyze the dynamic and noise properties of single and multielement lasers [1,2]. As we saw in chapter 5, it can be extended to produce a set of multimode rate equations, expanding in terms of the modes of the composite cavity.

An alternate description of a multielement optical resonator is produced by writing rate equations for several variables that somehow represent the field inside of each of the coupled elements [3-7]. This latter approach conveys more of the flavor of interactions among individual lasers, while the former approach takes a more global view. The resulting set of coupled rate equations is intuitively appealing--each field satisfies the rate equation for its own individual cavity, but is modified by the addition of a coupling term linking it to a neighboring cavity. In most treatments, the dynamical variables are chosen to be the amplitudes of the individual cavity modes (henceforth, the ICM's) that make up the lasing composite cavity mode (CCM). Such analyses have qualitatively predicted the properties of weakly coupled systems. However, they suffer from two flaws that severely limit their usefulness.

The first is that the CCM (which is the proper description for steady-state operation) is generally made up of more than one ICM from each cavity. In the case of weakly coupled systems, it consists of predominantly one ICM from each resonator, but the stronger the coupling is between cavities, the stronger the need is to include multiple ICM's from each cavity to accurately model the CCM. Consequently, any description of such a CCM in terms of two ICM's is going to be incomplete. There are some treatments that do take the coupling among other longitudinal modes [4-5] into account, and such treatments can be expected to give more accurate results than those that do not. The second flaw, however, afflicts *all* treatments that attempt to expand in terms of individual cavity modes.

The second problem involves the following point: *the complete set of modes of the individual cavities do not constitute a complete set when those cavities are coupled together.* In fact, they *never* constitute a sufficient description of the composite cavity mode [3]! This is a subtle point that bears a bit more explaining. When we solve for the modes of an isolated resonator, we have implicitly made the stipulation that all fields outside the resonator (or within some infinitesimal distance from the mirrors) are outgoing. This is a reasonable assumption, since the only source of light in an isolated laser lies inside the resonator, and any light encountered outside the resonator is indeed outgoing. The modes thus found lie in the *discrete* spectrum of the operator corresponding to wave propagation in the resonator. They form a complete set *only* for fields that are outgoing.

When we couple two resonators, however, there arise incoming fields in each cavity. In fact, coupling cannot take place without such fields. The modes of an isolated resonator cannot adequately describe such a field. A complete description of the field inside each cavity must include the modes corresponding to the *continuous* spectrum, corresponding to fields incident upon the cavity from the outside. Such a description must include a sum over the discrete modes, plus an integral over the continuous modes. However, a representation of this sort that includes the intermodal coupling leads to a set of integro-differential equations for the modal amplitudes that is more difficult to solve than the original problem. The conventional approach is to drop the continuous part of the spectrum and to hope that what is left is sufficiently complete to describe the field.

What are the results of dropping modes from a coupled-mode theory? The time evolution of each mode is determined by the scattering of energy from one mode into another. If we do not include a mode in a coupled-mode theory, then while the rate equations remaining will account for the energy scattered *out* of the remaining modes (and into the "lost" modes), there is no mechanism for the scattering of energy out of the "lost" modes back into the "kept" modes. In effect, then, the lost modes become "black holes," absorbing energy from the system and never returning it. Consequently, threshold gains calculated from such a theory are going to be overestimated, since they will take into account these spurious energy sinks. The amount of the overestimation depends upon the relative fraction of the CCM described by modes of the continuous spectrum. Unfortunately, for strongly coupled cavities, that amount is substantial. While this problem can be ameliorated somewhat by imposing fictitious boundary conditions upon the ICM's to force them to more closely match the CCM's (as is discussed in [4]), this method requires one to *a priori* possess fairly detailed knowledge of the CCM's.

It appears, then, that coupled-mode theory cannot easily provide quantitative information about the behavior of fields in composite cavity resonators. However, one of the attributes of coupled-mode theory--a description of the field by a few variables that somehow characterize the individual cavities--is still desirable. As we will show, we can produce such a description by choosing as each dynamical variable the amplitude of one of the traveling waves in each cavity *at some fixed point* within the cavity, rather than choosing the amplitude of an individual cavity mode. (Hence the moniker "local field" rate equations.) This choice, plus a little DC analysis, will yield a set of rate equations and *analytic* expressions for all coupling coefficients with no long summations or involved overlap integrals. Furthermore, because the treatment is based upon the *composite* cavity modes, it encounters none of the difficulties of standard coupled-mode theory. The method is powerful and general, yet conceptually quite simple. It relies on the approximation that the optical field adiabatically follows the characteristics of the resonator, an approximation that has been widely made and justified in chapter 5 [1]. In section 9.2 we will present the derivation in abstract form. In section 9.3 we apply it to the most common coupled system, a two-section longitudinally coupled-cavity laser and derive the coupling coefficients. In section 9.4, we show how a modification of the technique can incorporate multimode behavior in a single rate equation and justify the delay-differential equation composed by Lang and Kobayashi [8] to describe optical feedback. In section 9.5, we summarize the analysis.

9.2 General Theory

In chapter 5, we found that for single-mode lasers a suitable first-order rate equation is provided by first finding the steady-state eigenvalue equation for complex frequency, and then replacing the frequency $j\Omega$ by the differential operator d/dt. We then formally justified this approximation for both single and multimode systems and calculated the lowest-order correction terms. The assumption underlying this approximation can be stated in several equivalent ways. A rather formal statement of the approximation is that "linear operators commute with all variables except the electric field, which they act upon." Perhaps a more meaningful expression is that the only significant time derivatives are those of the electric field; time derivatives of other variables (for example, a fluctuating index of refraction) will be sufficiently small that they can be dropped. We shall refer to this approximation throughout the chapter as the "adiabatic approximation," because the electric field inside the resonator adiabatically follows the instantaneous characteristics of the resonator. It is an assumption widely made in the literature without comment, but it is implicitly assumed in any first-order rate equation.

We will attempt to characterize the field by a set of amplitudes $\{E_i(\mathbf{x}_i)\}$ of traveling waves at fixed points $\mathbf{x}_i$ within the composite cavity. As a practical matter, one would choose a single fixed point in each of the coupled cavities. In steady-state, it is simple to assume complex exponential behavior of the form $\exp(j\Omega t)$ and then to find a set of linear relations linking the field amplitudes $\{E_i\}$. The coefficients are typically functions of Ω. The process is well codified for several geometries [9,10]; a self-consistency requirement yields a set of linear equations of the form

$$\sum_j \Gamma_{ij}(\Omega)E_j = 0 \tag{1}$$

where each of the Γ_{ij} depends upon the complex frequency Ω. We shall adopt a matrix notation, where each of the fields E_i is a component of the vector $\tilde{E}$, and Γ_{ij} is a component of the matrix $\tilde{\tilde{\Gamma}}$. The steady-state eigenvalue equation (1), written in matrix notation, becomes

$$\tilde{\tilde{\Gamma}}(\Omega)\tilde{E} = \tilde{0} \tag{2}$$

where $\tilde{0}$ is the zero vector. Equation (2) has non-trivial solutions for $\tilde{E}$ only if $\tilde{\tilde{\Gamma}}$ is singular, and this requirement yields the lasing frequencies Ω.

We should like to find a set of rate equations of the form

$$\frac{d}{dt}\tilde{E} = \tilde{\tilde{T}}\tilde{E} \tag{3}$$

so our goal is to establish a correspondence between equations (3) and (2). Let us begin by working backwards. If we want to solve equation (3), we would assume exponential variation in $\tilde{E}$;

$$\tilde{E} \rightarrow \tilde{E}e^{j\Omega t} \tag{4}$$

in which case equation (3) would become

$$j\Omega\,\tilde{E} = \tilde{\tilde{T}}\tilde{E} \tag{5}$$

We know from [1] that equation (2) holds adiabatically for small fluctuations in the steady-state solutions, provided that we replace $j\Omega$ by the differential operator. If we define $\Gamma(\Omega) \equiv \det\tilde{\tilde{\Gamma}}(\Omega)$, then the non-trivial steady-state solutions to (2) are the eigenvectors corresponding to the roots of

$$\Gamma(\Omega) = 0 \tag{6}$$

Let us linearize equation (2) about a value Ω_0 that is a root of (6).

$$\left[\tilde{\tilde{\Gamma}}(\Omega_0) + (\Omega - \Omega_0)\tilde{\tilde{\Gamma}}_\Omega(\Omega_0)\right]\tilde{E} = \tilde{0} \tag{7}$$

where $\tilde{\tilde{\Gamma}}_\Omega$ is the derivative of $\tilde{\tilde{\Gamma}}$ with respect to Ω. Denote $\Omega - \Omega_0$ by $\Delta\Omega$. Then, we can multiply by $-j\tilde{\tilde{\Gamma}}_\Omega^{-1}$ to get

$$j\Delta\Omega\,\tilde{E} = -j\tilde{\tilde{\Gamma}}_\Omega^{-1}\tilde{\tilde{\Gamma}}\Big|_{\Omega=\Omega_0}\tilde{E} \tag{8}$$

Now, if we replace $j\Delta\Omega$ with d/dt, we have exactly equation (5), with $\tilde{\tilde{T}} = -j\tilde{\tilde{\Gamma}}_{\Omega}^{-1}\tilde{\tilde{\Gamma}}\big|_{\Omega=\Omega_0}$. Consequently, the desired rate equation for the field amplitudes oscillating at frequency Ω_0 is

$$\frac{d}{dt}\tilde{E} \equiv -j\tilde{\tilde{\Gamma}}_{\Omega}^{-1}(\Omega_0)\tilde{\tilde{\Gamma}}(\Omega_0)\tilde{E} \tag{9}$$

This expression not only gives us the desired rate equations and expressions for all the coupling coefficients; it also tells us just how accurate the entire rate equation (first-order differential equation) approximation really is. Here, the factor $j\Omega$ corresponds to the differential operator d/dt. For frequency ranges in which the linearization of equation (7) is a good match to $\tilde{\tilde{\Gamma}}$, the approximation is good; otherwise, it is not. However, even the simplest linearization is going to be a good approximation for variations in $\Omega - \Omega_0$ over some fraction, say, 1/10, of a longitudinal mode spacing. For almost all lasers, that frequency is well beyond the timescale of fluctuations of interest. Note that we don't actually have to possess the exact value of Ω_0; we simply have to be within this domain of the root, where the linearization provides a good match to $\tilde{\tilde{\Gamma}}$.

It can be shown that $\tilde{\tilde{\Gamma}}$ can always be chosen such that $\Gamma(\Omega)$ possesses no finite singularities. Therefore, a Taylor series expansion of Γ has an infinite radius of convergence in the Ω-plane. Consequently, we can take a Taylor series at *any* point Ω_i, and by replacing each factor of $j\Omega$ by the operator d/dt, we can construct a higher-order rate equation of arbitrarily high accuracy over an arbitrarily large frequency domain, all within the adiabatic approximation. As a practical matter, the equation is simplest and most useful if we linearize about one of the roots of Γ that corresponds to a low-threshold CCM, since the first term of the series is all that is needed. However, for certain situations, e.g., distant optical feedback, a slight variation on this technique can give a close fit to Γ over a number of longitudinal mode spacings, as we will see in section 9.4. For now, however, we will take an explicit example of two longitudinally coupled resonators and produce the rate equations for the optical field.

9.3 Example: A Two-Section Coupled Cavity Laser

As an example to illustrate the simplicity of this technique, we shall derive local field rate equations for a two-section longitudinally coupled cavity laser, illustrated in figure 9.1. It consists of two sections of lengths L_1 and L_2, terminated on the outside by mirrors with amplitude reflectivities r_0 and r_3, respectively. They are separated by a gap, which is characterized by its transmission and reflection coefficients t_{12}, t_{21}, r_{11}, and r_{22}, as illustrated. We shall derive rate equations for the amplitudes of the traveling wave fields in each cavity that are traveling toward the gap, as measured at the gap (E_1 and E_2 in the figure). We denote the waves propagating away from the gap by E'_1 and E'_2.

For an optical field at frequency Ω, we can write the relations linking the fields by inspection [9]. They are

$$\begin{aligned} E_1 &= r_0 e^{\varphi_1} E'_1 \\ E'_1 &= r_{11} E_1 + t_{21} E_2 \\ E_2 &= r_3 e^{\varphi_2} E'_2 \\ E'_2 &= r_{22} E_2 + t_{12} E_1 \end{aligned} \qquad (10)$$

where φ_1 and φ_2 are defined by

$$\varphi_1 \equiv -2j\Omega\,\mu_1 L_1/c, \quad \varphi_2 \equiv -2j\Omega\,\mu_2 L_2/c \qquad (11)$$

and μ_1 and μ_2 are the (complex) indices of refraction in each cavity. Elimination of E'_1 and E'_2 yields

$$\begin{aligned} E_1 &= \frac{e^{-\varphi_1}}{r_0 r_{11}} E_1 + \frac{t_{21}}{r_{11}} E_2 \\ E_2 &= \frac{e^{-\varphi_2}}{r_3 r_{22}} E_2 + \frac{t_{12}}{r_{22}} E_1 \end{aligned} \qquad (12)$$

Consequently, we can write the matrix $\tilde{\Gamma}(\Omega)$ as

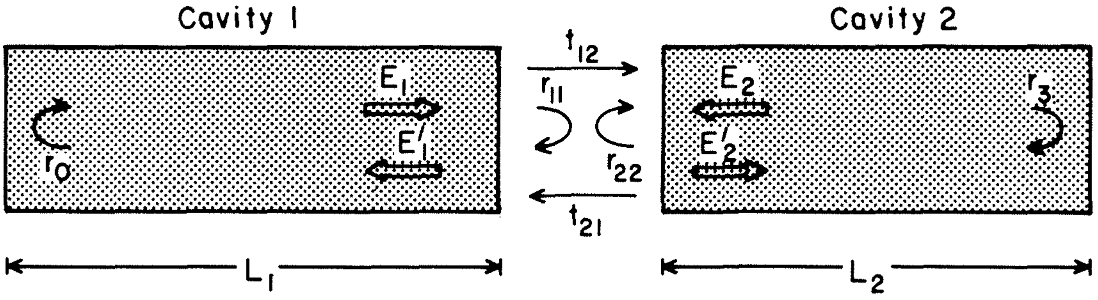

Figure 9.1: Schematic of a two-section coupled cavity laser. The gap is characterized by reflectivities r_{11} and r_{22}, and transmissivities t_{21} and t_{22}. The reflectivities at the ends are r_0 and r_3. The lengths are L_1 and L_2, and the (complex) indices of refraction (incorporating gain or loss) are μ_1 and μ_2. All fields are measured at the gap in each laser cavity. Primed fields are the amplitudes of the waves traveling away from the gap; unprimed fields are the amplitudes of the waves traveling toward the gap.

$$\overset{\approx}{\Gamma}(\Omega) \equiv \begin{pmatrix} \dfrac{e^{-\varphi_1}}{r_0 r_{11}} - 1 & \dfrac{t_{21}}{r_{11}} \\ \dfrac{t_{12}}{r_{22}} & \dfrac{e^{-\varphi_2}}{r_3 r_{22}} - 1 \end{pmatrix} \tag{13}$$

For most cases of interest, the gap is short enough that the transmission and reflection coefficients of the gap are independent of frequency over the gain linewidth of the lasing medium. Consequently, we can drop their derivatives. The derivative of $\overset{\approx}{\Gamma}$ becomes

$$\overset{\approx}{\Gamma}_\Omega = \begin{pmatrix} \dfrac{2j\mu_1 L_1}{c} \dfrac{e^{-\varphi_1}}{r_0 r_{11}} & 0 \\ 0 & \dfrac{2j\mu_2 L_2}{c} \dfrac{e^{-\varphi_2}}{r_3 r_{22}} \end{pmatrix} \tag{14}$$

Since $\overset{\approx}{\Gamma}_\Omega$ is diagonal, inverting it is trivial. The matrix that enters the first-order rate equation (9), $-\overset{\approx}{\Gamma}_\Omega^{-1}\overset{\approx}{\Gamma}$, is given by

$$\begin{pmatrix} \dfrac{c}{2j\mu_1 L_1}(r_0 r_{11} e^{\varphi_1} - 1) & \dfrac{-c}{2j\mu_1 L_1} \dfrac{t_{21}}{r_{11}} r_0 r_{11} e^{\varphi_1} \\ \dfrac{-c}{2j\mu_2 L_2} \dfrac{t_{12}}{r_{22}} r_3 r_{22} e^{\varphi_2} & \dfrac{c}{2j\mu_2 L_2}(r_3 r_{21} e^{\varphi_2} - 1) \end{pmatrix} \tag{15}$$

If we write the rate equation system as

$$\frac{dE_1}{dt} = j\omega_1 E_1 + j\kappa_{21} E_2 \tag{16a}$$

$$\frac{dE_2}{dt} = j\omega_2 E_2 + j\kappa_{12} E_1 \tag{16b}$$

then we have

$$\omega_1 = \frac{c}{2j\mu_1 L_1}(r_0 r_{11} e^{\varphi_1} - 1) \tag{17a}$$

$$\omega_2 = \frac{c}{2j\mu_2 L_2}(r_3 r_{22} e^{\varphi_2} - 1) \tag{17b}$$

$$\kappa_{21} = \frac{-c}{2j\mu_1 L_1} t_{21}(r_0 e^{\varphi_1}) \tag{17c}$$

$$\kappa_{12} = \frac{-c}{2j\mu_2 L_2} t_{12}(r_3 e^{\varphi_2}) \tag{17d}$$

and the eigenvalue equation defining the lasing frequency, $\Gamma(\Omega) = 0$, is

$$\left[\frac{e^{-\varphi_1}}{r_0 r_{11}} - 1\right]\left[\frac{e^{-\varphi_2}}{r_3 r_{22}} - 1\right] = \frac{t_{21} t_{12}}{r_{11} r_{22}} \tag{18}$$

The last term on the right-hand side is significant; we will give it a special designation,

$$K \equiv \frac{t_{21}t_{12}}{r_{11}r_{22}} \tag{19}$$

It is a well-known result of microwave theory that for a lossless two-port network characterized by transmission and reflection coefficients t_{21}, t_{12}, r_{11}, and r_{22}, K is always negative and real.

Let us compare equation (17) for the coupling coefficients of the local fields with the coupling coefficients derived from coupled-mode theory (not including the continuous spectrum) [4]:

$$\kappa_{\nu\sigma} = -\sum_{\mu}\left\{(\Omega_{1\nu} - \omega_{\mu})\int_{V_1} \mu_1^2 e_{1\nu} e_{c\mu} dV \int_{V_2} \mu_2^2 e_{2\sigma} e_{c\mu} dV\right\} \tag{20}$$

where $\Omega_{1\nu}$ is the resonant frequency of the *νth* ICM, ω_{μ} is the resonant frequency of the *μth* CCM, μ_1 is the index of refraction used to define the ICM in cavity 1, μ_c is the actual index of refraction seen by the CCM, $e_{1\nu}$ is the field pattern of the *νth* ICM, and $e_{c\mu}$ is the field pattern of the *μth* CCM. The advantage of local field equations begins to appear. In coupled-mode theory, one must solve for the complete field patterns of both the ICM's and CCM's, as well as the lasing eigenfrequencies ω_{μ}; perform many overlap integrals between the different modes; and finally sum over all of the composite cavity modes. As many as 400 terms in the summation [4] may be necessary before the expression (20) converges. On the other hand, one need only solve for a root of the eigenvalue equation (and in fact, only get close to a root!) to use local field equations.

By ingoring the presence of self-coupling coefficients, Marcuse [5] has heuristically calculated cross-coupling coefficents based on considerations of power flow. The cross-coupling coefficients for a given system can vary, depending upon how one chooses to normalize the fields (the effect of a change in field normalization is to multiply one and divide the other cross-coupling coefficient by the same constant); nevertheless, there are irreconcilable differences between equations (17c-d) and the heuristic formulas. The latter are lacking the final parenthetical expression in each of (17c-d).

As a comparison of the local field rate equation-derived coefficients, the heuristic formulas, and numerical results based on coupled-mode theory, we consider the particular case of two identical cavities. We take $\mu_1 L_1 = \mu_2 L_2 \equiv \mu L$, $\varphi_1 = \varphi_2 \equiv \varphi$, and $r_0 = r_3 = 1$. The reference planes around the gap can be chosen so that $r_{11} = -r_{22} \equiv r$, and r is positive real. In this case, the secular equation can be solved analytically.

$$(e^{-\varphi} - r)(e^{-\varphi} + r) = t_{21}t_{12} \rightarrow e^{-\varphi} = \sqrt{r^2 + t_{21}t_{12}} \tag{21}$$

The intercavity coupling coefficients become

$$\kappa_{21} = \frac{-c}{2j\mu L} t_{21} \frac{1}{\sqrt{r^2 + t_{21}t_{12}}} , \quad \kappa_{12} = \frac{-c}{2j\mu L} t_{12} \frac{1}{\sqrt{r^2 + t_{21}t_{12}}} \tag{22}$$

Allowing for differences in field normalizations, these are the same as Marcuse's heuristic formulas, with the addition of a correction factor $1/(\sqrt{r^2 + t_{21}t_{12}})$. As we mentioned, for a lossless gap, $K \equiv t_{12}t_{21}/r_{11}r_{22}$ must be negative real. Thus, our definitions of r_{11} and r_{22} require that the product $t_{12}t_{21}$ be positive real; since $|r|^2 + |t|^2 = 1$ for a lossless gap, the correction factor is simply 1, and the heuristic formulas are correct.

However, for lossy gaps, numerical calculations show that the heuristic formulas fall short by a factor "close to one-half" [5]. For a lossy gap, $|r|^2 + |t|^2 < 1$; consequently, the correction factor is going to increase somewhat. How large will it get? As the gap losses increase, the transmission will become negligibly small compared to the reflectivity, which will approach the dielectric reflectivity of one surface of the gap. In this limit, then, the correction term will become

$$\frac{1}{\sqrt{r^2 + t_{21}t_{12}}} \rightarrow \frac{1}{r} \tag{23}$$

and r simply approaches the dielectric reflectivity of the first surface of the gap. For a GaAs/air interface, that reflectivity is $r=0.55$, which exactly accounts for the discrepancy between heuristic and numerical results.

It is important to note that the correction term is real only for the cases of equal optical path length, equal gain, and equal reflectors on both lasers, and the gap must be either lossless or an integral number of quarter-wavelengths long. These are rather specialized circumstances, and are unlikely to occur in a practical device. In general, one must use the exact formulas (17) to be assured of the correct coupling coefficients.

For cavities of unequal length, not only will the coupling coefficients differ from the heuristic formulas, but, as we can see from (17), they will in general be different for different longitudinal modes of the resonator system. This becomes apparent by considering the case of a "master-slave" combination wherein one laser is pumped much harder than the other and the coupling is weak. Take laser number 1 as the master, with laser number 2 biased well below threshold. Then roots of the dispersion equation occur for values of Ω_0 near those where $\exp(-\varphi_1) - r_{11}r_0 = 0$. While one coupling coefficient, κ_{21}, is closely given by the heuristic formula

$$\kappa_{21} = \frac{-c}{2j\mu_1 L_1}\frac{t_{21}}{r_{11}} \tag{24}$$

(although there is the correction of r_{11} to be included), the other,

$$\kappa_{12} = \frac{-c}{2j\mu_2 L_2} t_{12} r_3 e^{-\varphi_2} \tag{25}$$

will be far smaller, and of a completely different phase, than that predicted by the heuristic formulas. For different longitudinal modes, the imaginary part of $\varphi_2(\Omega)$ will vary. Hence, different longitudinal modes of the coupled system see different coupling coefficients.

There is still more that we can glean from these formulas. E_i are the amplitudes of a field oscillating at frequency Ω_0. If Ω_0 is not exactly a root of the dispersion equation (18), then E_1 and E_2 will also be oscillatory. If, however, Ω_0 is exactly a root of the dispersion equation, then the field amplitudes will be stationary, and their time derivatives will be zero. In that case, we can relate the intensities at the mirrors of the light in each cavity from equations (16):

$$\frac{I_1}{I_2} = \frac{\mu_1^2 |E_1|^2}{\mu_2^2 |E_2|^2} = \left|\frac{\mu_1}{\mu_2}\right|^2 \left|\frac{\kappa_{21}}{\omega_1}\right|^2 = \left|\frac{\mu_1}{\mu_2}\right|^2 \left|\frac{\omega_2}{\kappa_{12}}\right|^2 \tag{26}$$

Obviously, the self-coupling coefficients cannot be neglected [5]; such an assumption is tantamount to assuming that all of the light lies in one cavity or the other. In fact, the parenthetical terms in (17a-b) also appear in the dispersion equation (on the left-hand side); neither can go to zero unless the coupling factor K (and the coupling between the cavities) vanishes as well. If the gap disappears, the coupling is perfect (and K diverges); only if the transmission goes to zero does K go to zero; then, as we would expect, the two cavities operate independently and the ratio of intensities truly does diverge or vanish, depending upon which cavity reaches threshold first.

The need for rate equations above and beyond the steady-state dispersion equation (18) arises in considerations of the dynamics of the device. Both the self- and cross-coupling coefficients depend upon the carrier density; knowledge of their dependence thereon is necessary for a small-signal analysis. Because of their accuracy and simplicity, the formulas in (17) are more suitable to such treatments than either heuristic or numerical formulas.

9.4 Distant Feedback and the Delay-Differential Equation

Let us now consider the case of a distant feedback mirror, corresponding, for example, to a small reflection off of a distant optical element. In this case, the longitudinal mode spacing of the composite system may only be a few MHz, while the bandwidth of the laser may be a few GHz. In this case, we must approximate Γ over many cycles of its periodicity (over a range of Ω that encompasses many roots) to gain a valid rate equation. However, we can accomplish exactly that.

We derived our rate equation by assuming exponential time variation. This assumption converted time differentials into factors $j\Omega$, and the adiabatic approximation justified in [1] allows us to convert them back again. However, we can generalize this process by viewing $\tilde{\Gamma}(\Omega)$ as the Fourier transform of a linear operator. Thus, if we can approximate $\tilde{\Gamma}$ by a sum of functions of Ω that are transforms of linear operators, then inverting the transform gives us a set of linear rate equations in terms of those linear operators.

To illustrate this, we shall calculate the rate equation for a short cavity coupled to a lossy, much longer cavity (cavity 2 is taken to be the longer cavity). Let us eliminate E_2 from the equation system so as to consider only a single field. Elimination of E_2 from equation (12) yields

$$\left[\left(\frac{e^{-\varphi_1}}{r_0 r_{11}} - 1\right) - K\left(\frac{e^{-\varphi_2}}{r_3 r_{22}} - 1\right)^{-1}\right]E_1 = 0 \qquad (27)$$

By characterizing the field by a single dynamical variable, we have reduced the matrix equation to a scalar equation $\Gamma E_1 = 0$. The assumption of low return reflectivity means that

$$r_3 r_{22} e^{\varphi_2} << 1$$

so we can drop the second "1" in equation (27), which becomes

$$\left[\left(\frac{e^{-\varphi_1}}{r_0 r_{11}} - 1\right) - K\left(\frac{r_3 r_{22}}{e^{-\varphi_2}}\right)\right]E_1 = 0 \qquad (28)$$

Now, the right parenthetical term in (28) is much smaller than 1; the left parenthetical term, which can be written as

$$e^{-\varphi_1 - \ln r_0 r_{11}} - 1, \qquad (29)$$

is therefore also much smaller than 1 when equation (27) is satisfied. Therefore, since the exponential is equal to 1 plus something much less than 1, it can be approximated by the first two terms of its Taylor series:

$$e^{-\varphi_1 - \ln r_0 r_{11}} \approx 1 - (\varphi_1 + 2jN\pi) - \ln r_0 r_{11} \tag{30}$$

where $-2jN\pi$ is the nearest integral multiple of $2j\pi$ to the lasing frequency. Using these two approximations, we find that Γ becomes

$$\Gamma(\Omega) = -\varphi_1 - 2jN\pi - \ln r_0 r_{11} - K r_3 r_{22} e^{\varphi_2} \tag{31}$$

Now we recall the definition of $\varphi_1 = \frac{-2j\Omega\,\mu_1 L_1}{c}$. Multiply by $c/2\mu_1 L_1$ to get

$$\left[j\Omega - j\left(\frac{cN\pi}{2\mu_1 L_1} - j\frac{c}{2\mu_1 L_1}\ln r_0 r_{11}\right) - \frac{c}{2\mu_1 L_1} K r_{22} r_3\, e^{-2j\Omega\,\mu_2 L_2/c}\right] E_1 = 0 \tag{32}$$

We define the following quantities:

$$\tau \equiv \frac{2\mu_2 L_2}{c},\ \kappa \equiv \frac{c}{2\mu_1 L_1} K r_2 r_3,\ \Omega_0 \equiv \frac{cN\pi}{2\mu_1 L_1} - j\frac{c}{2\mu_1 L_1}\ln r_0 r_{11} \tag{33}$$

Then (32) can be written as

$$\left[j\Omega - j\Omega_0 - \kappa e^{-j\Omega\tau}\right] E_1 = 0 \tag{34}$$

Now, using the Fourier transform relations, we still find that the factor $j\Omega$ converts to the differential operator d/dt; however, we can now interpret the exponential $\exp(-j\Omega\tau)$ as a time delay of τ. The relevant rate equation is

$$\frac{dE_1(t)}{dt} = j\Omega_0 E_1(t) + \kappa E_1(t-\tau) \tag{35}$$

This equation is, of course, Lang and Kobayashi's delay-differential equation [8]. Explicitly evaluating the coupling coefficient, we get

$$\kappa = \frac{c}{2\mu_1 L_1} t_{21} t_{12} \frac{r_3}{r_{11}} \tag{36}$$

For a single dielectric interface (the case considered in [8]) this expression is the same as was given in the reference. Although the equation was heuristically derived in [8] by adding a delayed feedback term to a standard rate equation, we have formally justified it and have extended it to the case of a lossy coupling.

Consequently, the delay-differential equation is equivalent to the full set of multimode rate equations for the modes of the composite cavity.

9.5 Conclusions

While it may be desirable to analyze coupled systems in terms of the fields in the individual cavities, grave problems are encountered if one attempts to use the modes of the individual cavities and achieve quantitatively correct equations. Either one is forced to use an integral representation of the field in each cavity or use an incomplete set of basis functions. Even in the latter case, the number of longitudinal modes required for a given accuracy may be undesirably large; such is almost certainly the case in strongly coupled lasers.

An alternate representation, which does not run into the problems of coupled-mode theory, is to derive local field rate equations. Such a treatment can yield quite simple expressions for the self- and cross-coupling coefficients. The formalism relies on the development of a set of frequency-dependent relations between the different field amplitudes and the subsequent conversion of those relations into a set of first-order differential equations for the fields. Since the fields from which the basic relations are derived are based on the composite cavity modes, a local field theory possesses none of the difficulties of a theory based upon individual cavity modes.

We treated the case of two longitudinally coupled laser cavities and calculated the coupling coefficients between the fields in the two cavities. We calculated the corrections to Marcuse's heuristic formulas and showed that they agreed with numerical calculations, while providing simple analytic formulas for the self- and cross-coupling coefficients.

We then showed how the formalism can be extended to generally derive linear rate equations from approximations of $\tilde{\Gamma}(\Omega)$. As an example, we derived and justified the previously heuristically derived delay-differential equation of Lang and Kobayashi and calculated the coupling coefficient of the delayed term resulting from a general coupling element.

References

[1] R. J. Lang and A. Yariv, IEEE J. Quant. Elect., vol. QE-21, pp. 1683-1688 (1985).

[2] R. J. Lang and A. Yariv, IEEE J. Quant. Elect., vol. QE-22, pp. 436-449 (1986).

[3] R. J. Lang and A. Yariv, "Local field rate equations for coupled optical resonators," unpub.

[4] D. Marcuse, IEEE J. Quant. Elect., vol. QE-21, pp. 1819-1826 (1985).

[5] D. Marcuse, IEEE J. Quant. Elect., vol. QE-22, pp. 223-226 (1986).

[6] D. Marcuse and T-P Lee, IEEE J. Quant. Elect., vol. QE-20, pp. 166-176 (1984).

[7] G. Agrawal, J. Appl. Phys., vol. 56, pp. 3110-3115 (1984).

[8] R. Lang and K. Kobayashi, IEEE J. Quant. Elect., vol. QE-16, pp. 347-355 (1980).

[9] C. H. Henry and R. F. Kazarinov, IEEE J. Quant. Elect., vol. QE-21, pp. 255-263 (1985).

[10] R. J. Lang, J. Salzman and A. Yariv, paper #FBB5, presented at Conference on Integrated and Guided Wave Optics, Atlanta, Georgia, February 26-28, 1986.

[11] R. J. Lang and A. Yariv, "Coupling coefficients for coupled-cavity lasers," unpub.

*

*

*